Global numerical modeling of magnetized plasma in a linear device

Magnussen, Michael Løiten; Rasmussen, Jens Juul; Naulin, Volker; Madsen, Jens

Publication date:
2017

Document Version
Publisher's PDF, also known as Version of record

Global numerical modeling of magnetized plasma in a linear device

A thesis submitted for the degree of
Doctor of Philosophy

to the
Department of Physics
Technical University of Denmark

Technical University of Denmark

by
Michael Løiten

Global numerical modeling of magnetized plasma in a linear device

Supervisor:	Prof. Jens Juul Rasmussen Technical University of Denmark
Co-supervisors:	Prof. Volker Naulin Technical University of Denmark Researcher Jens Madsen Technical University of Denmark
Examiners:	Reader Dr. Bogdan Hnat University of Warwick Assoc. Prof. Dr. Alexander Kendl Universität Innsbruck Assoc. Prof. Anders Peter Andersen Technical University of Denmark

Submitted to the Technical University of Denmark on March 6$^{\text{th}}$ 2017

The latest version of this document together with the numerical code can be found at celma-project.github.io.

Abstract

Understanding the turbulent transport in the plasma-edge in fusion devices is of utmost importance in order to make precise predictions for future fusion devices. The plasma turbulence observed in linear devices shares many important features with the turbulence observed in the edge of fusion devices, and are easier to diagnose due to lower temperatures and a better access to the plasma. In order to gain greater insight into this complex turbulent behavior, numerical simulations of plasma in a linear device are performed in this thesis.

Here, a three-dimensional drift-fluid model is derived from first principles for a magnetized plasma in a linear device. To account for the fluctuations at the same level as the background plasma, the traditional split between background and fluctuations has not been made. The model is implemented using the BOUT++ framework and is solved numerically. Special attention is given to the treatment of the singularity at the cylinder axis, and at the inversion of the non-linear elliptic equation, which is done to obtain the electrical potential. The evolution of the plasma through the steady-state, linear phase, and turbulent phase is investigated and compared for different B-field strengths. It is found that drift-waves are responsible for the onset of turbulence, and that the turbulent radial flux is causing a flattening of the density profiles. Coherent structures from the intermittent radial flux in the turbulent state are investigated.

Results of simulations using the Boussinesq approximation is compared to full simulations. It is found that the Boussinesq approximation leads to an unphysical increase of the electrical potential as ions and electrons are lost at a different rate.

Finally, the results from the full simulations are compared with simulations performed at different ionization levels, using a simple model for plasma interaction with neutrals. It is found that the steady state and the saturated state of the system bifurcates when the neutral interaction dominates the electron-ion collisions.

Keywords: Cylindrical plasma, Drift-fluid equations, Numerical modeling, Drift-waves, Plasma turbulence, Coherent structures, Sheath boundary condition

Resumé

For at kunne lave præcise forudsigelser om udviklingen af et plasma i fusionsmaskiner er forståelsen af turbulent transport på plasmaranden yderst vigtig. Den plasmaturbulens, der observeres i lineære maskiner har mange af de samme karakteristika som den i fusionsmaskiner, men den er nemmere at karakterisere, da temperaturene er lavere og plasmaet er lettere tilgængeligt. I denne afhandling er numeriske simuleringer af et magnitseret plasma i en lineær maskine udført for at få bedre indsigt i den komplekse turbulente transport, der finder sted der.

Der udledes en tredimensionel drift-fluid model fra første principper for et magnitseret plasma i en lineær maskine. For at tage højde for fluktuationer i samme størrelsesorden som baggrundsplasmaet, er der ikke foretaget den traditionelle opdeling i baggrundsplasma og fluktuationer. Modellen er implementeret ved brug af BOUT++ frameworket og bliver løst numerisk. Der bliver lagt særlig vægt på hvordan singulariteten på cylinder aksen behandles og på inversionen af den ikke-lineære elliptiske ligning, der benyttes til at finde det elektriske potentiale. Udviklingen af plasmaet gennem ligevægtstilstand, den lineære fase og den turbulente fase bliver undersøgt og sammenlignet for forskellige B-felt styrker. Det konstateres at driftbølger forårsager turbulens og at den radielle flux af plasma leder til en udfladning af tæthedsprofilerne. Ydermere undersøges koherente strukturer i den radielle flux i den turbulente fase.

Resultaterne fra simuleringer hvor Boussinesq approksimationen bruges sammenlignes med simuleringer for det fulde system. Det ses at Boussinesq approksimationen fører til en ufysisk øgning af det elektriske potentiale, da elektroner og ioner forsvinder med forskellige rater. Endeligt bliver resultaterne fra simuleringer af det fulde system sammelignet med simuleringer af forskellige ioniseringsniveauer ved at bruge en simpel model for plasma-neutral vekselvirkninger. Det konstateres at ligevægtstilstanden og den turbulente tilstand bifurkerer når vekselvirkningen med neutrale dominerer over elektron-ion kollisioner.

Acknowledgments

During the work of this thesis I have had the wonderful opportunity to work with, discuss with, and obtain help from many people which I here would like to pay my homage to.

I would like the express my gratitude towards my supervisors Prof. Jens Juul Rasmussen and Prof. Volker Naulin for giving me the opportunity to carry out this work in the PPFE group. The many discussions with Prof. Rasmussen, who has always met me with patience and a joyful spirit, has been of great help. Our discussions about linear wave theory and plasma turbulence has been particularly helpful. Further, the invaluable help on the numerical treatment of the cylinder axis singularity and the inversion algorithm for the potential from Prof. Naulin is highly appreciated. So is his grand overview in plasma physics and his remarkable skill to draw fast conclusions from complex models.

Next, I would like to thank my co-supervisor, researcher Jens Madsen for his insight in theoretical and numerical methods and for his patience with my many questions. I have also benefited greatly from senior scientist Anders Henry Nielsen for his expertise in the usage of the super computers.

Besides my colleagues at PPFE, I have had the pleasure to work with PPFE's collaborators at the University of York. My wholehearted appreciation goes to Senior Lecturer Dr. Benjamin D. Dudson, whom has hosted my research stays, for his indispensable help, for prioritizing his valuable time to discussions with me and for being so forthcoming. My thanks also goes to Dr. Jarrod Leddy, Dr. Peter Hill, Dr. David Dickinson and Dr. Brendan Shanahan for our fruitful discussions. I also acknowledge the rest of the BOUT++-team for their technical assistance and their continuous efforts making BOUT++ better.

I would like to thank my close colleagues which I have been so lucky to share an office with, namely Dr. Ning Yan, Frederik Treue, Dr. Asger Schou Jacobsen, Alexander Simon Thrysøe, Jeppe Miki Busk Olsen, Aslak Sindbjerg Poulsen and Galina Avdeeva. Thank you for the good discussions and the great humor in the office. I would especially like to thank Alexander Simon Thrysøe for the lengthy discussion we have had about physics and mathematics, and for the friendship with him and his wife outside the office time.

Besides my colleagues, I have had the most fortunate chance to get to know Dr. Clemens Schäfermeier. I would like to thank him for our great bicycle trips, and our many good discussions about philosophy, physics and the Ph.D.-student life.

I would like to thank Alexander Simon Thrysøe, Assoc. Prof. Mirko Salewski and Dr. Asger Schou Jacobsen for proof-reading this manuscript.

I would like to thank my family for always supporting me. Finally, I would like to dedicate a very special thank you to my wife, Lenka Magnussen, who has supported me so much during the whole thesis, and for having taken so good care of our son during the moments when daddy have had to work late. I could really not have done this without your support!

Contents

Chapter 1

Introduction

We will here motivate to the work performed in this thesis by putting it in a larger context. The introduction is meant for a broad audience, and only a minimal knowledge of physics is required. At the end of this chapter, an outline of the structure of the thesis will be given.

1.1 Motivation

The ultimate motivation of this thesis is set by the goal of providing clean energy to a growing population with an increasing standard of living. One projection of the increased energy demand[1] is given in fig. 1.1.

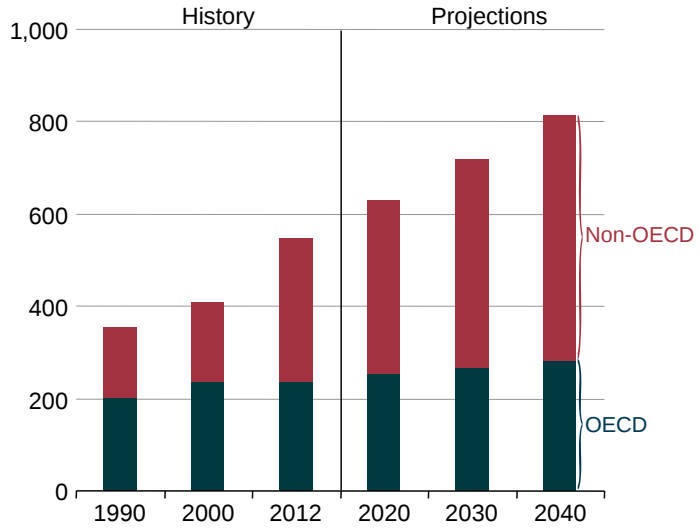

Figure 1.1: Historic and projected energy consumption from [1]. The ordinate is given in quadrillion British thermal unit, which approximately equals 10^{18} *J.*

As the bulk-part of the current energy consumption is provided by limited energy sources, a more sustainable approach is needed.

One candidate for a more sustainable energy production is energy production through thermonuclear fusion. We will here give a short summary of the process. For more

[1]Words like "energy consumption" and "energy production" will here refer to conversions of the same amount of energy from between a low and high entropy state.

introduction on the topic, see [2]. If two nuclei can overcome the electrostatic Coulomb-barrier (with the "help" of quantum tunneling), they can fuse into a heavier nucleus. A fusion reaction will release a surplus of energy if the mass of the resulting nucleus is lighter than the sum of the two initial nuclei. The main reaction sought is the $D-T$ reaction, which can be summarized as

$$D + T \rightarrow He^4 + n + 17.6MeV,$$

where the deuterium D can be distilled from sea water, whereas the tritium T must be produced as it is only scarcely available with its short half-life of 12.3 years. The easiest way to obtain T with current day technologies is by breeding it from lithium through the process

$$Li^6 + n \rightarrow T + He^4 + 4.8MeV$$
$$Li^7 + n \rightarrow T + He^4 + n - 2.5MeV.$$

The need of Li could theoretically be replaced by tritium gained from the $D-D$ reaction

$$D + D \rightarrow T + p + 4.03MeV.$$

However, this reaction is a much harder to achieve as it requires substantially higher temperatures. The energy from the resulting ions in these reactions will help to keep the high temperatures needed for fusion to take place, whereas the neutrons will heat water in a heat exchanger to boiling temperatures. The energy in the water will then be converted to electricity through a conventional turbine. In such respect the fusion reactor will be nothing but a high-tech water boiler.

Man-made thermonuclear fusion delivering energy on the grid has yet to be achieved. It is still unclear whether or not it can be produced in technological and economical feasible way. The ITER project [3], with its first plasma operation planned in 2025, is meant to give a better answer to this question by yielding a tenfold energy output of the energy input. The goal of ITER is not to supply the grid with energy. This is planned to be done by the prototype fusion reactor DEMO, which is still in the planning phase, and is meant to answer questions about economically viability.

Scientific and economical feasibility aside, the research of could be driven by the high energy yield alone. To illustrate this let's look at some very approximated numbers, only to get an idea of what ballpark we are in. We can assume that on average a UK citizen uses 195 kWh per day[2][4]. If we now assume a population 12 billion people [5], and that the average consumption per person is 195 kWh per day, we can make a crude estimate on how long the fusion resources will last. The estimate is show in fig. 1.2[3].

The question is therefore: Why have not man-made fusion been made yet? In order to answer this, we can summarize the challenges with the following quote by Sebastien Balibar [10]:

[2] As a comparison to this, MacKay makes an optimistic estimate that UK could yield 180 kWh per person per day from renewable sources with current day technologies [4]

[3] It should not be swept under the rug that the fusion process is creating harmful isotopes by activating the materials in the reactor itself. However, the half-life of these isotopes are much lower than the isotopes from the nuclear waste of a conventional fission reactors. The fusion material is considered to be safe approximately 100 years after operation [6], wheras the nuclear waste from fission have half-lives of thousands to millions of years [7]. It should also be noted that catastrophic events like meltdowns are physically not possible in a fusion reactor.

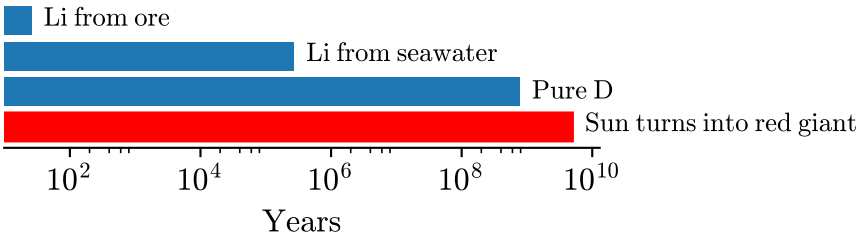

Figure 1.2: Estimated years one could power the world on fusion with a population of 12 *billion people using in average* 195 *kWh per day. It is assumed that all available Li is used for fusion based on the* $D-T$ *reaction, and that all available D is used for the for fusion based on the* $D-D$ *reaction. With the approximated numbers obtained from [5, 4, 8, 9].*

> Fusion is like trying to put the Sun in a box - but we don't know how to make the box.

As the plasma in a working reactor will be held at temperatures at several 10 keV (which translates to several 100 million Kelvin), conventional materials can not be used as a "box". Instead, as the plasma will be in an ionized state, the plasma can be kept in place using a strong magnetic field, as each individual particle of species α is subjected to the Lorentz force

$$\boldsymbol{F}_\alpha = q_\alpha \left(\boldsymbol{E} + \boldsymbol{v}_\alpha \times \boldsymbol{B}\right),$$

and will therefore (at least to first order) move freely parallel to the magnetic field, but be locked to a magnetic field in the perpendicular direction. Thus, the "box" which until now has proven most successful[4] , and which ITER will be based on, is the tokamak, depicted in fig. 1.3.

In the tokamak a twisted, closed magnetic field in a toroidal configuration is used to keep the plasma in place. Close to the toroidal axis the magnetic field closes itself[5] without intersecting with the materials of the tokamak. Hence, the magnetic fields are creating nested magnetic surfaces. These field lines are referred to as "closed" field lines. Moving radially outwards from the toroidal axis the magnetic field is no longer closing only on itself, but rather through a material surface. These field lines are referred to as "open" field lines. In order to remove impurity production and plasma recycling away from the main plasma, the open field lines are diverted away from the main plasma to divertor plates[6]. Thus, when moving radially, the plasma is transitioning from the *plasma edge*, through the position of the *Last Closed Field Surface* (LCFS) to the region of open field lines, called the *Scrape-Off Layer* (SOL). Since the plasma particle motion is constrained in the radial direction because of the gyration, large pressure gradients develops around the LCFS. Instabilities in the edge region can develop from these gradients, both on the macroscopic (machine size) scale in form of ELMs [14], but also on the microscopic scale (usually in the order of mm − cm) such as interchange instabilities [15] and drift-waves [16]. The microscopic instabilities develop into turbulence, and this turbulence is

[4] Alternative concepts such as the "stellarator" and the "spherical tokamak" are areas of active research, and could turn out to serve as better options for the "box" in the future.

[5] Possibly after an infinite number of toroidal revolutions.

[6] Diverting the plasma has a lot of other benefits as described in detail in [12, 13].

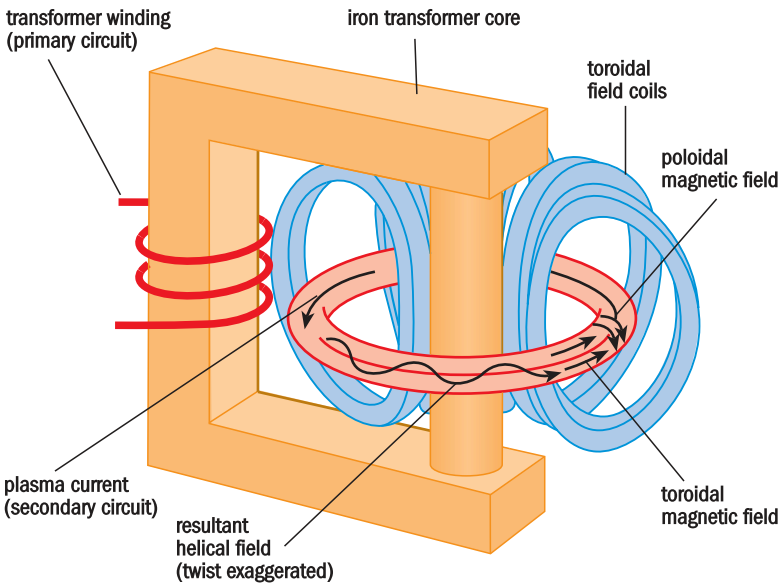

Figure 1.3: Simplified schematics of the tokamak from [11]. A more detailed view of the ITER tokamak can be found in [3].

believed to be the cause of the increased transport levels[7] which exceeds those predicted by *classical* transport from colliding particles, and those predicted by neoclassical theory (which includes transport effect arising from the magnetic field geometry) [18].

Although advances has been done in the last decades, the turbulent processeses in the edge and SOL are still not fully understood. There are for example a lot of open questions related to coherent structures called *blobs* which emerges from the turbulence [19]. In other words, the "box" is "leaking", and we would like a better understanding of how and why it is leaking. The success of ITER achieving a high energy gain would be bleak if it turns out that part of the divertor got melted due to unforeseen turbulent events.

The turbulent processeses in the edge and SOL of a tokamak are hard to analyze, as several physical processeses can be active at once. If one can get a good overview of the individual physical processes first, studying the full system will become easier. An additional challenge of understanding the processeses is that measurements around the LCFS is difficult in a tokamak due the high temperatures and due to the challenge of properly resolve the spatial and temporal scales with few measuring points. One can overcome these obstacles by analyzing processes similar to those found in around the LCFS in linear devices. In such a device, the interchange instability can be eliminated if the machine operates with a straight magnetic field. The temperatures are also lower in a linear device, which makes plasma measurements easier. Hence, they are beneficial for benchmarking numerical codes. Linear machines can usually be operated so that the plasma is freely streaming towards a material surface, which is similar to the situation found in the SOL where the plasma is diverted to the divertor plates with help of the magnetic fields.

This brings us to the aim of this thesis: To numerically simulate some of the

[7] In the so called H-mode this turbulent transport can be suppressed down to the neoclassical levels by a strong shear flow [17].

processes taking place in a linear machine in order to gain insight in non-curvature driven instabilities. Linear machines in themselves are interesting for fusion research and is besides turbulent studies used for material testing [20], studies of *magnetic reconnection* with *X-points* [21] and studies of *plasma detachment* [22] to mention some. We will however limit the scope of this thesis to include only turbulent processes in a straight magnetic field.

Next, let us also state how accurate we would like to be when investigating the plasma. One could say that one want the investigation to be 100 % accurate and include all known physic in the investigation, following the quantum mechanical wave-function of each particle as a function of time. Although tempting, it is easy to show that such a task is not feasible with the present day computer technologies. Imagine just to assign a number to each particle in a $1\,\mathrm{m}^3$ box with a particle density of $10^{18}\,\mathrm{m}^{-3}$ particles[8] using 4 bytes. This would require 4 exabytes of storage. Therefore, we seek to simplify the system while still retaining the important details. The task of simplifaction is comparable to investigation of the time it takes for a white ball takes to fall. Does it matter that the ball is white? One could imagine that there are some reflection properties of the white ball which alters the fall-time. However, such an effect would most likely be negligible. The fact that the ball is white would be far more relevant if we would like to find the cooling time of the ball.

Therefore, instead of following every single particle, we will make some averages on the system which gives us a fluid like description of the plasma. We will further simplify the system by investigating which terms in our model which is small compared to the rest of the terms. This gives us a model which we be can be used to investigate physics happening at a slower scale than the frequency the ions gyrates around the magnetic field line (which in our linear machine is a couple of hundred kHz), and spatial scale around the ion gyration radius taken at the electron temperature (which in our case is around a cm). Notice that we by doing so have excluded physical processes like propagation of electromagnetic waves through the plasma. Although out of scope of our investigation, such a process is important when for example looking at heating of the plasma using electromagnetic waves. We will in our model use a global approach, meaning that we will model the entire plasma, rather than the traditional approach where only fluctuations are investigated.

As such, this thesis does not answer ultimate questions such as: "How can the plasma be operated in order to make man made fusion energy be economically viable." Rather, this thesis makes a very humble contribution needed to answer such questions. More precisely, this thesis aims to answer the following questions:

- What model is suitable for modeling the low frequency turbulence observed in a linear machine?
- What numerical approaches can be used for solving our model?
- How is the plasma evolving in a linear machine?
- Are sheared poloidal flows, suppressing the turbulence transport, found in our model?
- Can coherent structures as blobs and holes be found from our model?
- To what extent does the approximation know as the Boussinesq-approximation, which is often done, alter the solution?
- Does our model capture the features reported in the literature?

[8] These are approximately the particle numbers we will work with in this thesis.

1.2 Thesis structure

The remainder of this thesis is structured into 5 main-parts.

As we would like to simulate a set of equation derived more or less from first principles, the part I is dedicated to the derivation of the CELMA model. To enable full transparency of the derivation, most intermediate calculation step are also shown. As such, this thesis is addressed to a readership familiar with basic concepts of plasma physics. Readers familiar with these derivations may readily skip these intermediate steps, but should pay extra attention to the derivation of the modified vorticity equation, as (to the author's best knowledge) this is not given elsewhere. In chapter 2 the derivation of the fluid equations is done by taking moments of the Fokker-Planck equation including a particle source. The first two fluid moments is taken, and the fluid closure is done by assuming a constant temperature. These equations are further refined using the drift-fluid approximation in chapter 3, where also the fluid drifts are given. In chapter 4 we restrict the system to only be valid for a slowly varying B-field, whereas in chapter chapter 5 a straight magnetic field in a cylinder geometry is imposed. The boundary conditions of the model is also given in chapter 5. The alternative model, which uses the Boussinesq approximation is given in chapter chapter 6 before part I is concluded by a summary in chapter 7.

In part II all the details of the numerical implementation is given. Chapter 8 describes the built-in options from the BOUT++ framework which is used in this thesis, and is followed by implementations which are not included in the BOUT++ in chapter 9. The verification of the numerical implementation is given in chapter 10.

Finally, the results from the numerical simulations are given in part III. The setup is briefly given in chapter 11, followed by a description of the phases of the model in chronological order. Chapter 12 describes the steady state found from the simulations. The system is perturbed and the following linear state is described in chapter 13 together with simplified linear drift-wave theory. The resulting turbulent state is presented in chapter 14, the characteristic of the fluctuation is given in chapter 15, and a description of the sheared poloidal flows are found in chapter 16. Investigation of how the system scales with varying B-field strength is given in chapter 17, and the comparison with the model using Boussinesq approximation is given in chapter 18. How the system scales with the ionization degree is given in chapter 19, and an analysis of the performance of the code is give in chapter 20.

A summary of the conclusion and outlook of this thesis is given in part IV.

To supplement, appendices are given in part V, and are referred to throughout the text.

Part I

Derivation of the CELMA model

Chapter 2

The kinetic equation

We will here derive the fluid equations used in the rest of this thesis from the Fokker-Planck equation [1] by following the approach of [24], but we will in addition include a source term. This source will either add or subtract particles to the distribution function depending on its sign. Readers familiar with the topic may skip to section 2.3.

We are looking at a distribution function $f_\alpha(\boldsymbol{r}, \boldsymbol{v}, t)$ of species α, at point $\boldsymbol{z}(t) = (\boldsymbol{r}(t), \boldsymbol{v}(t))$ in the phase-space at time t. The particles obey the conservation equation

$$\partial_t f_\alpha + \partial_{\boldsymbol{z}} \left([\mathrm{d}_t \boldsymbol{z}] \, f_\alpha \right) = S'_\alpha,$$

where S'_α is a source in the distribution function for species α. We will here use a source which fulfills the following:

$$\int S'_\alpha \, \mathrm{d}^3 v = S_{n,\alpha} \qquad \text{Particles are created.}$$

$$\int m_\alpha \boldsymbol{v} S'_\alpha \, \mathrm{d}^3 v = 0 \qquad \text{They are created with zero bulk velocity.}$$

$$\int \frac{m_\alpha \boldsymbol{v}^2}{2} S'_\alpha \, \mathrm{d}^3 v = S_{E,\alpha} \qquad \text{They have a finite energy when created.}$$

Using that

$$\begin{aligned} \mathrm{d}_t \boldsymbol{r} &= \boldsymbol{v} \\ \mathrm{d}_t \boldsymbol{v} &= \frac{q_\alpha}{m_\alpha} \left(\boldsymbol{E}' + \boldsymbol{v} \times \boldsymbol{B}' \right) \\ \partial_{\boldsymbol{v}} \left(\boldsymbol{E}' + \boldsymbol{v} \times \boldsymbol{B}' \right) &= 0, \end{aligned}$$

where $\boldsymbol{E}'$ and $\boldsymbol{B}'$ are the total (microscopic) fields, we get

$$\partial_t f_\alpha + \boldsymbol{v} \cdot \nabla f_\alpha + \frac{q_\alpha}{m_\alpha} \left(\boldsymbol{E}' + \boldsymbol{v} \times \boldsymbol{B}' \right) \cdot \partial_{\boldsymbol{v}} f_\alpha = S_\alpha.$$

2.1 Fokker-Planck equation

We now introduce $\boldsymbol{E}$ and $\boldsymbol{B}$, which are the fields averaged over several Debye lengths. To incorporate the microscopic fluctuations of the fields, we introduce the collision operator

$$C_\alpha = \sum_\gamma C_{\alpha\gamma}(f_\alpha, f_\gamma)$$

[1] This equation can again be derived from the Klimontovich equation (see for example [23]).

In the scope of this thesis, we will consider only elastic collisions between fully ionized, cold ions, electrons and cold neutrals (which only act as a static background). In other words, we will let $\gamma \in \{e, i, n\}$ (denoting electrons, ions and neutrals), so that

$$C_\alpha = C_{\alpha\beta}(f_\alpha, f_\beta) + C_{\alpha n}(f_\alpha, f_n)$$

where $\alpha, \beta \in \{e, i\}$ and $\alpha \neq \beta$. Furthermore, the collision operator has the following properties:

$$\int C_{\alpha\gamma} \, \mathrm{d}^3 v = 0 \qquad \text{Particle conservation}$$

$$\int m_\alpha \boldsymbol{v} C_{\alpha\gamma} \, \mathrm{d}^3 v = -\int m_\alpha \boldsymbol{v} C_{\gamma\alpha} \, \mathrm{d}^3 v \qquad \text{Momentum conservation}$$

$$\int \frac{m_\alpha \boldsymbol{v}^2}{2} C_{\alpha\gamma} \, \mathrm{d}^3 v = -\int \frac{m_\alpha \boldsymbol{v}^2}{2} C_{\gamma\alpha} \, \mathrm{d}^3 v \qquad \text{Energy conservation}$$

The resulting Fokker-Planck equation reads

$$\partial_t f_\alpha + \boldsymbol{v} \cdot \nabla f_\alpha + \frac{q_\alpha}{m_\alpha} (\boldsymbol{E} + \boldsymbol{v} \times \boldsymbol{B}) \cdot \partial_{\boldsymbol{v}} f_\alpha = S_\alpha + C_\alpha. \tag{2.1}$$

2.2 Moments of Fokker-Planck

To follow the distribution functions in a 6-dimensional phase-space as a function of time is quite a daunting task. Instead, we will follow some averages of the distribution function. This comes at the price of losing kinetic information in the system, like for example Landau damping. We will use eq. (A.1) to denote a weighted velocity average (a moment) of the Fokker-Planck equation. This means that $\langle 1 \rangle_{f_a} = n_a$ is the density of species α. From this, we define

$$\langle \boldsymbol{v}_\alpha \rangle_{f_a} \stackrel{\text{def}}{=} \boldsymbol{u}_a \qquad \text{Macroscopic fluid velocity for } \alpha,$$

$$\langle m_\alpha n_\alpha \boldsymbol{v}_\alpha \boldsymbol{v}_\alpha \rangle_{f_a} \stackrel{\text{def}}{=} \overline{\overline{\boldsymbol{\Pi}}}_\alpha \qquad \text{Momentum flux for } \alpha.$$

We call the difference between the velocity of a single particle and the macroscopic fluid velocity $\boldsymbol{w}$, so that

$$\boldsymbol{w}_\alpha = \boldsymbol{v} - \boldsymbol{u}_\alpha.$$

From this, we define the scalar pressure p_α, the pressure tensor $\overline{\overline{\boldsymbol{P}}}_\alpha$ and the stress tensor $\overline{\overline{\boldsymbol{\pi}}}_\alpha$ as

$$\frac{n_\alpha m_\alpha \langle w_\alpha^2 \rangle_{f_a}}{3} \stackrel{\text{def}}{=} p_\alpha = n_\alpha T_\alpha$$

$$n_\alpha m_\alpha \langle \boldsymbol{w}_\alpha \boldsymbol{w}_\alpha \rangle_{f_a} \stackrel{\text{def}}{=} \overline{\overline{\boldsymbol{P}}}_\alpha$$

$$\overline{\overline{\boldsymbol{\pi}}}_\alpha \stackrel{\text{def}}{=} \overline{\overline{\boldsymbol{P}}}_\alpha - \overline{\overline{\boldsymbol{I}}} p_\alpha$$

where $\overline{\overline{\boldsymbol{I}}}$ is the identity tensor. Finally, we define

$$\int m_\alpha \boldsymbol{v} C_{\alpha\gamma}(f) \, \mathrm{d}^3 v \stackrel{\text{def}}{=} \boldsymbol{R}_{\gamma\to\alpha},$$

where $\boldsymbol{R}_{\gamma\to\alpha}$ is the friction force on α given by γ.

2.2.1 Zeroth moment

We will now work through the zeroth moment term by term by applying $\langle n_\alpha \cdot \rangle_{f_a} = n_\alpha \langle \cdot \rangle_{f_a}$ on eq. (2.1). We have that

$$\begin{aligned}\langle \partial_t n_\alpha \rangle_{f_a} &= \partial_t n_\alpha \langle 1 \rangle_{f_a} \\ &= \partial_t n_\alpha,\end{aligned}$$

that

$$\begin{aligned}\langle n_\alpha \boldsymbol{v} \cdot \nabla \rangle_{f_a} &= \langle n_\alpha \nabla \cdot \boldsymbol{v} \rangle_{f_a} \\ &= \int \nabla \cdot \boldsymbol{v} f_a \, \mathrm{d}^3 v \\ &= \nabla \cdot \int \boldsymbol{v} f_a \, \mathrm{d}^3 v \\ &= \nabla \cdot \langle n_\alpha \boldsymbol{v} \rangle_{f_a} \\ &= \nabla \cdot (n_\alpha \langle \boldsymbol{v} \rangle_{f_a}) \\ &= \nabla \cdot (n_\alpha \boldsymbol{u}_\alpha)\end{aligned}$$

$\boldsymbol{x}$ and $\boldsymbol{v}$ are independent coordinates.

and

$$\begin{aligned}\langle n_\alpha \frac{q_\alpha}{m_\alpha} \boldsymbol{E} \cdot \partial_{\boldsymbol{v}} \rangle_{f_a} =& n_\alpha \frac{q_\alpha}{m_\alpha} \langle \partial_{\boldsymbol{v}} \cdot \boldsymbol{E} \rangle_{f_a} \\ =& \frac{q_\alpha}{m_\alpha} \int \partial_{\boldsymbol{v}} \cdot (\boldsymbol{E} f_\alpha) \, \mathrm{d}^3 v \\ =& \frac{q_\alpha}{m_\alpha} \int_{\partial_\Omega} \boldsymbol{E} f_\alpha \, \mathrm{d}S \\ =& 0,\end{aligned}$$

$\boldsymbol{E}$ independent of $\boldsymbol{v}$

Gauss divergence theorem

$f_\alpha \Big|_{\pm\infty} = 0$

and further that

$$\begin{aligned}\langle n_\alpha \frac{q_\alpha}{m_\alpha} \boldsymbol{v} \times \boldsymbol{B} \cdot \partial_{\boldsymbol{v}} \rangle_{f_a} =& n_\alpha \frac{q_\alpha}{m_\alpha} \langle \boldsymbol{v} \times \boldsymbol{B} \cdot \partial_{\boldsymbol{v}} \rangle_{f_a} \\ =& \frac{q_\alpha}{m_\alpha} \left(\int \partial_{\boldsymbol{v}} \cdot [\boldsymbol{v} \times \boldsymbol{B} f_\alpha] \, \mathrm{d}^3 v - \int f_\alpha \partial_{\boldsymbol{v}} \cdot [\boldsymbol{v} \times \boldsymbol{B}] \, \mathrm{d}^3 v \right) \\ =& \frac{q_\alpha}{m_\alpha} \left(\int_{\partial_\Omega} \boldsymbol{v} \times \boldsymbol{B} f_\alpha \, \mathrm{d}S - \int f_\alpha \partial_{\boldsymbol{v}} \cdot [\boldsymbol{v} \times \boldsymbol{B}] \, \mathrm{d}^3 v \right) \\ =& 0.\end{aligned}$$

Vanishing surface integral, and $\boldsymbol{v} \times \boldsymbol{B} \perp \partial_{\boldsymbol{v}}$

The source term gives

$$\int S'_\alpha \, \mathrm{d}^3 v = S_{n,\alpha}$$

We assume that the plasma consists of only one type of ions (i.e. all the ions have the same ionization, and are in the same excitation state). Extension to this would require a distribution function for each type of atom for each ionization for each excitation state. We will further assume that the creation of electrons and ions to this state happens instantaneously (that is, no intermediate ionization or excitation takes place). If we take

fully ionized helium as an example, this would mean that one ion, and two electrons would be created instantaneously. More generally, N_i ions and ZN_i electrons will be created for the charge number Z. In other words, we have that

$$S_{n,e} = ZS_{n,i} \overset{\text{def}}{=} S_n. \tag{2.2}$$

Finally the collision term gives

$$\int C_{\alpha\beta} \, \mathrm{d}^3 v = 0.$$

Thus our continuity equation becomes

$$\partial_t n_\alpha + \nabla \cdot (n_\alpha \boldsymbol{u}_\alpha) = S_{n,\alpha}. \tag{2.3}$$

2.2.2 First moment

We will now work through the first moment term by term by applying $\langle m_\alpha n_\alpha \boldsymbol{v} \cdot \rangle_{f_a} = m_\alpha n_\alpha \langle \boldsymbol{v} \cdot \rangle_{f_a}$ on eq. (2.1). We have that

$$\begin{aligned} \langle \partial_t m_\alpha n_\alpha \boldsymbol{v} \rangle_{f_a} &= \partial_t m_\alpha n_\alpha \langle \boldsymbol{v} \rangle_{f_a} \\ &= \partial_t \left(m_\alpha n_\alpha \boldsymbol{u}_\alpha \right), \end{aligned}$$

that

$$\begin{aligned} \langle m_\alpha n_\alpha \boldsymbol{v}\boldsymbol{v} \cdot \nabla \rangle_{f_a} &= \nabla \cdot \langle m_\alpha n_\alpha \boldsymbol{v}\boldsymbol{v} \rangle_{f_a} \\ &= \nabla \cdot \overline{\overline{\boldsymbol{\Pi}}}_\alpha \end{aligned} \qquad \begin{array}{l} \boldsymbol{x} \text{ and } \boldsymbol{v} \text{ are} \\ \text{independent} \\ \text{coordinates} \end{array}$$

and

$$\begin{aligned} \langle n_\alpha \boldsymbol{v} q_\alpha \boldsymbol{E} \cdot \partial_{\boldsymbol{v}} \rangle_{f_a} =& n_\alpha q_\alpha \langle \boldsymbol{v}\boldsymbol{E} \cdot \partial_{\boldsymbol{v}} \rangle_{f_a} && \boldsymbol{E} \text{ independent} \\ =& n_\alpha q_\alpha \langle \boldsymbol{v} \partial_{\boldsymbol{v}} \cdot \boldsymbol{E} \rangle_{f_a} && \text{of } \boldsymbol{v} \\ =& n_\alpha q_\alpha \left(\langle \partial_{\boldsymbol{v}} \cdot [\boldsymbol{v}\boldsymbol{E}] \rangle_{f_a} - \langle \boldsymbol{E} \partial_{\boldsymbol{v}} \cdot \boldsymbol{v} \rangle_{f_a} \right) \\ =& n_\alpha q_\alpha \left(\frac{1}{n_\alpha} \int \partial_{\boldsymbol{v}} \cdot [\boldsymbol{v}\boldsymbol{E} f_\alpha] \, \mathrm{d}^3 v - \boldsymbol{E} \langle 1 \rangle_{f_a} \right) \\ =& n_\alpha q_\alpha \left(\frac{1}{n_\alpha} \int_{\partial\Omega} \partial_{\boldsymbol{v}} \cdot [\boldsymbol{v}\boldsymbol{E} f_\alpha] \, \mathrm{d}S - \boldsymbol{E} \right) && f_\alpha \Big|_{\pm\infty} = 0 \\ =& - n_\alpha q_\alpha \boldsymbol{E} \end{aligned}$$

further that

$$\begin{aligned} \langle n_\alpha q_\alpha \boldsymbol{v}\boldsymbol{v} \times \boldsymbol{B} \cdot \partial_{\boldsymbol{v}} \rangle_{f_a} =& n_\alpha q_\alpha \langle \boldsymbol{v}\boldsymbol{v} \times \boldsymbol{B} \cdot \partial_{\boldsymbol{v}} \rangle_{f_a} \\ =& q_\alpha \left(\int \partial_{\boldsymbol{v}} \cdot [\boldsymbol{v}\boldsymbol{v} \times \boldsymbol{B} f_\alpha] \, \mathrm{d}^3 v - \int f_\alpha \partial_{\boldsymbol{v}} \cdot [\boldsymbol{v}\boldsymbol{v} \times \boldsymbol{B}] \, \mathrm{d}^3 v \right) \\ =& q_\alpha \left(\int_{\partial_\Omega} \boldsymbol{v}\boldsymbol{v} \times \boldsymbol{B} f_\alpha \, \mathrm{d}S - \int f_\alpha \partial_{\boldsymbol{v}} \cdot [\boldsymbol{v}\boldsymbol{v} \times \boldsymbol{B}] \, \mathrm{d}^3 v \right) && \begin{array}{l} \text{Vanishing} \\ \text{surface integral} \end{array} \\ =& - q_\alpha \left(\int f_\alpha \boldsymbol{v} \partial_{\boldsymbol{v}} \cdot [\boldsymbol{v} \times \boldsymbol{B}] \, \mathrm{d}^3 v + \int f_\alpha \partial_{\boldsymbol{v}} \cdot [\boldsymbol{v}] \, \boldsymbol{v} \times \boldsymbol{B} \, \mathrm{d}^3 v \right) && \boldsymbol{v} \times \boldsymbol{B} \perp \partial_{\boldsymbol{v}} \end{aligned}$$

$$
\begin{aligned}
&= - q_\alpha \int f_\alpha 1 \boldsymbol{v} \, \mathrm{d}^3 v \times \boldsymbol{B} \\
&= - q_\alpha n_\alpha \boldsymbol{u_\alpha} \times \boldsymbol{B}.
\end{aligned}
$$

As we assume that the particles will be generated without any momentum, we have that

$$\int m_a \boldsymbol{v} S'_\alpha \, \mathrm{d}^3 v = 0.$$

Finally, we use the following collision operator

$$\int m_a \boldsymbol{v} C_\alpha \, \mathrm{d}^3 v = \sum_\gamma \int m_a \boldsymbol{v} C_{\alpha\gamma} \, \mathrm{d}^3 v = \int m_a \boldsymbol{v} C_{\alpha\beta} \, \mathrm{d}^3 v + \int m_a \boldsymbol{v} C_{\alpha n} \, \mathrm{d}^3 v = \boldsymbol{R}_{\beta\to\alpha} + \boldsymbol{R}_{n\to\alpha},$$

where the subscript n in $\boldsymbol{R}$ denotes neutrals. Thus, our momentum equation can now be written as

$$\partial_t \left(n_\alpha m_\alpha \boldsymbol{u}_\alpha \right) + \nabla \cdot \overline{\overline{\boldsymbol{\Pi}}}_\alpha - q_\alpha n_\alpha \left(\boldsymbol{E} + \boldsymbol{u_\alpha} \times \boldsymbol{B} \right) = \boldsymbol{R}_{\beta\to\alpha} + \boldsymbol{R}_{n\to\alpha} \tag{2.4}$$

The first term can be written as

$$\partial_t \left(n_\alpha m_\alpha \boldsymbol{u}_\alpha \right) = n_\alpha m_\alpha \partial_t \left(\boldsymbol{u}_\alpha \right) + \boldsymbol{u}_\alpha m_\alpha \partial_t n_\alpha$$

The second term can be expanded further by observing that

$$
\begin{aligned}
\overline{\overline{\boldsymbol{\Pi}}}_\alpha =& \langle m_\alpha n_\alpha \boldsymbol{v}\boldsymbol{v} \rangle_{f_a} \\
=& m_\alpha n_\alpha \langle \boldsymbol{v}\boldsymbol{v} \rangle_{f_a} \\
=& m_\alpha n_\alpha \langle \left(\boldsymbol{w}_\alpha + \boldsymbol{u}_\alpha \right) \left(\boldsymbol{w}_\alpha + \boldsymbol{u}_\alpha \right) \rangle_{f_a} \\
=& m_\alpha n_\alpha \langle \boldsymbol{w}_\alpha \boldsymbol{w}_\alpha + \boldsymbol{u}_\alpha \boldsymbol{w}_\alpha + \boldsymbol{w}_\alpha \boldsymbol{u}_\alpha + \boldsymbol{u}_\alpha \boldsymbol{u}_\alpha \rangle_{f_a} \\
=& m_\alpha n_\alpha \left(\langle \boldsymbol{w}_\alpha \boldsymbol{w}_\alpha \rangle_{f_a} + \boldsymbol{u}_\alpha \langle \boldsymbol{w}_\alpha \rangle_{f_a} + \langle \boldsymbol{w}_\alpha \rangle_{f_a} \boldsymbol{u}_\alpha + \boldsymbol{u}_\alpha \boldsymbol{u}_\alpha \langle 1 \rangle_{f_a} \right) \\
=& m_\alpha n_\alpha \left(\langle \boldsymbol{w}_\alpha \boldsymbol{w}_\alpha \rangle_{f_a} + \boldsymbol{u}_\alpha \boldsymbol{u}_\alpha \right) \\
=& \overline{\overline{\boldsymbol{P}}}_\alpha + m_\alpha n_\alpha \boldsymbol{u}_\alpha \boldsymbol{u}_\alpha \\
=& \overline{\overline{\boldsymbol{\pi}}}_\alpha + \overline{\overline{\boldsymbol{I}}} p_\alpha + m_\alpha n_\alpha \boldsymbol{u}_\alpha \boldsymbol{u}_\alpha.
\end{aligned}
$$

$\boldsymbol{w}_\alpha$ fluctuates around mean, so averages to 0

The pressure tensor $\overline{\overline{\boldsymbol{P}}}_\alpha$ would be isotropic if the particles were free to move in all directions. However, charged particles gyrate whenever moving with a vector component perpendicular to the magnetic field. Thus, the pressure along the magnetic field line is different from the pressure perpendicular to it. Nevertheless, we can observe from the definitions that the tensors must be symmetric.

The stress tensor is assumed to be small compared to the other terms, and can be further written as

$$\overline{\overline{\boldsymbol{\pi}}} = \overline{\overline{\boldsymbol{\pi}}}^S + \overline{\overline{\boldsymbol{\pi}}}^C + \overline{\overline{\boldsymbol{\pi}}}^G$$

where $\overline{\overline{\boldsymbol{\pi}}}^S$ is the viscosity which comes as a consequence of similar species velocity shear, $\overline{\overline{\boldsymbol{\pi}}}^C$ comes from velocity compression along the magnetic field and $\overline{\overline{\boldsymbol{\pi}}}^G$ is attributed to finite Larmor radius (FLR) effects [24].

The second term of eq. (2.4) can now be written as

$$\begin{aligned}\nabla \cdot \overline{\overline{\mathbf{\Pi}}}_\alpha =& \nabla \cdot \overline{\overline{\boldsymbol{\pi}}}_\alpha + \nabla \cdot \overline{\overline{\boldsymbol{I}}} p_\alpha + m_\alpha \nabla \cdot (n_\alpha \boldsymbol{u}_\alpha \boldsymbol{u}_\alpha) \\ =& \nabla \cdot \overline{\overline{\boldsymbol{\pi}}}_\alpha + \nabla p_\alpha + m_\alpha n_\alpha \boldsymbol{u}_\alpha \cdot \nabla \boldsymbol{u}_\alpha + m_\alpha \nabla \cdot (n_\alpha \boldsymbol{u}_\alpha) \boldsymbol{u}_\alpha.\end{aligned}$$

$\nabla \cdot (\boldsymbol{ab}) = \boldsymbol{a} \cdot \nabla \boldsymbol{b} + (\nabla \cdot \boldsymbol{a}) \boldsymbol{b}$

Thus, eq. (2.4) can be written

$$\begin{aligned}& n_\alpha m_\alpha \partial_t (\boldsymbol{u}_\alpha) + \boldsymbol{u}_\alpha m_\alpha \partial_t n_\alpha + m_\alpha n_\alpha \boldsymbol{u}_\alpha \cdot \nabla \boldsymbol{u}_\alpha + m_\alpha \nabla \cdot (n_\alpha \boldsymbol{u}_\alpha) \boldsymbol{u}_\alpha \\ &= -\nabla \cdot \overline{\overline{\boldsymbol{\pi}}}_\alpha - \nabla p_\alpha + q_\alpha n_\alpha (\boldsymbol{E} + \boldsymbol{u}_{\boldsymbol{\alpha}} \times \boldsymbol{B}) + \boldsymbol{R}_{\beta \to \alpha} + \boldsymbol{R}_{n \to \alpha}\end{aligned}$$

$$\begin{aligned}& n_\alpha m_\alpha (\partial_t \boldsymbol{u}_\alpha + \boldsymbol{u}_\alpha \cdot \nabla \boldsymbol{u}_\alpha) + (\partial_t n_\alpha + \nabla \cdot [n_\alpha \boldsymbol{u}_\alpha]) m_\alpha \boldsymbol{u}_\alpha \\ &= -\nabla \cdot \overline{\overline{\boldsymbol{\pi}}}_\alpha - \nabla p_\alpha + q_\alpha n_\alpha (\boldsymbol{E} + \boldsymbol{u}_{\boldsymbol{\alpha}} \times \boldsymbol{B}) + \boldsymbol{R}_{\beta \to \alpha} + \boldsymbol{R}_{n \to \alpha}\end{aligned}$$

Insert continuity equation (eq. (2.3))

$$\begin{aligned}& n_\alpha m_\alpha (\partial_t \boldsymbol{u}_\alpha + \boldsymbol{u}_\alpha \cdot \nabla \boldsymbol{u}_\alpha) \\ &= -\nabla \cdot \overline{\overline{\boldsymbol{\pi}}}_\alpha - \nabla p_\alpha + q_\alpha n_\alpha (\boldsymbol{E} + \boldsymbol{u}_{\boldsymbol{\alpha}} \times \boldsymbol{B}) + \boldsymbol{R}_{\beta \to \alpha} + \boldsymbol{R}_{n \to \alpha} - S_{\alpha,n} m_\alpha \boldsymbol{u}_\alpha. \qquad (2.5)\end{aligned}$$

If we now introduce $\mathrm{d}_{t,\alpha} = \partial_t + \boldsymbol{u}_\alpha \cdot \nabla$ and insert this into eq. (2.5), we get

$$n_\alpha m_\alpha \mathrm{d}_{t,\alpha} \boldsymbol{u}_\alpha = -\nabla \cdot \overline{\overline{\boldsymbol{\pi}}}_\alpha - \nabla p_\alpha + q_\alpha n_\alpha (\boldsymbol{E} + \boldsymbol{u}_{\boldsymbol{\alpha}} \times \boldsymbol{B}) + \boldsymbol{R}_{\beta \to \alpha} + \boldsymbol{R}_{n \to \alpha} - S_{\alpha,n} m_\alpha \boldsymbol{u}_\alpha \qquad (2.6)$$

2.3 Set of equations

We have found that the two first moments of the Fokker-Planck equations (eqs. (2.3) and (2.6)) can be written like

$$\partial_t n_\alpha + \nabla \cdot (n_\alpha \boldsymbol{u}_\alpha) = S_{n,\alpha} \qquad (2.7)$$

$$\begin{aligned}n_\alpha m_\alpha \mathrm{d}_{t,\alpha} \boldsymbol{u}_\alpha =& -\nabla \cdot \overline{\overline{\boldsymbol{\pi}}}_\alpha - \nabla p_\alpha + q_\alpha n_\alpha (\boldsymbol{E} + \boldsymbol{u}_{\boldsymbol{\alpha}} \times \boldsymbol{B}) \\ &+ \boldsymbol{R}_{\beta \to \alpha} + \boldsymbol{R}_{n \to \alpha} - S_{\alpha,n} m_\alpha \boldsymbol{u}_\alpha \qquad (2.8)\end{aligned}$$

where $\mathrm{d}_{t,\alpha} = \partial_t + \boldsymbol{u}_\alpha \cdot \nabla$, and $\boldsymbol{R}_{\gamma \to \alpha}$ denotes the force acting on species α by γ, i.e. the resistivity. Both the resistivity and the viscosity tensor depend on the temperature[2].

We could go on with our derivation and include the second moment, namely the energy equation, which can be used to evolve the temperature in time. The energy equation will depend on a quantity belonging to the next moment, namely the heat flux Q, due to the $\boldsymbol{v} \cdot \nabla f_\alpha$ term in eq. (2.1). The heat flux equation would again depend on a quantity belonging to the next order, and so on.

In other words, we would need a way to properly "close" the system. One often used method to close the set of equations, is the one suggested by Braginskii in his paper from 1965 [25]. This suggestion builds on the kinetic closure of gases derived by Chapman and Enskog [26, 27]. A brief overview of this closure method is given in [28]. Briefly, the closure procedure uses that the mean free path is much larger than the ion Larmor

[2]Temperatures will be specified in terms of energy in this thesis as the temperature in the equations always appear in juxtaposition with the Boltzmann constant k_B. This way of specifying the temperature is common in the literature.

radius (i.e. the plasma is magnetized), and uses this as an expansion parameter. This gives an analytical expression for $\boldsymbol{R}_{\beta\to\alpha}$ (see appendix C) and the components of $\overline{\overline{\boldsymbol{\pi}}}_\alpha$ (see appendix D). The resulting set of equations from this derivation is known as the Braginskii equations.

In this thesis, the closure of the system will be done in a much simpler way. If we assume that the electrons are isothermal, they can be described by a constant temperature, and hence there is no need for an equation to evolve T_e or T_i in time. We will further assume that the ions are cold (T_i is isothermal with a constant temperature equal 0). When deriving the set of equation using the drift-fluid approach (see chapter 3 for details) we will therefore assume that the velocity component perpendicular to the magnetic field is much lower than the ion sound speed. This is in direct contradiction to our assumption of an isothermal system, which requires that the fluid velocity is much larger than the ion sound speed, so that any difference in temperature is quickly smoothed out. In spite of this, we choose to use the assumption as it gives a much simpler system to solve and analyze. Improvements to this crude approximation is therefore subject to future work.

Chapter 3

The drift fluid equations

The non-linear, coupled set of equation (2.7) and (2.8) consists of one continuity equation per species and one momentum equation per direction per species. With one electron fluid and one ion fluid, this totals 8 partial differential equations (PDEs) in a three-dimensional space. Resolving all the details in these equations is computationally heavy, and we will here seek ways of simplifying the equations to lessen the computational demand.

To do so we will exploit the difference in the parallel and the perpendicular dynamics. Due of the gyration of the particles, the dynamics parallel to the magnetic field are much faster than the dynamics perpendicular to the magnetic field. As a consequence, the gradients perpendicular to the magnetic field tend to be much larger than the gradients parallel to the magnetic field. We can exploit this by using a coarser grid in the parallel direction as compared to the perpendicular direction. By these two arguments, we have a good motivation to split our equations into perpendicular and parallel parts.

Next, the computational demand is further lessened through the so-called drift ordering of the perpendicular velocities. This reduces the details we can get out of the set of equations, but has the advantage that the perpendicular velocities can be solved algebraically. The drifts are summarized in eqs. (3.13) and (3.15).

3.1 Decomposition

We will here decompose equation (2.8) into a part which is parallel to the magnetic field, and on which is perpendicular to the magnetic field. The unit vector parallel to the magnetic field is defined as

$$\boldsymbol{b} \stackrel{\text{def}}{=} \boldsymbol{B}/B, \tag{3.1}$$

where $B = \|\boldsymbol{B}\|$. By using eq. (3.1), we can rearrange equation (2.8) in the following way

$$\begin{aligned}
n_\alpha m_\alpha \mathrm{d}_{t,\alpha}\boldsymbol{u}_\alpha &= -\nabla p_\alpha - \nabla\cdot\overline{\overline{\boldsymbol{\pi}}}_\alpha + q_\alpha n_\alpha(\boldsymbol{E}+\boldsymbol{u}_\alpha\times\boldsymbol{B}) + \boldsymbol{R}_{\beta\to\alpha} + \boldsymbol{R}_{n\to\alpha} - S_{\alpha,n}m_\alpha\boldsymbol{u}_\alpha \\
\frac{n_\alpha m_\alpha \mathrm{d}_{t,\alpha}\boldsymbol{u}_\alpha}{n_\alpha q_\alpha B} &= -\frac{\nabla p_\alpha + \nabla\cdot\overline{\overline{\boldsymbol{\pi}}}_\alpha}{n_\alpha q_\alpha B} + \frac{q_\alpha n_\alpha \boldsymbol{E}}{n_\alpha q_\alpha B} + \frac{q_\alpha n_\alpha \boldsymbol{u}_\alpha\times\boldsymbol{B}}{n_\alpha q_\alpha B} + \frac{\boldsymbol{R}_{\beta\to\alpha}}{n_\alpha q_\alpha B} + \frac{\boldsymbol{R}_{n\to\alpha}}{n_\alpha q_\alpha B} - \frac{S_{\alpha,n}m_\alpha\boldsymbol{u}_\alpha}{n_\alpha q_\alpha B} \\
\frac{1}{\omega_{c\alpha}}\mathrm{d}_{t,\alpha}\boldsymbol{u}_\alpha &= -\frac{\nabla p_\alpha}{n_\alpha q_\alpha B} + \frac{\boldsymbol{E}}{B} + \boldsymbol{u}_\alpha\times\boldsymbol{b} - \frac{\nabla\cdot\overline{\overline{\boldsymbol{\pi}}}_\alpha}{n_\alpha q_\alpha B} + \frac{\boldsymbol{R}_{\beta\to\alpha}}{n_\alpha q_\alpha B} + \frac{\boldsymbol{R}_{n\to\alpha}}{n_\alpha q_\alpha B} - \frac{S_{\alpha,n}\boldsymbol{u}_\alpha}{n_\alpha\omega_{c\alpha}},
\end{aligned} \tag{3.2}$$

where $\omega_{c\alpha} = \dfrac{q_\alpha B}{m_\alpha}$ is the cyclotron frequency for species α.[1]

In general, an arbitrary vector $\boldsymbol{a}$ can be written $\boldsymbol{a} = \boldsymbol{a} \cdot \overline{\overline{\boldsymbol{I}}}$, where $\overline{\overline{\boldsymbol{I}}}$ is the identity tensor of rank 2. We introduce the rank-2 tensor $\boldsymbol{bb}$, which is the outer product of twice the unity vector along $\boldsymbol{B}$. Thus,

$$\boldsymbol{a} = \boldsymbol{a} \cdot \left(\overline{\overline{\boldsymbol{I}}} + \boldsymbol{bb} - \boldsymbol{bb}\right) = \underbrace{\boldsymbol{a} \cdot \left(\overline{\overline{\boldsymbol{I}}} - \boldsymbol{bb}\right)}_{\boldsymbol{a}_\perp} + \underbrace{(\boldsymbol{a} \cdot \boldsymbol{b})\, \boldsymbol{b}}_{\boldsymbol{a}_\parallel}. \tag{3.3}$$

In other words, we can find the parallel component (with respect to the magnetic field) by taking the dot product with $\boldsymbol{b}$ and use the result to find the magnitude along $\boldsymbol{b}$. We further observe that

$$\begin{aligned} -\boldsymbol{b} \times (\boldsymbol{b} \times \boldsymbol{a}) &= -\boldsymbol{b}\,(\boldsymbol{b} \cdot \boldsymbol{a}) + \boldsymbol{a}\,(\boldsymbol{b} \cdot \boldsymbol{b}) \\ &= \left(\overline{\overline{\boldsymbol{I}}} - \boldsymbol{bb}\right) \cdot \boldsymbol{a}. \end{aligned} \qquad \begin{array}{l} \boldsymbol{a} \times (\boldsymbol{b} \times \boldsymbol{c}) = \\ \boldsymbol{b}\,(\boldsymbol{a} \cdot \boldsymbol{c}) - \\ \boldsymbol{c}\,(\boldsymbol{a} \cdot \boldsymbol{c}) \end{array}$$

By using the electrostatic approximation $\partial_t \boldsymbol{B} \simeq 0$[2] (see appendix E for details). At the same time we will assume $\nabla \boldsymbol{b} \simeq 0$, which gives

$$\begin{aligned} ([\mathrm{d}_{t,\alpha}\boldsymbol{a}] \cdot \boldsymbol{b})\, \boldsymbol{b} &= \left(\left[\frac{\partial}{\partial t}\boldsymbol{a}\right] \cdot \boldsymbol{b}\right) \boldsymbol{b} + ([\boldsymbol{u}_\alpha \cdot \nabla \boldsymbol{a}] \cdot \boldsymbol{b})\, \boldsymbol{b} && \text{Assume } \partial_t \boldsymbol{b} = 0 \\ &= \frac{\partial}{\partial t}\left([\boldsymbol{a} \cdot \boldsymbol{b}]\, \boldsymbol{b}\right) + ([\boldsymbol{u}_\alpha \cdot \nabla \boldsymbol{a}] \cdot \boldsymbol{b})\, \boldsymbol{b} && \boldsymbol{v} \cdot \boldsymbol{w} = \boldsymbol{w} \cdot \boldsymbol{v} \\ &= \frac{\partial}{\partial t}\left([\boldsymbol{a} \cdot \boldsymbol{b}]\, \boldsymbol{b}\right) + (\boldsymbol{u}_\alpha \cdot [\boldsymbol{b} \cdot \nabla \boldsymbol{a}])\, \boldsymbol{b} && \nabla \cdot (\boldsymbol{vw}) = \boldsymbol{v}\nabla \cdot \boldsymbol{w} + \boldsymbol{w}\nabla \cdot \boldsymbol{v} \\ &= \frac{\partial}{\partial t}\left(a_\parallel \boldsymbol{b}\right) + (\boldsymbol{u}_\alpha \cdot [\nabla\,(\boldsymbol{a} \cdot \boldsymbol{b}) - \boldsymbol{a} \cdot \nabla \boldsymbol{b}])\, \boldsymbol{b} && \text{Assume } \nabla \boldsymbol{b} \text{ is negligible} \\ &= \frac{\partial}{\partial t}\boldsymbol{a}_\parallel + \left(\boldsymbol{u}_\alpha \cdot \nabla a_\parallel\right) \boldsymbol{b} \\ &= \frac{\partial}{\partial t}\boldsymbol{a}_\parallel + \boldsymbol{u}_\alpha \cdot \left(\nabla \left[a_\parallel\right] \boldsymbol{b}\right) && \nabla(v\boldsymbol{w}) = v\nabla(\boldsymbol{w}) + \nabla(v)\boldsymbol{w} \\ &= \frac{\partial}{\partial t}\boldsymbol{a}_\parallel + \boldsymbol{u}_\alpha \cdot \left(\nabla \left[a_\parallel \boldsymbol{b}\right] - a_\parallel \nabla \left[\boldsymbol{b}\right]\right) && \text{Assume } \nabla \boldsymbol{b} \text{ is negligible} \\ &= \frac{\partial}{\partial t}\boldsymbol{a}_\parallel + \boldsymbol{u}_\alpha \cdot \nabla \boldsymbol{a}_\parallel \\ &= \mathrm{d}_{t,\alpha}\boldsymbol{a}_\parallel, \end{aligned} \tag{3.4}$$

Further we have that

$$\begin{aligned} ([\nabla \boldsymbol{a}] \cdot \boldsymbol{b})\, \boldsymbol{b} &= (\boldsymbol{b} \cdot [\nabla \boldsymbol{a}])\, \boldsymbol{b} && c\boldsymbol{v} = \boldsymbol{v}c \text{ in } \mathbb{R} \\ &= \boldsymbol{b}\,(\boldsymbol{b} \cdot [\nabla \boldsymbol{a}]) && \partial_\parallel \overset{\text{def}}{=} \boldsymbol{b} \cdot \nabla \\ &= \boldsymbol{b}\left(\partial_\parallel \boldsymbol{a}\right) && \nabla_\parallel \overset{\text{def}}{=} \boldsymbol{bb} \cdot \nabla \\ &= \nabla_\parallel \boldsymbol{a}, \end{aligned}$$

[1] Note that the "frequency" can be negative because of the sign of q_α. However, this is just a "remnant" of the vector version of this quantity: The angular frequency $\boldsymbol{\omega}_{c\alpha} = \dfrac{q_\alpha \boldsymbol{B}}{m_\alpha}$, where the $\pm$ sign from q_α tells us if a particle is rotating clockwise or counter-clockwise.

[2] $\simeq$ will here be translated to "approximately equal to".

and for rank-2 tensors, we define

$$\left(\nabla \cdot \overline{\overline{\boldsymbol{A}}}\right)_{\parallel} \stackrel{\text{def}}{=} \left(\left[\nabla \cdot \overline{\overline{\boldsymbol{A}}}\right] \cdot \boldsymbol{b}\right) \boldsymbol{b}.$$

For further references, we also define all the gradient operators used in this thesis here. We will use a field aligned coordinate system (i.e. a system where $\boldsymbol{b}$ is parallel to one of the basis vectors), which gives

$$\begin{array}{lll} \partial_{\parallel} \stackrel{\text{def}}{=} \boldsymbol{b} \cdot \nabla & \nabla_{\parallel} \stackrel{\text{def}}{=} \boldsymbol{bb} \cdot \nabla & \nabla_{\perp} \stackrel{\text{def}}{=} \nabla - \nabla_{\parallel} \\ \nabla^2 = \nabla \cdot \nabla & \nabla_{\parallel}^2 = \nabla \cdot \nabla_{\parallel} & \nabla_{\perp}^2 = \nabla \cdot \nabla_{\perp} = \nabla \cdot \left(\nabla - \nabla_{\parallel}\right) = \nabla^2 - \nabla_{\parallel}^2 \end{array}$$

This means that if we right dot eq. (3.2) with $\boldsymbol{bb}$, we get

$$\left(\frac{1}{\omega_{c\alpha}} \mathrm{d}_{t,\alpha} \boldsymbol{u}_{\alpha}\right) \cdot \boldsymbol{bb} = \left(-\frac{\nabla p_{\alpha}}{n_{\alpha} q_{\alpha} B} + \frac{\boldsymbol{E}}{B} + \boldsymbol{u}_{\alpha} \times \boldsymbol{b} - \frac{\nabla \cdot \overline{\overline{\boldsymbol{\pi}}}_{\alpha}}{n_{\alpha} q_{\alpha} B} + \frac{\boldsymbol{R}_{\beta \to \alpha}}{n_{\alpha} q_{\alpha} B} + \frac{\boldsymbol{R}_{n \to \alpha}}{n_{\alpha} q_{\alpha} B} - \frac{S_{\alpha,n} \boldsymbol{u}_{\alpha,\parallel}}{n_{\alpha} \omega_{c\alpha}}\right) \cdot \boldsymbol{bb}$$

$$\frac{1}{\omega_{c\alpha}} \mathrm{d}_{t,\alpha} \boldsymbol{u}_{\alpha,\parallel} = -\frac{\nabla_{\parallel} p_{\alpha}}{n_{\alpha} q_{\alpha} B} + \frac{\boldsymbol{E}_{\parallel}}{B} - \frac{\left(\nabla \cdot \overline{\overline{\boldsymbol{\pi}}}_{\alpha}\right)_{\parallel}}{n_{\alpha} q_{\alpha} B} + \frac{\boldsymbol{R}_{\beta \to \alpha,\parallel}}{n_{\alpha} q_{\alpha} B} + \frac{\boldsymbol{R}_{n \to \alpha,\parallel}}{n_{\alpha} q_{\alpha} B} - \frac{S_{\alpha,n} \boldsymbol{u}_{\alpha,\parallel}}{n_{\alpha} \omega_{c\alpha}} \tag{3.5}$$

If we subtract eq. (3.5) from eq. (3.2), and use that $\nabla_{\perp} = \nabla - \nabla_{\parallel}$ and $\boldsymbol{a} \times \boldsymbol{b} = \boldsymbol{a}_{\perp} \times \boldsymbol{b}$, we get

$$\begin{aligned} \frac{1}{\omega_{c\alpha}} \mathrm{d}_{t,\alpha} \boldsymbol{u}_{\alpha,\perp} = &- \frac{\nabla_{\perp} p_{\alpha}}{n_{\alpha} q_{\alpha} B} + \frac{\boldsymbol{E}_{\perp}}{B} + \boldsymbol{u}_{\alpha,\perp} \times \boldsymbol{b} \\ &- \frac{\left(\nabla \cdot \overline{\overline{\boldsymbol{\pi}}}_{\alpha}\right)_{\perp}}{n_{\alpha} q_{\alpha} B} + \frac{\boldsymbol{R}_{\beta \to \alpha,\perp}}{n_{\alpha} q_{\alpha} B} + \frac{\boldsymbol{R}_{n \to \alpha,\perp}}{n_{\alpha} q_{\alpha} B} - \frac{S_{\alpha,n} \boldsymbol{u}_{\alpha,\perp}}{n_{\alpha} \omega_{c\alpha}} \end{aligned} \tag{3.6}$$

3.2 Velocity drifts

The goal of the drift ordering is to split eq. (3.6) in different orders, yielding algebraic equations for each order of $\boldsymbol{u}_{\alpha,\perp}$. From eq. (B.16) in appendix B, we have that eq. (3.6) can be written in orders of ε as[3]

$$\begin{aligned} \overbrace{\frac{1}{\omega_{c\alpha}} \mathrm{d}_{t,\alpha} \boldsymbol{u}_{\alpha,\perp}}^{\varepsilon^1} = &\overbrace{-\frac{\nabla_{\perp} p_{\alpha}}{n_{\alpha} q_{\alpha} B} + \frac{\boldsymbol{E}_{\perp}}{B} + \boldsymbol{u}_{\alpha,\perp} \times \boldsymbol{b}}^{\varepsilon^0} \\ &\overbrace{- \frac{\left(\nabla \cdot \overline{\overline{\boldsymbol{\pi}}}_{\alpha}\right)_{\perp}}{n_{\alpha} q_{\alpha} B} + \frac{\boldsymbol{R}_{\beta \to \alpha,\perp}}{n_{\alpha} q_{\alpha} B} + \frac{\boldsymbol{R}_{n \to \alpha,\perp}}{n_{\alpha} q_{\alpha} B} - \frac{S_{\alpha,n} \boldsymbol{u}_{\alpha,\perp}}{n_{\alpha} \omega_{c\alpha}}}^{\varepsilon^1}, \end{aligned} \tag{3.7}$$

where the order of the term is indicated above the term. We can now solve eq. (3.7) for $\boldsymbol{u}_{\alpha,\perp}$ by using perturbation theory. To do this, we first assume that

$$\boldsymbol{u}_{\alpha,\perp} = \varepsilon^0 \boldsymbol{u}_{\alpha,0,\perp} + \varepsilon^1 \boldsymbol{u}_{\alpha,1,\perp} + \varepsilon^2 \boldsymbol{u}_{\alpha,2,\perp} + \ldots, \tag{3.8}$$

[3] Note that we write the viscosity part as order $\mathcal{O}(\varepsilon)$, as we for ions assume that $\mu\varepsilon^2 < \varepsilon$.

where

$$\varepsilon^0 \boldsymbol{u}_{\alpha,0,\perp} \gg \varepsilon^1 \boldsymbol{u}_{\alpha,1,\perp} \gg \varepsilon^2 \boldsymbol{u}_{\alpha,2,\perp} \gg \dots,$$

since $\varepsilon \ll 1$.

The basic idea is to split equation eq. (3.7) into one equation for each order (i.e. equation m would only contain $\mathcal{O}(\varepsilon^m)$ terms). In this way, the solution to the $\mathcal{O}(\varepsilon^0)$ equation will be an approximate solution to the system. The first order correction would be given by the solution of the $\mathcal{O}(\varepsilon^1)$ equation, which will depend on the $\mathcal{O}(\varepsilon^0)$ solution due to the non-linearities in $\boldsymbol{u}_{\alpha,\perp}$. The second order correction will be given by the solution of the $\mathcal{O}(\varepsilon^2)$ equation, which depends on the $\mathcal{O}(\varepsilon^1)$ solution, and so on. We note that this is the same strategy as was used for system closure by Chapman, Enskog and Braginskii as stated in [27, 26, 25].

In this thesis, we are only interested in an accuracy in the order of $\mathcal{O}(\varepsilon^1)$. Therefore, we truncate eq. (3.8) after the first order and get

$$\boldsymbol{u}_{\alpha,\perp} \simeq \varepsilon^0 \boldsymbol{u}_{\alpha,0,\perp} + \varepsilon^1 \boldsymbol{u}_{\alpha,1,\perp}. \tag{3.9}$$

If we insert eq. (3.9) into eq. (3.7), we get

$$\overbrace{\frac{1}{\omega_{c\alpha}} \mathrm{d}_{t,\alpha} \varepsilon^0 \boldsymbol{u}_{\alpha,0,\perp}}^{\varepsilon^1} + \overbrace{\frac{1}{\omega_{c\alpha}} \mathrm{d}_{t,\alpha} \varepsilon^1 \boldsymbol{u}_{\alpha,1,\perp}}^{\varepsilon^2} = \overbrace{-\frac{\nabla_\perp p_\alpha}{n_\alpha q_\alpha B} + \frac{\boldsymbol{E}_\perp}{B} + \varepsilon^0 \boldsymbol{u}_{\alpha,0,\perp} \times \boldsymbol{b}}^{\varepsilon^0} + \overbrace{\boldsymbol{u}_{\alpha,1,\perp} \times \boldsymbol{b}}^{\varepsilon^1}$$
$$\overbrace{-\frac{\left(\nabla \cdot \overline{\overline{\boldsymbol{\pi}}}_\alpha\right)_\perp}{n_\alpha q_\alpha B} + \frac{\boldsymbol{R}_{\beta\to\alpha,\perp}}{n_\alpha q_\alpha B} + \frac{\boldsymbol{R}_{n\to\alpha,\perp}}{n_\alpha q_\alpha B} - \frac{S_{\alpha,n} \boldsymbol{u}_{\alpha,\perp}}{n_\alpha \omega_{c\alpha}}}^{\varepsilon^1}.$$

As $\mathrm{d}_{t,\alpha}$ is a function of $\boldsymbol{u}_{\alpha,\perp}$, it should be accounted for in the ordering. If we introduce the notation $\mathrm{d}^m_{t,\alpha}$, where a superscript ^{m} denotes the order, we have that

$$\begin{aligned}
\mathrm{d}^0_{t,\alpha} \boldsymbol{u}_{\alpha,\perp} &= 0 && \text{No } \varepsilon^0 \text{ terms in LHS of eq. (3.7)} \\
\mathrm{d}^1_{t,\alpha} \boldsymbol{u}_{\alpha,\perp} &= \frac{\partial}{\partial t} \boldsymbol{u}_{\alpha,0,\perp} + \boldsymbol{u}_{\alpha,0,\perp} \cdot \nabla \boldsymbol{u}_{\alpha,0,\perp} + \boldsymbol{u}_{\alpha,\parallel} \cdot \nabla \boldsymbol{u}_{\alpha,0,\perp} \\
\mathrm{d}^2_{t,\alpha} \boldsymbol{u}_{\alpha,\perp} &= \frac{\partial}{\partial t} \varepsilon \boldsymbol{u}_{\alpha,1,\perp} + \boldsymbol{u}_{\alpha,0} \cdot \nabla \varepsilon \boldsymbol{u}_{\alpha,1,\perp} + \varepsilon \boldsymbol{u}_{\alpha,1} \cdot \nabla \boldsymbol{u}_{\alpha,0,\perp} + \boldsymbol{u}_{\alpha,\parallel} \cdot \nabla \varepsilon \boldsymbol{u}_{\alpha,1,\perp} \\
&\vdots
\end{aligned}$$

This gives the following set of equations

$$\mathcal{O}(\varepsilon^0): \qquad 0 = \overbrace{-\frac{\nabla_\perp p_\alpha}{n_\alpha q_\alpha B} + \frac{\boldsymbol{E}_\perp}{B} + \varepsilon^0 \boldsymbol{u}_{\alpha,0,\perp} \times \boldsymbol{b}}^{\varepsilon^0} \tag{3.10}$$

$$\mathcal{O}(\varepsilon^1): \qquad \overbrace{\frac{1}{\omega_{c\alpha}} \mathrm{d}^1_{t,\alpha} \varepsilon^0 \boldsymbol{u}_{\alpha,0,\perp}}^{\varepsilon^1} = \overbrace{\boldsymbol{u}_{\alpha,1,\perp} \times \boldsymbol{b}}^{\varepsilon^1} - \overbrace{\frac{\left(\nabla \cdot \overline{\overline{\boldsymbol{\pi}}}_\alpha\right)_\perp}{n_\alpha q_\alpha B} + \frac{\boldsymbol{R}_{\beta\to\alpha,\perp}}{n_\alpha q_\alpha B} + \frac{\boldsymbol{R}_{n\to\alpha,\perp}}{n_\alpha q_\alpha B} - \frac{S_{\alpha,n} \boldsymbol{u}_{\alpha,\perp}}{n_\alpha \omega_{c\alpha}}}^{\varepsilon^1} \tag{3.11}$$

$\vdots$

3.3 Zeroth order perpendicular terms

We will now solve eq. (3.10) for $\boldsymbol{u}_{\alpha,0,\perp}$. This can be done by cross multiply eq. (3.10) with $\boldsymbol{b}$, which yields

$$\begin{aligned}
0 &= -\frac{\nabla_\perp p_\alpha}{n_\alpha q_\alpha B} \times \boldsymbol{b} + \frac{\boldsymbol{E}_\perp}{B} \times \boldsymbol{b} + (\boldsymbol{u}_{\alpha,0,\perp} \times \boldsymbol{b}) \times \boldsymbol{b} \\
&= -\frac{\nabla_\perp p_\alpha \times \boldsymbol{b}}{n_\alpha q_\alpha B} + \frac{\boldsymbol{E}_\perp \times \boldsymbol{b}}{B} + \boldsymbol{b} \times (\boldsymbol{b} \times \boldsymbol{u}_{\alpha,0,\perp}) \\
-\boldsymbol{b} \times (\boldsymbol{b} \times \boldsymbol{u}_{\alpha,0,\perp}) &= -\frac{\nabla_\perp p_\alpha \times \boldsymbol{b}}{n_\alpha q_\alpha B} + \frac{\boldsymbol{E}_\perp \times \boldsymbol{b}}{B} \\
\boldsymbol{u}_{\alpha,0,\perp} &= -\frac{\nabla_\perp p_\alpha \times \boldsymbol{b}}{n_\alpha q_\alpha B} + \frac{\boldsymbol{E}_\perp \times \boldsymbol{b}}{B}.
\end{aligned} \tag{3.12}$$

As we assume electrostatic conditions, we have that $\boldsymbol{E} = -\nabla\phi$, so $\boldsymbol{E}_\perp = -\nabla_\perp\phi$ and $\boldsymbol{E}_\parallel = -\nabla_\parallel\phi$, and we can rewrite eq. (3.12) as

$$\boldsymbol{u}_{\alpha,0,\perp} = \underbrace{-\frac{\nabla_\perp p_\alpha \times \boldsymbol{b}}{q_\alpha n_\alpha B}}_{\boldsymbol{u}_{\alpha,d}} \underbrace{-\frac{\nabla_\perp \phi \times \boldsymbol{b}}{B}}_{\boldsymbol{u}_E} \tag{3.13}$$

$u_{\alpha,d}$ is called the diamagnetic drift. It is important to notice that this drift is opposite for electrons and ions. This is contrary to $\boldsymbol{u}_E$, called the $\boldsymbol{E} \times \boldsymbol{B}$-drift, which causes the same drift direction irrespective of charge.

3.4 First order perpendicular terms

Once $\boldsymbol{u}_{\alpha,0,\perp}$ is known, the algebraic equation for $\boldsymbol{u}_{\alpha,1,\perp}$ can be found by crossing eq. (3.11) with $\boldsymbol{b}$. Assuming electrostatic conditions, this yields

$$\begin{aligned}
(\mathrm{d}_{t,\alpha}\boldsymbol{a}) \times \boldsymbol{b} &= (\partial_t \boldsymbol{a} + \boldsymbol{u}_\alpha \cdot \nabla \boldsymbol{a}) \times \boldsymbol{b} && \text{Electrostatic conditions} \\
&= \partial_t (\boldsymbol{a} \times \boldsymbol{b}) + ([\boldsymbol{u}_\alpha \cdot \nabla \boldsymbol{a}] \times \boldsymbol{b}) && \nabla(\boldsymbol{v}\times\boldsymbol{w}) = (\nabla\boldsymbol{v})\times\boldsymbol{w} - (\nabla\boldsymbol{w})\times\boldsymbol{v} \\
&= \partial_t (\boldsymbol{a} \times \boldsymbol{b}) + \boldsymbol{u}_\alpha \cdot (\nabla [\boldsymbol{a} \times \boldsymbol{b}] + [\nabla \boldsymbol{b}] \times \boldsymbol{a}) && \text{Electrostatic conditions} \\
&= \partial_t (\boldsymbol{a} \times \boldsymbol{b}) + \boldsymbol{u}_\alpha \cdot (\nabla [\boldsymbol{a} \times \boldsymbol{b}]) \\
&= \mathrm{d}_{t,\alpha} (\boldsymbol{a} \times \boldsymbol{b}) .
\end{aligned}$$

This gives

$$\begin{aligned}
\left(\frac{1}{\omega_{c\alpha}} \mathrm{d}^1_{t,\alpha} \boldsymbol{u}_{\alpha,0,\perp}\right) \times \boldsymbol{b} = &(\boldsymbol{u}_{\alpha,1,\perp} \times \boldsymbol{b}) \times \boldsymbol{b} + \frac{\boldsymbol{R}_{\beta\to\alpha,\perp}}{n_\alpha q_\alpha B} \times \boldsymbol{b} + \frac{\boldsymbol{R}_{n\to\alpha,\perp}}{n_\alpha q_\alpha B} \times \boldsymbol{b} \\
&- \frac{\left(\nabla \cdot \overline{\overline{\boldsymbol{\pi}}}_\alpha\right)_\perp}{n_\alpha q_\alpha B} \times \boldsymbol{b} - \frac{S_{\alpha,n} \boldsymbol{u}_{\alpha,0,\perp}}{n_\alpha \omega_{c\alpha}} \times \boldsymbol{b} \\
-\boldsymbol{b} \times (\boldsymbol{b} \times \boldsymbol{u}_{\alpha,1,\perp}) = &-\frac{1}{\omega_{c\alpha}} \mathrm{d}^1_{t,\alpha} (\boldsymbol{u}_{\alpha,0,\perp} \times \boldsymbol{b}) + \frac{\boldsymbol{R}_{\beta\to\alpha,\perp} \times \boldsymbol{b}}{n_\alpha q_\alpha B} + \frac{\boldsymbol{R}_{n\to\alpha,\perp} \times \boldsymbol{b}}{n_\alpha q_\alpha B} \\
&- \frac{\left(\nabla \cdot \overline{\overline{\boldsymbol{\pi}}}_\alpha\right)_\perp \times \boldsymbol{b}}{n_\alpha q_\alpha B} - \frac{S_{\alpha,n} \boldsymbol{u}_{\alpha,0,\perp}}{n_\alpha \omega_{c\alpha}} \times \boldsymbol{b}
\end{aligned}$$

$$\boldsymbol{u}_{\alpha,1,\perp} = -\frac{1}{\omega_{c\alpha}}\mathrm{d}^1_{t,\alpha}\left(\boldsymbol{u}_{\alpha,0,\perp}\times\boldsymbol{b}\right) + \frac{\boldsymbol{R}_{\beta\to\alpha,\perp}\times\boldsymbol{b}}{n_\alpha q_\alpha B} + \frac{\boldsymbol{R}_{n\to\alpha,\perp}\times\boldsymbol{b}}{n_\alpha q_\alpha B} - \frac{\left(\nabla\cdot\overline{\overline{\boldsymbol{\pi}}}_\alpha\right)_\perp\times\boldsymbol{b}}{n_\alpha q_\alpha B} - \frac{S_{\alpha,n}\boldsymbol{u}_{\alpha,0,\perp}}{n_\alpha\omega_{c\alpha}}\times\boldsymbol{b}. \tag{3.14}$$

By substituting eq. (3.13) in eq. (3.14), we obtain

$$\begin{aligned}
\boldsymbol{u}_{\alpha,1,\perp} =& -\frac{1}{\omega_{c\alpha}}\mathrm{d}^1_{t,\alpha}\left(\left[-\frac{\nabla_\perp p_\alpha\times\boldsymbol{b}}{n_\alpha q_\alpha B} - \frac{\nabla_\perp\phi\times\boldsymbol{b}}{B}\right]\times\boldsymbol{b}\right) + \frac{\boldsymbol{R}_{\beta\to\alpha,\perp}\times\boldsymbol{b}}{n_\alpha q_\alpha B} + \frac{\boldsymbol{R}_{n\to\alpha,\perp}\times\boldsymbol{b}}{n_\alpha q_\alpha B} \\
&- \frac{\left(\nabla\cdot\overline{\overline{\boldsymbol{\pi}}}_\alpha\right)_\perp\times\boldsymbol{b}}{n_\alpha q_\alpha B} - \frac{S_{\alpha,n}}{n_\alpha\omega_{c\alpha}}\left(-\frac{\nabla_\perp p_\alpha\times\boldsymbol{b}}{n_\alpha q_\alpha B} - \frac{\nabla_\perp\phi\times\boldsymbol{b}}{B}\right)\times\boldsymbol{b} \\
=& -\frac{1}{\omega_{c\alpha}}\mathrm{d}^1_{t,\alpha}\left(-\frac{\boldsymbol{b}\times[\boldsymbol{b}\times\nabla_\perp p_\alpha]}{n_\alpha q_\alpha B} - \frac{\boldsymbol{b}\times[\boldsymbol{b}\times\nabla_\perp\phi]}{B}\right) + \frac{\boldsymbol{R}_{\beta\to\alpha,\perp}\times\boldsymbol{b}}{n_\alpha q_\alpha B} + \frac{\boldsymbol{R}_{n\to\alpha,\perp}\times\boldsymbol{b}}{n_\alpha q_\alpha B} \\
&- \frac{\left(\nabla\cdot\overline{\overline{\boldsymbol{\pi}}}_\alpha\right)_\perp\times\boldsymbol{b}}{n_\alpha q_\alpha B} - \frac{S_{\alpha,n}}{n_\alpha\omega_{c\alpha}}\left(-\frac{\boldsymbol{b}\times[\boldsymbol{b}\times\nabla_\perp p_\alpha]}{n_\alpha q_\alpha B} - \frac{\boldsymbol{b}\times[\boldsymbol{b}\times\nabla_\perp\phi]}{B}\right) \\
=& -\frac{1}{\omega_{c\alpha}}\mathrm{d}^1_{t,\alpha}\left(\frac{\nabla_\perp p_\alpha}{n_\alpha q_\alpha B} + \frac{\nabla_\perp\phi}{B}\right) + \frac{\boldsymbol{R}_{\beta\to\alpha,\perp}\times\boldsymbol{b}}{n_\alpha q_\alpha B} + \frac{\boldsymbol{R}_{n\to\alpha,\perp}\times\boldsymbol{b}}{n_\alpha q_\alpha B} \\
&- \frac{\left(\nabla\cdot\overline{\overline{\boldsymbol{\pi}}}_\alpha\right)_\perp\times\boldsymbol{b}}{n_\alpha q_\alpha B} - \frac{S_{\alpha,n}}{n_\alpha\omega_{c\alpha}}\left(\frac{\nabla_\perp p_\alpha}{n_\alpha q_\alpha B} + \frac{\nabla_\perp\phi}{B}\right).
\end{aligned}$$

Definition of perp. vectors

Hence,

$$\boldsymbol{u}_{\alpha,1,\perp} = \underbrace{\frac{1}{\omega_{c\alpha}}\mathrm{d}^1_{t,\alpha}\left(-\frac{\nabla_\perp p_\alpha}{n_\alpha q_\alpha B} - \frac{\nabla_\perp\phi}{B}\right)}_{\boldsymbol{u}_{\alpha,p}} + \underbrace{\frac{\boldsymbol{R}_{\beta\to\alpha,\perp}\times\boldsymbol{b}}{n_\alpha q_\alpha B}}_{\boldsymbol{u}_{\alpha,R}} + \underbrace{\frac{\boldsymbol{R}_{n\to\alpha,\perp}\times\boldsymbol{b}}{n_\alpha q_\alpha B}}_{\boldsymbol{u}_{\alpha,\mathrm{Ped}}} \underbrace{-\frac{\left(\nabla\cdot\overline{\overline{\boldsymbol{\pi}}}_\alpha\right)_\perp\times\boldsymbol{b}}{n_\alpha q_\alpha B}}_{\boldsymbol{u}_{\alpha,\nu}} \underbrace{-\frac{S_{\alpha,n}}{n_\alpha\omega_{c\alpha}}\left(\frac{\nabla_\perp p_\alpha}{n_\alpha q_\alpha B} + \frac{\nabla_\perp\phi}{B}\right)}_{\boldsymbol{u}_{\alpha,S}} \tag{3.15}$$

For further reference, we call $\boldsymbol{u}_{\alpha,p}$ the polarization drift, $\boldsymbol{u}_{\alpha,R}$ the resistive drift, $\boldsymbol{u}_{\alpha,\mathrm{Ped}}$ the Pedersen drift as it is related to the Pedersen conductivity given in for example [29], $\boldsymbol{u}_{\alpha,\nu}$ the viscous drift and $\boldsymbol{u}_{\alpha,S}$ the source drift. Note that even though the material derivative in the polarization drift contains parallel derivatives, the resulting vector is purely perpendicular. Finally, we observe that the drift direction for ions and electrons are opposite for all first order drifts due to the charge dependence. For a physical interpretation of the drifts, see [30].

Chapter 4

The model in a slowly varying B-field

In the previous chapter, we derived the fluid drifts from the drift-fluid approximation. We will now insert the fluid drifts into the continuity equations without making any assumption on the *topology* of the $\boldsymbol{B}$-field. We will, however, assume that the $\boldsymbol{B}$-field varies slowly in space and time[1], and that the plasma consists of only one type of atomic element.

By inserting the fluid drifts into the electron continuity equation, we will obtain an equation for the temporal evolution of n. Then, we will sum the electron continuity equation with the ion continuity equation, which will yield an equation for the current balance. These equations will be general for any topology assuming a slowly varying $\boldsymbol{B}$-field, electrostatic conditions and that the drift ordering holds.

In chapter 5 we will constrain the system by specifying a straight magnetic field and zero temperature. From this, we will simplify the system further. The equation for the temporal evolution of the modified vorticity can then be extracted from the current balance equation. Readers familiar with the topic can skip the derivation of the drift-continuity equation, but should read section 4.3.1 and section 4.5 as this gives the start-point of the derivation of the modified vorticity equation.

4.1 The drift-continuity equation

From eq. (2.7), and the fluid drifts presented in chapter 3, we have that

$$\partial_t n_\alpha + \nabla \cdot (n_\alpha \boldsymbol{u}_\alpha) = S_{n,\alpha}$$
$$\partial_t n_\alpha + \nabla \cdot (n_\alpha[\boldsymbol{u}_{\alpha,d} + \boldsymbol{u}_E + \boldsymbol{u}_{\alpha,p} + \boldsymbol{u}_{\alpha,R} + \boldsymbol{u}_{\alpha,\mathrm{Ped}} + \boldsymbol{u}_{\alpha,\nu} + \boldsymbol{u}_{\alpha,S} + \boldsymbol{u}_{\alpha,\parallel}]) = S_{n,\alpha}. \quad (4.1)$$

In order to simplify this equation we will first introduce the curvature operator and the collisional frequencies. Then we will evaluate the divergence terms one by one.

4.1.1 The curvature operator

To ease the calculations, we will introduce the curvature operator. Assuming we are working in a field aligned Clebsch coordinate system (see appendix H), where $\boldsymbol{b}$ is parallel to one of the basis vectors, we have that

$$\nabla_\perp f \times \boldsymbol{b} = -\boldsymbol{b} \times \nabla_\perp f = -\boldsymbol{b} \times (\nabla - \nabla_\parallel) f = -\boldsymbol{b} \times (\nabla - \boldsymbol{b}\boldsymbol{b} \cdot \nabla) f = \nabla f \times \boldsymbol{b}$$

[1]Note that we already used this assumption in eq. (3.4).

as the crossed product of two parallel vectors yields 0. Therefore, we can write

$$\begin{aligned}
-\nabla\cdot\left(\frac{\nabla_\perp f\times\boldsymbol{b}}{B}\right) &= -\nabla\cdot\left(\frac{\nabla f\times\boldsymbol{b}}{B}\right)\\
&= \nabla\cdot\left(\frac{\boldsymbol{b}}{B}\times\nabla f\right) && \nabla\cdot(\boldsymbol{a}\times\boldsymbol{b}) = \boldsymbol{b}\cdot(\nabla\times\boldsymbol{a}) - \boldsymbol{a}\cdot(\nabla\times\boldsymbol{b})\\
&= \nabla f\cdot\left(\nabla\times\frac{\boldsymbol{b}}{B}\right) - \frac{\boldsymbol{b}}{B}\cdot(\nabla\times[\nabla f]) && \nabla\times\nabla f = 0\\
&= \nabla f\cdot\left(\nabla\times\frac{\boldsymbol{b}}{B}\right) && \nabla\times(f\boldsymbol{a}) = f(\nabla\times\boldsymbol{a}) - \boldsymbol{a}\times(\nabla f)\\
&= \nabla f\cdot\left(\frac{1}{B}[\nabla\times\boldsymbol{b}] - \boldsymbol{b}\times\left[\nabla\frac{1}{B}\right]\right)\\
&= \frac{1}{B}\nabla f\cdot[\nabla\times\boldsymbol{b}] - \left(\boldsymbol{b}\times\left[\nabla\frac{1}{B}\right]\right)\cdot\nabla f\\
&= \frac{1}{B}\nabla f\cdot[\nabla\times\boldsymbol{b}] + \left(\left[\nabla\frac{1}{B}\right]\times\boldsymbol{b}\right)\cdot\nabla f && \boldsymbol{a}\cdot(\boldsymbol{b}\times\boldsymbol{c}) =\\
&= \frac{1}{B}\nabla f\cdot[\nabla\times\boldsymbol{b}] + \left[\nabla\frac{1}{B}\right]\cdot(\boldsymbol{b}\times\nabla f) && \boldsymbol{b}\cdot(\boldsymbol{c}\times\boldsymbol{a}) =\\
&\overset{\text{def}}{=} \mathcal{C}(f), && \boldsymbol{c}\cdot(\boldsymbol{a}\times\boldsymbol{b}) \qquad (4.2)
\end{aligned}$$

which is non-zero only if the $\boldsymbol{B}$ field curves.

4.1.2 Collisional drifts

From equation (2.6) in [25], we have that

$$\boldsymbol{R}_{i\to e} = \boldsymbol{R}_u + \boldsymbol{R}_T,$$

where

$$\boldsymbol{R}_u = -\frac{m_e n_e}{\tau_e}\left(0.51\left[\boldsymbol{u}_{e,\parallel} - \boldsymbol{u}_{i,\parallel}\right] + \left[\boldsymbol{u}_{e,\perp} - \boldsymbol{u}_{i,\perp}\right]\right)$$

and

$$\boldsymbol{R}_T = -0.71 n_e\nabla T_e - \frac{3}{2}\frac{n_e}{\omega_e\tau_e}\boldsymbol{b}\times\nabla T_e.$$

τ_e is the inverse of the electron-ion collision frequency ν_{ei} (given analytically in appendix C.1). Assuming constant T_e, we get that

$$\boldsymbol{R}_{i\to e} = \boldsymbol{R}_u = -m_e n_e\nu_{ei}\left(0.51\left[\boldsymbol{u}_{e,\parallel} - \boldsymbol{u}_{i,\parallel}\right] + \left[\boldsymbol{u}_{e,\perp} - \boldsymbol{u}_{i,\perp}\right]\right). \qquad (4.3)$$

Later, we will insert eq. (4.3) into the resistive drift $\boldsymbol{u}_{\alpha,R}$. As $\boldsymbol{u}_{\alpha,R}$ is already a first order drift, and since we are only interested in an accuracy of only $\mathcal{O}(\varepsilon)$, we substitute only the zeroth order drifts into the perpendicular velocities in eq. (4.3). This yields

$$\begin{aligned}
\boldsymbol{R}_{i\to e} &= -m_e n_e\nu_{ei}\left(0.51\left[\boldsymbol{u}_{e,\parallel} - \boldsymbol{u}_{i,\parallel}\right] + \left[(\boldsymbol{u}_{e,d} + \boldsymbol{u}_E) - (\boldsymbol{u}_{i,d} + \boldsymbol{u}_E)\right]\right)\\
&= -m_e n_e\nu_{ei}\left(0.51\left[\boldsymbol{u}_{e,\parallel} - \boldsymbol{u}_{i,\parallel}\right] + \left[\left(-\frac{\nabla_\perp p_e\times\boldsymbol{b}}{q_e n_e B} - \frac{\nabla_\perp\phi\times\boldsymbol{b}}{B}\right) - \left(-\frac{\nabla_\perp p_i\times\boldsymbol{b}}{q_i n_i B} - \frac{\nabla_\perp\phi\times\boldsymbol{b}}{B}\right)\right]\right)
\end{aligned}$$

$$= - m_e n_e \nu_{ei} \left(0.51 \left[\boldsymbol{u}_{e,\parallel} - \boldsymbol{u}_{i,\parallel} \right] + \frac{\nabla_\perp \left(p_e + p_i \right) \times \boldsymbol{b}}{enB} \right)$$

for the resistive force density acting on the electrons by the ions. From momentum conservation we have that $\boldsymbol{R}_{i \to e} = -\boldsymbol{R}_{e \to i}$, which gives

$$\frac{\boldsymbol{R}_{\beta \to \alpha}}{q_\alpha} = - \frac{\boldsymbol{R}_{i \to e}}{\left| \frac{q_\alpha}{e} \right| e}.$$

Inserting this into $\boldsymbol{u}_{\alpha,R}$ of eq. (3.15) yields

$$\begin{aligned}
\boldsymbol{u}_{\alpha,R} =& \frac{\boldsymbol{R}_{\beta \to \alpha} \times \boldsymbol{b}}{n_\alpha q_\alpha B} \\
=& - \frac{\boldsymbol{R}_{i \to e,\perp} \times \boldsymbol{b}}{n_\alpha \left| \frac{q_\alpha}{e} \right| eB} \\
=& - \frac{1}{n_\alpha \left| \frac{q_\alpha}{e} \right| eB} \left(-m_e n_e \nu_{ei} \left[0.51 \left(\boldsymbol{u}_{e,\parallel} - \boldsymbol{u}_{i,\parallel} \right) + \frac{\nabla_\perp \left(p_e + p_i \right) \times \boldsymbol{b}}{enB} \right] \times \boldsymbol{b} \right) && \boldsymbol{a}_\parallel \times \boldsymbol{b} = 0 \\
=& \frac{m_e n_e \nu_{ei}}{n_\alpha \left| \frac{q_\alpha}{e} \right| eB} \left(\frac{\nabla_\perp \left[p_e + p_i \right] \times \boldsymbol{b}}{enB} \right) \times \boldsymbol{b} && \text{Quasi-neutrality} \\
=& \frac{m_e \nu_{ei}}{eB} \boldsymbol{b} \times \left(\boldsymbol{b} \times \frac{\nabla_\perp \left[p_e + p_i \right]}{enB} \right) && -\boldsymbol{b} \times \boldsymbol{b} \times \boldsymbol{a} = \boldsymbol{a}_\perp \\
=& - m_e \nu_{ei} \frac{\nabla_\perp \left(p_e + p_i \right)}{n \left(eB \right)^2}
\end{aligned} \tag{4.4}$$

Next, there will also be a resistive force density on the electrons and ions from the collisions with neutrals. To address this force drift, we start by assuming that

$$\boldsymbol{R}_{n \to \alpha} = -m_\alpha n_\alpha \nu_{\alpha n} \left(\left[\boldsymbol{u}_{\alpha,\parallel} - \boldsymbol{u}_{n,\parallel} \right] + \left[\boldsymbol{u}_{\alpha,\perp} - \boldsymbol{u}_{n,\perp} \right] \right),$$

where $\nu_{\alpha n}$ is given analytically in appendices C.1 and C.2. As we here want to model the neutrals as a static background, we get that

$$\boldsymbol{R}_{n \to \alpha} = -m_\alpha n_\alpha \nu_{\alpha n} \left(\boldsymbol{u}_{\alpha,\parallel} + \boldsymbol{u}_{\alpha,\perp} \right). \tag{4.5}$$

Equation (4.5) will be substituted into the $\boldsymbol{u}_{\alpha,R}$ drift of eq. (3.15). As this is already a first order drift, we substitute only the zeroth order drifts into eq. (4.5). This gives

$$\boldsymbol{R}_{n \to \alpha} = -m_\alpha n_\alpha \nu_{\alpha n} \left(\boldsymbol{u}_{\alpha,\parallel} - \frac{\nabla_\perp p_\alpha \times \boldsymbol{b}}{q_\alpha n_\alpha B} - \frac{\nabla_\perp \phi \times \boldsymbol{b}}{B} \right). \tag{4.6}$$

Inserting eq. (4.6) into the Pedersen drift of eq. (3.15) yields

$$\begin{aligned}
\boldsymbol{u}_{\alpha,\mathrm{Ped}} =& - \frac{m_\alpha n_\alpha \nu_{\alpha n}}{n_\alpha q_\alpha B} \left(\boldsymbol{u}_{\alpha,\parallel} - \frac{\nabla_\perp p_\alpha \times \boldsymbol{b}}{q_\alpha n_\alpha B} - \frac{\nabla_\perp \phi \times \boldsymbol{b}}{B} \right) \times \boldsymbol{b} && \text{Definition of perp. vectors} \\
=& - \frac{\nu_{\alpha n}}{\omega_{c\alpha}} \left(\frac{\nabla_\perp p_\alpha}{q_\alpha n_\alpha B} + \frac{\nabla_\perp \phi}{B} \right).
\end{aligned}$$

4.2 Zeroth order perpendicular terms

We will now evaluate the individual terms of eq. (4.1), starting with the zeroth order terms. By using the curvature operator from eq. (4.2), we find that the $\boldsymbol{E}\times\boldsymbol{B}$ term gives

$$\begin{aligned}\nabla\cdot(n_\alpha \boldsymbol{u}_E) &= n_\alpha \nabla\cdot\boldsymbol{u}_E + \boldsymbol{u}_E\cdot\nabla n_\alpha \\ &= n_\alpha \nabla\cdot\frac{-\nabla_\perp\phi\times\boldsymbol{b}}{B} + \boldsymbol{u}_E\cdot\nabla n_\alpha \\ &= n_\alpha \mathcal{C}(\phi) + \boldsymbol{u}_E\cdot\nabla n_\alpha. \end{aligned} \tag{4.7}$$

and the diamagnetic term gives

$$\nabla\cdot(n_\alpha \boldsymbol{u}_{\alpha,d}) = -\nabla\cdot\left(n_\alpha\frac{\nabla_\perp p_\alpha\times\boldsymbol{b}}{q_\alpha n_\alpha B}\right) = -\nabla\cdot\left(\frac{\nabla_\perp p_\alpha\times\boldsymbol{b}}{q_\alpha B}\right) = \mathcal{C}\left(\frac{p_\alpha}{q_\alpha}\right). \tag{4.8}$$

In other words, we find that $n\nabla\cdot\boldsymbol{u}_{\alpha,d}$ cancels $\boldsymbol{u}_{\alpha,d}\cdot\nabla n$ in the absence of magnetic field inhomogeneities. This cancellation is referred to as *diamagnetic cancellation* in the literature [31].

4.3 First order perpendicular terms

We will here discuss the resistivity terms and the source term of eq. (4.1). The discussion of the polarization and the viscous term will be given in section 4.3.1.

From eq. (4.4) we get that

$$\nabla\cdot(n_\alpha \boldsymbol{u}_{e,R}) = -\nabla\cdot\left(\left|\frac{q_\alpha}{e}\right| m_e\nu_{ei}\frac{\nabla_\perp\left[p_e+p_i\right]}{n\left[eB\right]^2}\right) = -\nabla\cdot\left(\left|\frac{q_\alpha}{e}\right| m_e\nu_{ei}\frac{\nabla_\perp\left[p_e+p_i\right]}{\left[eB\right]^2}\right) \tag{4.9}$$

We will from this point on assume that all collision frequencies are constant. As seen from appendix C when assuming quasi-neutrality:

$$\nu_{ei}\propto\frac{n}{T_e^{3/2}}\ln\Lambda\propto\frac{n}{T_e^{3/2}}\ln\left(n\left[\frac{T_e}{n}\right]^{3/2}\right).$$

As we assume constant electron temperature, we get

$$\partial_i\nu_{ei}\propto\partial_i\left(n\ln\left[n^{-1/2}\right]\right)\propto-\frac{1}{2}\left(\partial_i n\right)\left(\ln\left[n\right]+1\right)\approx\frac{1}{2}\left(\partial_i n\right)\ln\left(n\right).$$

As the logarithm of n is slowly varying for high n, we see that the approximation is good as long as the gradients in n are small. Using this in eq. (4.9) gives

$$\nabla\cdot(n_\alpha \boldsymbol{u}_{\alpha,R}) = -\left|\frac{q_\alpha}{e}\right|\frac{m_e\nu_{ei}}{e^2}\nabla\cdot\left(\frac{\nabla_\perp\left[p_e+p_i\right]}{B^2}\right) = -\left|\frac{q_\alpha}{e}\right|\frac{1}{\mu}\frac{m_i\nu_{ei}}{e^2}\nabla\cdot\left(\frac{\nabla_\perp\left[p_e+p_i\right]}{B^2}\right), \tag{4.10}$$

where we have used $\mu\overset{\text{def}}{=}\frac{m_i}{m_e}$. Note that although this term may be small as it is $\propto m_e$, we keep it as the term contributes to perpendicular diffusion of n through the divergence of

the pressure gradients. This diffusion removes small scales from the system as it flattens the gradients.

Next, the Pedersen drift term yields

$$\nabla\cdot(n_\alpha \boldsymbol{u}_{\alpha,\mathrm{Ped}}) = \nabla\cdot\left(-n_\alpha\frac{\nu_{\alpha n}}{\omega_{c\alpha}}\left[\frac{\nabla_\perp p_\alpha}{q_\alpha n_\alpha B}+\frac{\nabla_\perp\phi}{B}\right]\right) = \nabla\cdot\left(-n_\alpha\frac{\nu_{\alpha n}}{\omega_{c\alpha}}\left[\frac{\nabla_\perp p_\alpha}{q_\alpha n_\alpha B}+\frac{\nabla_\perp\phi}{B}\right]\right),$$

and the source term yields

$$\nabla\cdot(n_\alpha \boldsymbol{u}_{\alpha,S}) = \nabla\cdot\left(-n_\alpha\frac{S_{\alpha,n}}{n_\alpha\omega_{c\alpha}}\left[\frac{\nabla_\perp p_\alpha}{n_\alpha q_\alpha B}+\frac{\nabla_\perp\phi}{B}\right]\right) = -\nabla\cdot\left(\frac{S_{\alpha,n}}{\omega_{c\alpha}}\left[\frac{\nabla_\perp p_\alpha}{n_\alpha q_\alpha B}+\frac{\nabla_\perp\phi}{B}\right]\right).$$

4.3.1 Polarization and viscosity

For further reference, it suffice to observe that $\boldsymbol{u}_{e,p}\propto\frac{1}{\omega_{ce}}$, and that electron viscosity is of order $\mathcal{O}(\varepsilon^2)$ as seen from eq. (B.16).

For the ions, we note that a material derivative appears in the polarization drift in eq. (3.15). The material derivative must be treated with care. Because of the advective term in the material derivative, we will have that

$$\nabla\cdot \mathrm{d}_t\boldsymbol{v} \neq \mathrm{d}_t\left(\nabla\cdot\boldsymbol{v}\right).$$

One should also use the advection term carefully. It appears that all the drifts can contribute to the advective part of the material derivative, but only the parallel velocity and the $\boldsymbol{E}\times\boldsymbol{B}$-drift contributes to the advection. Although not trivially seen in the drift-fluid picture, it comes as a consequence of what is being referred to as *gyroviscous cancellation* [32, 33]. Briefly explained, the cancellation comes as a consequence of the viscous part of the stress tensor cancels the diamagnetic drift. This means that

$$\begin{aligned}
&\nabla\cdot(n\boldsymbol{u}_{i,p}+n\boldsymbol{u}_{i,\nu})\\
\simeq&\nabla\cdot\left(n\frac{1}{\omega_{ci}}\left[\partial_t+(\boldsymbol{u}_E+\boldsymbol{u}_{i,\parallel})\cdot\nabla\right]\left[-\frac{\nabla_\perp\phi}{B}\right]\right)\\
=&-\nabla\cdot\left(\frac{n}{\omega_{ci}}\left[\mathrm{d}_t^E+\boldsymbol{u}_{i,\parallel}\cdot\nabla\right]\frac{\nabla_\perp\phi}{B}\right) \qquad (4.11)\\
=&-\nabla\cdot\left(\frac{1}{\omega_{ci}}\left[\left(\mathrm{d}_t^E+\boldsymbol{u}_{i,\parallel}\cdot\nabla\right)\left(\frac{\nabla_\perp\phi}{B}n\right)-\frac{\nabla_\perp\phi}{B}\left(\mathrm{d}_t^E+\boldsymbol{u}_{i,\parallel}\cdot\nabla\right)n\right]\right)\\
=&-\nabla\cdot\left(\frac{1}{\omega_{ci}}\left[\mathrm{d}_t^E+\boldsymbol{u}_{i,\parallel}\cdot\nabla\right]\left[\frac{\nabla_\perp\phi}{B}n\right]\right)+\nabla\cdot\left(\frac{1}{\omega_{ci}}\frac{\nabla_\perp\phi}{B}\left[\mathrm{d}_t^E+\boldsymbol{u}_{i,\parallel}\cdot\nabla\right]n\right). \qquad (4.12)
\end{aligned}$$

We see that we can insert Z times the ion continuity equation in the last term of eq. (4.12). Since eq. (4.12) is of order ε, only the ε^0 terms will be used for the perpendicular drifts. In other words, terms of order ε^2 will be neglected. Using only order ε^0-terms, Z times the ion continuity equation reads

$$\begin{aligned}
\partial_t n+\nabla\cdot(n[\boldsymbol{u}_{i,d}+\boldsymbol{u}_E+\boldsymbol{u}_{i,\parallel}]) &= S_{i,n}\\
\partial_t n+\nabla\cdot(n\boldsymbol{u}_{i,d})+\nabla\cdot(n\boldsymbol{u}_E)+\nabla\cdot(n\boldsymbol{u}_{i,\parallel}) &= S_{i,n} \qquad \text{eqs. (4.7)}\\
\partial_t n+\frac{1}{e}\mathcal{C}\left(p_i\right)+n\mathcal{C}(\phi)+\boldsymbol{u}_E\cdot\nabla n+n\nabla\cdot\boldsymbol{u}_{i,\parallel}+\boldsymbol{u}_{i,\parallel}\cdot\nabla n &= S_{i,n} \qquad \text{and (4.8)}
\end{aligned}$$

$$\begin{aligned}\partial_t n + \boldsymbol{u}_E \cdot \nabla n + \boldsymbol{u}_{i,\parallel} \cdot \nabla n &= S_{i,n} - \frac{1}{e}\mathcal{C}\left(p_i\right) - n\mathcal{C}(\phi) - n\nabla \cdot \boldsymbol{u}_{i,\parallel} \\ \left(\mathrm{d}_t^E + \boldsymbol{u}_{i,\parallel} \cdot \nabla\right) n &= S_{i,n} - \frac{1}{e}\mathcal{C}\left(p_i\right) - n\mathcal{C}(\phi) - n\nabla \cdot \boldsymbol{u}_{i,\parallel}.\end{aligned} \tag{4.13}$$

where we have defined

$$\mathrm{d}_t^E = \partial_t + \boldsymbol{u}_E \cdot \nabla$$

Inserting eq. (4.13) into eq. (4.12) yields

$$\begin{aligned}&\nabla \cdot (n\boldsymbol{u}_{i,p} + n\boldsymbol{u}_{i,\nu}) \\ \simeq &-\nabla \cdot \left(\frac{1}{\omega_{ci}}\left[\mathrm{d}_t^E + \boldsymbol{u}_{i,\parallel} \cdot \nabla\right]\left[\frac{\nabla_\perp \phi}{B} n\right]\right) + \nabla \cdot \left(\frac{1}{\omega_{ci}}\frac{\nabla_\perp \phi}{B}\left[S_{i,n} - \frac{1}{e}\mathcal{C}\left(p_i\right) - n\mathcal{C}(\phi) - n\nabla \cdot \boldsymbol{u}_{i,\parallel}\right]\right).\end{aligned} \tag{4.14}$$

This equation has a central part in the current balance equation as it ultimately will be responsible for the time derivative of the modified vorticity in chapter 5.

4.4 The electron density equation

We can now use our results to derive an equation for the time derivative of the electron density. Based on the quasi-neutral assumption in appendix B.2, the evolution of the density can be described by both the electron continuity equation and the ionization number Z times the ion continuity equation. The two should differ only slightly. We can therefore choose to use the electron continuity equation to calculate the evolution of the density. This gives

$$\partial_t n_e + \nabla \cdot (n_e[\boldsymbol{u}_{e,d} + \boldsymbol{u}_E + \boldsymbol{u}_{e,p} + \boldsymbol{u}_{e,R} + \boldsymbol{u}_{e,\mathrm{Ped}} + \boldsymbol{u}_{e,\nu} + \boldsymbol{u}_{e,S} + \boldsymbol{u}_{e,\parallel}]) = S_{n,e}. \tag{4.15}$$

We neglect $\boldsymbol{u}_{e,\nu}$ as this drift is of $\mathcal{O}(\varepsilon^2)$. Next, we observe that $\boldsymbol{u}_{e,p}$, $\boldsymbol{u}_{e,\mathrm{Ped}}$ and $\boldsymbol{u}_{e,S}$ are small compared to the rest of the terms as they are proportional the electron mass through the ω_{ce}^{-1} factor. Using that $n_e \simeq n$, we get that

$$\begin{aligned}\partial_t n &\simeq -\nabla \cdot \left(n\left[\boldsymbol{u}_E + \boldsymbol{u}_{e,D} + \boldsymbol{u}_{e,R} + \boldsymbol{u}_{e,\parallel}\right]\right) + S_{e,n} \\ &= -\boldsymbol{u}_E \nabla \cdot n - n\nabla \cdot \boldsymbol{u}_E - \nabla \cdot (n\boldsymbol{u}_{e,D}) - \nabla \cdot (n\boldsymbol{u}_{e,R}) - \nabla \cdot \left(n\boldsymbol{u}_{e,\parallel}\right) + S_{e,n} \\ \mathrm{d}_t^E n &= -n\mathcal{C}(\phi) + \frac{1}{e}\mathcal{C}(\phi) + \frac{1}{\mu}\frac{m_i \nu_{ei}}{e^2}\nabla \cdot \left(\frac{\nabla_\perp \left[p_e + p_i\right]}{B^2}\right) - \nabla \cdot \left(n\boldsymbol{u}_{e,\parallel}\right) + S_{e,n}.\end{aligned} \tag{4.16}$$

4.5 Current conservation equation

Equation (4.16) gives the equation to solve the density in time. Similarly, we could make an equation that evolves $\boldsymbol{u}_{\alpha,\perp}$ in time, which would require one equation per species for each perpendicular direction. However, as we will see later, all the information we need for evolving $\boldsymbol{u}_{\alpha,\perp}$ in time are contained in the parallel part of the vorticity equation ($(\nabla \times \boldsymbol{v}_E) \cdot \boldsymbol{b}$). This equation can be derived from the current conservation, which we

present in this section. If we multiply the two continuity equations of eq. (4.1) with q_α, and add them, we get by applying quasi-neutrality that

$$\begin{aligned} q_i\partial_t n_i + q_i\nabla\cdot(n_i\boldsymbol{u}_i) + q_e\partial_t n_e + q_e\nabla\cdot(n_e\boldsymbol{u}_e) =& q_i S_{i,n} + q_e S_{e,n} \\ Ze\partial_t n_i + Ze\nabla\cdot(n_i\boldsymbol{u}_i) - e\partial_t n_e - e\nabla\cdot(n_e\boldsymbol{u}_e) =& eZS_{i,n} - eS_{e,n} \\ e\partial_t n + e\nabla\cdot(n\boldsymbol{u}_i) - e\partial_t n - e\nabla\cdot(n\boldsymbol{u}_e) =& eZS_{i,n} - eS_{e,n} \\ \nabla\cdot(en\boldsymbol{u}_i - en\boldsymbol{u}_e) =& e\left(ZS_{i,n} - S_{e,n}\right). \end{aligned}$$

Quasi-neutrality

If we use eq. (2.2) together with $\boldsymbol{j} = \sum_\alpha q_\alpha n_\alpha \boldsymbol{u}_\alpha$, we get that

$$\begin{aligned} \nabla\cdot\boldsymbol{j} =& e\left(S_n - S_n\right) \\ \nabla\cdot\left(\boldsymbol{j}_\perp + \boldsymbol{j}_\parallel\right) =& 0 \\ \nabla\cdot\boldsymbol{j}_\perp =& -\nabla\cdot\boldsymbol{j}_\parallel. \end{aligned}$$

This gives

$$\nabla\cdot(n[\boldsymbol{u}_{i,\perp} - \boldsymbol{u}_{e,\perp}]) = -\frac{1}{e}\nabla\cdot\boldsymbol{j}_\parallel.$$

Once again, we can neglect the electron drifts proportional to the electron mass as these terms are small. This gives

$$\nabla\cdot(n[\boldsymbol{u}_E - \boldsymbol{u}_E + \boldsymbol{u}_{i,d} - \boldsymbol{u}_{e,d} + \boldsymbol{u}_{i,p} + \boldsymbol{u}_{i,R} - \boldsymbol{u}_{e,R} + \boldsymbol{u}_{i,\mathrm{Ped}} + \boldsymbol{u}_{i,\nu} + \boldsymbol{u}_{i,S}]) = -\frac{1}{e}\nabla\cdot\boldsymbol{j}_\parallel. \tag{4.17}$$

The $\boldsymbol{E}\times\boldsymbol{B}$ drift in eq. (4.17) cancels as the drift is equal for electrons and ions. The diamagnetic terms yield

$$\begin{aligned} \nabla\cdot(n\boldsymbol{u}_{e,d}) - \nabla\cdot(n\boldsymbol{u}_{i,d}) &= \nabla\cdot\left(n\frac{-\nabla_\perp p_e}{-n_e eB}\right) - \nabla\cdot\left(n\frac{-\nabla_\perp p_i}{n_i ZeB}\right) \\ &= -\frac{1}{e}\left[\mathcal{C}(p_e) + \mathcal{C}\left(p_i\right)\right] \\ &= -\frac{1}{e}\left[\mathcal{C}\left(p_e + p_i\right)\right]. \end{aligned}$$

Quasi-neutrality

$\mathcal{C}(f)+\mathcal{C}(g) = \mathcal{C}(f+g)$

From eqs. (4.17) and (4.10) we can see that the resistivity terms cancels as the terms will have opposite sign for electrons and ions. Next, the electron Pedersen drift is negligible due to the electron mass, whereas the ion Pedersen drift can be split into

$$\begin{aligned} \nabla\cdot(n\boldsymbol{u}_{i,\mathrm{Ped}}) &= -\nabla\cdot\left(\frac{n\nu_{in}}{\omega_{ci}}\left[\frac{\nabla_\perp p_i}{eZn_iB} + \frac{\nabla_\perp\phi}{B}\right]\right) \\ &= -n\nabla\cdot\left(\frac{\nu_{in}}{\omega_{ci}}\left[\frac{\nabla_\perp p_i}{enB} + \frac{\nabla_\perp\phi}{B}\right]\right) - \left(\frac{\nu_{in}}{\omega_{ci}}\left[\frac{\nabla_\perp p_i}{enB} + \frac{\nabla_\perp\phi}{B}\right]\right)\cdot\nabla n. \end{aligned} \tag{4.18}$$

$Zn_i \simeq n$

This means that eq. (4.17) can be written as

$$-\frac{1}{e}\nabla\cdot\boldsymbol{j}_\parallel = \nabla\cdot(n[\boldsymbol{u}_{i,d} - \boldsymbol{u}_{e,d} + \boldsymbol{u}_{i,\mathrm{Ped}} + \boldsymbol{u}_{i,p} + \boldsymbol{u}_{i,\nu} + \boldsymbol{u}_{i,S}])$$

$$
\begin{aligned}
&= -\frac{1}{e}\left[\mathcal{C}\left(p_e + p_i\right)\right] \\
&\quad - n\nabla\cdot\left(\frac{\nu_{in}}{\omega_{ci}}\left[\frac{\nabla_\perp p_i}{enB} + \frac{\nabla_\perp \phi}{B}\right]\right) - \left(\frac{\nu_{in}}{\omega_{ci}}\left[\frac{\nabla_\perp p_i}{enB} + \frac{\nabla_\perp \phi}{B}\right]\right)\cdot\nabla n \\
&\quad - \nabla\cdot\left(\frac{1}{\omega_{ci}}\left[\mathrm{d}_t^E + \boldsymbol{u}_{i,\parallel}\cdot\nabla\right]\left[\frac{\nabla_\perp \phi}{B} n\right]\right) \\
&\quad + \nabla\cdot\left(\frac{1}{\omega_{ci}}\frac{\nabla_\perp \phi}{B}\left[S_{i,n} - \frac{1}{e}\mathcal{C}\left(p_i\right) - n\mathcal{C}(\phi) - n\nabla\cdot\boldsymbol{u}_{i,\parallel}\right]\right) \\
&\quad - \nabla\cdot\left(\frac{S_{i,n}}{\omega_{ci}}\left[\frac{\nabla_\perp p_i}{n_i q_i B} + \frac{\nabla_\perp \phi}{B}\right]\right) \\
\frac{1}{e}\nabla\cdot\boldsymbol{j}_\parallel =& \frac{1}{e}\left[\mathcal{C}\left(p_e + p_i\right)\right] \\
&\quad + n\nabla\cdot\left(\frac{\nu_{in}}{\omega_{ci}}\left[\frac{\nabla_\perp p_i}{enB} + \frac{\nabla_\perp \phi}{B}\right]\right) + \left(\frac{\nu_{in}}{\omega_{ci}}\left[\frac{\nabla_\perp p_i}{enB} + \frac{\nabla_\perp \phi}{B}\right]\right)\cdot\nabla n \\
&\quad + \nabla\cdot\left(\frac{1}{\omega_{ci}}\left[\mathrm{d}_t^E + \boldsymbol{u}_{i,\parallel}\cdot\nabla\right]\left[\frac{\nabla_\perp \phi}{B} n\right]\right) \\
&\quad - \nabla\cdot\left(\frac{1}{\omega_{ci}}\frac{\nabla_\perp \phi}{B}\left[S_{i,n} - \frac{1}{e}\mathcal{C}\left(p_i\right) - n\mathcal{C}(\phi) - n\nabla\cdot\boldsymbol{u}_{i,\parallel}\right]\right) \\
&\quad + \nabla\cdot\left(\frac{S_{i,n}}{\omega_{ci}}\left[\frac{\nabla_\perp p_i}{n_i q_i B} + \frac{\nabla_\perp \phi}{B}\right]\right). \qquad (4.19)
\end{aligned}
$$

So far, we have balanced the divergence of the parallel currents with the divergence of the perpendicular currents (using the drifts). From this we have obtained a time derivative from the ion polarization drift (the third term in eq. (4.19)). In the next chapter, we will see how the ion polarization term turns into the time derivative of the parallel vorticity of the $\boldsymbol{E}\times\boldsymbol{B}$-drift under the assumption of a homogeneous B-field. The homogeneous B-field will simplify our work of extracting the vorticity. Therefore, we end our derivations in a slowly varying B-field here.

Chapter 5

The CELMA model

We will now use the above derived equation in a homogeneous magnetic field, assuming cold ions and constant electron temperature in a cylindrical geometry.

The resulting model will from here be referred to as the CELMA model, an abbreviation of **C**onsistent **E**quations in a **L**inear **MA**chine[1].

We will end up with a coupled set of four PDEs, which we can use to evolve the density, the sum of the parallel momentum densities, the current and the modified vorticity in time together with a boundary equation which gives the potential at the given time-step. In other words, the final set equations is a considerable reduction of the original system consisting, which consisted of eight coupled PDEs. The final set of equations is found in eqs. (5.21) to (5.26).

The aim is to model something similar to what is observed in linear plasma devices. Several types of linear machines exists, all with different purposes. For example has the Q-machines have been used for the study quiescent alkali plasmas [34] and machines like Magnum-PSI [20] have mainly been used for the study plasma-wall interactions. Here, we would restrict our attention to mainly helicon type plasmas, where a helicon wave are responsible for the plasma creation [35, 36]. No momentum is added to the plasma in this creation process. The plasma creation process will in this thesis therefore just be approximated by the source variable S_n, which we keep constant in time.

Helicon devices operational during the writing of this thesis includes VINETA [37][2](depicted in fig. 5.1), PANTA (previously LMD-U) [38] and CSDX [39]. Although we restrict our scope to helicon devices, it is also possible to model devices like the LAPD [40, 41] with CELMA by properly adjusting the sources.

[1] This should not be confused with PELMA, **P**erfect **E**quations in a **L**inear **MA**chine. As we have seen, there is an inconsistent approximation to use a constant temperature whilst $\frac{u^c}{c_s^c} \simeq \sqrt{\varepsilon}$, but this approximation is consistently implemented.

[2] Now VINETA II [21], mainly used for magnetic reconnection studies.

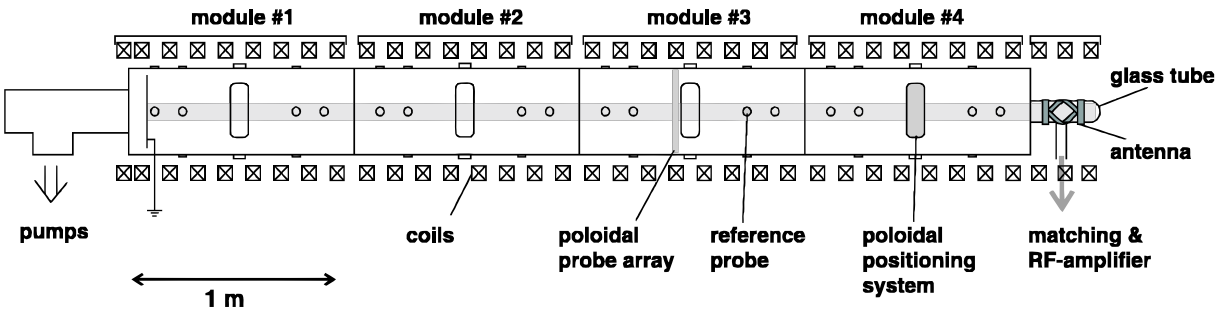

Figure 5.1: Sketch of VINETA (from [37]).

5.1 The density equation

We will now simplify the electron density equation (eq. (4.16)) using $B = \text{const}$ (so that $\mathcal{C}(f) = 0$), $T_e = \text{const}$ and $T_i \simeq 0$. This yields

$$\begin{aligned}
\mathrm{d}_t^E n &= -n\mathcal{C}(\phi) + \frac{1}{e}\mathcal{C}(\phi) + \frac{1}{\mu}\frac{m_i\nu_{ei}}{e^2}\nabla\cdot\left(\frac{\nabla_\perp\left[p_e+p_i\right]}{B^2}\right) - \nabla\cdot\left(n\boldsymbol{u}_{e,\parallel}\right) + S_n && p_i = 0 \\
&= \frac{1}{\mu}\frac{m_i T_e\nu_{ei}}{B^2e^2}\nabla_\perp^2 n - \nabla\cdot\left(n\boldsymbol{b}u_{e,\parallel}\right) + S_n && B = \text{const} \\
&= \frac{1}{\mu}\frac{m_i T_e\nu_{ei}}{B^2e^2}\nabla_\perp^2 n - \boldsymbol{b}\cdot\nabla\left(nu_{e,\parallel}\right) + S_n && \partial_i\boldsymbol{b} = 0 \\
&= \frac{1}{\mu}\frac{m_i T_e\nu_{ei}}{B^2e^2}\nabla_\perp^2 n - \partial_\parallel\left(nu_{e,\parallel}\right) + S_n.
\end{aligned}$$

Using that $\rho_s = \dfrac{c_s}{\omega_{ci}} = \sqrt{\dfrac{T_e}{m_i}}\dfrac{m_i}{eB} = \sqrt{\dfrac{T_e m_i}{e^2B^2}}$ we find that

$$\boxed{\mathrm{d}_t^E n = \frac{\rho_s^2\nu_{ei}}{\mu}\nabla_\perp^2 n - \partial_\parallel\left(nu_{e,\parallel}\right) + S_n.} \tag{5.1}$$

5.2 The vorticity equation

After the derivations in chapter 4, we are in the position to find the vorticity with our current approximations. Strictly speaking, the vorticity Ω of a fluid field is defined as $\nabla\times\boldsymbol{u}$ [42]. Thus, Ω tells us something about the *local* rotation[3] of the velocity field. In this thesis, a slightly different definition will be used:

$$\boxed{\frac{\nabla_\perp^2\phi}{B} \overset{\text{def}}{=} \Omega.}$$

Note that this is only the parallel part of the local rotation of the advective vorticity:

$$(\nabla\times\boldsymbol{u}_E)\cdot\boldsymbol{b} = \left(-\nabla\times\frac{\nabla\phi\times\boldsymbol{b}}{B}\right)\cdot\boldsymbol{b} \qquad \nabla\frac{1}{B}\simeq 0$$

[3]Note that a sheared laminar flow can cause a non-zero vorticity, and that irrational vortices exists. An intutive way to check whether a flow has a non-zero vorticity, is to check if a infinitesimal imagined stamp will rotate if introduced in a point of the flow.

$$
\begin{aligned}
&= \frac{1}{B}\left(\nabla \times \boldsymbol{b} \times \nabla\phi\right) \cdot \boldsymbol{b} && \nabla \times (\boldsymbol{A} \times \boldsymbol{B}) = \\
&= \frac{1}{B}\left(\boldsymbol{b}\left[\nabla \cdot \nabla\phi\right] - \nabla\phi\left[\nabla \cdot \boldsymbol{b}\right] + \left[\nabla\phi \cdot \nabla\right]\boldsymbol{b} - \left[\boldsymbol{b} \cdot \nabla\right]\nabla\phi\right) \cdot \boldsymbol{b} && \boldsymbol{A}(\nabla \cdot \boldsymbol{B}) - \\
&= \frac{1}{B}\left(\boldsymbol{b}\left[\nabla \cdot \nabla\phi\right] - \left[\boldsymbol{b} \cdot \nabla\right]\nabla\phi\right) \cdot \boldsymbol{b} && \nabla \cdot \boldsymbol{b} \simeq 0 \text{ and} \\
&= \frac{1}{B}\left(\boldsymbol{b} \cdot \boldsymbol{b}\left[\nabla \cdot \nabla\phi\right] - \boldsymbol{b} \cdot \left[\boldsymbol{b} \cdot \nabla\right]\nabla\phi\right) && \nabla\boldsymbol{b} \simeq 0 \\
&= \frac{1}{B}\left(\nabla^2\phi - \boldsymbol{b} \cdot \left[\nabla\boldsymbol{b}\cdot\right]\nabla\phi\right) \\
&= \frac{1}{B}\left(\nabla^2\phi - \left[\boldsymbol{b} \cdot \nabla\right]\boldsymbol{b} \cdot \nabla\phi\right) \\
&= \frac{1}{B}\left(\nabla^2\phi - \nabla \cdot \left[\boldsymbol{b}\boldsymbol{b} \cdot \nabla\phi\right]\right) \\
&= \frac{1}{B}\left(\nabla_\perp^2\phi\right),
\end{aligned}
$$

where we in the last line have used that $\nabla_\perp^2 = \nabla^2 - \nabla_\parallel^2 = \nabla^2 - \nabla \cdot [\boldsymbol{b}\boldsymbol{b} \cdot \nabla]$. This term will come from the polarization drift defined in eq. (3.15). However, as we are deriving the vorticity equation from the conservation of charge (see eq. (4.17)), we already have a term on the form $\nabla \cdot (n\boldsymbol{u}_{i,p})$. As such, it makes sense to define the **D**ensity modified vorticity Ω^D (or simply just "the modified vorticity") as

$$
\boxed{\Omega^D \stackrel{\text{def}}{=} \nabla \cdot \left(n\frac{\nabla_\perp\phi}{B}\right).} \tag{5.2}
$$

In the end, we will evolve Ω^D in time unless we use the Boussinesq approximation (see chapter 6), where we instead will evolve Ω. We will start the derivation by investigating the left hand side of eq. (4.19) term by term.

The diamagnetic contribution

$$
\frac{1}{e}\left[\mathcal{C}(p_e + p_i)\right].
$$

disappears as $\mathcal{C}(f)$ vanishes for a straight magnetic field.

The next two terms, which originate from the Pedersen drift eq. (4.18), can be rewritten using that we are dealing with cold ions. We get

$$
\begin{aligned}
\nabla \cdot (n\boldsymbol{u}_{i,\text{Ped}}) =& n\nabla \cdot \left(\frac{\nu_{in}}{\omega_{ci}}\frac{\nabla_\perp\phi}{B}\right) + \left(\frac{\nu_{in}}{\omega_{ci}}\frac{\nabla_\perp\phi}{B}\right) \cdot \nabla n && \text{Const } B \\
=& n\frac{\nu_{in}}{\omega_{ci}}\frac{\nabla_\perp^2\phi}{B} + \frac{\nu_{in}}{\omega_{ci}}\frac{\nabla_\perp\phi}{B} \cdot \nabla n \\
=& \frac{\nu_{in}}{\omega_{ci}}\left(n\Omega + \frac{\nabla_\perp\phi}{B} \cdot \nabla n\right).
\end{aligned}
$$

The next terms are arising from the sum of the divergence of the ion polarization drift and ion viscosity drift multiplied with the density (that is eq. (4.14)). The first term of eq. (4.14) yields

$$
\nabla \cdot \left(\frac{1}{\omega_{ci}}\left[\mathrm{d}_t^E + \boldsymbol{u}_{i,\parallel} \cdot \nabla\right]\left[\frac{\nabla_\perp\phi}{B}n\right]\right)
$$

$$
\begin{aligned}
=&\nabla\cdot\left(\frac{1}{\omega_{ci}}\partial_t\left[\frac{\nabla_\perp\phi}{B}n\right]\right)+\nabla\cdot\left(\frac{1}{\omega_{ci}}\boldsymbol{u}_E\cdot\nabla\left[\frac{\nabla_\perp\phi}{B}n\right]\right)+\nabla\cdot\left(\frac{1}{\omega_{ci}}\boldsymbol{u}_{i,\parallel}\cdot\nabla\left[\frac{\nabla_\perp\phi}{B}n\right]\right) && B=\text{const}\\
=&\frac{1}{\omega_{ci}}\nabla\cdot\left(\partial_t\left[\frac{\nabla_\perp\phi}{B}n\right]\right)+\frac{1}{\omega_{ci}}\nabla\cdot\left(\boldsymbol{u}_E\cdot\nabla\left[\frac{\nabla_\perp\phi}{B}n\right]\right)+\frac{1}{\omega_{ci}}\nabla\cdot\left(u_{i,\parallel}\boldsymbol{b}\cdot\nabla\left[\frac{\nabla_\perp\phi}{B}n\right]\right) && \text{Assume interchangibility of derivatives}\\
=&\frac{1}{\omega_{ci}}\partial_t\left(\nabla\cdot\left[\frac{\nabla_\perp\phi}{B}n\right]\right)+\frac{1}{\omega_{ci}}\nabla\cdot\left(\boldsymbol{u}_E\cdot\nabla\left[\frac{\nabla_\perp\phi}{B}n\right]\right)+\frac{1}{\omega_{ci}}\nabla\cdot\left(u_{i,\parallel}\partial_\parallel\left[\frac{\nabla_\perp\phi}{B}n\right]\right) && \text{eq. (5.2)}\\
=&\frac{1}{\omega_{ci}}\partial_t\Omega^D+\frac{1}{\omega_{ci}}\nabla\cdot\left(\boldsymbol{u}_E\cdot\nabla\left[\frac{\nabla_\perp\phi}{B}n\right]\right)+\frac{1}{\omega_{ci}}\nabla\cdot\left(u_{i,\parallel}\partial_\parallel\left[\frac{\nabla_\perp\phi}{B}n\right]\right).
\end{aligned}
$$

As we have no curvature, the second term of eq. (4.14) gives

$$
\begin{aligned}
&-\nabla\cdot\left(\frac{1}{\omega_{ci}}\frac{\nabla_\perp\phi}{B}\left[S_{i,n}-\frac{1}{e}\mathcal{C}(p_i)-n\mathcal{C}(\phi)-n\nabla\cdot\boldsymbol{u}_{i,\parallel}\right]\right)\\
=&-\frac{1}{\omega_{ci}}\nabla\cdot\left(\frac{\nabla_\perp\phi}{B}\left[S_{i,n}-n\nabla\cdot\left(\boldsymbol{b}u_{i,\parallel}\right)\right]\right) && \partial_i\boldsymbol{b}=0\\
=&-\frac{1}{\omega_{ci}}\nabla\cdot\left(\frac{\nabla_\perp\phi}{B}\left[S_{i,n}-n\boldsymbol{b}\cdot\nabla u_{i,\parallel}\right]\right)\\
=&-\frac{1}{\omega_{ci}}\nabla\cdot\left(\frac{\nabla_\perp\phi}{B}\left[S_{i,n}-n\partial_\parallel u_{i,\parallel}\right]\right)\\
=&-\frac{1}{\omega_{ci}}\nabla\cdot\left(\frac{\nabla_\perp\phi}{B}S_{i,n}\right)+\frac{1}{\omega_{ci}}\nabla\cdot\left(\frac{\nabla_\perp\phi}{B}n\partial_\parallel u_{i,\parallel}\right).
\end{aligned}
$$

This means that the polarization contribution from eq. (4.19) can be written as

$$
\begin{aligned}
&\frac{1}{\omega_{ci}}\partial_t\Omega^D+\frac{1}{\omega_{ci}}\nabla\cdot\left(\boldsymbol{u}_E\cdot\nabla\left[\frac{\nabla_\perp\phi}{B}n\right]\right)+\frac{1}{\omega_{ci}}\nabla\cdot\left(u_{i,\parallel}\partial_\parallel\left[\frac{\nabla_\perp\phi}{B}n\right]\right)\\
-&\frac{1}{\omega_{ci}}\nabla\cdot\left(\frac{\nabla_\perp\phi}{B}S_{i,n}\right)+\frac{1}{\omega_{ci}}\nabla\cdot\left(\frac{\nabla_\perp\phi}{B}n\partial_\parallel u_{i,\parallel}\right).
\end{aligned}
$$

Further on, the contribution from the source can be rewritten. Under the assumption of cold ions ($T_i=0$), we can simplify the source term in eq. (4.19) to

$$
\begin{aligned}
\nabla\cdot\left(\frac{S_{i,n}}{\omega_{ci}}\left[\frac{\nabla_\perp p_i}{neB}+\frac{\nabla_\perp\phi}{B}\right]\right)=&\nabla\cdot\left(\frac{S_{i,n}}{\omega_{ci}}\left[\frac{\nabla_\perp\phi}{B}\right]\right) && T_i\simeq 0\\
=&\frac{1}{\omega_{ci}}\nabla\cdot\left(S_{i,n}\left[\frac{\nabla_\perp\phi}{B}\right]\right). && \text{Const } B
\end{aligned}
$$

Finally, the RHS of eq. (4.19) reads

$$
\frac{1}{e}\nabla\cdot\boldsymbol{j}_\parallel=\frac{1}{e}\nabla\cdot\left(\boldsymbol{b}j_\parallel\right)=\frac{1}{e}\boldsymbol{b}\cdot\nabla j_\parallel=\frac{1}{e}\partial_\parallel j_\parallel. \qquad \partial_i\boldsymbol{b}=0
$$

5.2.1 Collecting terms

From the derivations above, eq. (4.19) can now be rewritten to

$$
\frac{\nu_{in}}{\omega_{ci}}\left(n\Omega+\frac{\nabla_\perp\phi}{B}\cdot\nabla n\right)
$$

$$
\begin{aligned}
&+\frac{1}{\omega_{ci}}\partial_t\Omega^D+\frac{1}{\omega_{ci}}\nabla\cdot\left(\boldsymbol{u}_E\cdot\nabla\left[\frac{\nabla_\perp\phi}{B}n\right]+u_{i,\parallel}\partial_\parallel\left[\frac{\nabla_\perp\phi}{B}n\right]+\frac{\nabla_\perp\phi}{B}n\partial_\parallel u_{i,\parallel}\right)-\frac{1}{\omega_{ci}}\nabla\cdot\left(\frac{\nabla_\perp\phi}{B}S_{i,n}\right)\\
&+\frac{1}{\omega_{ci}}\nabla\cdot\left(S_{i,n}\left[\frac{\nabla_\perp\phi}{B}\right]\right)\\
=&\frac{1}{e}\partial_\parallel j_\parallel.
\end{aligned}
$$

Rearranging yields

$$
\begin{aligned}
\frac{1}{\omega_{ci}}\partial_t\Omega^D=&-\frac{\nu_{in}}{\omega_{ci}}\left(n\Omega+\frac{\nabla_\perp\phi}{B}\cdot\nabla n\right)\\
&-\frac{1}{\omega_{ci}}\nabla\cdot\left(\boldsymbol{u}_E\cdot\nabla\left[\frac{\nabla_\perp\phi}{B}n\right]+u_{i,\parallel}\partial_\parallel\left[\frac{\nabla_\perp\phi}{B}n\right]+\frac{\nabla_\perp\phi}{B}n\partial_\parallel u_{i,\parallel}\right)\\
&+\frac{1}{e}\partial_\parallel j_\parallel.
\end{aligned}
\tag{5.3}
$$

Note that $\frac{1}{\omega_{ci}}\nabla\cdot\left(\frac{\nabla_\perp\phi}{B}S_{i,n}\right)$ arising from the time derivative of n_i in the polarization term of the current conservation equation has canceled with the same term with opposite sign arising from the source term of the current conservation equation.

We can simplify eq. (5.3) even further by first observing that

$$
u_{i,\parallel}\partial_\parallel\left[\frac{\nabla_\perp\phi}{B}n\right]+\frac{\nabla_\perp\phi}{B}n\partial_\parallel u_{i,\parallel}=\partial_\parallel\left(u_{i,\parallel}\frac{\nabla_\perp\phi}{B}n\right),
$$

and using the fact that in cylindrical coordinates we have that $\partial_z\boldsymbol{e}_i=\partial_z\boldsymbol{e}^i=0$. This yields

$$
\begin{aligned}
\frac{1}{\omega_{ci}}\partial_t\Omega^D=&-\frac{\nu_{in}}{\omega_{ci}}\left(n\Omega+\frac{\nabla_\perp\phi}{B}\cdot\nabla n\right)\\
&-\frac{1}{\omega_{ci}}\nabla\cdot\left(\boldsymbol{u}_E\cdot\nabla\left[\frac{\nabla_\perp\phi}{B}n\right]\right)-\frac{1}{\omega_{ci}}\partial_\parallel\nabla\cdot\left(u_{i,\parallel}\frac{\nabla_\perp\phi}{B}n\right)\\
&+\frac{1}{e}\partial_\parallel j_\parallel.
\end{aligned}
\tag{5.4}
$$

Note that the $-\frac{1}{\omega_{ci}}\nabla\cdot\left(u_{i,\parallel}\partial_\parallel\left[\frac{\nabla_\perp\phi}{B}n\right]\right)$ term arises from the parallel advection in the polarization term, whereas the $-\frac{1}{\omega_{ci}}\nabla\cdot\left(\frac{\nabla_\perp\phi}{B}n\partial_\parallel u_{i,\parallel}\right)$ term arises from the ion continuity equation.

Next, we see from appendix J that

$$
\frac{1}{\omega_{ci}}\nabla\cdot\left(\boldsymbol{u}_E\cdot\nabla\left[\frac{\nabla_\perp\phi}{B}n\right]\right)=\frac{1}{\omega_{ci}}\frac{1}{B\rho}\{\phi,\Omega^D\}+\frac{1}{\omega_{ci}}\frac{1}{2\rho}\{\boldsymbol{u}_E^2,n\}.
\tag{5.5}
$$

Where the Poisson brackets described in appendix I has been used. A similar expression is expected to be found for other geometries as well, at least as long as the B field is constant. When this is not the case, terms arising from $\nabla\frac{1}{B}$ are expected.

The evolution of the modified vorticity can now be written as

$$\begin{aligned}\frac{1}{\omega_{ci}}\partial_t\Omega^D =& -\frac{\nu_{in}}{\omega_{ci}}\left(n\Omega + \frac{\nabla_\perp\phi}{B}\cdot\nabla n\right)\\ &-\frac{1}{\omega_{ci}\rho}\left(\frac{1}{B}\{\phi,\Omega^D\}+\frac{1}{2}\{\boldsymbol{u}_E^2,n\}\right)-\frac{1}{\omega_{ci}}\partial_\parallel\nabla\cdot\left(u_{i,\parallel}\frac{\nabla_\perp\phi}{B}n\right)\\ &+\frac{1}{e}\partial_\parallel j_\parallel.\end{aligned} \tag{5.6}$$

5.3 Parallel current and momentum density

In order to solve the system of equations, we need to determine $u_{\alpha,\parallel}$. This could be done by evolving the ion momentum equation and the electron momentum equation in time. However, as we are calculating $\frac{1}{e}\partial_\parallel\left(ne\left[u_{i,\parallel}-u_{e,\parallel}\right]\right)$ in eq. (5.6), we require that this term is of high precision. This is because the vorticity is a first order term, and loss of numerical precision can be high when subtracting $u_{i,\parallel}$ and $u_{e,\parallel}$ if they are almost equal to each other. As a result, the numerical error may pollute the calculated order of the modified vorticity.

Therefore, we will instead evolve the parallel current equation in time. We also choose to evolve the sum of the parallel density momentum equations in time. As will be shown, this is to high accuracy the same as evolving density times the parallel ion velocity in time. The variation of the $nu_{i,\parallel}$ field is smaller than the variation in the $u_{i,\parallel}$ as the sheath boundary condition (to be treated in section 5.5) will accelerate the ions to the ion acoustic speed, and thus create a lower density around the sheath as compared with the rest of the parallel domain. A smaller variation in the domain has the advantage that the difference in magnitude of the largest and smallest eigenvalues decreases, which is beneficial for the stiffness of the system [43].

To derive the current equation and the parallel momentum density equation, we will start from eq. (2.4). We have that

$$\begin{aligned}\partial_t\left(n_\alpha m_\alpha\boldsymbol{u}_\alpha\right) =& -\nabla\cdot\overline{\overline{\boldsymbol{\Pi}}}_\alpha + q_\alpha n_\alpha\left(\boldsymbol{E}+\boldsymbol{u_\alpha}\times\boldsymbol{B}\right)+\boldsymbol{R}_{\beta\to\alpha}+\boldsymbol{R}_{n\to\alpha}\\ =& -\nabla\cdot\overline{\overline{\boldsymbol{\pi}}}_\alpha-\nabla p_\alpha - m_\alpha n_\alpha\boldsymbol{u}_\alpha\cdot\nabla\boldsymbol{u}_\alpha - m_\alpha\nabla\cdot\left(n_\alpha\boldsymbol{u}_\alpha\right)\boldsymbol{u}_\alpha\\ &+q_\alpha n_\alpha\left(\boldsymbol{E}+\boldsymbol{u_\alpha}\times\boldsymbol{B}\right)+\boldsymbol{R}_{\beta\to\alpha}+\boldsymbol{R}_{n\to\alpha}\\ \boldsymbol{b}\cdot\partial_t\left(n_\alpha m_\alpha\boldsymbol{u}_\alpha\right) =& \boldsymbol{b}\cdot\Big(-\nabla\cdot\overline{\overline{\boldsymbol{\pi}}}_\alpha-\nabla p_\alpha - m_\alpha n_\alpha\left[\boldsymbol{u}_\alpha\cdot\nabla\right]\boldsymbol{u}_\alpha - m_\alpha\boldsymbol{u}_\alpha\nabla\cdot\left[n_\alpha\boldsymbol{u}_\alpha\right]\\ &+q_\alpha n_\alpha\left[\boldsymbol{E}+\boldsymbol{u_\alpha}\times\boldsymbol{B}\right]+\boldsymbol{R}_{\beta\to\alpha}+\boldsymbol{R}_{n\to\alpha}\Big) \qquad \partial_i\boldsymbol{b}\\ \partial_t\left(n_\alpha m_\alpha u_{\alpha,\parallel}\right) =& -\left(\nabla\cdot\overline{\overline{\boldsymbol{\pi}}}_\alpha\right)_\parallel-\partial_\parallel p_\alpha - m_\alpha n_\alpha\left(\boldsymbol{u}_\alpha\cdot\nabla\right)u_{\alpha,\parallel}-m_\alpha u_{\alpha,\parallel}\nabla\cdot\left(n_\alpha\boldsymbol{u}_\alpha\right)\\ &+q_\alpha n_\alpha\boldsymbol{E}_\parallel+\boldsymbol{R}_{\beta\to\alpha,\parallel}+\boldsymbol{R}_{n\to\alpha,\parallel}.\end{aligned} \tag{5.7}$$

We observe that $\nabla\cdot\left(n_\alpha\boldsymbol{u}_\alpha\right)$ is a part of the continuity equation, and we will exploit this. From quasi-neutrality, we have that $\partial_t Zn_i\simeq\partial_t n_e\simeq\partial_t n$. At the same time, since the created charge is zero, we have that $ZS_{i,n}=S_{e,n}$. This must mean that $Z\nabla\cdot\left(n_i\boldsymbol{u}_i\right)\simeq\nabla\cdot\left(n_e\boldsymbol{u}_e\right)$, which leads us to the conclusion that $\frac{|q_\alpha|}{e}\nabla\cdot\left(n_\alpha\boldsymbol{u}_\alpha\right)\simeq\nabla\cdot\left(n_e\boldsymbol{u}_e\right)$. Inserting this into eq. (5.7) yields

$$\partial_t\left(n_\alpha m_\alpha\boldsymbol{u}_\alpha\right) = -\left(\nabla\cdot\overline{\overline{\boldsymbol{\pi}}}_\alpha\right)_\parallel-\partial_\parallel p_\alpha - m_\alpha n_\alpha\left(\boldsymbol{u}_\alpha\cdot\nabla\right)u_{\alpha,\parallel}-m_\alpha u_{\alpha,\parallel}\frac{e}{|q_\alpha|}\nabla\cdot\left(n_e\boldsymbol{u}_e\right)$$

$$
\begin{aligned}
&+ q_\alpha n_\alpha \boldsymbol{E}_\parallel + \boldsymbol{R}_{\beta\to\alpha,\parallel} + \boldsymbol{R}_{n\to\alpha,\parallel} \\
=&- \left(\nabla\cdot\overline{\overline{\boldsymbol{\pi}}}_\alpha\right)_\parallel - \partial_\parallel p_\alpha - m_\alpha n_\alpha \left(\boldsymbol{u}_\alpha\cdot\nabla\right) u_{\alpha,\parallel} - m_\alpha u_{\alpha,\parallel}\frac{e}{|q_\alpha|}\left(-\partial_t n_e + S_{e,n}\right) \\
&+ q_\alpha n_\alpha \boldsymbol{E}_\parallel + \boldsymbol{R}_{\beta\to\alpha,\parallel} + \boldsymbol{R}_{n\to\alpha,\parallel} && \text{eq. (5.1)} \\
=&- \left(\nabla\cdot\overline{\overline{\boldsymbol{\pi}}}_\alpha\right)_\parallel - \partial_\parallel p_\alpha - m_\alpha n_\alpha \left(\boldsymbol{u}_\alpha\cdot\nabla\right) u_{\alpha,\parallel} \\
&- m_\alpha u_{\alpha,\parallel}\frac{e}{|q_\alpha|}\left(\boldsymbol{u}_E\cdot\nabla n_e - \frac{\rho_s^2\nu_{ei}}{\mu}\nabla_\perp^2 n_e + \partial_\parallel\left[n_e u_{e,\parallel}\right] - S_{e,n} + S_{e,n}\right) \\
&+ q_\alpha n_\alpha \boldsymbol{E}_\parallel + \boldsymbol{R}_{\beta\to\alpha,\parallel} + \boldsymbol{R}_{n\to\alpha,\parallel} && \text{Only perpendicular } \boldsymbol{u}_E \text{ advection [33]} \\
=&- \left(\nabla\cdot\overline{\overline{\boldsymbol{\pi}}}_\alpha\right)_\parallel - \partial_\parallel p_\alpha - m_\alpha n_\alpha \left(\boldsymbol{u}_E + \boldsymbol{u}_{\alpha,\parallel}\right)\cdot\nabla u_{\alpha,\parallel} \\
&- m_\alpha u_{\alpha,\parallel}\frac{e}{|q_\alpha|}\left(\boldsymbol{u}_E\cdot\nabla n_e - \frac{\rho_s^2\nu_{ei}}{\mu}\nabla_\perp^2 n_e + \partial_\parallel\left[n_e u_{e,\parallel}\right]\right) \\
&+ q_\alpha n_\alpha \boldsymbol{E}_\parallel + \boldsymbol{R}_{\beta\to\alpha,\parallel} + \boldsymbol{R}_{n\to\alpha,\parallel} && \text{eq. (D.1)} \\
=&\frac{4\eta_{\alpha,0}}{3}\partial_z^2 u_{\alpha,\parallel} - \partial_\parallel p_\alpha - m_\alpha n_\alpha \boldsymbol{u}_E\cdot\nabla u_{\alpha,\parallel} - m_\alpha n_\alpha \boldsymbol{u}_{\alpha,\parallel}\cdot\nabla u_{\alpha,\parallel} \\
&- m_\alpha u_{\alpha,\parallel}\frac{e}{|q_\alpha|}\left(\boldsymbol{u}_E\cdot\nabla n_e - \frac{\rho_s^2\nu_{ei}}{\mu}\nabla_\perp^2 n_e + \partial_\parallel\left[n_e u_{e,\parallel}\right]\right) \\
&+ q_\alpha n_\alpha \boldsymbol{E}_\parallel + \boldsymbol{R}_{\beta\to\alpha,\parallel} + \boldsymbol{R}_{n\to\alpha,\parallel} \\
=&\frac{4\eta_{\alpha,0}}{3}\partial_z^2 u_{\alpha,\parallel} - \partial_\parallel p_\alpha - m_\alpha n_\alpha \boldsymbol{u}_E\cdot\nabla u_{\alpha,\parallel} - m_\alpha n_\alpha u_{\alpha,\parallel}\boldsymbol{b}\cdot\nabla u_{\alpha,\parallel} \\
&- m_\alpha u_{\alpha,\parallel}\frac{e}{|q_\alpha|}\left(\boldsymbol{u}_E\cdot\nabla n_e - \frac{\rho_s^2\nu_{ei}}{\mu}\nabla_\perp^2 n_e + \partial_\parallel\left[n_e u_{e,\parallel}\right]\right) \\
&+ q_\alpha n_\alpha \boldsymbol{E}_\parallel \pm 0.51 m_e n_e \nu_{ei}\left(u_{e,\parallel} - u_{i,\parallel}\right) - m_\alpha n_\alpha \nu_{\alpha n} u_{\alpha,\parallel} && \begin{array}{l}+ \text{ for } \alpha = i \\ - \text{ for } \alpha = e\end{array} \\
=&\frac{4\eta_{\alpha,0}}{3}\partial_z^2 u_{\alpha,\parallel} - \partial_\parallel p_\alpha - m_\alpha n_\alpha \boldsymbol{u}_E\cdot\nabla u_{\alpha,\parallel} - m_\alpha n_\alpha u_{\alpha,\parallel}\partial_\parallel u_{\alpha,\parallel} \\
&- m_\alpha u_{\alpha,\parallel}\frac{e}{|q_\alpha|}\left(\boldsymbol{u}_E\cdot\nabla n_e - \frac{\rho_s^2\nu_{ei}}{\mu}\nabla_\perp^2 n_e + \partial_\parallel\left[n_e u_{e,\parallel}\right]\right) && \begin{array}{l} j_\parallel = e(Z n_i u_{i,\parallel} - n_e u_{e,\parallel}) \\ \simeq e(n_e u_{i,\parallel} - n_e u_{e,\parallel}) \\ = e n_e (u_{i,\parallel} - u_{e,\parallel})\end{array} \\
&+ q_\alpha n_\alpha \boldsymbol{E}_\parallel \mp 0.51 m_e \nu_{ei}\frac{j_\parallel}{e} - m_\alpha n_\alpha \nu_{\alpha n} u_{\alpha,\parallel} \\
=&- m_\alpha n_\alpha \boldsymbol{u}_E\cdot\nabla u_{\alpha,\parallel} - m_\alpha u_{\alpha,\parallel}\frac{e}{|q_\alpha|}\boldsymbol{u}_E\cdot\nabla n_e - m_\alpha n_\alpha u_{\alpha,\parallel}\partial_\parallel u_{\alpha,\parallel} - m_\alpha u_{\alpha,\parallel}\frac{e}{|q_\alpha|}\partial_\parallel\left(n_e u_{e,\parallel}\right) \\
&- \partial_\parallel p_\alpha + q_\alpha n_\alpha \boldsymbol{E}_\parallel \\
&\mp 0.51 m_e \nu_{ei}\frac{j_\parallel}{e} + m_\alpha u_{\alpha,\parallel}\frac{e}{|q_\alpha|}\frac{\rho_s^2\nu_{ei}}{\mu}\nabla_\perp^2 n_e - m_\alpha n_\alpha \nu_{\alpha n} u_{\alpha,\parallel} + \frac{4\eta_{\alpha,0}}{3}\partial_z^2 u_{\alpha,\parallel}
\end{aligned}
$$

$$
\begin{aligned}
m_\alpha \partial_t\left(n_\alpha u_{\alpha,\parallel}\right) =&- m_\alpha n_\alpha \boldsymbol{u}_E\cdot\nabla u_{\alpha,\parallel} - m_\alpha u_{\alpha,\parallel}\frac{e}{|q_\alpha|}\boldsymbol{u}_E\cdot\nabla n_e \\
&- m_\alpha u_{\alpha,\parallel}\left(n_\alpha\partial_\parallel u_{\alpha,\parallel} + \frac{e}{|q_\alpha|}\partial_\parallel\left[n_e u_{e,\parallel}\right]\right) - \partial_\parallel p_\alpha + q_\alpha n_\alpha \boldsymbol{E}_\parallel \\
&+ \nu_{ei}\left(\mp 0.51 m_e\frac{j_\parallel}{e} + m_\alpha u_{\alpha,\parallel}\frac{e}{|q_\alpha|}\frac{\rho_s^2}{\mu}\nabla_\perp^2 n_e\right) \\
&- m_\alpha n_\alpha \nu_{\alpha n} u_{\alpha,\parallel} + \frac{4\eta_{\alpha,0}}{3}\partial_z^2 u_{\alpha,\parallel}.
\end{aligned} \tag{5.8}
$$

Notice that

1. We have collected the parallel advection terms of the electron density equation and of the parallel momentum density equation.
2. We have collected the resistivity terms arising from the electron density equation and those arising from the parallel momentum density equation.

This means that the parallel momentum density for ions reads (using that $p_i = 0$ as $T_i = 0$)

$$\begin{aligned}
m_i\partial_t\left(n_iu_{i,\parallel}\right) =& -m_in_i\boldsymbol{u}_E\cdot\nabla u_{\alpha,\parallel} - m_iu_{\alpha,\parallel}\frac{1}{Z}\boldsymbol{u}_E\cdot\nabla n_e - m_iu_{i,\parallel}\left(n_i\partial_\parallel u_{i,\parallel} + \frac{1}{Z}\partial_\parallel\left[n_eu_{e,\parallel}\right]\right) + Zen_i\boldsymbol{E}_\parallel \\
&+ \nu_{ei}\left(-0.51m_e\frac{j_\parallel}{e} + m_iu_{i,\parallel}\frac{\rho_s^2}{\mu}\frac{1}{Z}\nabla_\perp^2 n_e\right) - m_in_i\nu_{in}u_{i,\parallel} + \frac{4\eta_{i,0}}{3}\partial_z^2u_{i,\parallel} \qquad \text{Quasi-neutrality} \\
\frac{1}{Z}m_i\partial_t\left(nu_{i,\parallel}\right) =& -\frac{m_i}{Z}\boldsymbol{u}_E\cdot\nabla\left(u_{i,\parallel}n\right) - m_iu_{i,\parallel}\frac{1}{Z}\left(n\partial_\parallel u_{i,\parallel} + \partial_\parallel\left[nu_{e,\parallel}\right]\right) + en\boldsymbol{E}_\parallel \\
&+ \nu_{ei}\left(-0.51m_e\frac{j_\parallel}{e} + \frac{1}{Z}m_iu_{i,\parallel}\frac{\rho_s^2}{\mu}\nabla_\perp^2 n\right) - \frac{1}{Z}m_in\nu_{in}u_{i,\parallel} + \frac{4\eta_{i,0}}{3}\partial_z^2u_{i,\parallel},
\end{aligned} \tag{5.9}$$

and that the momentum density for electrons reads

$$\begin{aligned}
m_e\partial_t\left(n_eu_{e,\parallel}\right) =& -m_e\boldsymbol{u}_E\cdot\nabla\left(u_{e,\parallel}n_e\right) - m_eu_{e,\parallel}\left(n_e\partial_\parallel u_{e,\parallel} + \partial_\parallel\left[n_eu_{e,\parallel}\right]\right) \\
&- \partial_\parallel p_e + q_en_e\boldsymbol{E}_\parallel \\
&+ \nu_{ei}\left(0.51m_e\frac{j_\parallel}{e} + m_eu_{e,\parallel}\frac{\rho_s^2}{\mu}\nabla_\perp^2 n_e\right) - m_en_e\nu_{en}u_{e,\parallel} + \frac{4\eta_{e,0}}{3}\partial_z^2u_{e,\parallel} \qquad \text{Quasi-neutrality} \\
m_e\partial_t\left(nu_{e,\parallel}\right) =& -m_e\boldsymbol{u}_E\cdot\nabla\left(u_{e,\parallel}n\right) - m_eu_{e,\parallel}\left(n\partial_\parallel u_{e,\parallel} + \partial_\parallel\left[nu_{e,\parallel}\right]\right) \\
&- \partial_\parallel p_e - en\boldsymbol{E}_\parallel \\
&+ \nu_{ei}\left(0.51m_e\frac{j_\parallel}{e} + m_eu_{e,\parallel}\frac{\rho_s^2}{\mu}\nabla_\perp^2 n\right) - m_en\nu_{en}u_{e,\parallel} + \frac{4\eta_{e,0}}{3}\partial_z^2u_{e,\parallel}.
\end{aligned} \tag{5.10}$$

5.3.1 Parallel momentum density equation

We can obtain the total momentum density of the plasma by adding eq. (5.9) and eq. (5.10). We obtain

$$\begin{aligned}
\frac{1}{Z}m_i\partial_t\left(nu_{i,\parallel}\right) + m_e\partial_t\left(nu_{e,\parallel}\right) =& -\frac{m_i}{Z}\boldsymbol{u}_E\cdot\nabla\left(u_{i,\parallel}n\right) - m_e\boldsymbol{u}_E\cdot\nabla\left(u_{e,\parallel}n\right) \\
&- \frac{m_i}{Z}u_{i,\parallel}\left(n\partial_\parallel u_{i,\parallel} + \partial_\parallel\left[nu_{e,\parallel}\right]\right) - m_eu_{e,\parallel}\left(n\partial_\parallel u_{e,\parallel} + \partial_\parallel\left[nu_{e,\parallel}\right]\right) \\
&- \partial_\parallel p_e + en\boldsymbol{E}_\parallel - en\boldsymbol{E}_\parallel \\
&+ \nu_{ei}\left(-0.51m_e\frac{j_\parallel}{e} + \frac{m_i}{Z}u_{i,\parallel}\frac{\rho_s^2}{\mu}\nabla_\perp^2 n\right) + \nu_{ei}\left(0.51m_e\frac{j_\parallel}{e} + m_eu_{e,\parallel}\frac{\rho_s^2}{\mu}\nabla_\perp^2 n\right) \\
&- \frac{m_i}{Z}n\nu_{in}u_{i,\parallel} - m_en\nu_{en}u_{e,\parallel} \\
&+ \frac{4\eta_{i,0}}{3}\partial_z^2u_{i,\parallel} + \frac{4\eta_{e,0}}{3}\partial_z^2u_{e,\parallel} \\
=& -\frac{m_i}{Z}\boldsymbol{u}_E\cdot\nabla\left(u_{i,\parallel}n\right) - m_e\boldsymbol{u}_E\cdot\nabla\left(u_{e,\parallel}n\right) \\
&- m_iu_{i,\parallel}\frac{1}{Z}\left(n\partial_\parallel u_{i,\parallel} + \partial_\parallel\left[nu_{e,\parallel}\right]\right) - m_eu_{e,\parallel}\left(n\partial_\parallel u_{e,\parallel} + \partial_\parallel\left[nu_{e,\parallel}\right]\right)
\end{aligned}$$

$$
\begin{aligned}
&- \partial_\parallel p_e + \nu_{ei}\left(\frac{m_i}{Z}u_{i,\parallel}\frac{\rho_s^2}{\mu}\nabla_\perp^2 n + m_e u_{e,\parallel}\frac{\rho_s^2}{\mu}\nabla_\perp^2 n\right)\\
&- \frac{1}{Z}m_i n\nu_{in}u_{i,\parallel} - m_e n\nu_{en}u_{e,\parallel}\\
&+ \frac{4\eta_{i,0}}{3}\partial_z^2 u_{i,\parallel} + \frac{4\eta_{e,0}}{3}\partial_z^2 u_{e,\parallel}\\
\frac{m_i}{Z}\partial_t\left(nu_{i,\parallel}\right) \simeq &- \frac{m_i}{Z}\boldsymbol{u}_E\cdot\nabla\left(u_{i,\parallel}n\right) - m_i u_{i,\parallel}\frac{1}{Z}\left(n\partial_\parallel u_{i,\parallel} + \partial_\parallel\left[nu_{e,\parallel}\right]\right)\\
&- \partial_\parallel p_e + \nu_{ei}\frac{m_i}{Z}u_{i,\parallel}\frac{\rho_s^2}{\mu}\nabla_\perp^2 n - \frac{1}{Z}m_i n\nu_{in}u_{i,\parallel} - m_e n\nu_{en}u_{e,\parallel}\\
&+ \frac{4\eta_{i,0}}{3}\partial_z^2 u_{i,\parallel} + \frac{4\eta_{e,0}}{3}\partial_z^2 u_{e,\parallel}\\
\partial_t\left(nu_{i,\parallel}\right) = &- \frac{Z}{m_i}\frac{m_i}{Z}\boldsymbol{u}_E\cdot\nabla\left(u_{i,\parallel}n\right) - \frac{Z}{m_i}\frac{m_i}{Z}u_{i,\parallel}\left(\frac{1}{Z}n\partial_\parallel u_{i,\parallel} + \partial_\parallel\left[nu_{e,\parallel}\right]\right)\\
&- \frac{Z}{m_i}T_e\partial_\parallel n + \frac{Z}{m_i}\nu_{ei}\frac{m_i}{Z}u_{i,\parallel}\frac{\rho_s^2}{\mu}\nabla_\perp^2 n - \frac{Z}{m_i}\frac{1}{Z}m_i n\nu_{in}u_{i,\parallel} - \frac{Zm_e}{m_i}n\nu_{en}u_{e,\parallel}\\
&+ \frac{Z4}{m_i 3}\left(\eta_{i,0}\partial_z^2 u_{i,\parallel} + \eta_{e,0}\partial_z^2 u_{e,\parallel}\right)
\end{aligned}
$$

$m_i \gg m_e$

Assume that $u_{e,\parallel}$ and its gradients is approximately of same order as $u_{i,\parallel}$ and its gradients

Constant T_e

$$
\begin{aligned}
\partial_t\left(nu_{i,\parallel}\right) \simeq &- \boldsymbol{u}_E\cdot\nabla\left(u_{i,\parallel}n\right) - u_{i,\parallel}\left(n\partial_\parallel u_{i,\parallel} + \partial_\parallel\left[nu_{e,\parallel}\right]\right)\\
&- \frac{Z}{m_i}T_e\partial_\parallel n + \nu_{ei}u_{i,\parallel}\frac{\rho_s^2}{\mu}\nabla_\perp^2 n - n\left(\nu_{in}u_{i,\parallel} + \frac{Z}{\mu}\nu_{en}u_{e,\parallel}\right)\\
&+ \frac{Z4}{m_i 3}\left(\eta_{i,0}\partial_z^2 u_{i,\parallel} + \eta_{e,0}\partial_z^2 u_{e,\parallel}\right).
\end{aligned}
\tag{5.11}
$$

5.3.2 Parallel current equation

We can obtain the equation for the time evolution of the parallel current by multiplying eq. (5.9) with $\frac{q_i}{m_i}$ and add it with the $\frac{q_e}{m_e}$ multiplication of eq. (5.10). Multiplication of eq. (5.9) with $\frac{q_i}{m_i}$ yields

$$
\begin{aligned}
\frac{q_i}{m_i}\frac{1}{Z}m_i\partial_t\left(nu_{i,\parallel}\right) = &- \frac{q_i}{m_i}\frac{Z}{m_i}\boldsymbol{u}_E\cdot\nabla\left(u_{i,\parallel}n\right) - \frac{q_i}{m_i}m_i u_{i,\parallel}\frac{1}{Z}\left(n\partial_\parallel u_{i,\parallel} + \partial_\parallel\left[nu_{e,\parallel}\right]\right) + \frac{q_i}{m_i}en\boldsymbol{E}_\parallel\\
&+ \frac{q_i}{m_i}\nu_{ei}\left(-0.51m_e\frac{j_\parallel}{e} + \frac{m_i}{Z}u_{i,\parallel}\frac{\rho_s^2}{\mu}\nabla_\perp^2 n\right) - \frac{q_i}{m_i}\frac{1}{Z}m_i n\nu_{in}u_{i,\parallel} + \frac{q_i}{m_i}\frac{4\eta_{i,0}}{3}\partial_z^2 u_{i,\parallel}\\
e\partial_t\left(nu_{i,\parallel}\right) = &- e\boldsymbol{u}_E\cdot\nabla\left(u_{i,\parallel}n\right) - eu_{i,\parallel}\left(n\partial_\parallel u_{i,\parallel} + \partial_\parallel\left[nu_{e,\parallel}\right]\right) + \frac{Ze^2}{m_i}n\boldsymbol{E}_\parallel\\
&+ \frac{Ze}{m_i}\nu_{ei}\left(-0.51m_e\frac{j_\parallel}{e} + \frac{m_i}{Z}u_{i,\parallel}\frac{\rho_s^2}{\mu}\nabla_\perp^2 n\right) - en\nu_{in}u_{i,\parallel} + \frac{Ze}{m_i}\frac{4\eta_{i,0}}{3}\partial_z^2 u_{i,\parallel}.
\end{aligned}
\tag{5.12}
$$

whereas multiplication of eq. (5.10) with $\frac{q_e}{m_e}$ yields

$$
\frac{q_e}{m_e}m_e\partial_t\left(nu_{e,\parallel}\right) = - \frac{q_e}{m_e}m_e\boldsymbol{u}_E\cdot\nabla\left(u_{e,\parallel}n\right) - \frac{q_e}{m_e}m_e u_{e,\parallel}\left(n\partial_\parallel u_{e,\parallel} + \partial_\parallel\left[nu_{e,\parallel}\right]\right)
$$

$$
\begin{aligned}
&- \frac{q_e}{m_e}\partial_\parallel p_e - \frac{q_e}{m_e} en \boldsymbol{E}_\parallel \\
&+ \frac{q_e}{m_e}\nu_{ei}\left(0.51 m_e \frac{j_\parallel}{e} + m_e u_{e,\parallel}\frac{\rho_s^2}{\mu}\nabla_\perp^2 n\right) - \frac{q_e}{m_e} m_e n \nu_{en} u_{e,\parallel} + \frac{q_e}{m_e}\frac{4\eta_{e,0}}{3}\partial_z^2 u_{e,\parallel} \\
-e\partial_t\left(n u_{e,\parallel}\right) =& e\boldsymbol{u}_E\cdot\nabla\left(u_{e,\parallel} n\right) + e u_{e,\parallel}\left(n\partial_\parallel u_{e,\parallel} + \partial_\parallel\left[n u_{e,\parallel}\right]\right) \\
&+ \frac{e}{m_e}\partial_\parallel p_e + \frac{e^2}{m_e} n\boldsymbol{E}_\parallel \\
&- \frac{e}{m_e}\nu_{ei}\left(0.51 m_e \frac{j_\parallel}{e} + m_e u_{e,\parallel}\frac{\rho_s^2}{\mu}\nabla_\perp^2 n\right) + e n \nu_{en} u_{e,\parallel} - \frac{e}{m_e}\frac{4\eta_{e,0}}{3}\partial_z^2 u_{e,\parallel}.
\end{aligned}
\tag{5.13}
$$

Adding eq. (5.12) with eq. (5.13) yields

$$
\begin{aligned}
e\partial_t\left(n u_{i,\parallel}\right) - e\partial_t\left(n u_{e,\parallel}\right) =& - e\boldsymbol{u}_E\cdot\nabla\left(u_{i,\parallel} n\right) + e\boldsymbol{u}_E\cdot\nabla\left(u_{e,\parallel} n\right) \\
&- e u_{i,\parallel}\left(n\partial_\parallel u_{i,\parallel} + \partial_\parallel\left[n u_{e,\parallel}\right]\right) + e u_{e,\parallel}\left(n\partial_\parallel u_{e,\parallel} + \partial_\parallel\left[n u_{e,\parallel}\right]\right) \\
&+ \frac{e}{m_e}\partial_\parallel p_e + \frac{Ze^2}{m_i} n\boldsymbol{E}_\parallel + \frac{e^2}{m_e} n\boldsymbol{E}_\parallel \\
&+ \frac{Ze}{m_i}\nu_{ei}\left(-0.51 m_e \frac{j_\parallel}{e} + \frac{m_i}{Z} u_{i,\parallel}\frac{\rho_s^2}{\mu}\nabla_\perp^2 n\right) \\
&- \frac{e}{m_e}\nu_{ei}\left(0.51 m_e \frac{j_\parallel}{e} + m_e u_{e,\parallel}\frac{\rho_s^2}{\mu}\nabla_\perp^2 n\right) \\
&- e n \nu_{in} u_{i,\parallel} + e n \nu_{en} u_{e,\parallel} + \frac{Ze}{m_i}\frac{4\eta_{i,0}}{3}\partial_z^2 u_{i,\parallel} - \frac{e}{m_e}\frac{4\eta_{e,0}}{3}\partial_z^2 u_{e,\parallel} \\
\partial_t j_\parallel =& e\boldsymbol{u}_E\cdot\nabla\left(n\left[u_{e,\parallel} - u_{i,\parallel}\right]\right) \\
&- e u_{i,\parallel}\left(n\partial_\parallel u_{i,\parallel} + \partial_\parallel\left[n u_{e,\parallel}\right]\right) + e u_{e,\parallel}\left(n\partial_\parallel u_{e,\parallel} + \partial_\parallel\left[n u_{e,\parallel}\right]\right) \\
&+ \frac{e}{m_e}\partial_\parallel p_e + n e^2 \boldsymbol{E}_\parallel\left(\frac{Z}{m_i} + \frac{1}{m_e}\right) \\
&+ \nu_{ei}\left(-0.51 j_\parallel\left[\frac{Z}{\mu} + 1\right] + e\frac{\rho_s^2}{\mu}\nabla_\perp^2 n\left[u_{i,\parallel} - u_{e,\parallel}\right]\right) \\
&+ e n\left(-\nu_{in} u_{i,\parallel} + \nu_{en} u_{e,\parallel}\right) + \frac{Ze}{m_i}\frac{4\eta_{i,0}}{3}\partial_z^2 u_{i,\parallel} - \frac{e}{m_e}\frac{4\eta_{e,0}}{3}\partial_z^2 u_{e,\parallel} \qquad \tfrac{1}{m_e} \gg \tfrac{1}{m_i} \\
\simeq& - \boldsymbol{u}_E\cdot\nabla j_\parallel \\
&- e u_{i,\parallel}\left(n\partial_\parallel u_{i,\parallel} + \partial_\parallel\left[n u_{e,\parallel}\right]\right) + e u_{e,\parallel}\left(n\partial_\parallel u_{e,\parallel} + \partial_\parallel\left[n u_{e,\parallel}\right]\right) \\
&+ \frac{e}{m_e}\partial_\parallel p_e + \frac{e^2}{m_e} n\boldsymbol{E}_\parallel \\
&+ \nu_{ei}\left(-0.51 j_\parallel + \left[u_{i,\parallel} - u_{e,\parallel}\right] n e\frac{\frac{\rho_s^2}{\mu}\nabla_\perp^2 n}{n}\right) \\
&+ e n\left(-\nu_{in} u_{i,\parallel} + \nu_{en} u_{e,\parallel}\right) - \frac{e}{m_e}\frac{4\eta_{e,0}}{3}\partial_z^2 u_{e,\parallel} \\
=& - \boldsymbol{u}_E\cdot\nabla j_\parallel \\
&- e u_{i,\parallel}\left(n\partial_\parallel u_{i,\parallel} + \partial_\parallel\left[n u_{e,\parallel}\right]\right) + e u_{e,\parallel}\left(n\partial_\parallel u_{e,\parallel} + \partial_\parallel\left[n u_{e,\parallel}\right]\right) \\
&+ \frac{e}{m_e}\partial_\parallel p_e + \frac{e^2}{m_e} n\boldsymbol{E}_\parallel
\end{aligned}
$$

$$
\begin{aligned}
&+ \nu_{ei}\left(-0.51 j_\parallel - j_\parallel \frac{\frac{\rho_s^2}{\mu}\nabla_\perp^2 n}{n}\right) \\
&+ en\left(-\nu_{in}u_{i,\parallel} + \nu_{en}u_{e,\parallel}\right) - \frac{e}{m_e}\frac{4\eta_{e,0}}{3}\partial_z^2 u_{e,\parallel} \qquad \text{Assume } 0.51 \gg \frac{\frac{\rho_s^2}{\mu}\nabla_\perp^2 n}{n} \\
=& - \boldsymbol{u}_E \cdot \nabla j_\parallel \\
&- e u_{i,\parallel}\left(n\partial_\parallel u_{i,\parallel} + \partial_\parallel\left[n u_{e,\parallel}\right]\right) + e u_{e,\parallel}\left(n\partial_\parallel u_{e,\parallel} + \partial_\parallel\left[n u_{e,\parallel}\right]\right) \\
&+ \frac{e}{m_e}T_e\partial_\parallel n + \frac{e^2}{m_e}n\boldsymbol{E}_\parallel - 0.51\nu_{ei}j_\parallel \\
&+ en\left(\nu_{en}u_{e,\parallel} - \nu_{in}u_{i,\parallel}\right) - \frac{e}{m_e}\frac{4\eta_{e,0}}{3}\partial_z^2 u_{e,\parallel} \\
=& - \boldsymbol{u}_E \cdot \nabla j_\parallel \\
&- en\left(u_{i,\parallel}\partial_\parallel u_{i,\parallel} - u_{e,\parallel}\partial_\parallel u_{e,\parallel}\right) - \frac{ne\left(u_{i,\parallel} - u_{e,\parallel}\right)}{n}\partial_\parallel\left(n u_{e,\parallel}\right) \\
&+ \frac{e}{m_e}T_e\partial_\parallel n + \frac{e^2}{m_e}n\boldsymbol{E}_\parallel - 0.51\nu_{ei}j_\parallel \\
&+ en\left(\nu_{en}u_{e,\parallel} - \nu_{in}u_{i,\parallel}\right) - \frac{e}{m_e}\frac{4\eta_{e,0}}{3}\partial_z^2 u_{e,\parallel}
\end{aligned}
$$

$$
\begin{aligned}
\partial_t j_\parallel \simeq& - \boldsymbol{u}_E \cdot \nabla j_\parallel \\
&- en\left(u_{i,\parallel}\partial_\parallel u_{i,\parallel} - u_{e,\parallel}\partial_\parallel u_{e,\parallel}\right) - \frac{j_\parallel}{n}\partial_\parallel\left(n u_{e,\parallel}\right) \\
&+ \frac{e}{m_e}T_e\partial_\parallel n + \frac{e^2}{m_e}n\boldsymbol{E}_\parallel - 0.51\nu_{ei}j_\parallel \\
&+ en\left(\nu_{en}u_{e,\parallel} - \nu_{in}u_{i,\parallel}\right) - \frac{e}{m_e}\frac{4\eta_{e,0}}{3}\partial_z^2 u_{e,\parallel}.
\end{aligned} \tag{5.14}
$$

We have now successfully derived all the equations we needed in order to evolve our system in time. We have used the continuity equation and the drifts in order to derive an equation evolving the electron density in time. Due to quasi-neutrality this also describes how the ion density evolves in time. We have used the conservation of charge to derive the modified vorticity equation. Both the parallel momentum density equation and the parallel current has been derived from the momentum density equation for electrons and ions. Before plugging these equations into a code which evolves them in time, we will normalize them.

5.4 Normalization

We will in this section normalize the set of equations derived in this chapter. The motivation for doing so is to write the equations in a unit-less manner, so that the evolved variables can be compared to each other in a more meaningful way. It will also simplify the system of equations by removing factors with units appearing in front of terms, possibly turning them into non-dimensional units which characterizes the system. Readers familiar with the procedure can readily skip until section 5.5, noting that we divide the density equation with n and convert it to an equation of the logarithmic normalized density as this ensures positivity of the density.

We will here normalize using the standard gyro-Bohm normalization[4].That is, we let

$$\breve{\boldsymbol{x}} = \frac{\boldsymbol{x}}{\rho_s} \qquad \breve{t} = t\omega_{ci} \qquad \breve{\boldsymbol{u}} = \frac{\boldsymbol{u}}{c_s} \qquad \breve{\phi} = \frac{e\phi}{T_{e,0}} \qquad \breve{n} = \frac{n}{n_0} \qquad \breve{T}_e = \frac{T_e}{T_{e,0}} \qquad \breve{B} = \frac{B}{B_0},$$

where the breve ($\breve{}$) denotes a normalized (unit less) quantity.

In order to take some shortcuts in the following derivations, we observe (from the Lorentz force) that $\|\boldsymbol{B}\|$ must have the same units as $\|\boldsymbol{E}\|/\|\boldsymbol{u}\|$. As a consequence $\|\boldsymbol{E}\|/\|\boldsymbol{B}\|$ must have the same units as $\|\boldsymbol{u}\|$. In the electrostatic approximation this means that $\|\nabla_\perp\phi\|/\|\boldsymbol{B}\|$ must have the same normalization as $\|\boldsymbol{u}\|$, and thus

$$\frac{\breve{\nabla}_\perp\breve{\phi}}{\breve{B}} = \frac{\frac{\nabla_\perp\phi}{B}}{c_s} = \frac{\nabla_\perp\phi}{c_s B}.$$

We can see that this is true by looking at the normalization of the individual quantities. Due to the spatial normalization, we must have that $\nabla = \breve{\nabla}/\rho_s$, so that

$$\begin{aligned}
\frac{\nabla_\perp\phi}{B}\frac{1}{c_s} =& \frac{\frac{1}{\rho_s}\frac{T_{e,0}}{e}\breve{\nabla}_\perp\breve{\phi}}{B_0\breve{B}}\frac{1}{c_s} && \rho_s = \frac{c_s}{\omega_{ci}} \\
=& \frac{\breve{\nabla}_\perp\breve{\phi}}{\breve{B}}\frac{\omega_{ci}}{c_s^2}\frac{T_{e,0}}{eB_0} && c_s = \sqrt{\frac{T_{e,0}}{m_i}} \\
=& \frac{\breve{\nabla}_\perp\breve{\phi}}{\breve{B}}\frac{eB_0 m_i}{m_i T_{e,0}}\frac{T_{e,0}}{eB_0} \\
=& \frac{\breve{\nabla}_\perp\breve{\phi}}{\breve{B}}.
\end{aligned}$$

From this we get that

$$\breve{\Omega} = \breve{\nabla}\cdot\frac{\breve{\nabla}_\perp\breve{\phi}}{\breve{B}} = \rho_s\nabla\cdot\frac{\frac{\nabla_\perp\phi}{B}}{c_s} = \rho_s\frac{\Omega}{c_s} = \frac{\Omega}{\omega_{ci}},$$

and that

$$\breve{\Omega}^D = \breve{\nabla}\cdot\left(\breve{n}\frac{\breve{\nabla}_\perp\breve{\phi}}{\breve{B}}\right) = \rho_s\nabla\cdot\left(\frac{\frac{n}{n_0}\frac{\nabla_\perp\phi}{B}}{c_s}\right) = \rho_s n_0\frac{\Omega^D}{c_s} = n_0\frac{\Omega^D}{\omega_{ci}}.$$

Furthermore, we normalize all time and frequency variables with ω_{ci}, and note that since the particle source S has the units of density per second, we must normalize it with n_0 and ω_{ci} to make it consistent with the continuity equation.

Finally, the normalization constant for the dynamic viscosities $\eta_{\alpha,n}$ can easily be found by looking at the dimensions of the RHS of eq. (5.8) and the corresponding $\eta_{\alpha,n}$. We have that the normalization constants corresponding to $m_\alpha\partial_t(nu_{\alpha,\|})$ must be $m_\alpha\omega_{ci}n_0c_s$ as we have normalized the time with ω_{ci}. As $\partial_z^2 u_{\alpha,\|}$ has the normalization constant $c_s/\rho_s^2 = \omega_{ci}/\rho_s$, then $\eta_{\alpha,n}$ can be normalized with $m_i\rho_s n_0 c_s$. We see that this normalization constant has the proper units of mass per meter seconds (or equivalently pascal seconds).

As a side note, we note that $\mathrm{d}_{t,\alpha} = \breve{\partial}_t\omega_{ci} + c_s([\breve{\boldsymbol{u}}_\alpha]\cdot\breve{\nabla})/\rho_s = \omega_{ci}\breve{\mathrm{d}}_{t,\alpha}$.

[4]Also known as: Bohm normalization

To summarize, we have the normalization

$$\breve{\boldsymbol{x}} = \frac{\boldsymbol{x}}{\rho_s} \qquad \breve{t} = t\omega_{ci} \qquad \breve{\boldsymbol{u}} = \frac{\boldsymbol{u}}{c_s} \qquad \breve{B} = \frac{B}{B_0}$$
$$\breve{\phi} = \frac{e\phi}{T_{e,0}} \qquad \breve{\Omega} = \frac{\Omega}{\omega_{ci}} \qquad \breve{\Omega}^D = \frac{\Omega^D}{n_0\omega_{ci}} \qquad \frac{\breve{\nabla}_\perp\breve{\phi}}{\breve{B}} = \frac{\nabla_\perp\phi}{Bc_s}$$
$$\breve{n} = \frac{n}{n_0} \qquad \breve{T}_e = \frac{T_e}{T_{e,0}} \qquad \breve{\nu}_x = \frac{\nu_x}{\omega_{ci}} \qquad \breve{S} = \frac{S}{n_0\omega_{ci}}$$
$$\breve{\eta}_{\alpha,n} = \frac{\eta}{m_i\rho_s n_0 c_s} \qquad \breve{\nabla} = \rho_s\nabla \qquad \breve{\partial}_t = \frac{1}{\omega_{ci}}\partial_t \qquad \breve{\mathrm{d}}_{t,\alpha} = \frac{1}{\omega_{ci}}\mathrm{d}_{t,\alpha},$$

or equivalently

$$\boldsymbol{x} = \breve{\boldsymbol{x}}\rho_s \qquad t = \frac{\breve{t}}{\omega_{ci}} \qquad \boldsymbol{u} = \breve{\boldsymbol{u}}c_s \qquad B = \breve{B}B_0$$
$$\phi = \breve{\phi}\frac{T_{e,0}}{e} \qquad \Omega = \breve{\Omega}\omega_{ci} \qquad \Omega^D = \breve{\Omega}^D\omega_{ci}n_0 \qquad \frac{\nabla_\perp\phi}{B} = c_s\frac{\breve{\nabla}_\perp\breve{\phi}}{\breve{B}}$$
$$n = \breve{n}n_0 \qquad T_e = \breve{T}_e T_{e,0} \qquad \nu_x = \breve{\nu}_x\omega_{ci} \qquad S = \breve{S}n_0\omega_{ci}$$
$$\eta = \breve{\eta}_{\alpha,n}m_i\rho_s n_0 c_s \qquad \nabla = \frac{1}{\rho_s}\breve{\nabla} \qquad \partial_t = \omega_{ci}\breve{\partial}_t \qquad \mathrm{d}_{t,\alpha} = \omega_{ci}\breve{\mathrm{d}}_{t,\alpha},$$

which means that

$$\nabla = \frac{1}{\rho_s}\breve{\nabla} \qquad \partial_t = \omega_{ci}\breve{\partial}_t \qquad \mathrm{d}_{t,\alpha} = \breve{\partial}_t\omega_{ci} + \frac{c_s(\breve{\boldsymbol{u}}_\alpha)\cdot\breve{\nabla}}{\rho_s} = \omega_{ci}\breve{\mathrm{d}}_{t,\alpha}.$$

We will now normalize the equations derived above, and we will from here on drop the breve to simplify the writing.

5.4.1 Normalization of the density equation

By normalizing eq. (5.1), we get

$$\begin{aligned}
n_0\omega_{ci}\mathrm{d}_t^E n &= \frac{\rho_s^2\omega_{ci}n_0}{\rho_s^2}\frac{\nu_{ei}}{\mu}\nabla_\perp^2 n - \frac{n_0c_s}{\rho_s}\partial_\parallel\left(nu_{e,\parallel}\right) + n_0\omega_{ci}S_n \\
n_0\omega_{ci}\mathrm{d}_t^E n &= \omega_{ci}n_0\frac{\nu_{ei}}{\mu}\nabla_\perp^2 n - n_0\omega_{ci}\partial_\parallel\left(nu_{e,\parallel}\right) + n_0\omega_{ci}S_n \\
\mathrm{d}_t^E n &= \frac{\nu_{ei}}{\mu}\nabla_\perp^2 n - \partial_\parallel\left(nu_{e,\parallel}\right) + S_n.
\end{aligned}$$

We will divide through by $1/n$ to ensure the non-negativity of the density when solving the equations numerically. This gives

$$\begin{aligned}
\mathrm{d}_t^E\ln(n) &= \frac{\nu_{ei}}{\mu}\frac{1}{n}\nabla_\perp^2 n - \frac{1}{n}\partial_\parallel\left(nu_{e,\parallel}\right) + \frac{S_n}{n} \\
&= \frac{\nu_{ei}}{\mu}\left(\nabla\cdot\left[\frac{1}{n}\nabla_\perp n\right] - \nabla\frac{1}{n}\cdot\nabla_\perp n\right) - \partial_\parallel u_{e,\parallel} - u_{e,\parallel}\frac{1}{n}\partial_\parallel n + \frac{S_n}{n}
\end{aligned}$$

$$
\begin{aligned}
&= \frac{\nu_{ei}}{\mu}\left(\nabla_\perp^2 \ln(n) - \frac{n}{n}\nabla\frac{1}{n}\cdot\nabla_\perp n\right) - \partial_\parallel u_{e,\parallel} - u_{e,\parallel}\partial_\parallel \ln(n) + \frac{S_n}{n} \\
&= \frac{\nu_{ei}}{\mu}\left(\nabla_\perp^2 \ln(n) - \nabla\ln(n^{-1})\cdot\nabla_\perp \ln(n)\right) - \partial_\parallel u_{e,\parallel} - u_{e,\parallel}\partial_\parallel \ln(n) + \frac{S_n}{n} \\
&= \frac{\nu_{ei}}{\mu}\left(\nabla_\perp^2 \ln(n) + \nabla\ln(n)\cdot\nabla_\perp \ln(n)\right) - \partial_\parallel u_{e,\parallel} - u_{e,\parallel}\partial_\parallel \ln(n) + \frac{S_n}{n}.
\end{aligned}
$$

We now have that

$$
\begin{aligned}
\nabla_\perp f\cdot\nabla g =& \nabla_\perp f\cdot\left(\nabla_\perp + \nabla_\parallel\right) g \\
=& \nabla_\perp f\cdot\nabla_\perp g + \nabla_\perp f\cdot\nabla_\parallel g \\
=& \nabla_\perp f\cdot\nabla_\perp g + \nabla_\perp f\cdot\left(\boldsymbol{b}\boldsymbol{b}\cdot\right)\nabla g \\
=& \nabla_\perp f\cdot\nabla_\perp g + \left(\boldsymbol{b}\cdot\nabla_\perp f\right)\left(\boldsymbol{b}\cdot\nabla g\right) \\
=& \nabla_\perp f\cdot\nabla_\perp g. \qquad (5.15)
\end{aligned}
$$

$\boldsymbol{b}\perp\boldsymbol{e}^\rho$ and $\boldsymbol{b}\perp\boldsymbol{e}^\theta$ in cylindrical coordinate system

This yields

$$
\mathrm{d}_t^E \ln(n) = \frac{\nu_{ei}}{\mu}\left(\nabla_\perp^2 \ln(n) + \nabla_\perp \ln(n)\cdot\nabla_\perp \ln(n)\right) - \partial_\parallel u_{e,\parallel} - u_{e,\parallel}\partial_\parallel \ln(n) + \frac{S_n}{n}. \qquad (5.16)
$$

5.4.2 Normalization of the modified vorticity equation

Next, normalization of eq. (5.4) yields

$$
\begin{aligned}
\frac{\omega_{ci}\omega_{ci}n_0}{\omega_{ci}}\partial_t\Omega^D =& -\frac{\nu_{in}\omega_{ci}}{\omega_{ci}}\left(\omega_{ci}n_0 n\Omega + \frac{c_s n_0}{\rho_s}\frac{\nabla_\perp\phi}{B}\cdot\nabla n\right) \\
&- \frac{1}{\omega_{ci}}\frac{1}{\rho\rho_s}\left(\frac{ec_s\rho_s}{T_{e,0}}\frac{1}{B}\frac{T_{e,0}}{e}\frac{1}{\rho_s}n_0\omega_{ci}\{\phi,\Omega^D\} + c_s^2\frac{1}{\rho_s}n_0\frac{1}{2}\{\boldsymbol{u}_E^2, n\}\right) \\
&- \frac{1}{\omega_{ci}}\frac{c_s n_0 c_s e}{\rho_s\rho_s}\partial_\parallel\nabla\cdot\left(u_{i,\parallel}n\frac{\nabla_\perp\phi}{B}\right) \\
&+ \frac{n_0 c_s e}{e\rho_s}\partial_\parallel j_\parallel \qquad j_\parallel = \sum_\alpha q_\alpha n_\alpha u_{\alpha,\parallel} \\
\omega_{ci}n_0\partial_t\Omega^D =& -\nu_{in}\left(\omega_{ci}n_0 n\Omega + \omega_{ci}n_0\frac{\nabla_\perp\phi}{B}\cdot\nabla_\perp n\right) \qquad \text{eq. (5.15)} \\
&- \frac{1}{\omega_{ci}}\frac{1}{\rho\rho_s}\left(c_s\omega_{ci}n_0\frac{1}{B}\omega_{ci}\{\phi,\Omega^D\} + c_s\omega_{ci}n_0\frac{1}{2}\{\boldsymbol{u}_E^2, n\}\right) \\
&- \frac{1}{\omega_{ci}}\omega_{ci}n_0\omega_{ci}\partial_\parallel\nabla\cdot\left(u_{i,\parallel}n\frac{\nabla_\perp\phi}{B}\right) \\
&+ n_0\omega_{ci}\partial_\parallel j_\parallel \\
\omega_{ci}n_0\partial_t\Omega^D =& -\nu_{in}\left(\omega_{ci}n_0 n\Omega + \omega_{ci}n_0\frac{\nabla_\perp\phi}{B}\cdot\nabla_\perp n\right) \\
&- \frac{1}{\omega_{ci}}\omega_{ci}n_0\omega_{ci}\frac{1}{\rho}\left(\frac{1}{B}\{\phi,\Omega^D\} + \frac{1}{2}\{\boldsymbol{u}_E^2, n\}\right) \\
&- \frac{1}{\omega_{ci}}\omega_{ci}n_0\omega_{ci}\partial_\parallel\nabla\cdot\left(u_{i,\parallel}n\frac{\nabla_\perp\phi}{B}\right) \\
&+ n_0\omega_{ci}\partial_\parallel j_\parallel
\end{aligned}
$$

$$\begin{aligned}\partial_t \Omega^D =& -\nu_{in}\left(n\Omega + \frac{\nabla_\perp \phi}{B}\cdot\nabla_\perp n\right)\\ &-\frac{1}{\rho}\left(\frac{1}{B}\{\phi,\Omega^D\}+\frac{1}{2}\{\boldsymbol{u}_E^2,n\}\right)-\partial_\parallel\nabla\cdot\left(u_{i,\parallel}n\frac{\nabla_\perp\phi}{B}\right)\\ &+\partial_\parallel j_\parallel,\end{aligned} \tag{5.17}$$

and

$$\begin{aligned}\omega_{ci}n_0\Omega^D &= \frac{n_0c_s}{\rho_s}\nabla\cdot\left(n\frac{\nabla_\perp\phi}{B}\right)\\ \Omega^D &= \nabla\cdot\left(n\frac{\nabla_\perp\phi}{B}\right).\end{aligned}$$

5.4.3 Normalization of the parallel momentum density equation

Further, we normalize eq. (5.11) in the following way

$$\begin{aligned}\omega_{ci}n_0c_s\partial_t\left(nu_{i,\parallel}\right) =& -c_s\frac{c_s}{\rho_s}n_0\boldsymbol{u}_E\cdot\nabla\left(u_{i,\parallel}n\right)-\frac{c_s}{\rho_s}n_0c_su_{i,\parallel}\left(n\partial_\parallel u_{i,\parallel}+\partial_\parallel\left[nu_{e,\parallel}\right]\right)\\ &-T_{e,0}\frac{1}{\rho_s}n_0\frac{Z}{m_i}T_e\partial_\parallel n+\omega_{ci}c_s\frac{1}{\rho_s^2}n_0\rho_s^2\nu_{ei}\frac{u_{i,\parallel}}{\mu}\nabla_\perp^2 n-n_0\omega_{ci}c_sn\left(\nu_{in}u_{i,\parallel}+\frac{Z}{\mu}\nu_{en}u_{e,\parallel}\right)\\ &+m_in_0\rho_sc_s\frac{1}{\rho_s^2}c_s\frac{4Z}{3m_i}\left(\eta_{i,0}\partial_z^2u_{i,\parallel}+\eta_{e,0}\partial_z^2u_{e,\parallel}\right)\\ =& -c_s\frac{c_s}{\rho_s}n_0\boldsymbol{u}_E\cdot\nabla\left(u_{i,\parallel}n\right)-\frac{c_s}{\rho_s}n_0c_su_{i,\parallel}\left(n\partial_\parallel u_{i,\parallel}+\partial_\parallel\left[nu_{e,\parallel}\right]\right)\\ &-c_s^2\frac{1}{\rho_s}n_0ZT_e\partial_\parallel n+\omega_{ci}c_sn_0\nu_{ei}\frac{u_{i,\parallel}}{\mu}\nabla_\perp^2n-n_0\omega_{ci}c_sn\left(\nu_{in}u_{i,\parallel}+\frac{Z}{\mu}\nu_{en}u_{e,\parallel}\right)\\ &+n_0\frac{c_s}{\rho_s}c_s\frac{4Z}{3}\left(\eta_{i,0}\partial_z^2u_{i,\parallel}+\eta_{e,0}\partial_z^2u_{e,\parallel}\right)\\ =& -c_s\omega_{ci}n_0\boldsymbol{u}_E\cdot\nabla\left(u_{i,\parallel}n\right)-\omega_{ci}n_0c_su_{i,\parallel}\left(n\partial_\parallel u_{i,\parallel}+\partial_\parallel\left[nu_{e,\parallel}\right]\right)\\ &-c_s\omega_{ci}n_0ZT_e\partial_\parallel n+\omega_{ci}c_sn_0\nu_{ei}\frac{u_{i,\parallel}}{\mu}\nabla_\perp^2n-n_0\omega_{ci}c_sn\left(\nu_{in}u_{i,\parallel}+\frac{Z}{\mu}\nu_{en}u_{e,\parallel}\right)\\ &+n_0\omega_{ci}c_s\frac{4Z}{3}\left(\eta_{i,0}\partial_z^2u_{i,\parallel}+\eta_{e,0}\partial_z^2u_{e,\parallel}\right)\\ \partial_t\left(nu_{i,\parallel}\right) =& -\boldsymbol{u}_E\cdot\nabla\left(u_{i,\parallel}n\right)-u_{i,\parallel}\left(n\partial_\parallel u_{i,\parallel}+\partial_\parallel\left[nu_{e,\parallel}\right]\right)\\ &-ZT_e\partial_\parallel n+\nu_{ei}\frac{u_{i,\parallel}}{\mu}\nabla_\perp^2n-n\left(\nu_{in}u_{i,\parallel}+\frac{Z}{\mu}\nu_{en}u_{e,\parallel}\right)\\ &+\frac{4Z}{3}\left(\eta_{i,0}\partial_z^2u_{i,\parallel}+\eta_{e,0}\partial_z^2u_{e,\parallel}\right).\end{aligned}$$

We notice how the ion mass in front of the electron pressure got transformed into a $1/\mu$ upon normalization.

5.4.4 Normalization of the parallel current equation

Finally, by using $\boldsymbol{E} = \dfrac{\breve{E}T_e}{e\rho_s}$, normalization of the parallel current can be done in the following way

$$
\begin{aligned}
\omega_{ci} e n_0 c_s \partial_t j_\parallel =& - e c_s \frac{c_s}{\rho_s} n_0 \boldsymbol{u}_E \cdot \nabla j_\parallel \\
& - e n_0 \rho_s c_s^2 n \left(u_{i,\parallel} \partial_\parallel u_{i,\parallel} - u_{e,\parallel} \partial_\parallel u_{e,\parallel} \right) - e n_0 \rho_s c_s^2 \frac{j_\parallel}{n} \partial_\parallel \left(n u_{e,\parallel} \right) \\
& + \frac{m_i}{m_i} \frac{e}{m_e} T_{e,0} \frac{1}{\rho_s} n_0 T_e \partial_\parallel n + \frac{m_i}{m_i} n_0 \frac{1}{\rho_s} \frac{T_{e,0}}{e} \frac{e^2}{m_e} n \boldsymbol{E}_\parallel - 0.51 \omega_{ci} e n_0 c_s \nu_{ei} j_\parallel \\
& + n_0 \omega_{ci} c_s e n \left(\nu_{en} u_{e,\parallel} - \nu_{in} u_{i,\parallel} \right) - m_i n_0 \rho_s c_s \frac{1}{\rho_s^2} c_s \frac{e}{m_e} \frac{4\eta_{e,0}}{3} \partial_z^2 u_{e,\parallel} \\
=& - \omega_{ci} e n_0 c_s \boldsymbol{u}_E \cdot \nabla j_\parallel \\
& - e n_0 \frac{c_s^2}{\rho_s} n \left(u_{i,\parallel} \partial_\parallel u_{i,\parallel} - u_{e,\parallel} \partial_\parallel u_{e,\parallel} \right) - e n_0 \frac{c_s^2}{\rho_s} \frac{j_\parallel}{n} \partial_\parallel \left(n u_{e,\parallel} \right) \\
& + \mu e \frac{T_{e,0}}{m_i} \frac{1}{\rho_s} n_0 T_e \partial_\parallel n + \mu n_0 \frac{1}{\rho_s} e \frac{T_{e,0}}{m_i} n \boldsymbol{E}_\parallel - 0.51 \omega_{ci} e n_0 c_s \nu_{ei} j_\parallel \\
& + \omega_{ci} e n_0 c_s n \left(\nu_{en} u_{e,\parallel} - \nu_{in} u_{i,\parallel} \right) - \mu e n_0 \frac{c_s}{\rho_s} c_s \frac{4\eta_{e,0}}{3} \partial_z^2 u_{e,\parallel} \\
=& - \omega_{ci} e n_0 c_s \boldsymbol{u}_E \cdot \nabla j_\parallel \\
& - \omega_{ci} e n_0 c_s n \left(u_{i,\parallel} \partial_\parallel u_{i,\parallel} - u_{e,\parallel} \partial_\parallel u_{e,\parallel} \right) - \omega_{ci} e n_0 c_s \frac{j_\parallel}{n} \partial_\parallel \left(n u_{e,\parallel} \right) \\
& + \mu e \frac{c_s^2}{\rho_s} n_0 T_e \partial_\parallel n + \mu e \frac{c_s^2}{\rho_s} n_0 n \boldsymbol{E}_\parallel - 0.51 \omega_{ci} e n_0 c_s \nu_{ei} j_\parallel \\
& + \omega_{ci} e n_0 c_s n \left(\nu_{en} u_{e,\parallel} - \nu_{in} u_{i,\parallel} \right) - \mu e n_0 \frac{c_s}{\rho_s} c_s \frac{4\eta_{e,0}}{3} \partial_z^2 u_{e,\parallel} \\
=& - \omega_{ci} e n_0 c_s \boldsymbol{u}_E \cdot \nabla j_\parallel \\
& - \omega_{ci} e n_0 c_s n \left(u_{i,\parallel} \partial_\parallel u_{i,\parallel} - u_{e,\parallel} \partial_\parallel u_{e,\parallel} \right) - \omega_{ci} e n_0 c_s \frac{j_\parallel}{n} \partial_\parallel \left(n u_{e,\parallel} \right) \\
& + \mu \omega_{ci} e n_0 c_s T_e \partial_\parallel n + \mu \omega_{ci} e n_0 c_s n \boldsymbol{E}_\parallel - 0.51 \omega_{ci} e n_0 c_s \nu_{ei} j_\parallel \\
& + \omega_{ci} e n_0 c_s n \left(\nu_{en} u_{e,\parallel} - \nu_{in} u_{i,\parallel} \right) - \mu \omega_{ci} e n_0 c_s \frac{4\eta_{e,0}}{3} \partial_z^2 u_{e,\parallel} \\
\partial_t j_\parallel =& - \boldsymbol{u}_E \cdot \nabla j_\parallel \\
& - n \left(u_{i,\parallel} \partial_\parallel u_{i,\parallel} - u_{e,\parallel} \partial_\parallel u_{e,\parallel} \right) - \frac{j_\parallel}{n} \partial_\parallel \left(n u_{e,\parallel} \right) \\
& + \mu T_e \partial_\parallel n + \mu n \boldsymbol{E}_\parallel - 0.51 \nu_{ei} j_\parallel \\
& + n \left(\nu_{en} u_{e,\parallel} - \nu_{in} u_{i,\parallel} \right) - \mu \frac{4\eta_{e,0}}{3} \partial_z^2 u_{e,\parallel}. \qquad (5.18)
\end{aligned}
$$

In appendix E we show that we are operating in the electrostatic regime, and $E_\parallel \simeq -\partial_\parallel \phi$ (both normalized and non-normalized). This gives

$$
\begin{aligned}
\partial_t j_\parallel \simeq& - \boldsymbol{u}_E \cdot \nabla j_\parallel \\
& - n \left(u_{i,\parallel} \partial_\parallel u_{i,\parallel} - u_{e,\parallel} \partial_\parallel u_{e,\parallel} \right) - \frac{j_\parallel}{n} \partial_\parallel \left(n u_{e,\parallel} \right)
\end{aligned}
$$

$$+ \mu T_e \partial_\parallel n - \mu n \partial_\parallel \phi - 0.51 \nu_{ei} j_\parallel$$
$$+ n \left(\nu_{en} u_{e,\parallel} - \nu_{in} u_{i,\parallel} \right) - \mu \frac{4\eta_{e,0}}{3} \partial_z^2 u_{e,\parallel}. \tag{5.19}$$

On the other hand, it can be beneficial to maintain $\partial_t \boldsymbol{A}$ for numerical reasons, as these terms can in fact prevent fast waves in the system [44]. Although electromagnetic effects are outside the scope of this thesis, the derivation of the parallel current equation where this effect is taken into account is given in appendix F.

5.5 Boundary conditions

Setting correct boundary conditions (BCs) when calculating PDEs of plasma quantities turns out to be a challenge. In the parallel direction there will be formation of plasma sheaths between the plasma and the material which is due to the difference in mobility between the ion species and the electron species [12]. This leads to a potential build-up on the material surface which affects the plasma upstream.

Unfortunately, the fluid description of the plasma breaks down at the sheath as mentioned in [45]. This is mainly due to the fact that there will be more ions than electrons in this area and the quasi-neutrality assumption breaks down. In other words, the fluid models are only valid up until the sheath entrance (SE), and a proper description in this area can only be accounted for with kinetic codes, solving for example the Fokker-Planck equation. One should notice that it is hard, and maybe even impossible, to tell where the bulk plasma ends and where the sheath begins.

There are mainly two challenges in setting the radial boundary conditions. Firstly, the plasma does not usually extent all the way to the chassis of the machine, but is gradually terminated as the temperature drops and neutral dynamics takes over towards the edge. Secondly, assuming that the plasma could extend all the way out to the chassis, the non-slip condition encountered in neutral fluid dynamics [42] is not necessarily valid as the plasma has no way to adhere to the surface as a neutral fluid would do.

The boundaries for the cylindrical plasma consist of four parts. In the parallel direction, we have the SE at one end. We could in principle place a SE at the other parallel end as well, which would be appropriate if the plasma streamed in both direction from some point. Instead, we have chosen to model the other parallel end as a stagnation point, i.e. a point where the parallel velocities are zero. Such a point exists if the plasma is streaming in two opposite directions and is encountered on for example open field lines in divertor plasmas. Radially, we have the outer radial boundary condition, and an artificial inner condition which is treated in section 9.4.

The boundary conditions will be set on n, $u_{i,\parallel}$, $u_{e,\parallel}$ and Ω. From these the boundary conditions, calculation of the boundary conditions of $\ln(n)$, $j_\parallel$, $nu_{i,\parallel}$ and Ω^D is straightforward. A summary of the boundary conditions used in this thesis is found in fig. 5.2.

5.5.1 Boundary conditions at the stagnation point

The boundary conditions at the opposite site of the SE in the cylinder varies from experiment to experiment (as does also the source term in the distribution function). By using a stagnation point, the model does not fully reflect any experimental linear devices,

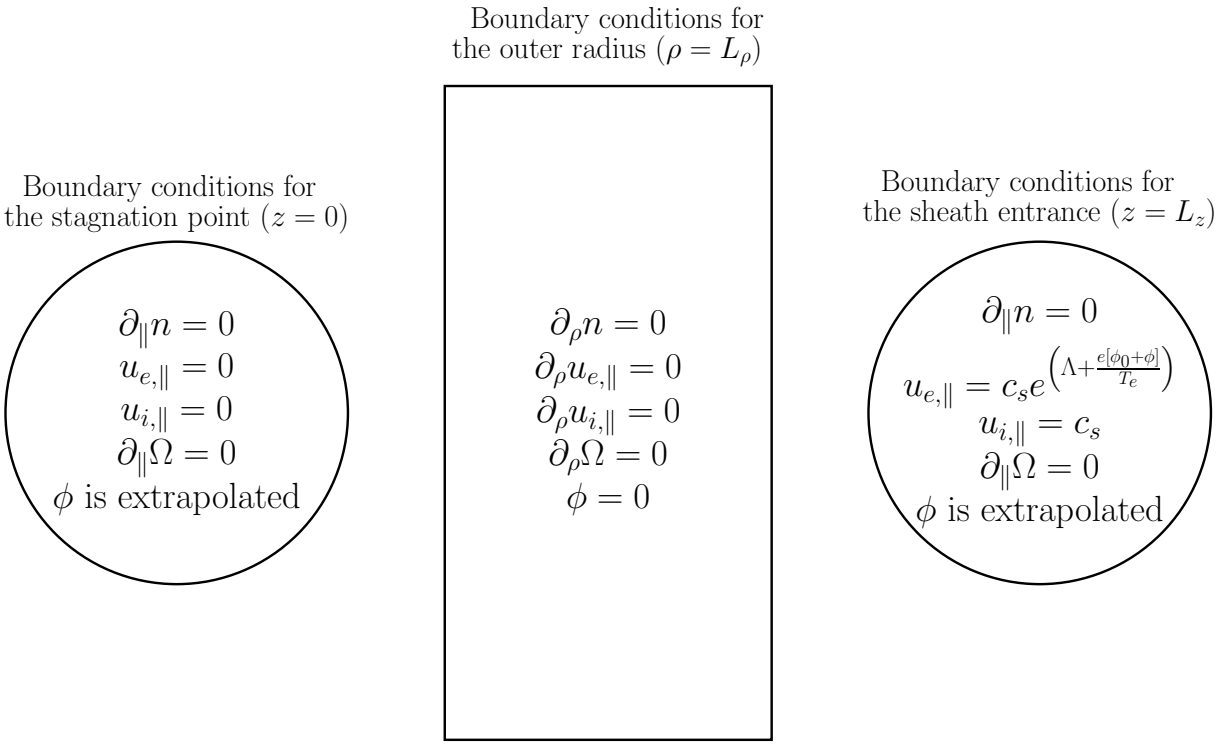

Figure 5.2: Boundary conditions used in this thesis.
The left circle represents the start of the domain where the stagnation BCs are used (i.e. the cylinder seen from the stagnation point towards the SE).
The rectangle represents the largest radius in the domain, where the radial boundary conditions are applied (i.e. the cylinder seen from above).
The right circle represents the end of the domain where the SE BCs are used.

but can help to shed light on features found in real life experiments. The stagnation condition acts as a kind of mirror. To be more specific the velocities changes sign at this point, and hence must be exactly zero there. The spinning of the plasma does not change from one side to the other across the mirror, and hence we get the following set of boundary conditions

$$\partial_\| n\Big|_0 = 0 \qquad u_{e,\|}\Big|_0 = 0 \qquad u_{i,\|}\Big|_0 = 0 \qquad \partial_\| \Omega\Big|_0 = 0$$

5.5.2 Boundary conditions at the SE

Following the calculations of Choudora and Bohm (see for example [12]), it is common practice to define the sheath entrance to be the place where the ion velocity reaches the ion sound speed (that is where $u_{i,\|} = c_s$), and we will adopt this practice here. Considering a quiescent plasma, one can calculate the equilibrium profiles which the plasma obtains in contact with materials, and use this to set the boundaries for $u_{i,\|}$ and $u_{e,\|}$ at the SE. This is then used to calculate the boundary condition

$$j_\|\Big|_{L_z} = en\Big|_{L_z}\left(u_{i,\|}\Big|_{L_z} - u_{e,\|}\Big|_{L_z}\right),$$

where L_z is the position of the SE. One should note though, that these boundary conditions are valid only in steady state.

Ion velocity at the SE

For the ion velocity, we have from steady state calculations defined the sheath entrance to be the point where

$$u_{i,\parallel}\Big|_{L_z} = c_s$$

Normalization gives

$$u_{i,\parallel}\Big|_{L_z} = 1$$

Electron velocity at the SE

Further, the steady state gives the following condition on the parallel electron velocity

$$u_{e,\parallel}\Big|_{L_z} = c_s \exp\left(\Lambda - \frac{e[\phi_0 + \phi]}{T_e}\right),$$

where ϕ_0 is an arbitrary potential and $\Lambda = \ln\left(\sqrt{\frac{\mu}{2\pi}}\right)$. Here, we set $\phi_0 = \Lambda T_e/e$, so that $\phi = 0$ for ambipolar flow[5]. Normalization gives

$$u_{e,\parallel}\Big|_{L_z} = \exp\left(\Lambda - \phi\right)$$

Density BC at the SE

Although the "standard" calculation for the sheath gives us conditions for setting the velocities in steady state, no such conditions exists for the density. Instead, one would have to rely on other arguments. In [45], Loizu et al. present a boundary condition for the density in a field line geometry, where the field lines are allowed to be tilted with respect to the end-plate. For a field line geometry where the field lines are perpendicular to the end-plate (which is the case in this thesis), the boundary condition reduces to

$$\begin{aligned}
\partial_\parallel n\big|_{L_z} &= -\frac{n}{c_s}\partial_\parallel u_{i,\parallel}\Big|_{L_z} \\
u_{i,\parallel}\partial_\parallel n\big|_{L_z} &= -n\partial_\parallel u_{i,\parallel}\big|_{L_z} && u_{i,\parallel}\big|_{L_z} = c_s \\
u_{i,\parallel}\partial_\parallel n\big|_{L_z} + n\partial_\parallel u_{i,\parallel}\big|_{L_z} &= 0 \\
\partial_\parallel\left(u_{i,\parallel}n\right)\big|_{L_z} &= 0 \\
\boldsymbol{b}\cdot\nabla\left(u_{i,\parallel}n\right)\big|_{L_z} &= 0 && \partial_i \boldsymbol{b} = 0 \\
\nabla\cdot\left(\boldsymbol{b}u_{i,\parallel}n\right)\big|_{L_z} &= 0
\end{aligned}$$

[5]With this choice, we have observed that the inversion algorithm for ϕ (see appendix K) numerically stable.

$$
\begin{aligned}
\nabla \cdot \left(\boldsymbol{u}_{i,\parallel} n\right)\big|_{L_z} &= 0 \\
\left(\nabla_\perp + \nabla_\parallel\right) \cdot \left(\boldsymbol{u}_{i,\parallel} n\right)\big|_{L_z} &= 0 \\
\nabla_\parallel \cdot \left(\boldsymbol{u}_{i,\parallel} n\right)\big|_{L_z} &= 0 \qquad \nabla_\parallel \cdot \boldsymbol{u}_{i,\perp} = 0 \\
\nabla_\parallel \cdot \left(\boldsymbol{u}_i n\right)\big|_{L_z} &= 0 \qquad \text{Continuity equation} \\
-\partial_t n|_{L_z} - \nabla_\perp \cdot \left(\boldsymbol{u}_i n\right)|_{L_z} + S_{i,n} &= 0 \\
\partial_t n|_{L_z} &= -\nabla_\perp \cdot \left(\boldsymbol{u}_i n\right)|_{L_z} + S_{i,n} \qquad (5.20)
\end{aligned}
$$

In other words, it says that the only change in the density (apart from the source) at the SE can come from perpendicular outflux. Another way to look at it is to consider

$$
\begin{aligned}
\left[\int \partial_\parallel \left(u_{i,\parallel} n\right) \, \mathrm{d}z\right]\Big|_{L_z} &= 0 \\
u_{i,\parallel} n\big|_{L_z} &= C
\end{aligned}
$$

which means that the flux through the SE is constant in time, which may be a too big constraint on the system.

One alternative is to set

$$
\partial_\parallel n\big|_{L_z} = 0
$$

If we follow the derivation of eq. (5.20) and use the ion continuity equation, this can be written as

$$
\begin{aligned}
-\partial_t n|_{L_z} - \nabla_\perp \cdot \left(\boldsymbol{u}_i n\right)|_{L_z} - n\partial_\parallel u_{i,\parallel}\big|_{L_z} + S_{i,n} &= 0 \\
\partial_t n|_{L_z} &= -\nabla_\perp \cdot \left(\boldsymbol{u}_i n\right)|_{L_z} - n\partial_\parallel u_{i,\parallel}\big|_{L_z} + S_{i,n}
\end{aligned}
$$

which means that the flux through the SE is no longer fixed. One should note that this boundary condition will try to enforce a zero gradient on n at the SE, which might be unphysical. Also, one should note that if one has a Neumann condition in both ends of the machine, the PDE is formally ill-posed, and the solutions found are unique only up to some constant. For such a system, the solution found will be specified by the initial condition. Although it is important to be aware of, it is not believed to change the physical behavior of the system as the dynamics are driven by its source and its sinks.

A third approach, which does not have the same problem, is to let the density be completely free at the sheath entrance and instead fix the value and the gradient at the stagnation point (where the velocities are 0) using a Cauchy boundary condition (not to be confused with a Robin or "mixed" boundary condition). This kind of boundary condition specifies the parallel dynamics fully. The derivatives of n at the last physical point before the SE can then be calculated numerically either by a one-sided stencil, or by extrapolating the solution to a ghost-point,[6] and use this as an *artificial boundary condition* [43].

A final possibility is to let the derived equation for the evolution of the density be valid at the boundary.

In the scope of this thesis the $\partial_\parallel n\big|_{L_z} = 0$ boundary condition has been chosen.

[6] A ghost-point is a point not belonging to the physical domain, but a helper point which makes it possible to use a centered scheme when evaluating a grid point closest to the physical boundary of the domain.

Potential BC at the SE

The potential in our equations is not being evolved in time directly, but is calculated by inverting either Ω or Ω^D for each drift plane (that is for each perpendicular plane). This inversion takes into account the outer radial boundary condition of ϕ. This outer radial boundary condition can be set from the material properties of the wall. On the other hand, we do not have any physical material constraint at the SE. We impose only that ϕ on the plate very close to the SE is set to an arbitrary constant. It is not clear how this is reflected at the SE in a non-steady state plasma.

However, parallel derivatives of the potential is being taken in our set of equations. In order to calculate the parallel derivative of ϕ in the last point before the SE, we need either to make a one sided stencil for this very point (as the value of the boundary, and thereby the value of the ghost-point is unknown), or we can extrapolate the value of ϕ to the ghost-point (as we anyway assume that ϕ is a smooth function in order to discretize the differential operators working on ϕ). The latter has been chosen in the current implementation, with the polynomial given in section 9.2.

Finally, it should be noted that although a fluid description cannot properly asset the conditions in the sheath, the sheath (especially the resistivity in the sheath) is important for the behavior of the plasma [38, 46]. As shown in [47], the change from a conductive to an isolating end plate changes whether the current density loop is closing inside or outside of the plasma. As $\nabla \cdot \boldsymbol{j}$ must be zero, the location of the closing affects the polarization drift, which is responsible for the generation of for zonal flows [48].

Vorticity BC at the SE

As with ϕ, the sheath boundary condition sets no constraint on the vorticity at the SE. However, as Ω is a variable being solved in time, a boundary condition is needed in order to fully specify the system. In the current implementation $\partial_\parallel \Omega\big|_{L_z} = 0$ has been chosen. Note that this may not be a particularly good boundary condition as it physically means that there can be no parallel shear in the perpendicular spinning at the SE.

5.5.3 Outer radial boundary conditions

The radial boundary conditions can in principle determine the results of the experiments entirely. This have been seen in experiments on for example the Mirabelle machine [49]. However, to correctly assess the physics, one would have to take into account the neutral interaction and the material properties of the wall. We will therefore focus on a much simplified approximation of the radial boundary conditions. In fact, we will let the radial boundary condition be approximately where the neutrals are dominating, and thus dampening out the plasma dynamics.

Density BC at outer radius

As the density will go toward 0 as we are approaching the wall, we could set

$$n\Big|_{L_\rho} = C,$$

where C is a small constant. Setting this too small, however, can give rise to numerical problems due to loss of precision.

In this thesis, another approach has been used. As the density profile is approximately Gaussian, the profile will be relatively flat towards the radial edge. We therefore set

$$\partial_\rho n\Big|_{L_\rho} = 0$$

Note, however, that this can be too restrictive if large coherent structures reaches the domain boundary.

Velocity BCs at outer radius

The parallel velocities are not constrained by any forces at the radial edge and can thus take any value. In this thesis we set

$$\partial_\rho u_{e,\parallel}\Big|_{L_\rho} = \partial_\rho u_{i,\parallel}\Big|_{L_\rho} = 0$$

although there in principle are no physical reason for why this should be.

Potential BC at outer radius

There are no sheath where the magnetic field lines are perpendicular to the material. Thus, if we assume that the chassis is an ideal conductor, the potential there should be at the floating potential if we exclude finite Larmor radius (FLR) effects. For that reason we assume that

$$\phi\Big|_{L_\rho} = 0$$

As the ion Larmor radius is larger than the electron Larmor radius, more ions than electron would be lost radially initially if FLR effect were included. This would result in a small potential difference which would increase the poloidal $\boldsymbol{E} \times \boldsymbol{B}$ drift.

Vorticity BC at outer radius

As stated in the introduction of section 5.5, there exists no analogue to the no-slip condition in plasmas. In other words, there is nothing which constrains the poloidal flow at the material surface. As a consequence, there will be nothing constraining the poloidal flow at the position where the plasma terminates (where neutrals are starting to dominate) radially. One could assume that

$$\partial_\parallel \Omega\Big|_{L_\rho} = 0,$$

which is set in this thesis, although no physical explanation for this is given.

5.5.4 Inner radial boundary conditions

Physically, there are no boundary condition around the central axis of a cylinder. However, we need some artificial boundary conditions around this area as our domain covers $\rho \in]0, L_\rho[$ (where L_ρ is the radius of the system) as we are using a finite difference (FD) scheme to calculate radial derivatives. As this is not related to the physics of the problem, the discussion is given in section 9.4.

5.6 The set of equations

As we will discuss further in chapter 9, we will replace the actual viscosities with artificial viscosities.

If we (only for simplicity) does not write out the viscosities, the set of equations read

$$\Omega^D = \nabla \cdot \left(n \frac{\nabla_\perp \phi}{B} \right) \tag{5.21}$$

$$\Omega = \frac{\nabla_\perp^2 \phi}{B} \tag{5.22}$$

$$\begin{aligned} \partial_t \ln(n) = &- \frac{1}{J} \{\phi, \ln(n)\} + \frac{\nu_{ei}}{\mu} \left(\nabla_\perp^2 \ln(n) + [\nabla_\perp \ln(n)]^2 \right) \\ &- \partial_\parallel u_{e,\parallel} - u_{e,\parallel} \partial_\parallel \ln(n) + \frac{S_n}{n} \end{aligned} \tag{5.23}$$

$$\begin{aligned} \partial_t \left(n u_{i,\parallel} \right) = &- \frac{1}{JB} \{\phi, u_{i,\parallel} n\} - u_{i,\parallel} \left(n \partial_\parallel u_{i,\parallel} + \partial_\parallel \left[n u_{e,\parallel} \right] \right) \\ &- Z T_e \partial_\parallel n + \nu_{ei} \frac{u_{i,\parallel}}{\mu} \nabla_\perp^2 n - n \left(\nu_{in} u_{i,\parallel} + \frac{Z}{\mu} \nu_{en} u_{e,\parallel} \right) \end{aligned} \tag{5.24}$$

$$\begin{aligned} \partial_t j_\parallel = &- \frac{1}{JB} \{\phi, j_\parallel\} \\ &- n \left(u_{i,\parallel} \partial_\parallel u_{i,\parallel} - u_{e,\parallel} \partial_\parallel u_{e,\parallel} \right) - \frac{j_\parallel}{n} \partial_\parallel \left(n u_{e,\parallel} \right) \\ &+ \mu T_e \partial_\parallel n - \mu n \partial_\parallel \phi - 0.51 \nu_{ei} j_\parallel \\ &+ n \left(\nu_{en} u_{e,\parallel} - \nu_{in} u_{i,\parallel} \right) \end{aligned} \tag{5.25}$$

$$\begin{aligned} \partial_t \Omega^D = &- \frac{1}{J} \left(\frac{1}{B} \{\phi, \Omega^D\} + \frac{1}{2} \{ \boldsymbol{u}_E^2, n \} \right) - \partial_\parallel \nabla \cdot \left(u_{i,\parallel} n \frac{\nabla_\perp \phi}{B} \right) \\ &+ \partial_\parallel j_\parallel - \nu_{in} \left(n \Omega + \frac{\nabla_\perp \phi}{B} \cdot \nabla_\perp n \right) \end{aligned} \tag{5.26}$$

From eqs. (5.21) to (5.26), we can calculate

$$\begin{aligned} n &= \exp\left(\ln(n)\right) \\ u_{i,\parallel} &= \frac{n u_{i,\parallel}}{n} \\ u_{e,\parallel} &= u_{i,\parallel} - \frac{j_\parallel}{n} \\ \Omega &= \frac{\Omega^D}{n} - \nabla_\perp \ln(n) \cdot \nabla_\perp \phi \end{aligned}$$

See section 9.3.2

Chapter 6

The Boussinesq approximation

We will in this chapter modify the obtained equations by using the so-called Boussinesq approximation. This approximation is also sometimes referred to as the local approximation. The name Boussinesq approximation is a bit of a misnomer, as this actually refers to a series of approximations in fluid mechanics where the small variation in density is one of them [42].

The usage of this approximation in drift fluid equations is not always sound, as the criterion for the approximation is easily broken. However, one argument to use the approximation is that one can make a set of equations which conserves energy without getting into the problem of having the polarization drift advecting itself (which leads to an infinite loop in the derivation).

6.1 The Boussinesq approximation in a slowly varying B-field

The goal of this approximation is to let n commute with the gradient in eq. (5.6). We start by splitting the density into a background profile $\overline{n}$ and the fluctuation δ_n. That is, we have

$$n = \overline{n} + \delta_n,$$

and we assume that $\overline{n} \gg \delta_n$. Order of magnitude estimates now give

$$\nabla\overline{n} \sim \frac{\overline{n}}{L_n} \qquad \nabla\delta_n = \nabla_\perp\delta_n + \nabla_\parallel\delta_n \sim \frac{\delta_n}{L_{\delta_n,\perp}} + \frac{\delta_n}{L_{\delta_n,\parallel}} \simeq \frac{\delta_n}{L_{\delta_n,\perp}},$$

where we have assumed that $L_{\delta_n,\perp} \ll L_{\delta_n,\parallel}$.

If we now normalize the densities with n_0 and the gradients with ρ_s, and write the normalized units with a breve ($\breve{}$), we find that

$$\breve{\nabla}\breve{\overline{n}} \sim \frac{\frac{\overline{n}}{n_0}}{\frac{L_n}{\rho_s}} = \frac{\overline{n}}{L_n}\frac{\rho_s}{n_0} \simeq \frac{\rho_s}{L_n}. \qquad \frac{\overline{n}}{n_0} \simeq 1$$

By assuming that $\dfrac{\rho_s}{L_n} \ll 1$[1] (meaning that the density gradient length scales are much

[1]Note that for the perpendicular velocities in appendix B, we assumed that $\dfrac{\rho_s}{L_{\boldsymbol{u}_\perp}} \sim \sqrt{\varepsilon}$

larger than ρ_s), we find that

$$\breve{\nabla}\breve{\overline{n}} \ll 1.$$

Further on, we have that

$$\breve{\nabla}\breve{\delta_n} \sim \frac{\frac{\delta_n}{n_0}}{\frac{L_{\delta_n}}{\rho_s}} = \frac{\delta_n}{L_{\delta_n,\perp}}\frac{\rho_s}{n_0}.$$

From our assumption about small perturbations, we know that $\frac{\delta_n}{n_0} \ll 1$. If we assume that $\frac{\rho_s}{L_{\delta_n,\perp}} \not\gg 1$. Then

$$\breve{\nabla}\breve{\delta_n} \ll 1.$$

In other words, we have that

$$\nabla(fn) \simeq n\nabla f.$$

Using the assumptions, we find that inserting this in eq. (4.11) yields

$$\begin{aligned}
\nabla\cdot\left(n\frac{1}{\omega_{ci}}\left[\mathrm{d}_t^E + \boldsymbol{u}_{i,\parallel}\cdot\nabla\right]\left[\frac{\nabla_\perp\phi}{B}\right]\right) =& n\nabla\cdot\left(\frac{1}{\omega_{ci}}\left[\mathrm{d}_t^E + \boldsymbol{u}_{i,\parallel}\cdot\nabla\right]\left[\frac{\nabla_\perp\phi}{B}\right]\right) \\
&+\left(\frac{1}{\omega_{ci}}\left[\mathrm{d}_t^E + \boldsymbol{u}_{i,\parallel}\cdot\nabla\right]\left[\frac{\nabla_\perp\phi}{B}\right]\right)\cdot\nabla n \\
\simeq& (\overline{n}+\delta_n)\,\nabla\cdot\left(\frac{1}{\omega_{ci}}\left[\mathrm{d}_t^E + \boldsymbol{u}_{i,\parallel}\cdot\nabla\right]\left[\frac{\nabla_\perp\phi}{B}\right]\right) \qquad \overline{n}\gg\delta_n \\
\simeq& \overline{n}\nabla\cdot\left(\frac{1}{\omega_{ci}}\left[\mathrm{d}_t^E + \boldsymbol{u}_{i,\parallel}\cdot\nabla\right]\left[\frac{\nabla_\perp\phi}{B}\right]\right).
\end{aligned}$$

Finally, we will assume a relatively flat density background profile, so that $n_0 \simeq \overline{n}$. This means that eq. (4.11) with the Boussinesq approximation yields

$$\begin{aligned}
\nabla\cdot\left(n\frac{1}{\omega_{ci}}\left[\mathrm{d}_t^E + \boldsymbol{u}_{i,\parallel})\cdot\nabla\right]\left[-\frac{\nabla_\perp\phi}{B}\right]\right) \simeq& n_0\nabla\cdot\left(\frac{1}{\omega_{ci}}\left[\mathrm{d}_t^E + \boldsymbol{u}_{i,\parallel}\cdot\nabla\right]\left[\frac{\nabla_\perp\phi}{B}\right]\right) \\
=& -n_0\nabla\cdot\left(\frac{1}{\omega_{ci}}\mathrm{d}_t^E\left[\frac{\nabla_\perp\phi}{B}\right]\right) - n_0\nabla\cdot\left(\frac{1}{\omega_{ci}}\boldsymbol{u}_{i,\parallel}\cdot\nabla\left[\frac{\nabla_\perp\phi}{B}\right]\right) \\
=& -n_0\nabla\cdot\left(\frac{1}{\omega_{ci}}\mathrm{d}_t^E\left[\frac{\nabla_\perp\phi}{B}\right]\right) - n_0\nabla\cdot\left(\frac{1}{\omega_{ci}}u_{i,\parallel}\partial_\parallel\left[\frac{\nabla_\perp\phi}{B}\right]\right).
\end{aligned} \tag{6.1}$$

Let us now briefly comment on the approximations made

1. $\overline{n} \gg \delta_n$: This approximation can be broken as the perturbation amplitudes can be large as seen in chapter 15.
2. $\frac{\rho_s}{L_n} \ll 1$: This approximation usually holds as the gradient scale length in the background density are long compared to ρ_s. However, they are not necessarily orders of magnitude larger.

3. $\overline{n} \simeq n_0$: This assumption is maybe the hardest to fulfill, as the gradients are usually non-vanishing.

We see that although the assumptions can be met, they are not generally true. As this approximation is done quite frequently in the literature, it is of interest to compare results with and without this approximation. This will be presented in chapter 18.

In the scope of this thesis, we will only do the approximation in the polarization term of the vorticity equation, and keep gradients of n elsewhere. A more rigorous study could be to investigate the set of equations from an energy conservation point of view, and from that find out which of the n's in the set of equations that should be transformed to n_0.

6.2 The Boussinesq approximation in the CELMA model

We will now see how the set of equations in the CELMA model is affected by the Boussinesq approximation. Continuing from eq. (6.1), using that $\nabla B = 0$, we get

$$
\begin{aligned}
&- n_0 \nabla \cdot \left(\frac{1}{\omega_{ci}} \mathrm{d}_t^E \left[\frac{\nabla_\perp \phi}{B} \right] \right) - n_0 \nabla \cdot \left(\frac{1}{\omega_{ci}} u_{i,\parallel} \partial_\parallel \left[\frac{\nabla_\perp \phi}{B} \right] \right) \\
&= - \frac{n_0}{\omega_{ci}} \left(\nabla \cdot \left[\mathrm{d}_t^E \left(\frac{\nabla_\perp \phi}{B} \right) \right] + \nabla \cdot \left[u_{i,\parallel} \partial_\parallel \left(\frac{\nabla_\perp \phi}{B} \right) \right] \right) \\
&= - \frac{n_0}{\omega_{ci}} \left(\nabla \cdot \left[(\partial_t + \boldsymbol{u}_E \cdot \nabla) \left(\frac{\nabla_\perp \phi}{B} \right) \right] + \nabla \cdot \left[u_{i,\parallel} \partial_\parallel \left(\frac{\nabla_\perp \phi}{B} \right) \right] \right) \\
&= - \frac{n_0}{\omega_{ci}} \left(\nabla \cdot \partial_t \left(\frac{\nabla_\perp \phi}{B} \right) + \nabla \cdot \left(\boldsymbol{u}_E \cdot \nabla \frac{\nabla_\perp \phi}{B} \right) + \nabla \cdot \left[u_{i,\parallel} \partial_\parallel \left(\frac{\nabla_\perp \phi}{B} \right) \right] \right) \\
&= - \frac{n_0}{\omega_{ci}} \partial_t \Omega - \frac{n_0}{\omega_{ci}} \left(\nabla \cdot \left[\boldsymbol{u}_E \cdot \nabla \frac{\nabla_\perp \phi}{B} \right] + \nabla \cdot \left[u_{i,\parallel} \partial_\parallel \left(\frac{\nabla_\perp \phi}{B} \right) \right] \right) \\
&= - \frac{n_0}{\omega_{ci}} \partial_t \Omega - \frac{n_0}{\omega_{ci}} \left(\nabla \cdot \left[\boldsymbol{u}_E \cdot \nabla \frac{\nabla_\perp \phi}{B} \right] + u_{i,\parallel} \partial_\parallel \Omega + \frac{\nabla_\perp \left(\partial_\parallel \phi \right)}{B} \cdot \nabla u_{i,\parallel} \right).
\end{aligned}
$$

Assume interchangibility of spatial and temporal derivatives

$\partial_\parallel = 0$

Following the derivation in appendix J (but this time without n) we see that in cylinder geometry

$$
\nabla \cdot \left[\boldsymbol{u}_E \cdot \nabla \frac{\nabla_\perp \phi}{B} \right] = \frac{1}{B\rho} \{\phi, \Omega\},
$$

so that

$$
\nabla \cdot \left(n \frac{1}{\omega_{ci}} \left[\mathrm{d}_t^E + \boldsymbol{u}_{i,\parallel}) \cdot \nabla \right] \left[- \frac{\nabla_\perp \phi}{B} \right] \right) \simeq - \frac{n_0}{\omega_{ci}} \partial_t \Omega - \frac{n_0}{\omega_{ci}} \left(\frac{1}{B\rho} \{\phi, \Omega\} + u_{i,\parallel} \partial_\parallel \Omega + \frac{\nabla_\perp \left(\partial_\parallel \phi \right)}{B} \cdot \nabla u_{i,\parallel} \right).
$$

If we now collect the terms as we did in eq. (5.3), we get

$$
\begin{aligned}
&\frac{\nu_{in}}{\omega_{ci}} \left(n\Omega + \frac{\nabla_\perp \phi}{B} \cdot \nabla n \right) \\
&+ \frac{n_0}{\omega_{ci}} \partial_t \Omega + \frac{n_0}{\omega_{ci}} \left(\frac{1}{B\rho} \{\phi, \Omega\} + u_{i,\parallel} \partial_\parallel \Omega + \frac{\nabla_\perp \left(\partial_\parallel \phi \right)}{B} \cdot \nabla u_{i,\parallel} \right)
\end{aligned}
$$

$$
\begin{aligned}
&+ \frac{1}{\omega_{ci}} \nabla \cdot \left(S_n \left[\frac{\nabla_\perp \phi}{B} \right] \right) \\
=&\partial_\parallel j_\parallel,
\end{aligned}
$$

which after rearranging yields

$$
\begin{aligned}
\frac{n_0}{\omega_{ci}} \partial_t \Omega =& - \frac{\nu_{in}}{\omega_{ci}} \left(n\Omega + \frac{\nabla_\perp \phi}{B} \cdot \nabla n \right) \\
&- \frac{n_0}{\omega_{ci}} \left(\frac{1}{B\rho} \{\phi, \Omega\} + u_{i,\parallel} \partial_\parallel \Omega + \frac{\nabla_\perp \left(\partial_\parallel \phi \right)}{B} \cdot \nabla u_{i,\parallel} \right) \\
&- \frac{1}{\omega_{ci}} \nabla \cdot \left(S_n \left[\frac{\nabla_\perp \phi}{B} \right] \right) \\
&+ \partial_\parallel j_\parallel.
\end{aligned}
$$

We note that as we have no time derivative of n, the source term does not cancel as it did without this approximation.

6.3 Normalization

Finally, normalization yields

$$
\begin{aligned}
\frac{n_0}{\omega_{ci}} \omega_{ci}^2 \partial_t \Omega =& - \frac{\omega_{ci} \nu_{in}}{\omega_{ci}} \left(n_0 \omega_{ci} n\Omega + \frac{c_s}{\rho_s} n_0 \frac{\nabla_\perp \phi}{B} \cdot \nabla n \right) \\
&- \frac{n_0}{\omega_{ci}} \left(\frac{1}{\rho_s} c_s \omega_{ci} \frac{1}{B\rho} \{\phi, \Omega\} + c_s \frac{1}{\rho_s} \omega_{ci} u_{i,\parallel} \partial_\parallel \Omega + \frac{1}{\rho_s} c_s \frac{1}{\rho_s} c_s \frac{\nabla_\perp \left(\partial_\parallel \phi \right)}{B} \cdot \nabla u_{i,\parallel} \right) \\
&- \frac{1}{\omega_{ci}} \frac{1}{\rho_s} n_0 \omega_{ci} c_s \nabla \cdot \left(S_n \left[\frac{\nabla_\perp \phi}{B} \right] \right) \\
&+ \frac{1}{\rho_s} n_0 c_s \partial_\parallel j_\parallel \\
n_0 \omega_{ci} \partial_t \Omega =& - \nu_{in} \left(n_0 \omega_{ci} n\Omega + \omega_{ci} n_0 \frac{\nabla_\perp \phi}{B} \cdot \nabla n \right) \\
&- \frac{n_0}{\omega_{ci}} \left(\omega_{ci}^2 \frac{1}{B\rho} \{\phi, \Omega\} + \omega_{ci}^2 u_{i,\parallel} \partial_\parallel \Omega + \omega_{ci}^2 \frac{\nabla_\perp \left(\partial_\parallel \phi \right)}{B} \cdot \nabla u_{i,\parallel} \right) \\
&- n_0 \omega_{ci} \nabla \cdot \left(S_n \left[\frac{\nabla_\perp \phi}{B} \right] \right) \\
&+ \omega_{ci} n_0 \partial_\parallel j_\parallel \\
\partial_t \Omega =& - \nu_{in} \left(n\Omega + \frac{\nabla_\perp \phi}{B} \cdot \nabla n \right) \\
&- \left(\frac{1}{B\rho} \{\phi, \Omega\} + u_{i,\parallel} \partial_\parallel \Omega + \frac{\nabla_\perp \left(\partial_\parallel \phi \right)}{B} \cdot \nabla u_{i,\parallel} \right) \\
&- \nabla \cdot \left(S_n \left[\frac{\nabla_\perp \phi}{B} \right] \right) \\
&+ \partial_\parallel j_\parallel.
\end{aligned}
$$

6.4 The vorticity equation

By using the Boussinesq approximation, we will evolve the vorticity Ω in time rather than the modified vorticity Ω^D, and get[2]

$$\begin{aligned}\partial_t \Omega = &- \nu_{in}\left(n\Omega + \frac{\nabla_\perp \phi}{B}\cdot\nabla n\right)\\ &- \left(\frac{1}{B\rho}\{\phi,\Omega\} + u_{i,\parallel}\partial_\parallel\Omega + \frac{\nabla_\perp\left(\partial_\parallel\phi\right)}{B}\cdot\nabla u_{i,\parallel}\right)\\ &- \nabla\cdot\left(S_n\left[\frac{\nabla_\perp\phi}{B}\right]\right)\\ &+ \partial_\parallel j_\parallel\end{aligned} \tag{6.2}$$

To see how good or bad this approximation is (at least in our system), we will compare it with results not using this approximation in part III.

[2] As in section 5.6 the artificial viscosities are not shown here, but they are used in the simulations.

Chapter 7

Summary

We have now derived the set of equations, referred to as the CELMA model, both with and without the Boussinesq approximation. We have seen how our dynamic system can be described by four coupled equations derived from the Fokker-Planck equations. These equations are used in a cylindrical domain, where we have specified a somewhat appropriate set of boundary conditions. In principle, we are ready to put the model into a code which performs the calculation, and thereby simulate the system. Before doing so, we need to address some caveats regarding the implementation. It is also important to verify that the machinery we use to solve the equations is actually working. We will do so in the next part, and we will in part III discuss the results of the simulations.

At this point, it is appropriate to discuss how the CELMA model compares to some of the earlier works aiming to simulate plasmas in linear devices using 3-D fluid models. The comparison is not exhaustive, as it is not including all the work done in the field, but highlights relevant work with interesting features.

One of the earlier works done by Schröder and Naulin [50] investigates how the statistical properties of their global model (CYTO) matches experiments in the VINETA machine. The model assumes a constant electron temperature, cold ions, and includes sheath boundary conditions. This model is appearing in various forms throughout the literature.

In [51], a numerical simulation of the Large Mirror Device is sought by using the Numerical Linear Device code. This model is spectrally decomposed in both the poloidal and the parallel direction. The parallel ion velocity is neglected, and as the parallel direction is periodic, it does not include any form of sheath BCs. Investigations of linear growth rates and non-linear turbulent saturation are performed with the model. Sasaki et al. uses a variation of this model to investigate zonal flows and streamers in [52].

Also, gyrofluid models have been used in investigations of turbulence in 3-D cylinder geometry. A modification of the GEM3 code is used for simulations related to the VINETA device (approximated as an annulus) in [53]. The model makes a split of scales between background and fluctuations, and is therefore not global. Furthermore, it does not include sheath boundary conditions. The paper concludes that the so-called neutral wind modification of the intermittency is negligible.

In devices with an axial current Kelvin-Helmholtz instabilities will typically appear. This is investigated using the BOUT code for simulations of LAPD plasmas in an annulus geometry in [54]. The model does not use the Boussinesq approximation, but neglects parallel advection of the evolved fields. No sheath BCs are used in the model. The companion paper [55] investigates the saturated turbulence state using the same set-up.

Further investigations of the LAPD is conducted in a Cartesian domain by Rogers and Ricci [56]. Here, both sheath BC and temperature dynamics are included. It is concluded that the Kelvin-Helmholtz instability dominates the plasma dynamics in the LAPD. Non-linear instability investigations of LAPD are performed by using the BOUT++ framework by Friedman et al. [57]. An annulus geometry is used, and a split between fluctuations and background is done to get an energy conserving model. The work concludes that non-linear instabilities may be more important than the linear ones, and that care should be taken when turbulence is being interpreted from the linear instabilities alone. No sheath is used in the work, which may alter the results. Finally, Fisher et al. [58] builds on Roger's and Ricci's work of [56], and uses the Global Bragniskii Solver in a Cartesian domain to compare blob sizes from the simulations with those detected by a fast-camera. A good agreement is found.

To conclude the model comparison, the models by Reiser will be discussed. In reference [59], a model without the Boussinesq approximation is derived. Energy conservation is ensured when sources and sinks are not present, and the model includes the sheath boundary condition. The model is used to investigate how the tungsten sputtered from a target are transported in the plasma. The work concludes that the Boussinesq approximation gives only a minor error in the energy compared to the full model for the parameters investigated. Finally, in [60], Reiser et al. introduces the Boussinesq approximation to reduce the computational cost, and investigate intermittent spiraling motion in NAGDIS-II. The observed predator-prey behavior from the simulations is compared with reduced models.

As such, the consistency of the CELMA model, which is properly treating the modified vorticity, the particle source and the parallel advections, and which includes sheath boundary conditions, is only matched by the model given in [59]. The two models differs in how the parallel dynamics is addressed, and how the modified vorticity is evolved in time. Reference [59] does not mention how the singularity at $\rho = 0$ is dealt with, and the work presents a different numerical scheme than what is used in the present work.

Part II

Implementation and verification

Chapter 8

Implementation using the BOUT++ framework

The CELMA code is available at celma-project.github.io, and is implemented using the BOUT++ framework [61, 62, 63]. Historically, BOUT++ builds on the BOUT code [64] (which again is build on the UEDGE code [65]). However, BOUT and BOUT++ have diverged, and should not be mixed. BOUT is a code designed to solve a specific set of equations, whereas BOUT++ is a framework containing tools specifically designed to solve magnetized plasma equations, and is not bound to a specific model. In BOUT++ the user can specify what set of equations solve to solve for, what built-in solver to use and how to discretize the derivative operators. The BOUT++ framework is open source and available at `https://github.com/boutproject/BOUT-dev`. For this thesis BOUT++ version 3.1 with checksum number `11e8f23624b90cbbc67f797ac73eccb9e855c9c4` has been used[1].

8.1 Spatial discretization

BOUT++ comes with a built-in set of spatial discretization operators. The operators used in the CELMA code are given in table 8.1.

Direction	First derivative stencil ($\partial_i f$)	Second derivative stencil ($\partial_i^2 f$)	Upwind stencil ($f\partial_i g$)
ρ	Centered second order	Centered second order	None
θ	Fast Fourier transform	Fast Fourier transform	None
z	Centered second order	Centered second order	First order upwinding

Table 8.1: Spatial operators used in the CELMA code.

The standard centered finite difference stencils have been used (see [43] for details). Further, the fast Fourier transform is implemented using the `fftw`-package [66]. Finally, the first order upwinding scheme is used for the following operators:

- $u_{e,\parallel}\partial_\parallel \ln(n)$
- $nu_{e,\parallel}\partial_\parallel u_{i,\parallel}$

[1] Note that at the end of this thesis, version 4.0.0 was released.

- $nu_{i,\parallel}\partial_\parallel u_{e,\parallel}$
- $\frac{j_\parallel}{n}\partial_\parallel u_{e,\parallel}$
- $u_{i,\parallel}\partial_\parallel \left(nu_{e,\parallel}\right)$

Note that whereas the upwinding makes the system more stable, it does so by introducing damping on the system through artificial numerical diffusion introduced by the discretization [43]. For this reason, upwinding is **NOT** used on the $u_{i,\parallel}\partial_\parallel\Omega$ term when using the Boussinesq approximation as this may introduce spurious vorticity from the numerics.

8.2 Boundary conditions

The boundaries are positioned halfway between grid points, as depicted in fig. 8.1.

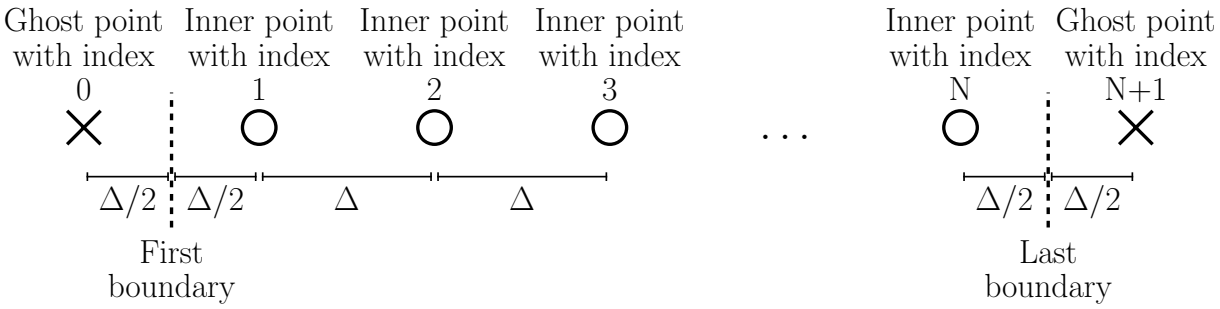

Figure 8.1: The boundaries are positioned halfway between grid points. Δ denotes the grid spacing between two grid points.

The boundary conditions are specified at the position of the boundary (the dashed horizontal lines in fig. 8.1). As there is no grid point at the boundary, the value is extrapolated to the ghost-point which is placed a distance $\Delta/2$ away from the boundary. We will here specify how these extrapolations are done within the BOUT++ framework. For implementation of artificial boundary conditions, see section 9.2.

For the Dirichlet boundary condition, the following 4th order extrapolation[2] is used

$$\begin{aligned} f_0 =& \frac{16}{5} f_{\text{First boundary}} - 3f_1 + f_2 - \frac{1}{5} f_3 \\ f_N =& \frac{16}{5} f_{\text{Last boundary}} - 3f_N + f_{N-1} - \frac{1}{5} f_{N-2}. \end{aligned}$$

For the Neumann boundary condition, a 4th order extrapolation[3] is used, reading

$$\begin{aligned} f_0 =& \frac{12}{11}\Delta f_{\text{First boundary}} + \frac{17f_1 + 9f_2 - 5f_3 + f_4}{22} \\ f_{N+1} =& \frac{12}{11}\Delta f_{\text{Last boundary}} + \frac{17f_N + 9f_{N-1} - 5f_{N-2} + f_{N-3}}{22}. \end{aligned}$$

[2] Derived using a Newton polynomial (using the four points around the edge of the domain of fig. 8.1 (including the ghost-point)), evaluated in the ghost-point.

[3] Derived using a one sided stencil (using the five points around the edge of the domain of fig. 8.1 (including the ghost-point)) of the first derivative evaluated at the boundary, solved for the ghost-point.

Finally, as the θ direction is periodical, the ghost-points are simply

$$\begin{aligned} f_{N+1} &= f_1 \\ f_0 &= f_N. \end{aligned}$$

8.3 Artificial viscosity

As mentioned in section 5.6, we have neglected the viscosities (as we assume that these are small). Instead, we add some artificial viscosities, which is needed for numerical stability (in addition to those added through the upwinding schemes). If there are no viscosities in the system, there is no mechanism (other than diffusion) which can remove the small scales (structures with a short gradient scale length) from the system. Scales which are smaller than what can be resolved by the grid will lead to problems like aliasing. These small scales can then build up and make the simulation crash[4].

For this reason, we add viscosities on the form

$$\begin{aligned} D_{f,\parallel,\text{art}}\nabla_\parallel^2 f + D_{f,\perp,\text{art}}\nabla_\perp^2 f &= D_{f,\parallel,\text{art}}\nabla\cdot(\boldsymbol{bb}\cdot\nabla)\,f + D_{f,\perp,\text{art}}\nabla_\perp^2 f \qquad \partial_i \boldsymbol{b} = 0 \\ &= D_{f,\parallel,\text{art}}\boldsymbol{b}\cdot\nabla\,(\boldsymbol{b}\cdot\nabla)\,f + D_{f,\perp,\text{art}}\nabla_\perp^2 f \\ &= D_{f,\parallel,\text{art}}\partial_\parallel^2 f + D_{f,\perp,\text{art}}\nabla_\perp^2 f, \end{aligned} \tag{8.1}$$

to all the evolved fields f.

In addition, a hyper-viscous term is added in the azimuthal direction for the Ω^D and Ω equations. This term is on the form

$$-D^H_{f,\theta,\text{art}}\partial_\theta^4 f.$$

The reason for this is that small scales grow up in the vorticity equations despite the filtering mentioned in section 9.5. To see that this term actually dampens higher modes, consider the example

$$\partial_t f = (-1)^{m+1} D\partial_x^{2m} f \qquad m \in \mathbb{N},$$

which we for simplicity assumes is periodical in x. For a certain wave number k, we now have (see appendix L for details)

$$\partial_t f_k = (-1)^{m+1}(ik)^{2m} D f_k,$$

where the $(-1)^{m+1}$ factor ensures that the time evolution of wave number k is decreasing for every choice of m. The artificial viscosity coefficients used in this thesis are given in table 8.2.

Higher coefficients are used in the parallel direction as the background gradients in this direction are much more gradual than the background gradients in the perpendicular gradients. In the end, both $D_{f,\parallel,\text{art}}\partial_\parallel^2 f$ and $D_{f,\perp,\text{art}}\nabla_\perp^2 f$ are small compared to the other terms. Notice that the artificial viscosities in Ω^D and Ω are smaller compared with the other fields. This is because the vorticity is usually quite filamented, and large artificial viscosities will not only remove the small scales, but also alter the physical behavior of the system.

[4] We will here use the word "crash" meaning that the simulation stops because of bad behavior the numerics. The simulation stops if a field reaches $\pm$`inf` or `nan` values (this can cause division by zero problems) or if the solver takes too small time-steps over a range of time because it cannot resolve unphysically large gradients.

Variable	$D_\parallel$	$D_\perp$	D_θ^{Hyper}
$\ln(n)$	40	$3.0 \cdot 10^{-3}$	0
$nu_{i,\parallel}$	40	$3.0 \cdot 10^{-3}$	0
$j_\parallel$	40	$3.0 \cdot 10^{-3}$	0
Ω^D	0.1	$2.4 \cdot 10^{-4}$	$5.81 \cdot 10^{-6}$
Ω	0.1	$2.4 \cdot 10^{-4}$	$5.81 \cdot 10^{-6}$

*Table 8.2: Artificial viscosities used in the CELMA code. Artificial viscosities to Ω^D is only added for the case where the Boussinesq approximation is **NOT** used. Artificial viscosities to Ω is only added for the case where the Boussinesq approximation is used.*

8.4 Time solver

This chapter will briefly discuss the time solver used in this thesis. BOUT++ provides a variety of time solvers, but the `cvode`[67] has been found to be a robust and fast time solver for solving eqs. (5.23) to (5.26) in time[5] .

As eqs. (5.23) to (5.26) contains no mixed temporal and spatial derivatives in the equations, the PDEs can first be discretized in the spatial dimension while keeping the time derivatives continuous. The set of PDEs is thereby rewritten to a set of ODEs (one for each of the discretized point in space) which needs to be solved simultaneously. This method is known as the "Method of Lines" (MOL) [43], and is widely used when solving a set of non-linear PDEs.

The problem can now be stated in the following way: Let $\boldsymbol{f} = \{\ln(n), nu_{i,\parallel}, j_\parallel, \Omega^D\}$, for $\ln(n)$, $nu_{i,\parallel}$, $j_\parallel$ and Ω^D discretized in space. That is, $\boldsymbol{f}$ is the tuple of the time dependent variables, and contains $\ln(n)_{0,0,0}$, $\ln(n)_{0,0,1} \ldots \ln(n)_{n_\rho,n_z,n_\theta}$, $\ldots nu_{i,\parallel_{0,0,0}}$, $\ldots \Omega^D_{n_\rho,n_z,n_\theta}$ where the subscripts denotes the grid index. Hence, we would like to solve

$$\frac{\partial \boldsymbol{f}(t)}{\partial t} = F(\boldsymbol{f}), \tag{8.2}$$

for $\boldsymbol{f}$, where $F(\cdot)$ denotes the nonlinear operator which contains discretized differential operators in the spatial dimension.

Equation (8.2) can be stepped forward in time by using an appropriate time solver, like Runge-Kutta or a Linear Multistep Method (LMM). Due to its good stability properties [43] an implicit LMM has been chosen[6] .

By a generic LMM, eq. (8.2) can be written

$$\begin{aligned}
\sum_{j=0}^{r} \alpha_j \boldsymbol{f}(t_{n+j}) =& k \sum_{j=0}^{r} \beta_j F(\boldsymbol{f}(t_{n+j}), t_{n+j}) \\
\alpha_r \boldsymbol{f}(t_{n+r}) + \sum_{j=0}^{r-1} \alpha_j \boldsymbol{f}(t_{n+j}) =& \beta_r F(\boldsymbol{f}(t_{n+r}), t_{n+r}) + k \sum_{j=0}^{r-1} \beta_j F(\boldsymbol{f}(t_{n+j}), t_{n+j})
\end{aligned}$$

[5] Implicit-Explicit (IMEX) approaches has also been tried in this thesis, but they have been found to be slower or crashing

[6] `cvode`'s variable step size Backward Differentiation Formula (BDF) of variable order (1-5) has been chosen. This includes the STAbility Limit Detection (STALD) algorithm, which detect linear stability regions, and chooses the step-size thereby.

$$\boldsymbol{f}(t_{n+r}) - \frac{\beta_r}{\alpha_r} F(\boldsymbol{f}(t_{n+r}), t_{n+r}) = \frac{k}{\alpha_r} \sum_{j=0}^{r-1} \beta_j F(\boldsymbol{f}(t_{n+j}), t_{n+j}) - \frac{1}{\alpha_r} \sum_{j=0}^{r-1} \alpha_j \boldsymbol{f}(t_{n+j}). \tag{8.3}$$

The method is implicit if $\beta_r \neq 0$. That is, the solution for the next time-step depends on the next time-step itself. In other words eq. (8.3) can be stated as an optimization problem. By defining $\frac{\beta_r}{\alpha_r} \stackrel{\text{def}}{=} \gamma$, we have

$$\boldsymbol{f}(t_{n+r}) - \gamma F(\boldsymbol{f}(t_{n+r}), t_{n+r}) - \frac{k}{\alpha_r} \sum_{j=0}^{r-1} \beta_j F(\boldsymbol{f}(t_{n+j}), t_{n+j}) + \frac{1}{\alpha_r} \sum_{j=0}^{r-1} \alpha_j \boldsymbol{f}(t_{n+j}) = G(\boldsymbol{f}(t_{n+r})) = 0.$$

Which we would like to solve for $\boldsymbol{f}(t_{n+r})$. This can be done by using Newton Raphson's method. I.e. we do a multivariate Taylor expansion of $G(\boldsymbol{f}(t_{n+r}))$ around an approximate point $\boldsymbol{f}_l(t_{n+r})$, and retain only the linear terms

$$G(\boldsymbol{f}(t_{n+r})) \simeq G(\boldsymbol{f}_l(t_{n+r})) + \left(\frac{\partial G(\boldsymbol{f}_l(t_{n+r}))}{\partial \boldsymbol{f}_l(t_{n+r})} \right) \left(\boldsymbol{f}(t_{n+r}) - \boldsymbol{f}_l(t_{n+r}) \right),$$

as $G(\boldsymbol{f}(t_{n+r})) = 0$, we get

$$0 \simeq G(\boldsymbol{f}_l(t_{n+r})) + \left(\frac{\partial G(\boldsymbol{f}_l(t_{n+r}))}{\partial \boldsymbol{f}_l(t_{n+r})} \right) \left(\boldsymbol{f}(t_{n+r}) - \boldsymbol{f}_l(t_{n+r}) \right).$$

The solution $\boldsymbol{f}(t_{n+r})$ to this problem can then serve as the next iteration, so that

$$\begin{aligned} \boldsymbol{f}_0(t_{n+r}) &= \boldsymbol{f}(t_{n+r-1}) \\ \boldsymbol{f}_{l+1}(t_{n+r}) &= \boldsymbol{f}_l(t_{n+r}) - \left(\frac{\partial G(\boldsymbol{f}_l(t_{n+r}))}{\partial \boldsymbol{f}_l(t_{n+r})} \right)^{-1} G(\boldsymbol{f}_l(t_{n+r})), \end{aligned}$$

where l denotes the $l-$th Newton iteration. The iterations can be rewritten to

$$\frac{\partial G(\boldsymbol{f}_l(t_{n+r}))}{\partial \boldsymbol{f}_l(t_{n+r})} \left(\boldsymbol{f}_{l+1}(t_{n+r}) - \boldsymbol{f}_l(t_{n+r}) \right) = - G(\boldsymbol{f}_l(t_{n+r})), \tag{8.4}$$

where

$$\begin{aligned} \frac{\partial G(\boldsymbol{f}(t_{n+r}))}{\partial \boldsymbol{f}(t_{n+r})} &= \frac{\partial}{\partial \boldsymbol{f}(t_{n+r})} \left(\boldsymbol{f}(t_{n+r}) - \gamma F(\boldsymbol{f}(t_{n+r}), t_{n+r}) - \frac{k}{\alpha_r} \sum_{j=0}^{r-1} \beta_j F(\boldsymbol{f}(t_{n+j}), t_{n+j}) + \frac{1}{\alpha_r} \sum_{j=0}^{r-1} \alpha_j \boldsymbol{f}(t_{n+j}) \right) \\ &= \mathbb{I} - \gamma \frac{\partial F(\boldsymbol{f}(t_{n+r}), t_{n+r})}{\partial \boldsymbol{f}(t_{n+r})} \\ &= \mathbb{I} - \gamma \mathbb{J}. \end{aligned} \tag{8.5}$$

By inserting eq. (8.5) in eq. (8.4), we get

$$(\mathbb{I} - \gamma \mathbb{J}) \left(\boldsymbol{f}_{l+1}(t_{n+r}) - \boldsymbol{f}_l(t_{n+r}) \right) = - G(\boldsymbol{f}_l(t_{n+r})).$$

which can be recast to

$$A\boldsymbol{x} = \boldsymbol{b}. \tag{8.6}$$

In other words, we need to invert A (that is $(\mathbb{I} - \gamma\mathbb{J})$) for each Newton iteration. As the system of equations in eq. (8.6) is rather large (and also generally non-symmetric), a robust and fast method is sought to solve for $\boldsymbol{x}$. This can be done by using the **G**eneralized **M**inimal **RES**idual method (GMRES).

This method approximates the exact solution of eq. (8.6) by a vector in the Krylov subspace (spanned by vectors obtained through the Arnoldi process), which minimizes the residual $\boldsymbol{r}_n = A\boldsymbol{x}_n - \boldsymbol{b}$. See [68] for details.

One of the advantages is that the Jacobian for the GMRES needs not to be expanded in memory as the Arnoldi process only needs to evaluate a Jacobian vector product [69].

The method is also easily preconditioned[7] , as shown in [70]. Although preconditioning is expected to give substantial speed-ups [67], it is outside the scope of this thesis.

In this thesis, the options for the time solver is given in table 8.3.

Variable	Value
Absolute tolerance	$1.0 \cdot 10^{-10}$
Relative tolerance	$1.0 \cdot 10^{-5}$
Max allowed iterations per step	$1.0 \cdot 10^{8}$

Table 8.3: Time solver options used in the CELMA code.

[7] To precondition means to find a P_L and/or P_R, which is easy to invert, and makes either $(P_L^{-1}A)\boldsymbol{x} = P_L^{-1}\boldsymbol{b}$, $(AP_R^{-1})P_R\boldsymbol{x} = \boldsymbol{b}$ or $(P_L^{-1}AP_R^{-1})\boldsymbol{x} = P_L^{-1}\boldsymbol{b}$ numerically easier to solve than eq. (8.6), as the matrices in parentheses is used in finding vectors spanning the Krylov subspace rather than A itself.

Chapter 9

Additional implementations

We will in this chapter describe additional implementations to the CELMA code, which (at the time of writing) is not included in the BOUT++ framework.

9.1 Composite derivatives

In eqs. (5.23) to (5.26) and eq. (6.2) there are some terms which are written as a combination of two or more FD schemes. These are

$$\{\phi, \cdot\}, \qquad \{\boldsymbol{u}_E^2, n\}, \qquad \partial_\parallel \nabla \cdot \left(u_{i,\parallel} n \frac{\nabla_\perp \phi}{B} \right) \qquad \text{and} \qquad \nabla \cdot \left(S_n \left[\frac{\nabla_\perp \phi}{B} \right] \right).$$

These can either be calculated by applying two (or more) different FD schemes consecutively to a field f, or by making a new FD stencil specifically for the operator under consideration.

Special care must be taken at the ghost-points if one chooses to apply two (or more) different FD schemes consecutively. To see this, we can call g the result of calculating the FD of a field f. As we are using centered stencils (as described in section 8.1), then the ghost-points of g is not calculated by the FD[12] .

9.1.1 Arakawa's stencil

As done in eq. (5.5), we can write $\boldsymbol{E} \times \boldsymbol{B}$-advective terms (that is the $\{\phi, \cdot\}$ terms) as Poisson brackets. The proof is found in appendix I. The benefits of writing terms in Arakawa's form are presented in his paper from 1966 [71]. In short, the paper shows that a naïve FD discretization of the Poisson bracket does not conserve energy and enstrophy. At the same time it gives an alternative way of discretize in orthogonal curvilinear coordinates in order to keep these quantities conserved. If the energy and enstrophy are not conserved, fake numerical generation of these quantities occur, which eventually will lead to a blow up of the simulation (in a way described by Phillips in [72]).

[1] There is by definition no way to apply a centered stencil to the last grid point.

[2] One could instead use a one-sided stencil on the ghost-points f when calculating the FD of f, so that the ghost-point of g would be known. This is however not done here.

9.1.2 Advection by $\boldsymbol{u}_E^2$

It is also possible to discretize the $\{\boldsymbol{u}_E^2, n\}$-term by using Arakawa's method. We observe that in cylindrical coordinates we have

$$\begin{aligned}
\{\boldsymbol{u}_E^2, n\} &= \left\{ \left(\frac{\nabla_\perp \phi}{B} \right)^2, n \right\} && \text{Constant } B \\
&= \left(\frac{1}{B} \right)^2 \left\{ \left(\left[\boldsymbol{e}^\rho \partial_\rho + \boldsymbol{e}^\theta \partial_\theta \right] \phi \right) \cdot \left(\left[\boldsymbol{e}^\rho \partial_\rho + \boldsymbol{e}^\theta \partial_\theta \right] \phi \right), n \right\} && \text{Orthogonality} \\
&= \left(\frac{1}{B} \right)^2 \left\{ g^{\rho\rho} \left(\partial_\rho \phi \right)^2 + g^{\theta\theta} \left(\partial_\theta \phi \right)^2, n \right\} \\
&= \left(\frac{1}{B} \right)^2 \left\{ \left(\partial_\rho \phi \right)^2 + \frac{1}{\rho^2} \left(\partial_\theta \phi \right)^2, n \right\}. && (9.1)
\end{aligned}$$

Here, care must be taken when treating the ghost-points. No ghost-points are needed in the θ direction, as this is periodic. Thus, for $\partial_\theta \phi$ we only need to make sure that we take the θ derivatives at the ghost-points in ρ.

For $\partial_\rho \phi$, we must re-apply the values in the ρ ghost-points as the derivative is not calculated there. For the inner ghost-point, the same procedure as used in section 9.4.1 can be used, whereas for the outer ghost-point, we can use eq. (9.4) for extrapolation to the ghost-point.

This way of discretizing is second order accurate, as indicated in table 10.1.

9.1.3 $\nabla \cdot (g \nabla_\perp f)$ terms

We have that

$$\begin{aligned}
\nabla \cdot (f \nabla_\perp g) =& f \nabla_\perp^2 g + \nabla f \cdot \nabla_\perp g \\
=& f \nabla_\perp^2 g + \nabla_\perp f \cdot \nabla_\perp g && \text{See appendix K.1.2} \\
=& f \left(g^{ij} \partial_i \partial_j + G^j \partial_j - \frac{1}{J} \partial_z \left(\frac{J}{g_{zz}} \partial_2 \right) \right) g + \left(e^\rho \partial_\rho + e^\theta \partial_\theta \right) f \cdot \left(e^\rho \partial_\rho + e^\theta \partial_\theta \right) g \\
=& f \left(g^{ij} \partial_i \partial_j + G^j \partial_j - \frac{1}{J} \partial_z \left(\frac{J}{g_{zz}} \partial_2 \right) \right) g + g^{\rho\rho} \partial_\rho f \partial_\rho g + g^{\rho\theta} \partial_\rho f \partial_\theta g + g^{\theta\rho} \partial_\theta f \partial_\rho g + g^{\theta\theta} \partial_\theta f \partial_\theta g. \\
& && (9.2)
\end{aligned}$$

As BOUT++ includes a numerical operator for $\nabla_\perp^2 g$ (as mentioned in appendix K.1.2), we could have used this operator for calculating $f \nabla_\perp^2 g$. However, from appendix H, we get that

$$\begin{aligned}
G^\rho &= \frac{1}{J} \\
G^z &= 0 \\
G^\theta &= 0 \\
g^{ij} &= 0 \qquad i \neq j \\
g^{\rho\rho} &= 1 \\
g^{\theta\theta} &= \frac{1}{\rho^2}
\end{aligned}$$

$$g^{zz}\partial_z^2 - \frac{1}{J}\partial_z\left(\frac{J}{g^{zz}}\partial_z\right) = 0,$$

for cylindrical coordinates. Thus, eq. (9.2) can be rewritten to

$$\begin{aligned} & f\left(g^{\rho\rho}\partial_\rho\partial_\rho + g^{\theta\theta}\partial_\theta\partial_\theta + G^\rho\partial_\rho\right)g + g^{\rho\rho}\partial_\rho f\partial_\rho g + g^{\theta\theta}\partial_\theta f\partial_\theta g \\ =& f\partial_\rho^2 g + f\frac{1}{\rho^2}\partial_\theta^2 g + f\frac{1}{\rho}\partial_\rho g + \partial_\rho f\partial_\rho g + \frac{1}{\rho^2}\partial_\theta f\partial_\theta g, \end{aligned} \tag{9.3}$$

Calculation of eq. (9.3) requires less arithmetic operations than eq. (9.2), and is therefore used in the CELMA code.

9.1.4 Parallel derivative of the divergence of the cross term

As $\partial_\parallel \nabla\cdot\left(u_{i,\parallel} n\frac{\nabla_\perp\phi}{B}\right)$ can be rewritten to $\partial_\parallel\nabla\cdot(g\nabla_\perp f)$, we just have to take care of the parallel ghost-points of $\nabla\cdot\left(u_{i,\parallel} n\frac{\nabla_\perp\phi}{B}\right)$ before taking the parallel derivative. We can use eq. (9.4) for calculation of the upper ghost-point, and eq. (9.5) for calculation of the lower ghost-point.

9.2 Extrapolation to the ghost-point

In the cases where no boundary is imposed (for the parallel derivative of ϕ mentioned in section 5.5 and in the composite derivatives mentioned in section 9.1), the following extrapolation [3]is used for the ghost-points

$$f_{N+1} = 4f_N - 6f_{N-1} + 4f_{N-2} - f_{N-3} \tag{9.4}$$

$$f_0 = 4f_1 - 6f_2 + 4f_3 - f_4, \tag{9.5}$$

where the indices refers to those indicated in fig. 8.1.

9.3 Obtaining ϕ

We observe that eqs. (5.23) to (5.26) depends on ϕ, but that ϕ is not described by an initial-boundary value problem equation. Instead, ϕ must be found by inverting either eq. (5.21) for the full model, or eq. (5.22) in for the Boussinesq model. We will in the following discuss two ways of doing so.

9.3.1 As a matrix inversion problem

The problem of obtaining ϕ can be posed as a matrix problem $A\boldsymbol{x} = \boldsymbol{b}$, where $\boldsymbol{x}$ is an array of all the spatial values of ϕ ordered in some way, and $\boldsymbol{b}$ is an array of all the spatial values of Ω^D ordered in the same way. Since we are working in an orthogonal coordinate

[3] Derived using a Newton polynomial (using the five points around the edge of the domain of fig. 8.1 (excluding the ghost-point)), and evaluate it in the ghost-point.

system, we have that $\Omega^D = \nabla \cdot \left(n\frac{\nabla_\perp \phi}{B} \right) = \nabla_\perp \cdot \left(n\frac{\nabla_\perp \phi}{B} \right)$, as no basis vector parallel to the magnetic field can be obtained from taking the derivative of the vector $n\frac{\nabla_\perp \phi}{B}$. Thus, in our case, we can solve the $A\boldsymbol{x} = \boldsymbol{b}$ system for each plane perpendicular to the magnetic field. That is, our matrix A would be a $n_x \times n_y$ matrix, where n_x and n_y is the number of points for the two perpendicular directions [4]. We note that if $\nabla \cdot \left(n\frac{\nabla_\perp \phi}{B} \right)$ were not purely perpendicular, we would have to solve $A\boldsymbol{x} = \boldsymbol{b}$ for the whole domain. In other words, the size of matrix A would be $n_x \times n_y \times n_z$, and would be considerably harder to solve numerically.

As noted in [73], for the finite difference case (that is when $P = 1$), the discretization of the elliptic equation $\nabla \cdot \left(n\frac{\nabla_\perp \phi}{B} \right) = \Omega^D$ can be formulated so that the resulting matrix is symmetric if special care is taken at the boundaries.

Solving for the ghost-points, meaning that the ghost-points would be one of the unknown in $A\boldsymbol{x} = \boldsymbol{b}$, would break the symmetry. Instead, one must reformulate the boundary condition in a way such that it becomes an equation for the ghost-point. The equation of the ghost-point can then be substituted into the equations for the first/last inner point (the point just before the boundary) and thus effectively eliminating the ghost-point from the set of equations.

To exemplify, consider a second order Dirichlet boundary condition with the boundary half between grid points for the equation $\partial_x^2 f = b$, where f_{-1} denotes the value at the ghost-point, f_{BC} denotes the value at the boundary and f_1 denotes the value at the first inner ghost-point. The boundary condition can now be written $\frac{f_{-1} + f_1}{2} = f_{\mathrm{BC}}$, and the equation for the first inner point could be written $\frac{f_{-1} + 2f_1 + f_2}{(\Delta x)^2} = b_1$. This would lead to the equation system

$$A \cdot \boldsymbol{f} = \boldsymbol{b}$$

$$\frac{1}{(\Delta x)^2} \begin{bmatrix} (\Delta x)^2\frac{1}{2} & (\Delta x)^2\frac{1}{2} & 0 & 0 & \dots \\ 1 & 2 & 1 & 0 & \dots \\ 0 & 1 & 2 & 1 & \dots \\ \vdots & \vdots & \vdots & \vdots & \ddots \end{bmatrix} \cdot \begin{bmatrix} f_{-1} \\ f_1 \\ f_2 \\ f_3 \\ \vdots \end{bmatrix} = \begin{bmatrix} f_{\mathrm{BC}} \\ b_1 \\ b_2 \\ b_3 \\ \vdots \end{bmatrix},$$

which is clearly non-symmetric.

The symmetric way to implement this would be to write $f_{-1} = 2f_{\mathrm{BC}} - f_1$ for the boundary condition, and substitute this into the 2nd order finite difference equation for the first inner ghost-point. This gives

$$\frac{f_{-1} + 2f_1 + f_2}{(\Delta x)^2} = b_1$$

[4] Note that in the BOUT++ implementation, y is chosen as the direction parallel to the magnetic field. This is due to historical reasons. n_y would be named n_z in BOUT++ convention. In order not to confuse readers unfamiliar with BOUT++, z is chosen as the coordinate along the magnetic field unless else is specified.

$$\frac{2f_{\text{BC}} - f_1 + 2f_1 + f_2}{(\Delta x)^2} = b_1$$
$$\frac{f_1 + f_2}{(\Delta x)^2} = b_1 - \frac{2f_{\text{BC}}}{(\Delta x)^2}.$$

The resulting matrix equation would read

$$A \cdot \boldsymbol{f} = \boldsymbol{b}$$
$$\frac{1}{(\Delta x)^2}\begin{bmatrix} 1 & 1 & 0 & 0 & \dots \\ 1 & 2 & 1 & 0 & \dots \\ 0 & 1 & 2 & 1 & \dots \\ \vdots & \vdots & \vdots & \vdots & \ddots \end{bmatrix} \cdot \begin{bmatrix} f_1 \\ f_2 \\ f_3 \\ \vdots \end{bmatrix} = \begin{bmatrix} b_1 - \dfrac{2f_{\text{BC}}}{(\Delta x)^2} \\ b_2 \\ b_3 \\ \vdots \end{bmatrix},$$

which is symmetric. Although difficult, one can show that the non-linear elliptic equation in its symmetric form can be singular positive definite and thus be solved using the conjugate gradient method [68].

9.3.2 The Naulin solver

The potential can also be found iteratively. The method first used by Naulin et al. in [74] will be presented here, and will be referred to as the Naulin solver.

The method can be used as long as

1. $\nabla \cdot \left(\dfrac{\nabla_\perp \phi}{B} \right) = \dfrac{\nabla_\perp^2 \phi}{B}$
2. $\nabla f \cdot \nabla_\perp g = \nabla_\perp f \cdot \nabla_\perp g$

Point 1. is satisfied in our system as B is constant, and because derivatives of the perpendicular basis vectors does not yield parallel components in our system. Point 2. is satisfied as the dot product of the perpendicular basis vectors and the parallel basis vector is zero. We then get that

$$\begin{aligned}
\Omega^D &= \nabla \cdot \left(n \frac{\nabla_\perp \phi}{B} \right) \\
&= n \nabla \cdot \left(\frac{\nabla_\perp \phi}{B} \right) + \frac{\nabla_\perp \phi}{B} \cdot \nabla n \\
&= n \frac{\nabla_\perp^2 \phi}{B} + \nabla n \cdot \frac{\nabla_\perp \phi}{B} \\
&= n \frac{\nabla_\perp^2 \phi}{B} + \nabla_\perp n \cdot \frac{\nabla_\perp \phi}{B} \\
\Omega^D &= n \frac{\nabla_\perp^2 \phi}{B} + \nabla_\perp n \cdot \frac{\nabla_\perp \phi}{B} \\
\frac{\Omega^D}{n} &= \Omega + \frac{1}{n} \nabla_\perp n \cdot \frac{\nabla_\perp \phi}{B} \\
\Omega &= \frac{\Omega^D}{n} - \nabla_\perp \ln(n) \cdot \frac{\nabla_\perp \phi}{B}.
\end{aligned}$$

Using square bracket superscript as iteration number, the algorithm can be stated in the following way:

1. Calculate $\Omega^{[i]} = \frac{\Omega^D}{n} - \nabla_\perp \ln(n) \cdot \frac{\nabla_\perp \phi^{[i]}}{B}$
2. Invert $\nabla_\perp^2 \frac{\phi^{[i+1]}}{B} = \Omega^{[i]}$ by the method described in appendix K.
3. Calculate $E_{\text{abs},L_\infty} = \max \left| \phi^{[i]} - \phi^{[i+1]} \right|$ and $E_{\text{rel},L_\infty} = \max \left| \frac{\phi^{[i]} - \phi^{[i+1]}}{\phi^{[i]}} \right|$
4. Check whether $E_{\text{abs},L_\infty} > \text{Tolerance}_{\text{abs}}$
   - If yes: Check $E_{\text{abs},L_\infty} > \text{Tolerance}_{\text{rel}}$
     - If yes: Assign $\phi^{[i+1]} \to \phi^{[i]}$, increase the iteration number, throw an error if the iteration number is above a predefined max iteration number, if not repeat from step 1.
     - Else, if no: Stop. Function returns
   - Else, if no: Stop. Function returns

The inversion algorithm requires inner and outer boundary condition in the radial direction of ϕ. The outer boundary condition is described in section 5.5.3, whereas the inner boundary condition is described in section 9.4.2. Table 9.1 states the options used in this thesis.

Variable	Value
Absolute tolerance	$1.0 \cdot 10^{-10}$
Relative tolerance	$1.0 \cdot 10^{-5}$
Max allowed iterations	$1.0 \cdot 10^{6}$

Table 9.1: Naulin solver options used in the CELMA code.

9.4 Treatment of the singularity

The cylindrical coordinate system has a singularity at the axis (where $\rho = 0$). In other words, functions are not well-defined in this point. One way to avoid this problem is to put the grid points close to, but not at the very axis. At the same time, as mentioned in section 5.5.4, there is a need of artificial boundary conditions as the domain covers $\rho \in]0, L_\rho[$.

9.4.1 Ghost-point for the radial derivative

We immediately observe that having a boundary condition at the singularity is a bad idea as functions are not well-defined in this point. It is also a bad idea to use one sided FD schemes around this point, as this will prevent communication of information through the axis.

One way to circumvent the problem is to put the innermost points in ρ, $\Delta\rho$ apart from each other, where $\Delta\rho$ is the grid spacing. I.e. the innermost points are both located $\frac{\Delta\rho}{2}$ from the axis, diametrically opposite of each other, as depicted on fig. 9.1. In this solution, the ghost-points for the innermost grid points in ρ (those closest to the singularity) will

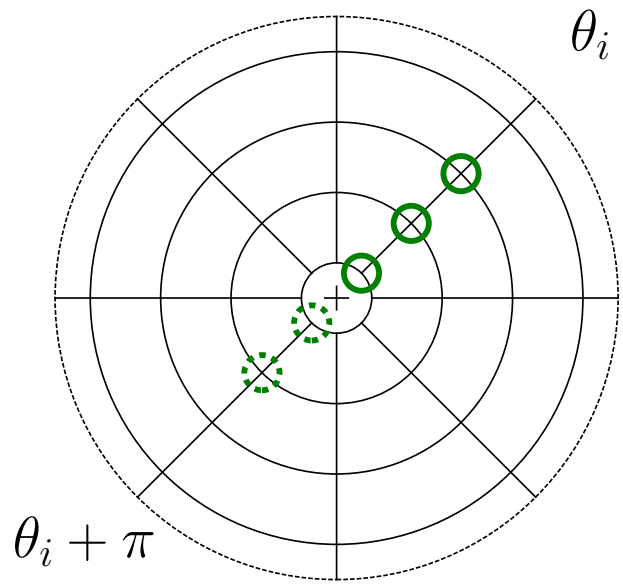

Figure 9.1: The solid lines black lines represent the coordinate curves of a mesh with 4 points in the ρ direction (excluding the outermost ghost-point depicted with a dashed black line), and 8 points in the θ-direction. The green solid circles represent the inner grid points at $\theta = \theta_i$, with the corresponding ghost-points at $\theta = \theta_i + \pi$ depicted as green dashed circles.

be set to the value of the innermost grid point which lies $\theta+\pi$ away. The next ghost-point will be set to the value of the second innermost internal point which lies $\theta + \pi$ away, and so on. In this thesis, only one ghost-point is used. With this method the second order FD stencil for the radial derivative becomes at the innermost point

$$\left.\frac{\partial f}{\partial \rho}\right|_{\rho=\frac{\Delta\rho}{2}} \simeq \frac{-f\left(-\frac{\Delta\rho}{2},\theta\right) + f\left(\frac{3\Delta\rho}{2},\theta\right)}{2\Delta\rho} = \frac{-f\left(\frac{\Delta\rho}{2},\theta+\pi\right) + f\left(\frac{3\Delta\rho}{2},\theta\right)}{2\Delta\rho}.$$

This method was used in [74], and is shown to be second order accurate in section 10.3.

9.4.2 The inner boundary condition for ϕ

We also need an artificial ghost-point for the innermost point in ρ for inversion method described in appendix K. As the inversion in the ρ direction will be done for each mode, the method described in section 9.4.1 is not directly applicable.

Instead, we can set the inner ghost-point depending on the evenness of the mode. If the mode is even, the mode under consideration would have the same value diametrically opposite of the innermost point. Notice that this is true for every point at the same radius. Hence, the ghost-point for the inner ρ value is set to the same as the value at the innermost ρ.

If the mode is odd, the mode under consideration has different signs at diametrically opposite positions. Thus, the ghost-point for the inner ρ value is set to the negative of the value at the innermost ρ. The method was first used in [74], and is depicted in fig. 9.2.

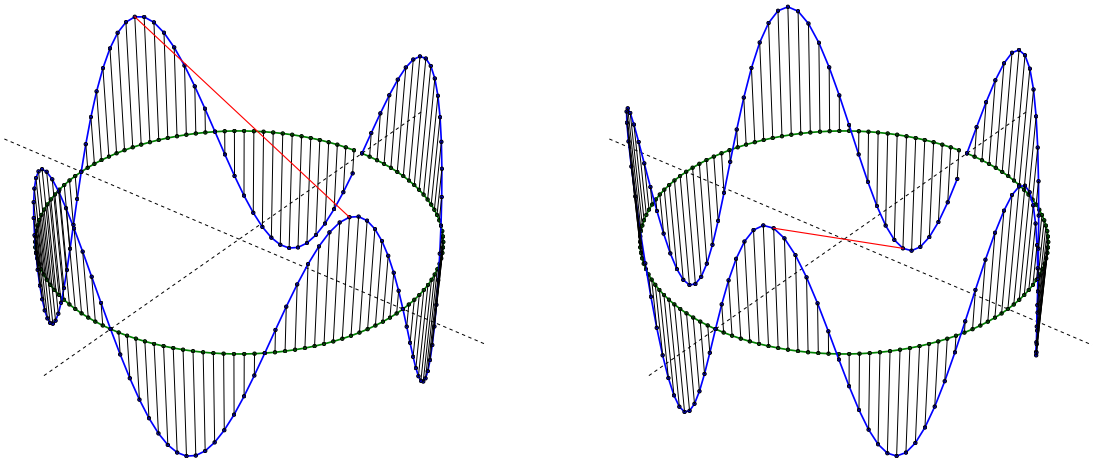

(a) An even mode. *(b) An odd mode.*

Figure 9.2: Two points diametrically opposite of each other has the same sign if the mode is even, but opposite signs if the mode is odd. The red solid line connects points diametrically opposite of each other.

9.5 Spectral filtering

In order to ensure that no aliasing will occur and thereby create a numerical instability like the one mentioned in [72], we must use a spectral filter in the periodic direction. Although sufficiently high viscosities or diffusion can prevent aliasing (such that all the higher modes are damped out), they typically also damp modes which we would like to include in our simulation. One way to get around this is to use spectral filters.

9.5.1 Orszag's 2/3 rule

As mentioned in [75], only the 2/3 of the topmost modes leads to aliasing. To see this, recall that only mode numbers equal to or less than $N/2$ can be represented exactly on a grid discretized with N points [76]. Next, consider two mode numbers m_1 and m_2 which adds up to a mode m_3. If $m_3 = m_1 + m_2 > N/2$, the mode will be interpreted as $m_1 + m_2 - N$ (i.e. it will be aliased to the negative frequencies). If we call M the highest mode we can have which would not give aliasing, we must require that

$$\begin{aligned} m_1 + m_2 - N &< -M \\ M + M - N &< -M \\ 2M - N &< -M \\ 3M &< N \\ M &< \frac{N}{3}. \end{aligned}$$

In order words, modes with mode number less than $N/3$ does not contribute to aliasing. Therefore, the name "2/3-rule" as M is 2/3 of the Nyquist frequency $M < (2/3)(N/2)$.

Thus, aliasing in this case is prevented if we set all modes with a mode number equal or above $N/3$ to zero. As we see in the next section, this does not completely eliminate the aliasing in a cylinder, due to radial coupling.

9.5.2 Radial coupling

As terms like $\{\phi, f\}$ effectively advects modes of f radially, we must ask ourselves what the smallest allowed wave length in the periodic direction is. Since the circumference is given by $C = 2\pi\rho$, and since the number of points in the periodic θ-direction is constant, we see that resolution is limited by the shortest allowed wave length at the outermost radius L_ρ. Let us now consider sinusoids on the form $\sin(kx)$ living on the circumference C at radius ρ. The wave number is then given by $k = \dfrac{2\pi m}{C}$, which means that the wavelength is

$$\lambda = \frac{C}{m}. \tag{9.6}$$

The smallest resolved wavelength on $\rho = L_\rho$, where L_ρ is the outermost radius, and is given by the Nyquist frequency. This gives the wavelength $\lambda_{\text{Nyquist}} = \dfrac{C_{L_\rho}}{n_\theta/2}$, where n_θ is the number of points in the θ direction. However, the smallest wavelength which does not give aliasing is given by the 2/3-rule, so that

$$\lambda_{\min} = \frac{C_{L_\rho}}{\frac{2}{3}\frac{n_\theta}{2}} = \frac{3C_{L_\rho}}{n_\theta}.$$

By rearranging eq. (9.6), we find that the largest allowed mode number for the circumference C at radius ρ is

$$m_{\max} = \left\lfloor \frac{C}{\lambda_{\min}} \right\rfloor,$$

where $\lfloor \cdot \rfloor$ denotes the floor function. Note that we take the floor as we are looking for the maximum allowed integer.

Chapter 10

Verification of the numerics

In order to find solutions which matches real life experiments (at least to a certain degree), we need to ensure that the assumptions in our models are sound. Of equal importance is it to check that the machinery handling the numerical calculation is correctly implemented. This can be done by code verification.

Quoting [63]:

> Code verification is a process of checking that the chosen set of partial differential equations is solved correctly and consistently, and is a purely mathematical exercise. Code verification is not concerned with verifying that the chosen numerical methods are appropriate for the chosen set of equations. Code verification is also not concerned with testing the ability of a given model to explain experimental observations. This testing is dealt with in the subsequent validation process.

Thus, a code can be verified numerically, but still fail to match the desired features of a real life experiment. In other words, it would have passed the verification, but failed the validation. If the code has successfully passed a validation test, but fails a verification test, the success of the validation is questionable. The success of the validation in this case could have been a mere coincident.

The verification process is thoroughly discussed in [77] and more condensed for the method of manufactured solution (MMS) in [78]. Note that the verification process can be time-consuming, and can be regarded as an art form in itself. Luckily, a major part of the implementation has already been verified in the BOUT++ framework using MMS in [63].

After a quick introduction of the concept of truncation errors, the MMS process will be briefly presented in section 10.2 before verification of additional implementations in the CELMA code is given in section 10.3.

10.1 Numerical errors

Our derivative operators are discretized in order to operate on a discretized grid. Doing so introduces an error, which depends on the order of approximation. To use a concrete example, let us consider the simplest differential equation

$$\frac{\mathrm{d}f(x)}{\mathrm{d}x} = g(x) \tag{10.1}$$

where $f(x)$ and $g(x)$ are arbitrary functions (not to be confused with the distribution function and a metric element). We seek to solve eq. (10.1) for $f(x)$.

Let us find the simplest approximation of the derivative in an arbitrary grid point x_0. We first Taylor expand $f(x)$ around x_0 and evaluate it in $x_0 + h$ (where h is the grid spacing). This gives

$$f(x_0 + h) = f(x_0) + h \left.\frac{\mathrm{d}f(x)}{\mathrm{d}x}\right|_{x=x_0} + \frac{h^2}{2}\left.\frac{\mathrm{d}^2 f(x)}{\mathrm{d}x^2}\right|_{x=x_0} + \mathcal{O}(h^3)$$

Subtraction of $f(x_0)$ and division by h now yields the following approximation of the derivative

$$\frac{f(x_0 + h) - f(x_0)}{h} = \left.\frac{\mathrm{d}f(x)}{\mathrm{d}x}\right|_{x=x_0} + \frac{h}{2}\left.\frac{\mathrm{d}^2 f(x)}{\mathrm{d}x^2}\right|_{x=x_0} + \mathcal{O}(h^2)$$

Hence, the local truncation error (LTE) we do in a single point by using this approximation is

$$\|e_{\text{LTE}}\| = \left\| \frac{f(x_0 + h) - f(x_0)}{h} - \left.\frac{\mathrm{d}f(x)}{\mathrm{d}x}\right|_{x=x_0} \right\| = \left\| \frac{h}{2}\left.\frac{\mathrm{d}^2 f(x)}{\mathrm{d}x^2}\right|_{x=x_0} + \mathcal{O}(h^2) \right\|$$

In other words, it scales with the grid spacing h to the first order. The global error in some L-norm n can be defined as

$$\|\boldsymbol{e}\|_{L_n} = \|\boldsymbol{f}_{\text{true}} - \boldsymbol{f}_{\text{numeric}}\|_{L_n}$$

where $\boldsymbol{f}_{\text{true}}$ is an array of the analytic solution in each grid point, and $\boldsymbol{f}_{\text{numeric}}$ is an array of the solution obtained numerically. From linear PDE theory we have that the global error should converge to the LTE order if the scheme is consistent (the LTE $\to 0$ as $h \to 0$) and numerically stable[1]. If convergence is observed, the implementation is verified.

10.2 Method of Manufactured Solution

For most PDEs, the true solution $\boldsymbol{f}_{\text{true}}$ is not known in advance. Sometimes a solution can be found in some special limits. If convergence is found for these special cases, the code is not generally verified. There could still be implementation mistakes (not discoverable in the limiting cases) which could have dire consequences when a more general solution is sought numerically. One way to get around the problem is to manufacture a solution.

Assume that we have a set of nonlinear spatio-temporal PDEs we would like to solve. Let us call the variables evolved in time $\boldsymbol{f} = \{\boldsymbol{u}_e, \boldsymbol{u}_i, n, \Omega^D, T_e, \ldots\}$. If there are no mixed spatial and temporal variables, we can write the set of nonlinear PDEs as

$$\frac{\partial \boldsymbol{f}}{\partial t} = F(\boldsymbol{f}) \;\Rightarrow\; \frac{\partial \boldsymbol{f}}{\partial t} - F(\boldsymbol{f}) = \boldsymbol{0}, \tag{10.2}$$

where $F(\cdot)$ is a nonlinear operator which contains the discretized spatial differential operators. As stated above, we do not know a priori which $\boldsymbol{f}$ which satisfies eq. (10.2).

[1] Note that the definition of stability depends on the context, see [43] for more details.

Therefore, we manufacture a set of functions $\boldsymbol{f}_M$ which does not satisfy eq. (10.2), but rather

$$\frac{\partial \boldsymbol{f}_M}{\partial t} - F(\boldsymbol{f}_M) = \boldsymbol{S}.$$

Note that $\boldsymbol{f}_M$ is an exact analytical solution of $\dfrac{\partial \boldsymbol{f}}{\partial t} = F(\boldsymbol{f}) + \boldsymbol{S}$. We can therefore solve $\dfrac{\partial \boldsymbol{f}}{\partial t} = F(\boldsymbol{f}) + \boldsymbol{S}$ numerically for $\boldsymbol{f}$, and find the global error (for each variable $\boldsymbol{u}_e, \boldsymbol{u}_i, n, \Omega^D, T_e, \ldots$ by

$$\|\boldsymbol{e}\|_{L_n} = \|\boldsymbol{f}_M - \boldsymbol{f}_{\text{numeric}}\|_{L_n}.$$

One can now test if the global error show the expected order of convergence. Note that $\boldsymbol{f}_M$ and the coefficients in the various terms in the PDEs does not need to be physical, but that in order to test all terms in this set of equations, the parameters of the simulation should be chosen so that the magnitude of each term are of a similar order of magnitude.

10.3 Method of Exact Solution

Since there are implementations in this thesis which are not covered by the BOUT++ framework (see chapter 9 for details), these implementations should be verified as well. All of these implementations are either differentiation operators, extrapolations or integration operators where an exact analytic solution can be found. Hence, one can use the approach of method of exact solutions (MES) to verify these operations, and there will be no need for manufacturing a solution.

Although it is simpler to perform MES than MMS, there are certain points one should be aware of. Especially since we are dealing with a periodic domain with a singularity in the center. Let us now call the function we are operating on with a discretized operator D for $f(\rho, \theta, z)$. Hence, the source S is given by $D[f(\rho, \theta, z)] = S$. If we are to take derivatives in the ρ direction, we must take care that

1. $f(\rho, \theta, z)$ must be of $\mathcal{C}^\infty$ along ρ, particularly at $f(\rho = 0, \theta, z)$.
   - This implies that the function must be single valued in $f(\rho = 0, \theta, z)$.
   - Even though the coordinate system have a singularity in $f(\rho = 0, \theta, z)$, the function may be continuous in a different coordinate system.
2. Boundary conditions in ρ must be satisfied.

If we are to take derivatives in the θ direction, we must take care that

1. $f(\rho, \theta, z)$ must be of $\mathcal{C}^\infty$ along θ, particularly at $f(\rho, \theta = 0, z)$ and $f(\rho, \theta = 2\pi, z)$
   - This implies that the function must be periodic.

Note that there are functions not fulfilling all the criteria that can give convergence.

10.3.1 Derivative operators

We will in this section use the following notation, which is consistent with BOUT++ notation (see footnote 1 in appendix H.2)

- `DDX(f)` for the second order discretization of $\partial_\rho f$.
- `D2DX2(f)` for the second order discretization of $\partial_\rho^2 f$.
- `DDZ(f)` for the spectral discretization of $\partial_\theta f$.
- `D2DZ2(f)` for the spectral discretization of $\partial_\theta^2 f$.

A function which satisfies most of the criteria in section 10.3 is

$$\begin{aligned} f(\rho,\theta,z) = &\sin\left(\frac{1}{\sqrt{2}}\rho[\cos(\theta)+\sin(\theta)]\frac{2\pi}{2L_\rho}\right) \\ &\exp\left(-\frac{1}{2w^2}\left[\rho^2+\rho_0^2-2\rho\rho_0(\cos[\theta-\theta_0])\right]\right) \\ &\left(\frac{\rho\cos[\theta]+L_\rho}{2L_\rho}\right)^2, \end{aligned} \tag{10.3}$$

where

$L_\rho = 30$	Cylinder radius
$w = \frac{4}{5}L_\rho$	Width of Gaussian
$\rho_0 = \frac{3}{10}L_\rho$	ρ - coordinate for center of Gaussian
$\theta_0 = \frac{5\pi}{4}$	θ - coordinate for center of Gaussian

The function is depicted in fig. 10.1a, and has the advantage that it is not symmetric across the axis. However, it is not $\mathcal{C}^\infty$ in $\rho = 0$, as the first derivative of the function (with respect to ρ) is multivalued there. As a consequence it is found that for example `DDX(DDX(f))` diverges rather than converges when applying MES to eq. (10.3)[2] [3]

Single operators

In order to check that the singularity is correctly implemented, we can check that `DDX(f)` is giving the expected order of convergence on eq. (10.3) as this is not symmetric. The error of the operation for 2^{11} points is shown in fig. 10.1b. It is important to notice that the error is not dominating at one particular point, but is spread out over domain. If the inner ghost-point were incorrectly implemented, this would be detected by a localized high error around $\rho = 0$, and it is expected that the correct order of convergence would not be found. In addition, we would like to check the convergence of `D2DX2`, `DDZ` and `D2DZ2` as these are used in the $\nabla \cdot (g[\nabla f])$ operator, and in the $\boldsymbol{u}_E^2$ advection of n. The results are given in table 10.1. We note that the derivatives in the ρ direction gives the expected second order convergence. We also see that although the derivatives in the θ direction seems not to be converging, the errors are quite small. This is because machine precision is quickly reached. That is, the loss of precision due to subtraction of two almost equal quantities becomes larger than the error from the discretization itself. The behavior is depicted in fig. 10.2. We therefore conclude that the schemes up until this point for convergent.

[2] The ghost-points are re-calculated after using the first operation on f.

[3] Note that convergence is found for eq. (10.3) when using `D2DX2(f)`, and that convergence for `DDX(DDX(f))` is found using functions which are of $\mathcal{C}^\infty$, but which are not symmetric.

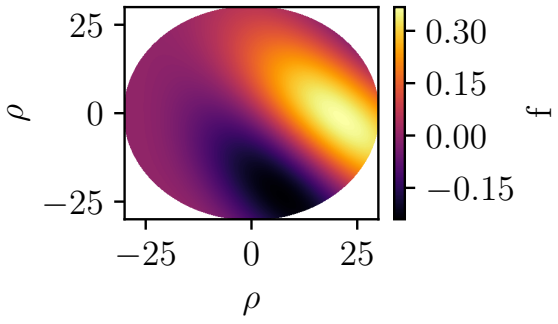

(a) Visualization of eq. (10.3)

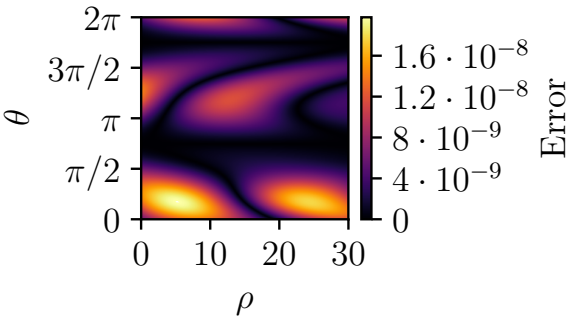

(b) Errors of `DDX(f)`, where f is given in eq. (10.3)

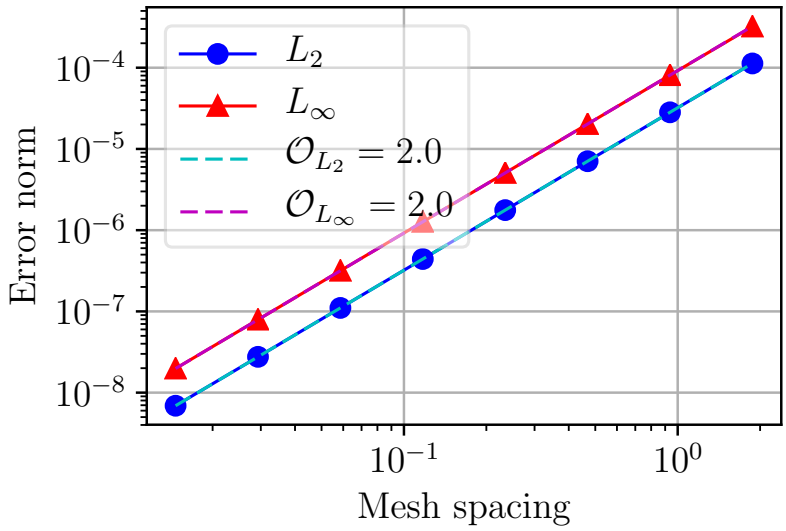

(c) Convergence rate of `DDX(f)`, where f is given in eq. (10.3)

Figure 10.1: An example of functions and errors found when using MES.

Finally, we will point out an important caveat. Several operators used in the CELMA code can be written as $\rho^{-m}\partial_\rho f$, and care must be taken as the division by ρ can appear to break the convergence. In the case of $\frac{\texttt{DDX}(f)}{\rho}$, the loss of expected convergence rate can be explained by looking at the finite difference stencil. We have that[4]

$$\frac{\mathrm{d}f}{\mathrm{d}x} - \texttt{DDX}(f) = \frac{\Delta^2}{6}\frac{\mathrm{d}^2 f}{\mathrm{d}x^2} + \mathcal{O}(\Delta^3),$$

where Δ denotes the grid spacing depicted in fig. 8.1. As the boundaries lay half between the grid points, $\rho|_{\text{Index}=1} = \frac{\Delta}{2}$. Thus, in this point, we have that

$$\left.\frac{\frac{\mathrm{d}f}{\mathrm{d}x}}{\rho}\right|_{\text{Index}=1} - \left.\frac{\texttt{DDX}(f)}{\rho}\right|_{\text{Index}=1} = \frac{\Delta}{3}\frac{\mathrm{d}^2 f}{\mathrm{d}x^2} + \mathcal{O}(\Delta^2)$$

[4] Found by Taylor expanding f around x_0, evaluating it in $x+\Delta$ and subtracting it from the function Taylor expanded around x_0 and evaluated in $x-\Delta$. The final result is divided by 2Δ.

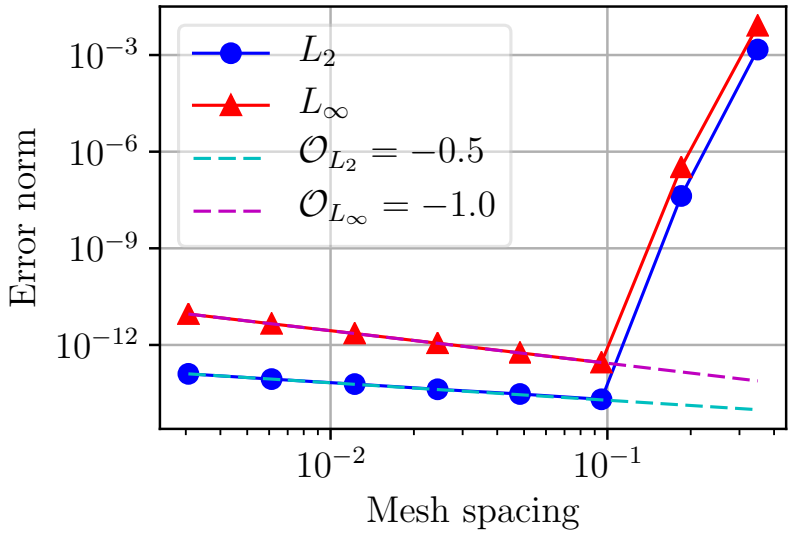

Figure 10.2: Divergence due to loss of precision of the operator `DDZ(f)`.

Therefore, the scheme is only 1st order convergent in Δ. As a function like ρ is known to machine precision, this does not imply that the operator is incorrectly implemented, only that verification of $\rho^{-m}\partial_\rho f$ thought MES is not suitable.

The Naulin Solver

For the Naulin Solver (described in section 9.3.2) we will use eq. (10.3) for n and a Cartesian Gaussian for ϕ. Specifically, we use

$$\phi = \exp\left(-\frac{1}{2w^2}[\rho^2 + \rho_0^2 - 2\rho\rho_0\cos(\theta - \theta_0)]\right) \tag{10.4}$$

with

$$w = \frac{1}{2}L_\rho \qquad \rho_0 = \frac{1}{5}L_\rho \qquad \theta_0 = \pi$$

for n[5]. The results are given in table 10.1. We note that the method seems to be non converging for when increasing the number of points in θ. However, since we are using a spectral discretization in the θ-direction, the error drops rapidly. As a result, the error arising from discretization in ρ quickly becomes dominant even with high resolution in the ρ direction. Hence, we conclude that the method is convergent.

Arakawa implementation of $\boldsymbol{u}_E^2$

We will now verify the implementation of the

$$\{\boldsymbol{u}_E^2, n\} = \left\{(\partial_\rho\phi)^2 + \frac{1}{\rho^2}(\partial_\theta\phi)^2, n\right\} = \left\{(\partial_\rho\phi)^2, n\right\} + \left\{\frac{1}{\rho^2}(\partial_\theta\phi)^2, n\right\}$$

[5]The same convergence rate was found if the functions were swapped.

term. As the Arakawa implementation of $\{\phi, \cdot\}$ was found convergent using MMS in [63], and because the treatment of the singularity was found to be convergent in section 10.3.1, we would here like to check that ghost-points are correctly calculated after doing the $\partial_\rho^2\phi$ operation. Hence, we seek to MES the term

$$\left\{\left(\partial_\rho\phi\right)^2, n\right\}.$$

As noted in footnote 3, we should here find a different function for ϕ as the first derivative with respect to ρ of eq. (10.3) has the problem that it is not single valued on the axis. Instead, we will use the function

$$\begin{aligned}\phi =& 10\left(6+\left[\frac{\rho}{L_\rho}\right]^3\right)\cos(2\theta)\\ &\left(\cos\left[2\pi\frac{\rho}{L_\rho}\right]+\sin\left[2\pi\frac{\rho}{L_\rho}\right]+\cos\left[6\pi\frac{\rho}{L_\rho}\right]+\cos\left[4\pi\frac{\rho}{L_\rho}\right]\right)\\ &\frac{1}{2}\left(1-\tanh\left[\frac{1}{8}\rho\right]\right)\end{aligned} \tag{10.5}$$

Note that since the Arakawa implementation does not use Fourier discretization, there is no problem that this function contains a sum of in θ. This means that we do not get the advantages of the spectral convergence rate. However, the errors in the ρ may dominate when successively making the grid spacing in θ smaller and vice versa. This is what happens when performing the MES test in the θ direction, as seen in table 10.1. One could of course increase the resolution even more in ρ, but this would make the test computationally expensive. Inspection of the error plot shows that the error is not dominating in any particular point, and we can therefore conclude that the implementation is convergent.

Finally, note that we are not applying the MES to $\frac{1}{2\rho}\left\{\left(\partial_\rho\phi\right)^2, n\right\}$, as the $\frac{1}{\rho}$ factor reduces the convergence rate as mentioned in section 10.3.1.

10.3.2 Extrapolation to ghost-points

The verification of extrapolation to the outer ghost-points in ρ was verified in section 10.3.1. What remains is to verify the parallel extrapolation of the ghost-points for ϕ, and to verify the sheath boundary condition for $j_\parallel$. Notice that the polynomials in section 9.2 are of fourth order. This is to avoid propagation of one point errors when the ghost-point is re-inserted in the finite difference approximation (FDA). For the sheath boundary condition, the following functions are used

$$\phi = \sin\left(\frac{1}{\sqrt{2}}[\rho+z]\frac{2\pi}{2L_\rho}\right) \tag{10.6}$$

$$n = \cos\left(\frac{2\pi z}{L_z}\right)\sin^2\left(\frac{2\pi\rho}{L_\rho}\right) \tag{10.7}$$

$$u_{i,\parallel} = \sin\left(\frac{z}{L_z}\right)\cos^2\left(2+2\pi\frac{\rho}{L_\rho}\right) \tag{10.8}$$

Notice that $u_{e,\parallel}$ is given by the sheath boundary condition and that this function does not need to be manufactured. The result of the MES is given in table 10.1.

10.3.3 Integration operators

Finally the integration operators are verified. Note that we are not using these routines when solving the set of PDEs, but to calculate the total particle number, the kinetic energy etc. We now define the hat function H as

$$H(d,s,c,w) = \frac{1}{2}\left(\tanh\left[s\left(d-\frac{c-w}{2}\right)\right] - \tanh\left[s\left(d-\frac{c-w}{2}\right)\right]\right) \tag{10.9}$$

The arguments of the function is the continuous variable d, steepness s, centering c and width w as input parameters And use the following equations in the verification process

$$f = \frac{H\left(\rho, 2, \frac{L_\rho}{2}, \frac{L_\rho}{4}\right)}{\int_0^{L_\rho} H\left(\rho, 2, \frac{L_\rho}{2}, \frac{L_\rho}{4}\right) \mathrm{d}\rho} \tag{10.10}$$

$$f = \frac{H\left(\theta, 2, \pi, \frac{\pi}{2}\right)}{\int_0^{2\pi} H\left(\theta, 2, \pi, \frac{\pi}{2}\right) \mathrm{d}\theta} \tag{10.11}$$

$$f = \frac{H\left(z, 0.07, \frac{L_z}{2}, \frac{L_z}{4}\right)}{\int_0^{L_z} H\left(z, 0.07, \frac{L_z}{2}, \frac{L_z}{4}\right) \mathrm{d}z} \tag{10.12}$$

The results for each direction is given in table 10.1.

10.3.4 Summary of convergence rates obtained

Operation	Direction	L_∞ order	L_2 order	L_∞ error 2^{11} points	L_2 error 2^{11} points	Equations used	Comment
$\texttt{DDX}(f)$	ρ	2.00	2.00	$1.99 \cdot 10^{-8}$	$6.90 \cdot 10^{-9}$	10.3	
$\texttt{D2DX2}(f)$	ρ	2.00	2.00	$1.58 \cdot 10^{-9}$	$5.07 \cdot 10^{-10}$	10.3	
$\frac{\texttt{DDX}(f)}{J}$	ρ	1.00	1.50	$3.16 \cdot 10^{-5}$	$4.48 \cdot 10^{-7}$	10.3	No 2nd order convergence. Errors dominating close to $\rho = 0$.
$\texttt{DDZ}(f)$	θ	-1.00	-0.54	$9.12 \cdot 10^{-12}$	$1.26 \cdot 10^{-13}$	10.3	Machine precision reached.
$\texttt{D2DZ2}(f)$	θ	-1.99	-1.57	$3.83 \cdot 10^{-9}$	$6.65 \cdot 10^{-11}$	10.3	Machine precision reached.
Naulin Solver	ρ	2.00	2.00	$3.19 \cdot 10^{-7}$	$1.65 \cdot 10^{-7}$	10.3 for n and 10.4 for ϕ	$n_\theta = 2^{12}$
Naulin Solver	θ	0.00	0.00	$7.98 \cdot 10^{-9}$	$4.13 \cdot 10^{-8}$	10.3 for n and 10.4 for ϕ	$n_\rho = 2^{12}$, errors from ρ discretization dominating
$\left\{(\partial_\rho \phi)^2, n\right\}$	ρ	2.00	2.00	$1.60 \cdot 10^{-7}$	$2.43 \cdot 10^{-8}$	10.3 for n and 10.5 for ϕ	$n_\theta = 2^{12}$
$\left\{(\partial_\rho \phi)^2, n\right\}$	θ	1.35	1.46	$1.12 \cdot 10^{-8}$	$8.41 \cdot 10^{-8}$	10.3 for n and 10.5 for ϕ	$n_\rho = 2^{12}$ Convergence found until $n_\theta = 2^9$
ϕ z-extrapolation	z	3.47	4.50	$5.60 \cdot 10^{-16}$	$5.86 \cdot 10^{-18}$	10.3	Machine precision reached.
$j_\parallel$ sheath	z	3.98	4.50	$2.38 \cdot 10^{-10}$	$2.18 \cdot 10^{-12}$	10.6 for ϕ, 10.7 for n and 10.8 for $u_{i,\parallel}$	
$\int f \, \mathrm{d}V$	ρ	2.01	–	$3.50 \cdot 10^{-9}$	–	10.10	$n_\theta = n_z = 512$
$\int f \, \mathrm{d}V$	θ	2.21	–	$2.03 \cdot 10^{-10}$	–	10.11	$n_\rho = n_z = 512$
$\int f \, \mathrm{d}V$	z	2.00	–	$2.01 \cdot 10^{-8}$	–	10.12	$n_\rho = n_\theta = 512$

Table 10.1: Results of the convergence tests

Part III

Numerical simulations

Chapter 11

Simulation set up

In this chapter the simulation setup will be discussed. The domain size, the initial conditions and the source function will be defined, and the resolution will be given together with a discussion of the observed see-sawing pattern in $j_\parallel$. How the simulations are being executed will be explained, and we will finish the chapter by specifying the hardware. For the implementation parameters, see tables 8.2, 8.3 and 9.1.

11.1 Domain size and normalizations

We will in this thesis use a physical domain size similar to the size of CSDX [39]. That is, we will use a cylinder length $L_z = 2.8\,\mathrm{m}$ and a plasma radius $L_\rho = 8\,\mathrm{cm}$. Note that the plasma radius is much less than the radius of the cylinder chassis.

Variable	Value	Units
L_ρ	0.08	m
L_z	2.80	m
n_0	$1 \cdot 10^{19}$	m^{-3}
n_n	0	m^{-3}
$T_{e,0}$	2.5	eV
m_i	$6.63 \cdot 10^{-26}$	kg
c_s	2.46	$\mathrm{km\ s}^{-1}$

Table 11.1: Fixed simulation parameters.

Variable	Range	Units
B_0	$0.02 - 0.01$	T
ω_{ci}	$48.4 - 242$	kHz
ρ_s	$5.08 - 1.02$	cm
L_ρ/ρ_s	$1.57 - 7.86$	
L_z/ρ_s	$55.0 - 275$	

Table 11.2: Variable simulation parameters.

These parameters can be translated to normalized units once we specify $T_{e,0}$, m_i and B_0. We will use $T_{e,0} = 2.5\,\mathrm{eV}$, the mass of singly ionized Argon as m_i, and let B_0 vary between 0.02 and 0.1 T. This sets the ion sound speed to $c_s \approx 2.46\ \mathrm{km\ s}^{-1}$. Further, it sets the ion cyclotron frequency to $\omega_{ci} \approx 2.42B \cdot 10^6\,\mathrm{T\,s}^{-1}$, which means that ω_{ci} is in the range of 48.4 kHz to 242 kHz for the specified magnetic field strengths. Consequently, as we print the output to the files after every $t\omega_{ci}$[1], this gives an output every 4-20 μs in

[1]Note that the internal time-step from the adaptive time solver is usually much smaller.

physical units. The specified c_s and ω_{ci} gives a hybrid radius of $\rho_s \approx 1.02B^{-1} \cdot 10^{-3}\,\mathrm{m\,T^{-1}}$, which with the specified magnetic field strengths will be in the range 5.08 cm to 1.02 cm.

We will use a normalized density $n_0 = 1 \cdot 10^{19}\,\mathrm{m^{-3}}$, and let the neutral density $n_n = 0$ unless else is specified. The numbers are summarized in tables 11.1 and 11.2.

11.2 Initial conditions and source specification

The coupled set of PDEs in eqs. (5.21) to (5.26) forms an initial-boundary value problem. The boundary conditions of this problem was given in section 5.5, but we have yet to define the initial conditions.

In the work presented here, we will use the following initial conditions of the normalized evolved quantities[2]

$$\ln(n) = 0 \qquad j_\parallel = 0 \qquad nu_{i,\parallel} = \frac{z}{L_z} \qquad \Omega^D = 0,$$

as this is not a solution to the equations, the steady state will be found numerically as explained in section 11.4.

Furthermore, we need to specify the source. Here, we have chosen the following shape of the source

$$S = AH(\rho, s_{\text{profile}}, c_{\text{profile}}, w_{\text{profile}}),$$

where H is defined in eq. (10.9), and $A = 8.25 \cdot 10^{21}\,\mathrm{m^{-3}\,s^{-1}}$ in physical units. With this choice the normalized n is around 1 for $B = 0.1\,\mathrm{T}$. The arguments of H are summarized in table 11.3, and S is depicted in figs. 12.1 and 12.2.

Variable	Value
s_{profile}	$5/L_\rho$
c_{profile}	0
w_{profile}	L_ρ

Table 11.3: Source parameters used in the simulations.

One could argue that the source should be increased close to the SE due to recycling at the end plate, The proper shape of the source can only be properly be accounted for if atomic physics and eventual electromagnetic waves generating the plasma is taken into account. Therefore, a flat parallel profile chosen for simplicity.

11.3 Resolution

In order to have a properly resolved grid, we need to properly resolve the gradient length scales. From the computational-time point of view, few grid points is preferable. If we assume that the maximum gradient length scale from the model is around ρ_s, we should

[2] Ω is used rather than Ω^D when simulating using the Boussinesq approximation

have $\frac{n_\rho}{L_\rho/\rho_s} > 1$. However, we have in this work found that $\frac{n_\rho}{L_\rho/\rho_s} \approx 1$ can give simulation crashes, so a radial resolution of $\frac{n_\rho}{L_\rho/\rho_s} \approx 3$ is aimed. The same argument goes for the poloidal direction, where $L_\theta = 2\pi L_\rho$.

As mentioned in chapter 3, the resolution in the parallel direction can be less since longer gradient scale lengths are found in the parallel direction as a consequence of the separation of scales. The sheath sets the gradient scale length in the parallel direction, as will be explained in section 12.1. Despite that the gradient scale sets a lower constraint on n_z, a grid-sized see-sawing pattern is observed in simulations with a flow towards an end-plate for low n_z. This problem has been observed in other plasma fluid codes dealing with sheath boundaries, but has to this author's best knowledge not been published. For the work presented here, the problem is encountered in $j_\parallel$ as is illustrated in fig. 11.1[3].

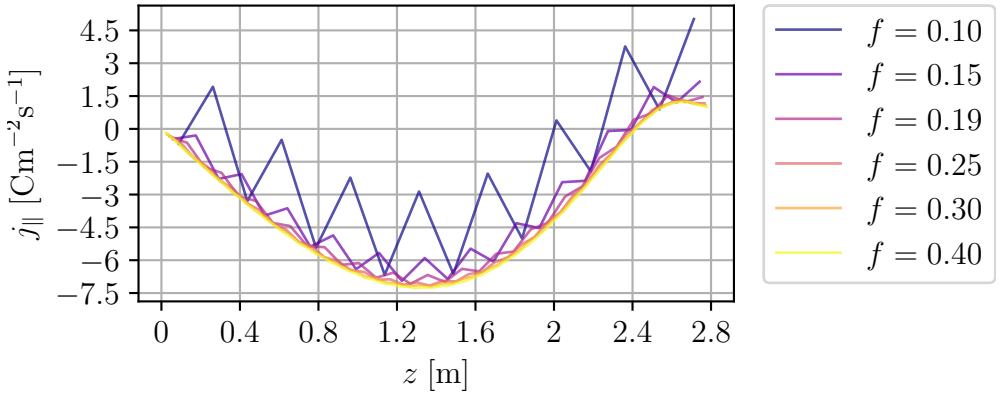

Figure 11.1: See-saw oscillations for $B = 0.06$ T in the steady-state using $16, 24, 32, 42, 50$ and 66 grid points in the parallel direction. f is defined in eq. (11.1)

To get a better understanding of this behavior, the different terms in eq. (5.25) has been plotted in fig. 11.2 in the steady-state. It is clear that the steady state is dominated by

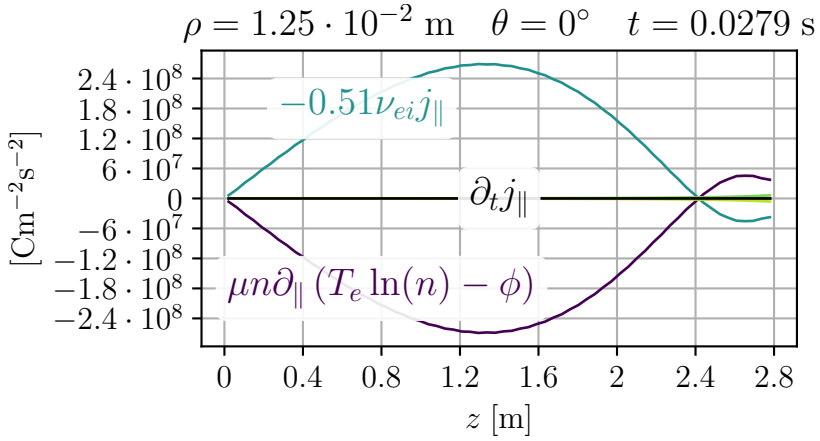

Figure 11.2: The different terms making up eq. (5.25) in the steady-state for $n_z = 66$ for $B = 0.06$. The parallel derivative of ϕ balances the parallel derivative of n almost exactly, and the difference is between these two is balanced by the resistivity.

[3]It should be noted that running the simulations with odd number of points show similar behavior to what is presented in fig. 11.1.

a balance between the Boltzmann response of the electrons and resistive terms. This is also seen for lower n_z, albeit with stronger oscillations in the Boltzmann response and the resistive term for decreasing n_z. The resistive term is $\propto j_\parallel$, and can therefore not be the cause of the observed see-sawing. Thus, we can conclude that the see-sawing behavior comes from the difference between the logarithm of the density and the potential.

One could imagine that the see-sawing came from catastrophic cancellation between $\ln(n)$ and ϕ. If this was the case, the see-sawing would be even worse for an increased mass ratio μ. In fact, the opposite behavior is observed. Running the simulations with H gives more see-sawing than with Ar. The explanation can be found by looking at the fraction f defined by

$$f \overset{\text{def}}{=} \frac{n_z}{L_z/\rho_s}, \tag{11.1}$$

which describes the resolution in terms of ρ_s. We can now observe that

$$f = \frac{n_z c_s}{L_z \omega_{ci}} = \frac{n_z \sqrt{T_e} m_i}{\sqrt{m_i} L_z Z e B} = \frac{n_z \sqrt{T_e m_i}}{L_z Z e B},$$

i.e. it is proportional to $\sqrt{m_i}$. On this argument, running simulations with singly ionized Ar gives a better resolution of $\sqrt{m_{\text{Ar}}/m_H} \approx 6.3$ compared to simulations with H. That increased oscillations has been observed with simulations done with increasing B and L_z strengthens the hypothesis as $f \propto 1/BL_z$.

To keep the oscillations at a minimum, we require $f > 0.2$ in the simulations performed here, which sets a lower bound on n_z. Ideally, we would like to reduce the number of parallel points to speed up the simulations. Therefore, some alternative strategies to lower the grid-size oscillation is discussed in the following.

Increased artificial viscosity will alleviate the problem. Unfortunately, it is found that the artificial viscosity coefficients needed for a smooth $j_\parallel$ makes the artificial viscosity term dominate, such that the steady state is defined by a balance between the Boltzmann terms, the resistive term and the artificial terms. The same holds true if the artificial viscous terms are changed with hyperviscous terms of order 4 (i.e. with ∂_z^4 terms).

To reformulate the problem into a finite volume problem seems to be a good idea as fluxes through the cell centers are conserved. However, the same grid-size oscillation problem has been found in finite volume models [79].

Finally, a split-scheme could lessen the problem. Since the discretization of $n\mu\partial_z(\ln(n) - \phi)$ is done with a centered FD scheme, odd and even grid points will be decoupled. That is, $\partial_z(\ln(n) - \phi)$ for odd grid points will only depend on the even points and vice versa. For advective terms references [80, 81] suggest a skew-symmetric split in the form $\nabla \cdot (a\boldsymbol{u}) = \frac{1}{2}[\nabla \cdot (a\boldsymbol{u}) + a\nabla \cdot \boldsymbol{u} + \boldsymbol{u} \cdot \nabla a]$ where all the right hand terms are discretized using centered difference schemes to get rid of the decoupling. Although arising from a divergence term, rewriting

$$n\mu\partial_z(\ln(n) - \phi) = \frac{1}{2}\left(\partial_z[n\mu(\ln(n) - \phi)] - [\ln(n) - \phi]\,\partial_z[n\mu] - n\mu\partial_z[\ln(n) - \phi]\right)$$

may help for the grid-size oscillations. This has, however, not been tried in the work presented in this thesis.

The grid size used in this thesis is given in table 11.4.

Variable	Value
n_ρ	32
n_z	66
n_θ	256

Table 11.4: Grid size used in the simulations.

11.4 Simulation execution

The simulations are executed in four steps.

First, the simulation is allowed to evolve freely to a steady-state condition using $n_\theta = 1$. This choice is justified by assuming axisymmetry in the steady state. A transient period with fast dynamics is observed before a slow settlement to the steady-state. The steady-state is found by visual inspection, and is defined to be the time when there is a minimal difference between two time-steps. The steady-state is usually reached between $2000 - 3000 t\omega_{ci}$. In order to ensure that the system has reached a steady state, the simulations are therefore executed until $4000 t\omega_{ci}$ is reached.

Secondly, the simulation is expanded to $n_\theta = 256$, and executed for additional $50 t\omega_{ci}$. This ensures that the system is still in an axisymmetric steady state.

Thirdly, white noise perturbation with an amplitude of $1 \cdot 10^{-6}$ is added to Ω^{D4} as this term is driving the non-linear advections through ϕ.

If the system is unstable to small perturbations, and if there are no "crashes" in the simulation, a saturated turbulence state is eventually reached.

11.5 Hardware

All the simulations presented here are carried out on the `A1` (Broadwell) partition of the `Marconi` supercomputer located at CINECA at Casalecchio di Reno (Bologna). At the time of writing the cluster operated with the following specifications [82]

1. Model: Lenovo NeXtScale
2. Architecture: Intel OmniPath Cluster
3. Nodes: 1512
4. Processors: 2×18-cores Intel Xeon $E5 - 2697$ v4 (Broadwell) at 2.30 GHz
5. Cores: 36 cores/node, 54432 cores in total
6. RAM: 128 GB/node, 3.5 GB/core
7. Internal Network: Intel OmniPath Architecture 2:1
8. Disk Space: 17PB (raw) of local storage
9. Peak Performance: 2 PFlop/s

In all the simulations, 2 nodes has been allocated using 48 cores. This has been found to give a good speed-up (as compared to use one node) with a good trade off between the ratio of time spent on arithmetics compared to communication (see chapter 20).

[4]Different approaches has been used for the perturbation. Although the route to the linear state may vary, the same growth rates and turbulent behavior are found.

Chapter 12

The steady state

The steady state is achieved as described in section 11.2. We will in this section discuss the shape of the resulting profiles, and the physics leading to these.

12.1 Parallel profiles

The resulting parallel profiles for the steady state are shown in fig. 12.1. It is found

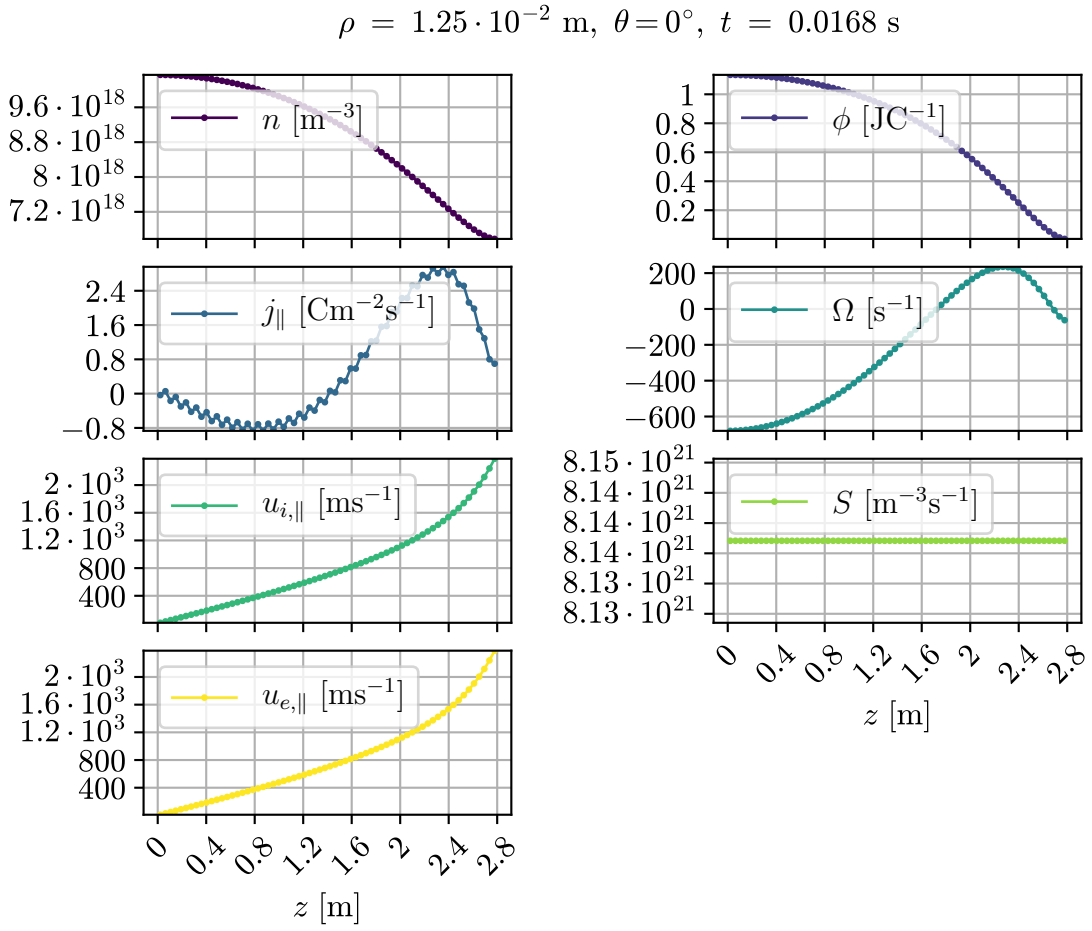

Figure 12.1: Parallel profiles in the steady state for $B = 0.1$ T. A dot on the line denotes a grid point.

that the shape of these profiles are mainly determined by the source and the boundary condition at the sheath entrance.

If we change the source amplitude, the values of the profiles changes, but the shape remains relatively constant. There exists a threshold on the source amplitude for the filling of the plasma cylinder. For source amplitudes under this threshold the cylinder is "emptied" for plasma. That is: The density remains low for all time-steps, and no density profile builds up. There also exists an upper limit on the source amplitude. Above this threshold, the radial density profiles are not developing, and the radial profiles remains flat. These thresholds are determined by the balance between number of particles created (the volume integrated source) and the particle outflow of the domain (the density flux integrated over the domain surface). In-between these two extremes, the parallel extent of the source determines the filling. That is: The parallel shape of the density is determined by the parallel extent of the source, and not so much by the shape of the source itself (i.e. if it is shaped as a sinusoid or if it is flat).

As mentioned above, also the boundary condition at the sheath entrance is critical for the parallel shape of the plasma profiles. If the boundary condition on the density is changed to for example Cauchy boundary condition (described in section 5.5.2), it is observed that the shape of the steady state profiles becomes much steeper close to the sheath entrance. Gradients that steep usually gives rise to numerical instabilities, unless the spatial resolution in this area is increased.

We observe that the potential profile in fig. 12.1 follows the density profile quite well. This relation is called the Boltzmann relation[1] and is expected because:

1. The pressure is balancing the electric field to first order, as seen in the ordering described in B.
2. We do not restrict the potential by any parallel boundary condition.

Next, the parallel velocity profiles are mainly arising from the parallel boundary condition. Both the ions and electrons are fixed to a zero velocity at the boundary opposite to the sheath. Furthermore, the ions are fixed to the ion sound velocity at the sheath entrance, whereas the electron velocity will regulate itself after the potential. If more electrons than ions were to escape, a potential difference would build up attracting more ions and pushing away more electrons. Any difference in the parallel velocities would lead to parallel currents.

The divergence of the current must be constant as a consequence of charge conservation. Any parallel derivatives in the parallel current not balancing the other terms in eq. (5.26) would lead to an acceleration of the plasma spinning. Therefore, the radial vorticity profile comes as a direct consequence of the parallel derivative of the current in that point. Due to this, one should take care that the see-sawing in the parallel current profile is kept to a minimum. The see-saw pattern seen in fig. 12.1 is at the maximum level allowed in this thesis, and arises from the poor parallel resolution mentioned in 11.3.

[1] The Boltzmann relation actually reads $n \simeq C \exp\left(\frac{e\phi}{T_e}\right)$ for an integration constant C. Since $1 > \phi\frac{e}{T_e}$ we get the approximate relation $n \simeq C\left(1 + \frac{e\phi}{T_e}\right)$ from the Taylor expansion, so $n \propto \phi$.

12.2 Radial profiles

The radial profiles are shown in fig. 12.2. As for the parallel direction, the shape of

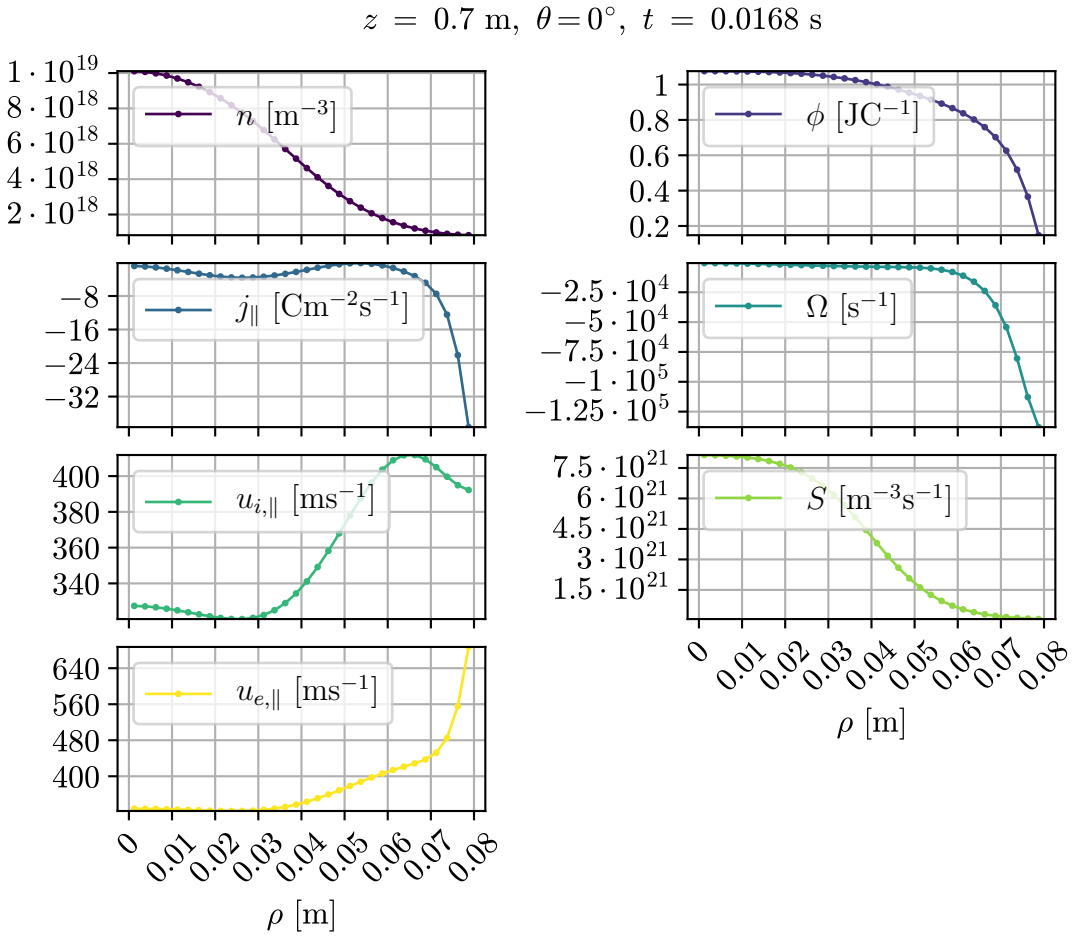

Figure 12.2: Radial profiles in steady state for $B = 0.1$ T. A dot on the line denotes a grid point.

the radial density profile is determined mainly by the source and the radial boundary conditions. The radial extent of the source plays a larger role in determining the radial density profile as compared with the shape of the source.

Despite having almost Boltzmann distributed electrons in the parallel direction at each radial point close to the axis, the Boltzmann relation does not apply in the radial direction. This is because the plasma is confined in the perpendicular direction by the strong magnetic field. Close to L_ρ the radial potential profile is affected more by the fixation potential to 0 at L_ρ. Thus, the values here differs from the density profile because of the zero gradient enforcement on n at L_ρ. As a result, $j_\parallel$ forms a boundary layer since $\mu n \partial_\parallel (T_e \ln[n] - \phi)$ diverges due to difference in boundary conditions between ϕ and n. This means that we get a sharp gradient in Ω as the parallel gradient in $j_\parallel$ is adding to the positive acceleration of the vorticity. The sharp gradient in Ω means that we will have a strong velocity shear in the poloidal velocity, as described further in chapter 16.

Chapter 13

The linear phase

The linear behavior of our system will here be investigated. In the end, we will conclude that the behavior coincides with what is found from simplified drift-wave theory.

After perturbing the system[1] as described in section 11.2, the perturbation noise vanishes, and poloidal modes start to appear. The modes will either grow or be damped in the linear phase, depending on the simulation parameters. As the perturbations are small, the dynamics in this linear phase comes purely from the linear part of the set of equations. In other words mode-mode coupling between different modes are negligible. If the system was purely linear, the growth of the modes would continue forever. However, our system is not purely linear, and mode coupling will start to become important once the perturbations have grown sufficiently big. The mix of linear and non-linear growth will eventually reach a saturated turbulence phase, which will be treated in chapter 14. We will here define the linear state as:

1. Starting once the initial perturbation has vanished and where the modes start to show an exponential-like growth or decay.
2. Ending at the time where any mode, which up to that point in time has been flat or damped, suddenly shows an exponential growth.

13.1 The linear growth

In addition to the growth explained above, the modes are rotating in the linear phase. This is indicated in fig. 13.2, where a clockwise rotation is observed. For further reference, one should note that the black dashed circles on the perpendicular part of the plot indicates the position of the maximum gradient of the density in the steady state, which is also the fixed ρ in the poloidal part of the plot.

We will now compare the direction of rotation of the perturbations with direction of rotation of the zeroth order drifts. Further, the gradients in both ϕ and n are pointing towards the center (i.e. towards negative ρ). From eq. (I.2) have that

$$u_{E,\theta} = \boldsymbol{u}_E \cdot \hat{\boldsymbol{e}}_\theta = \frac{1}{JB}\left(-\boldsymbol{e}_\theta \partial_\rho + \boldsymbol{e}_\rho \partial_\theta\right)\phi \cdot \frac{\boldsymbol{e}_\theta}{\rho} = -\frac{1}{J\rho B} g_{\theta\theta}\partial_\rho \phi = -\frac{\rho^2}{\rho^2 B}\partial_\rho \phi = -\frac{1}{B}\partial_\rho \phi,$$

[1] It has not been observed that the system reaches the linear phase unless perturbed. This could in theory happen if the noise at machine level assembles in just the right way so that it forms an unstable mode.

so the $\boldsymbol{u}_E$-drift is moving in the counter-clockwise direction[2]. Substituting $\nabla\phi$ with $\dfrac{T_e\nabla n}{q_e n}$ in eq. (I.2) gives the electron diamagnetic drift. We find that

$$u_{d,e,\theta} = \frac{T_e}{eB}\frac{\partial_\rho n}{n}.$$

That is, the diamagnetic drift is moving in the clockwise direction, opposite of the $\boldsymbol{E}\times\boldsymbol{B}$-drift direction. In absolute numbers, the $\boldsymbol{E}\times\boldsymbol{B}$-drift is approximately one order smaller than the diamagnetic drift at the position of maximum density gradient for our parameters. Hence, the perturbations are moving in the electron diamagnetic direction. This is one of the characteristic features of drift-waves [83]. To verify if the linear phase can be identified as drift-waves, we will proceed with a quick review of linear drift-waves.

13.2 Simplified linear drift-wave theory

Conceptually, a drift-wave is a wave which travels in the electron diamagnetic direction, and arises due to the mobility difference between electrons and ions. If one introduces a density (or pressure) perturbation in a homogeneous, magnetized plasma slab, the electrons will stream out of the perturbation along the magnetic field lines at a much faster rate than ions due to their higher mobility. This gives rise to a $\boldsymbol{E}$-field perturbation pointing in the direction of increased electron density. The $\boldsymbol{E}$-field gives in turn rise to a $\boldsymbol{E}\times\boldsymbol{B}$-drift perpendicular to the magnetic field. This process is depicted in fig. 13.1. The drift-waves has its counterpart in fluid dynamics as Rossby waves, where the $\boldsymbol{E}\times\boldsymbol{B}$

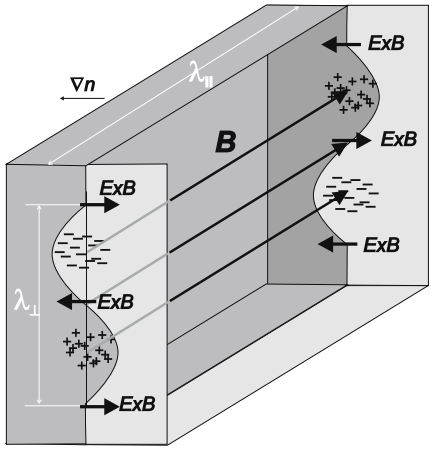

Figure 13.1: Sketch of a drift-wave in a slab. The arrows labeled with $\boldsymbol{E}\times\boldsymbol{B}$ indicate the position of the maximum $\boldsymbol{E}\times\boldsymbol{B}$-drift. Taken from [84].

drift equivalence comes from the Coriolis force [85].

A phase shift between the potential and density is necessary in order to get an instability. This can be seen from fig. 13.1 if one shifts the ion and electron clouds upwards or downwards so that the $\boldsymbol{E}\times\boldsymbol{B}$ arrows are shifted with respect to the density perturbations. For a mathematical demonstration of this, see for example [86].

[2] Note that the signs comes as a consequence of working in a left-handed system. This means that θ is increasing in the counter-clockwise direction.

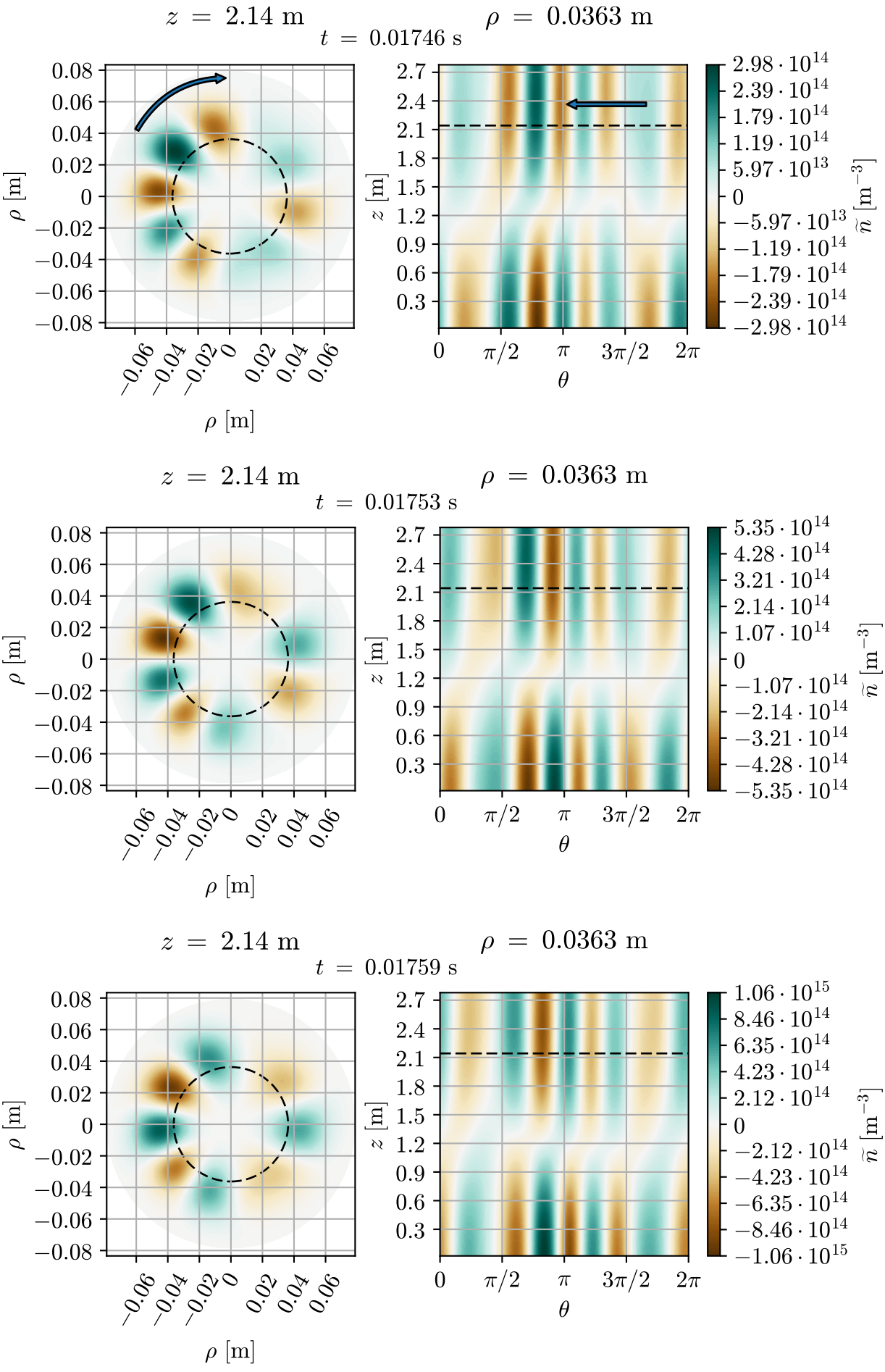

Figure 13.2: Rotation of the modes. The arrow indicates the direction of movements, whilst the dashed lines indicates where the data is sliced in the opposite plot. The B-field point into the paper.

A phase shift arises if the parallel motion of electrons arising from pressure gradients is delayed. Such a delay can have its origin in for example magnetic induction, Landau damping, or as in our case, due to resistivity.

To obtain a simple analytic expression of the drift-waves, we will recite the most important points given in the derivation in [87]. For a review of drift-waves, the reader is referred to [88]. We are here not concerned with neutral interaction. For an analytic expression where the neutral elastic collision dominates, see [89].

The derivation in [87] is done by considering a magnetized plasma in Cartesian coordinates with the assumptions of:

- Cold ions.
- Isothermal electrons.
- Electrostatic conditions.
- No electron inertia.
- Quasi-neutrality.
- n has only a gradient along x, where B is in the direction of z.

The electron and ion momentum equations are linearized together with the electron and ion continuity equations. No background electric field is assumed. Perturbation of n, u_e and ϕ are assumed to be on the form $A\exp\left(i[k_x x + k_y y - \omega t]\right)$, where $A \in \{n, u_e, \phi\}$, the wavenumbers k are real, and the angular frequency ω is complex. One can assure oneself that positive $\Im(\omega)$ causes exponential growth for increasing t, and a positive $\Re(\omega)$ causes the perturbation to move along y as the inverse wavelength k_y stays constant. After simplifying the system algebraically, one arrives at the equation

$$\partial_x^2\phi(x) + \frac{\partial_x n_0(x)}{n_0(x)}\partial_x\phi(x) + \left(k_y^2 + \frac{\omega_{ci}}{\omega}\frac{\partial_x n_0(x)}{n_0(x)}k_y - \frac{\omega^* + ib\sigma_\parallel}{\omega + ib\sigma_\parallel}\frac{\omega_{ci}^2}{c_s^2}\right)\phi(x) = 0, \tag{13.1}$$

where ω^* is the diamagnetic frequency, $\sigma_\parallel$ describes the conductivity in the system and b measures the extent of the perturbation compared to ρ_s. These quantities are defined as

$$\begin{aligned}
\omega^* &\stackrel{\text{def}}{=} k_y u_{De} = -\left(k_y\frac{T_e}{eB}\frac{\nabla n(x)\times \boldsymbol{b}}{n(x)}\right)\boldsymbol{e}_y = k_y\frac{T_e}{eB}\frac{\partial_x n(x)}{n(x)} \\
\sigma_\parallel &\stackrel{\text{def}}{=} \left(\frac{k_z}{k_y}\right)^2\frac{\omega_{ce}}{\nu_{ei}}\omega_{ci} \\
b &\stackrel{\text{def}}{=} (k_y\rho_s)^2
\end{aligned}$$

Left handed coordinate system

Equation (13.1) can be solved as a second order boundary value problem by properly defining the boundary conditions. However, an analytical solution is sought, so the approximation $\partial_x^2\phi(x) \simeq \partial_x\phi(x) \simeq 0$ is used. This is essentially is a statement that the perturbations are infinitely long in the x-direction. The final analytic dispersion relation now reads

$$\omega^2 + i\sigma_\parallel\left(\omega\left[1+b\right] - \omega^*\right) = 0. \tag{13.2}$$

Equation (13.2) gives two solutions, where the solutions with the greatest growth rates can be written

$$\Im(\omega) = -\frac{b\sigma}{2}$$

$$
\begin{aligned}
&- \frac{\sqrt{\sigma}}{2}\left(16[\omega^*]^2 + \sigma^2\left[b^2+2b+1\right]^2\right)^{1/4}\sin\left(\frac{1}{2}\operatorname{Arg}\left[-\sigma\left(b^2+2b+1\right)+4i\omega^*\right]\right)\\
&- \frac{\sigma}{2} \qquad (13.3)\\
\Re(\omega) = &- \frac{\sqrt{\sigma}}{2}\left(16[\omega^*]^2 + \sigma^2\left[b^2+2b+1\right]^2\right)^{1/4}\cos\left(\frac{1}{2}\operatorname{Arg}\left[-\sigma\left(b^2+2b+1\right)+4i\omega^*\right]\right),
\end{aligned}
$$

where Arg is the complex argument function. We note that the maximum growth in eq. (13.3) is obtained where ω^* has a maximum, which corresponds to the position of the minimum in $\partial_x n/n$. Analytical expression for the dispersion relation in cylinder geometry is not easy obtainable as a Fourier decomposition in the radial direction will not make sense due to the lack of periodicity in ρ. Despite this, analytic expression can still be obtainable by decomposition into Bessel functions, as done in a similar system in [90]. As we would like to compare the analytic growth rates with what is found from the simulations, we will use eq. (13.2) in slab coordinates as a comparison. In slab coordinates we let

$$x \to \rho \qquad\qquad y \to \rho\theta.$$

The wavenumber in the y-direction, can in cylindrical coordinates be approximated as

$$k_y \simeq k_\theta = \frac{2\pi}{\lambda_\theta} = \frac{2\pi}{\frac{2\pi\rho}{m_\theta}} = \frac{m_\theta}{\rho}.$$

Some important differences in the dispersion relations when using the slab approximation for a cylinder geometry is given in [89]. This includes discrepancies in the trends for the critical B-field needed for the onset of instability, and the trend of how the instability scales with mode numbers. These discrepancies arise from how ρ enters the differential operators in cylindrical geometry, and how the wavelength changes due to the curvature of the circle. From this, we see that the slab approximation becomes better for higher mode numbers m_θ, as short wave lengths "sees" the curvature less than for long wave lengths.

13.3 Analytical growth rates and angular frequencies

A visualization of the growth rates and angular frequencies in slab geometry calculated from eq. (13.2) is given in fig. 13.3. In the calculations we have taken $\partial_\rho n/n$ from the steady-state. We have also corrected for the poloidal $\boldsymbol{E}\times\boldsymbol{B}$-drift by adding $\dfrac{u_{E,\theta}}{\rho_{\text{ at max}|\partial_\rho n/n|}}$ to $\Re(\omega)$[3].

Finally, a value for k_z is needed in order to calculate eq. (13.2). By inspecting the perturbations of the simulations, we find that $\lambda_z \simeq 2L_z$ (see for example figs. 13.2 and 13.4). This gives $k_z \simeq \pi/L_z$, which is used in the calculations. This wavelength is a consequence of the Neumann boundary condition on the density in both ends of the cylinder. Note that k_z may be much larger than the machine length as explained in [91].

In fig. 13.3a we can observe that the modes with maximum growth increase with increasing B. This is also found in the simulations (see fig. 13.4). For the angular frequency in fig. 13.3a, we see that the mode number with minimum angular frequency is the mode number of maximum growth rate minus 1.

[3] In the analytical derivation $\partial_\rho\phi$ is assumed to be 0 in order to simplify the derivations. Thus, a correction is needed as this term is non-zero in the simulations.

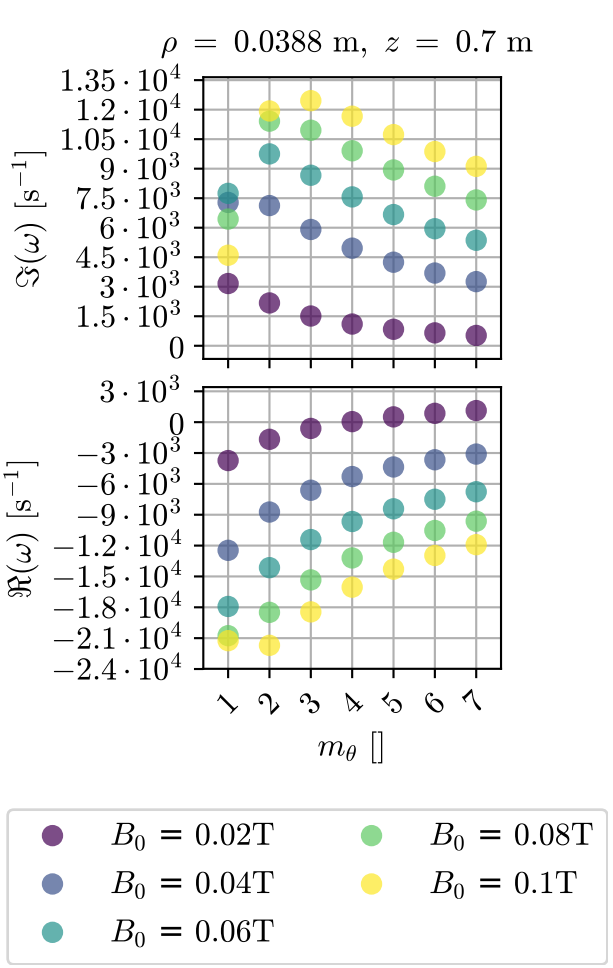

(a) Growth rates and angular frequencies obtained from eq. (13.2).

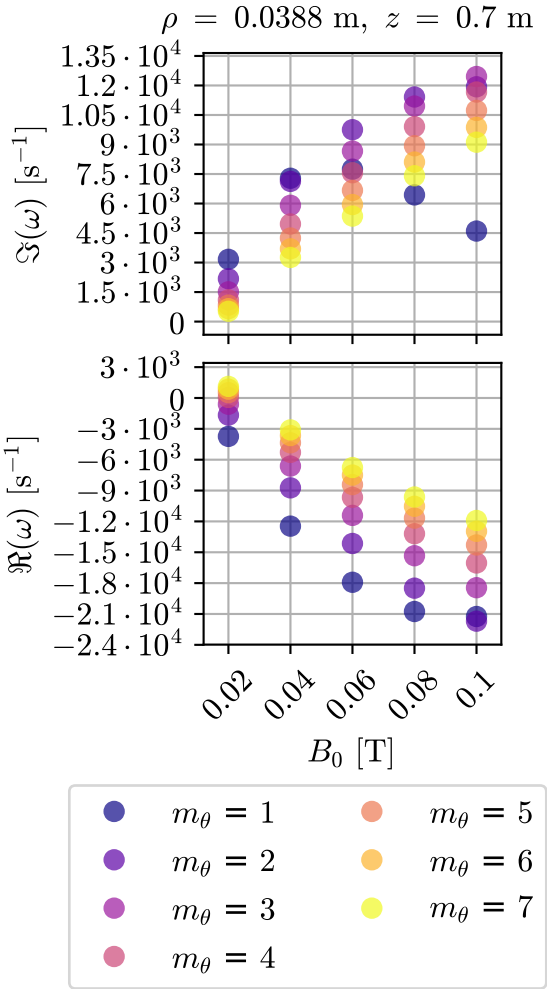

(b) Analytic growth rates and angular frequencies as a function of mode numbers.

Figure 13.3: Analytic growth rates and angular frequencies as a function of B_0.

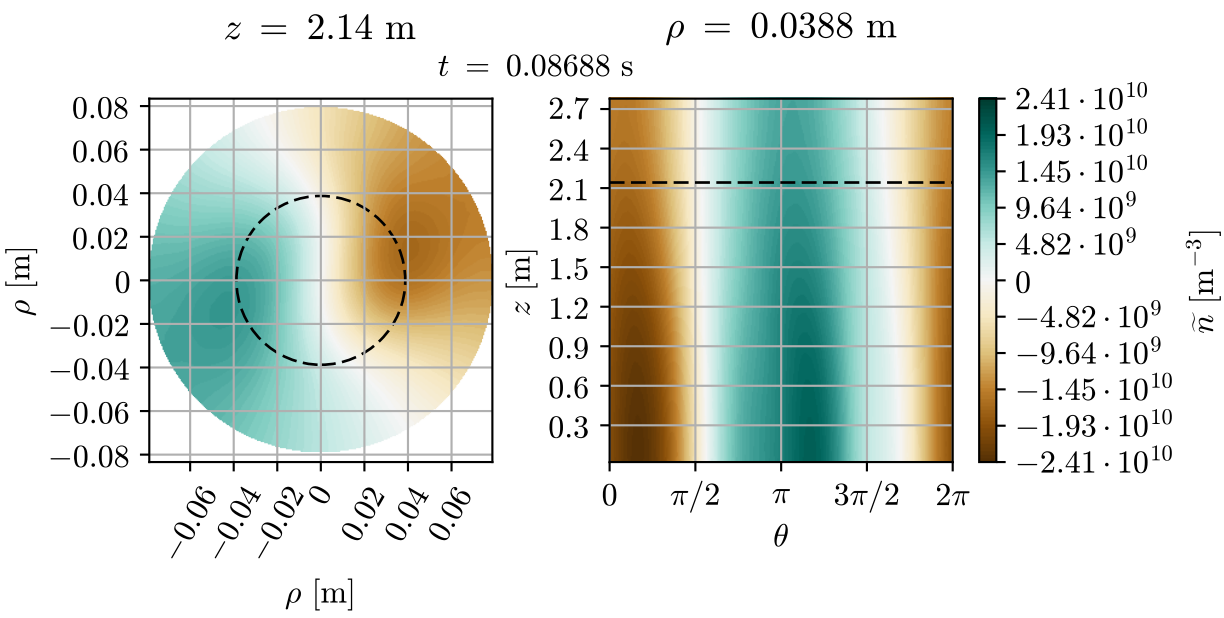

(a) $B = 0.02\ T$

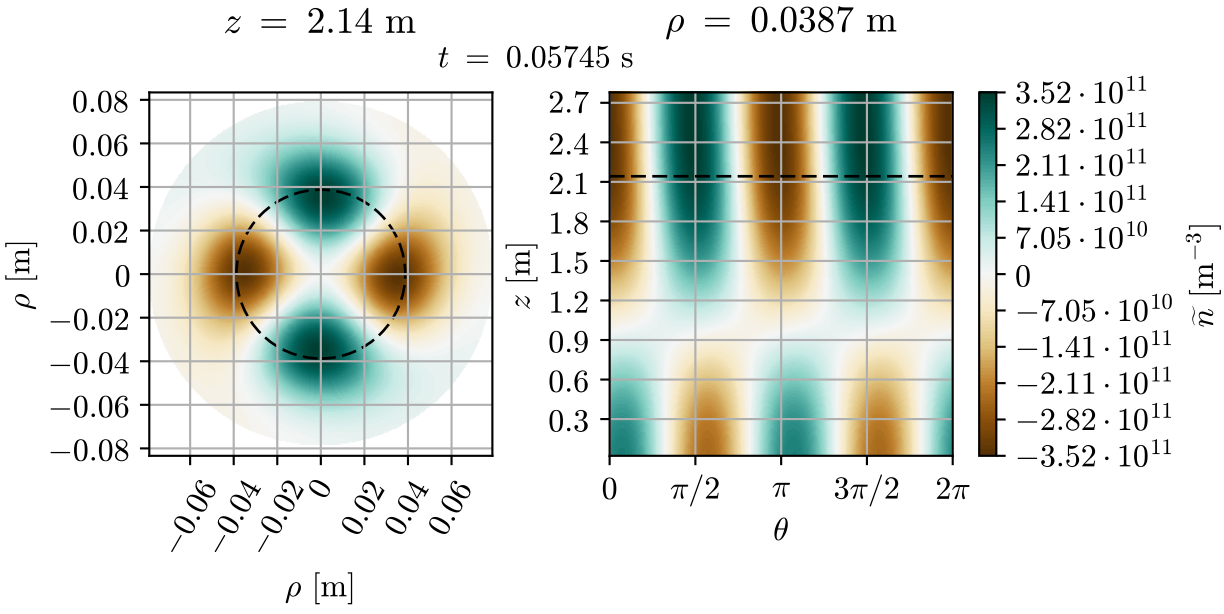

(b) $B = 0.04\ T$

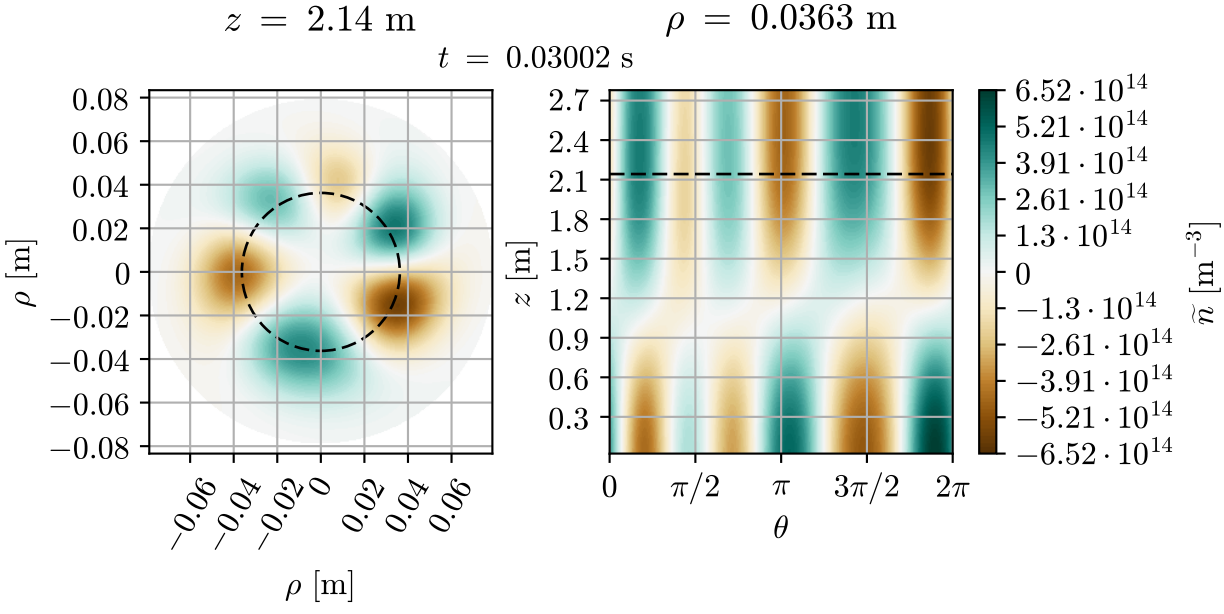

(c) $B = 0.06\ T$

Figure 13.4: The dominant mode depends on B. The B-field points into the paper, and the black dashed lines indicate the slicing of the opposite plot.

Figure 13.3a gives an alternative representation of fig. 13.3b. From fig. 13.3b we see that the growth rates of all modes are monotonically increasing with increasing B_0 (with an exception of $m_\theta = 1$). We can also observe that the angular frequency increases with increasing B_0. This might come as a surprise, as simpler models for the drift-wave predicts that $\Re(\omega) \propto \omega^* \propto 1/B$. This is true also for eq. (13.2) in the limit of large $\sigma_\parallel/\omega^*$ and small b, as pointed out in [87]. However, as shown in tables 13.1 and 13.2 this limit is not valid in our case, where $\Re(\omega)$ is increasing with B.

Variable	Values for $m_\theta = 4$ in the range $B_0 = 0.1 \rightarrow 0.02\,\mathrm{T}$	B_0-dependency
ω^*	$\sim -1 \cdot 10^5\,\mathrm{s}^{-1}$	$1/B$
b	$1 \rightarrow 27$	$1/B^2$
$\sigma_\parallel$	$6000 \rightarrow 275\,\mathrm{s}^{-1}$	B^2

Table 13.1: Values for ω^*, b and $\sigma_\parallel$ for $B_0 = 0.1 \rightarrow 0.02$ T and $m_\theta = 4$.

Variable	Values in the range $B_0 = 0.1 \rightarrow 0.02\,\mathrm{T}$
ρ at $\max\lvert\partial_\rho n/n\rvert$	$\simeq 0.037\,\mathrm{m}$
$\partial_\rho n/n$	$-38 \rightarrow -9\,\mathrm{m}^{-1}$
$u_{E,\theta}$	$50 - 125\ \mathrm{ms}^{-1}$

Table 13.2: Typical values for $B_0 = 0.1 \rightarrow 0.02$ T.

13.4 Growth rates and angular frequencies from the simulations

Growth rates and angular frequencies like those found in section 13.3 can also be obtained from the numerical simulations. From the individual time traces of the Fourier transformed modes of for example n, the growth rates can be extracted from the slope of the logarithm of the absolute value of the Fourier modes in the linear phase. The angular frequency can be found from

$$\Re[\omega_n(t)] = \frac{1}{T}\sum_{i=0}^{T-1} \frac{\mathrm{Arg}\left(\mathrm{FT}(n[t_{i+1}])\right) - \mathrm{Arg}\left(\mathrm{FT}(n[t_i])\right)}{\Delta t},$$

where T denotes the total number of time samples in the linear phase, and $i = 0$ denotes the first time point in the linear phase.

The time trace of the 7 first modes is depicted in fig. 13.5a. As the ordinate in fig. 13.5a is logarithmic, exponential grow will appear as straight lines. One should note,

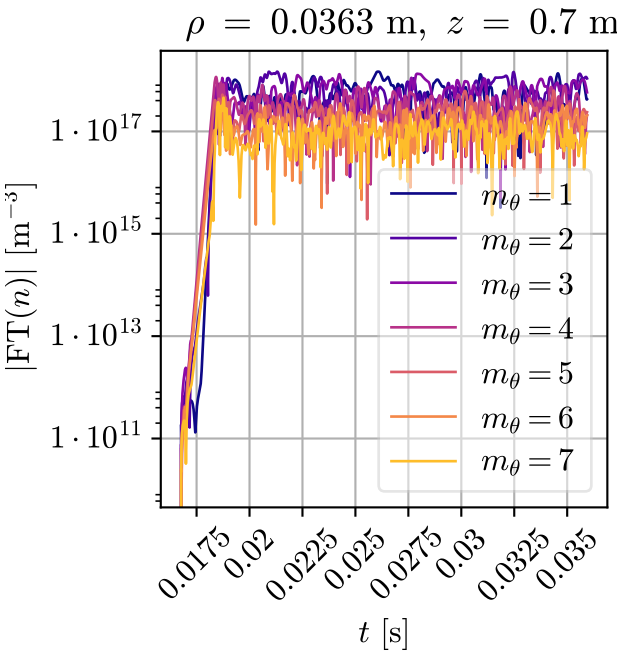

(a) Growth rate leading to saturated turbulence for $B = 0.1$ T.

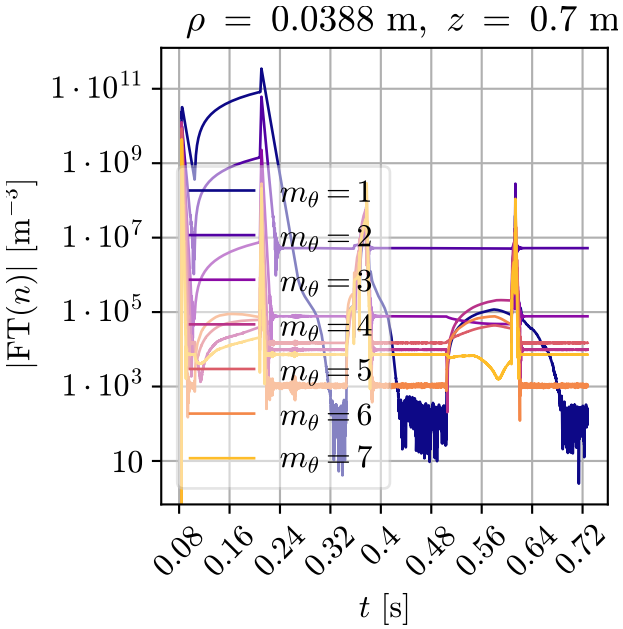

(b) For $B = 0.02\,T$ the system is stable against perturbation.

Figure 13.5: Time traces of the absolute value of the Fourier transform of the density in the periodic direction.

that contrary to what was found in section 13.3, $B = 0.02\,\mathrm{T}$ shows a decaying behavior[4] in fig. 13.5b. This can be explained by the viscosities, present in our model, but neglected in the derivation of the dispersion relation in section 13.2.

The growth rates and angular frequencies obtained from the simulations as a function of mode number is found in fig. 13.6a, where the error bars in the growth rates shows the spread in the linear fit, whereas the error bar in the angular frequency represents the standard-deviation. Both the trend and the values in fig. 13.6a matches approximately what was found in fig. 13.3a. However, the maximum growth rate is shifted to one higher mode number for all B-fields in the simulations. For lower values of B_0 the growth rates found in the simulation are less than what was found in the analytical expression. As a consequence, the growth rates for all mode numbers are negative for $B_0 = 0.02\,\mathrm{T}$. Likewise, the angular frequency is shifted to more positive numbers for lower values of B. Again $B_0 = 0.02\,\mathrm{T}$ shows an extreme behavior as it is rotating in the ion diamagnetic direction, opposite to the rotation of all the other B-fields. The mode number with the maximum negative rotation stays the same in both the analytic case and in the simulation case.

Figure 13.6a can also be visualized in a different way. In fig. 13.6b the B-field value is on the abscissa instead of the mode number. One can from figs. 13.3b and 13.6b observe that the agreement between the growth rates found in the simulation and growth rates found from the analytical expression are better for higher values of B_0. It can also be

[4] Although the time traces of fig. 13.5b shows a more complex behavior than simply growing or simplify decaying, we conclude that the mode is stable against perturbations as they remain small for all times. Every "attempt" of growth is followed by a rapid decay. The growth is observed if the mode stops rotating. A decay of the mode is observed when it starts rotating again. When the growth of the system is "flat" in fig. 13.5b, only noise is visible.

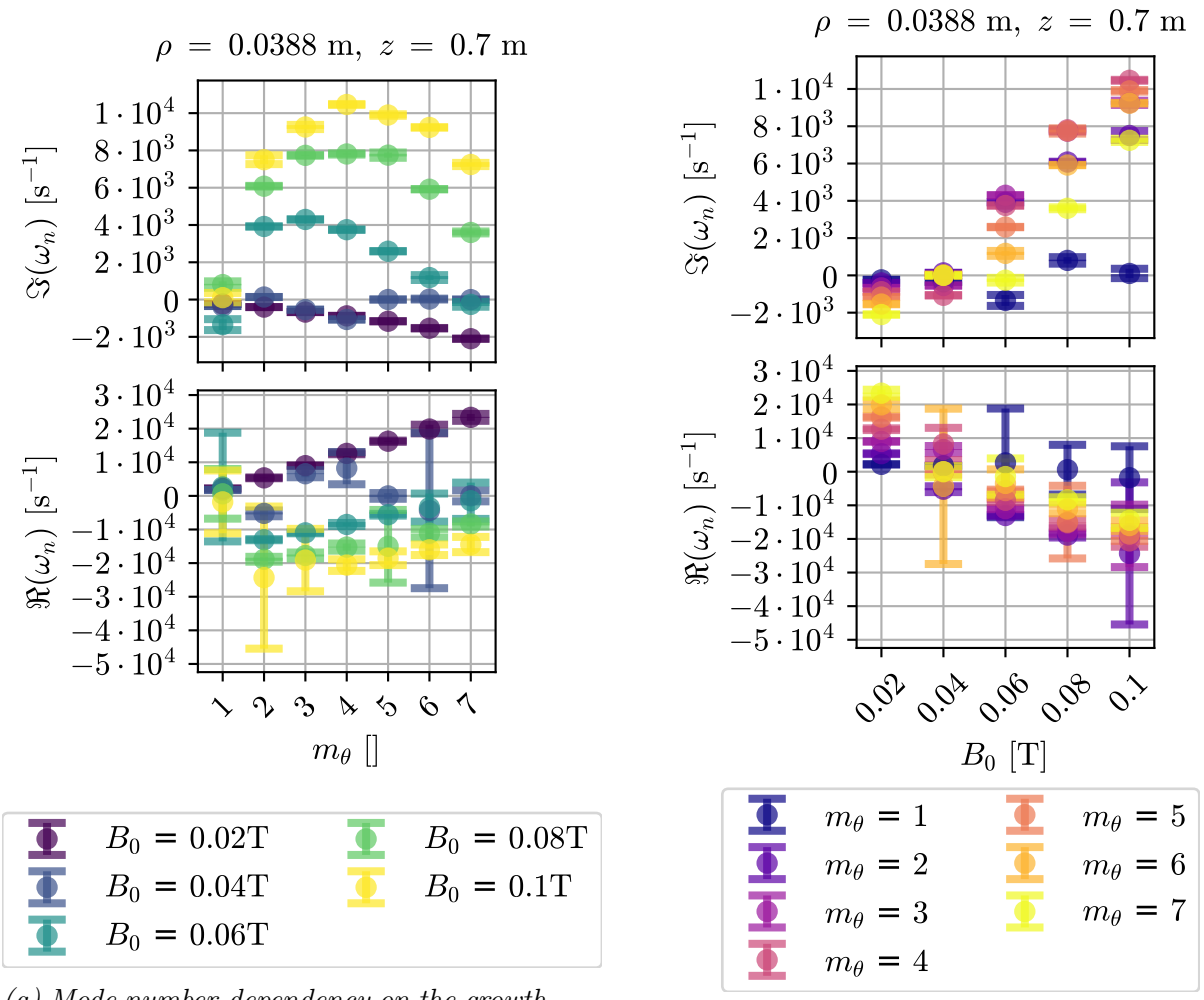

(a) Mode number-dependency on the growth rates and angular frequencies.

(b) B-dependency on the growth rates and angular frequencies.

Figure 13.6: Growth rates and angular frequencies obtained from the simulations.

observed that the angular frequency matches better for higher mode numbers. This is expected since the analytical expression was obtained from a slab geometry.

13.5 Phase shift

As explained in 13.2, the instability requires a certain phase shift Ψ between ϕ and n in order for the instability to occur. Here, we will investigate how the phase shift varies with the B-field.

As shown from the linear analysis in [87],

$$\Psi = \text{Arg}\left(\frac{\omega^* + ib\sigma_\parallel}{\omega + ib\sigma_\parallel}\right) \tag{13.4}$$

gives us the phase shift between n and ϕ for eq. (13.2).

We would also like to find the phase-shift between n and ϕ in the simulations. The simplest way to do so is to extract one mode of the time signal Fourier transformed in time, and get the phase shift from finding the angle between the imaginary and real part

for both ϕ and n. However, as shown in figs. 13.6a and 13.6b the standard-deviation of the frequency can be quite high, which means that the frequency can change a lot during the linear phase. The Hilbert transform could be used for finding the instantaneous phase-shift, but we will instead use a cross spectral density technique to give us the average phase-shift of the signals.

The cross spectral density can be found by first finding the cross correlation of the signals. In the cross correlation the signals are first shifted with a time shift τ with respect to each other. Excess parts of the signal will be padded with 0s in order for the signals to have the same length. The shifted signals are then multiplied and integrated over the time domain. The cross correlation is then given by

$$R_{n\phi}(\tau) = (n - \langle n \rangle_t) \star (\phi - \langle \phi \rangle_t),$$

where $(a \star b)(\tau) \overset{\text{def}}{=} \int_{-\infty}^{\infty} a^*(t) b(t+\tau)\, \mathrm{d}t$ denotes the cross correlation, and $a^*(t)$ denotes the complex conjugated. Note that the time average has been subtracted from the signals in order for the zero padding in order to make sense. The average time delay of the signals will therefore be the τ where the integral is the largest. As noted in [92], a positive $R_{n\phi}$ corresponds to a positive particle flux. In order to extract the phase-shift, we can Fourier transform $R_{n\phi}$ in order to get the cross spectrum density $S_{n\phi}$. As $S_{n\phi}$ is complex it can be written

$$S_{n\phi}(f) = \mathcal{F}[R_{n\phi}(\tau)] = |S_{n\phi}(f)| \exp\left(i\Psi(f)\right),$$

where $\mathcal{F}[R_{n\phi}(\tau)]$ denotes the Fourier transformed, and Ψ is the phase angle between n and ϕ. The dominating averaged phase shift will therefore be the Ψ corresponding to the largest $|S_{n\phi}(f)|$, and can as usual be found by $\Psi = \mathrm{Arg}(\Re[S_{n\phi}] + i\Im[S_{n\phi}])$.

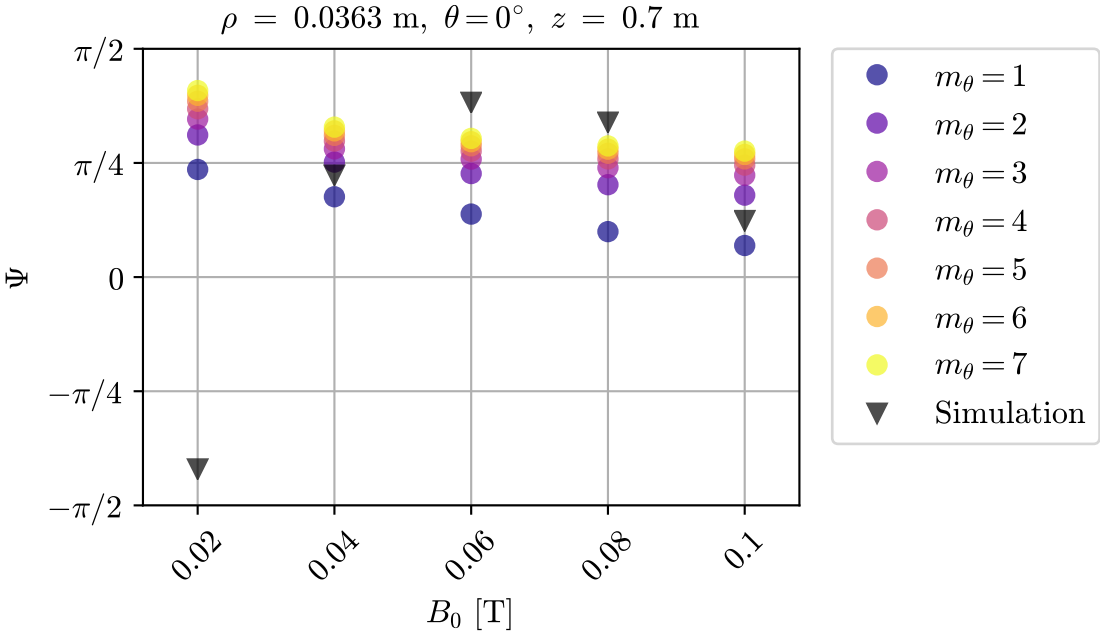

Figure 13.7: Phase shift as a function of B. The different modes are calculated from eq. (13.4)*, whereas the "Simulation" is the phase shift extracted from the simulations.*

Here, we will use the periodogram to estimate the cross spectral density from the discrete time series of n and ϕ. This corresponds to use a triangular window for the signals

(see [93] for details). The phase shifts from the simulations are shown in fig. 13.7 together with the phase shifts found from eq. (13.2). We note that a positive Ψ is equivalent to a growth of the instability [86], and a negative Ψ corresponds to a damping of the modes. Apart from $B = 0.02\,\mathrm{T}$ which were damped for all modes in the simulations, but had a small growth in the analytic expression, there is a qualitatively good match between the phase shifts in fig. 13.7.

13.6 Conclusion of the findings in the linear phase

We will now summarize our findings in the linear phase and draw some conclusions from this. In order to distinguish the drift-wave instability from for example the Kelvin Helmholtz instability (which shares many of the same characteristics with the drift-wave instability in terms of the dispersion relation), the points in the following list must be fulfilled [83, 94]:

1. $\widetilde{n}/n$ peaks approximately at the position of the absolute maximum of the density.
2. The perturbation has a finite parallel extension, typically in the order of the machine length.
3. The perturbations are propagating in the electron diamagnetic drift direction.
4. The density leads the potential.

From figs. 13.2 and 13.4 we can observe that point 1 is fulfilled. These figures also indicate that point 2 is fulfilled. Point 3 is fulfilled, with exception for $B_0 = 0.02\,\mathrm{T}$, as shown in figs. 13.2, 13.6a and 13.6b. Finally, one can observe that point 4 is observed in fig. 13.7.

From this we conclude that the instability under investigation is the drift-wave instability. The same conclusion has been reached for in VINETA in [37].

Chapter 14

The turbulent phase

The linear phase is succeeded by a transition phase to the saturated phase. In this phase, the linear modes become large enough for non-linear effects to affect the dynamics of the system. We will start this chapter by briefly explain how this interaction brings the system into the saturated steady state.

14.1 Transition to saturated turbulence

Through the non-linear interactions (in particular through the non-linear advective terms) energy from the unstable, growing modes spreads to neighboring modes in the k-spectrum. This can be seen around $t = 0.0175\,\mathrm{s}$ in fig. 13.5a, where $m_\theta = 1$ suddenly shows a growth with a higher growth rate than the rest of the modes. The transfer of energy can by studied through three-wave coupling under the assumptions that only neighboring modes in the k-spectrum interact (the weak turbulence assumption), and that four-wave and higher-wave couplings are negligible. This has been done in for example [95, 96].

The cascading of energy through the different modes is what eventually brings the system into a saturated turbulence phase. In an attempt to describe how this happens, an idealized case of fluid turbulence was considered by Kolmogorov and Oboukhov in their 1941 theory of turbulence [97]. The main assumptions of the theory is that the energy fed into the system in a narrow range of k, and that the dissipation of energy only happens at the smallest scales, which (in the k-spectrum) is well separated from the injection of energy. In other words, there will be a mechanism feeding the turbulence with structures of a certain size. These structures break up into smaller structures (the energy is cascading to higher k), which again break up into smaller structures, all the way until a viscous sink removes the energy from the system. The famous decay rate $\propto k^{-5/3}$ is then found for the energy through dimensional arguments.

If the system is constrained to two effective dimension, the system can display an inverse cascade of the energy [98]. This means that energy can be fed into the system at one range, and it will grow until some mechanism removes the energy at a macroscopic scale. The inverse energy cascade discussed in [98] is a consequence of the fact that the enstrophy (global integrated vorticity) and energy is conserved simultaneously. The analysis predicts a decay rate $\propto k^{-5/3}$ for the energy, and a decay rate of $\propto k^{-3}$ for the enstrophy. In the 2-D turbulence, structures are allowed to merge together and form larger structures as vortex stretching cannot occur in the system [99]. The analysis of the cascading property becomes complicated if dissipations are allowed in the system so

that the energy and the enstrophy is not conserved. It becomes even more complicated if the system is allowed to have some dynamics in the third dimension. In a quasi 2-D system, there is still is energy cascading towards the smaller structures. However, if the dynamics for some reason is constrained in one dimension, an inverse cascade of energy can be observed. For example can the Earth's atmosphere be considered as almost 2-dimensional as height of the atmosphere is small compared to the longitudinal and latitudinal dimension, and an inverse cascade of energy is observed in for example [100].

The turbulence in a plasma displays a more complex behavior than the turbulence in a neutral fluids due to more degrees of freedom through the electromagnetic forces. Despite this, the plasma turbulence shares many of the cascading properties found in neutral fluid turbulence. Although the decay rates vary, a cascading behavior from an initial range to a dissipative range is found. In addition, a 2-D cascading behavior can occur if the plasma is strongly magnetized as this introduces a dimensional anisotropy. Due to the magnetic field, the perpendicular displacement of fluid parcels is much more restricted than the displacement along the field lines. The 2-D turbulence in plasma physics arises naturally from models like the Charney-Hasegawa-Mima model [101] and Hasegawa-Wakatani [102], and has also been observed experimentally in linear machines [103].

The turbulence will reach a steady state once the input of energy through the source is balanced by the dissipation of energy. On the transition from the quasi-linear phase to the turbulent phase an overshoot in the energy is observed (see fig. 14.1). As a consequence the

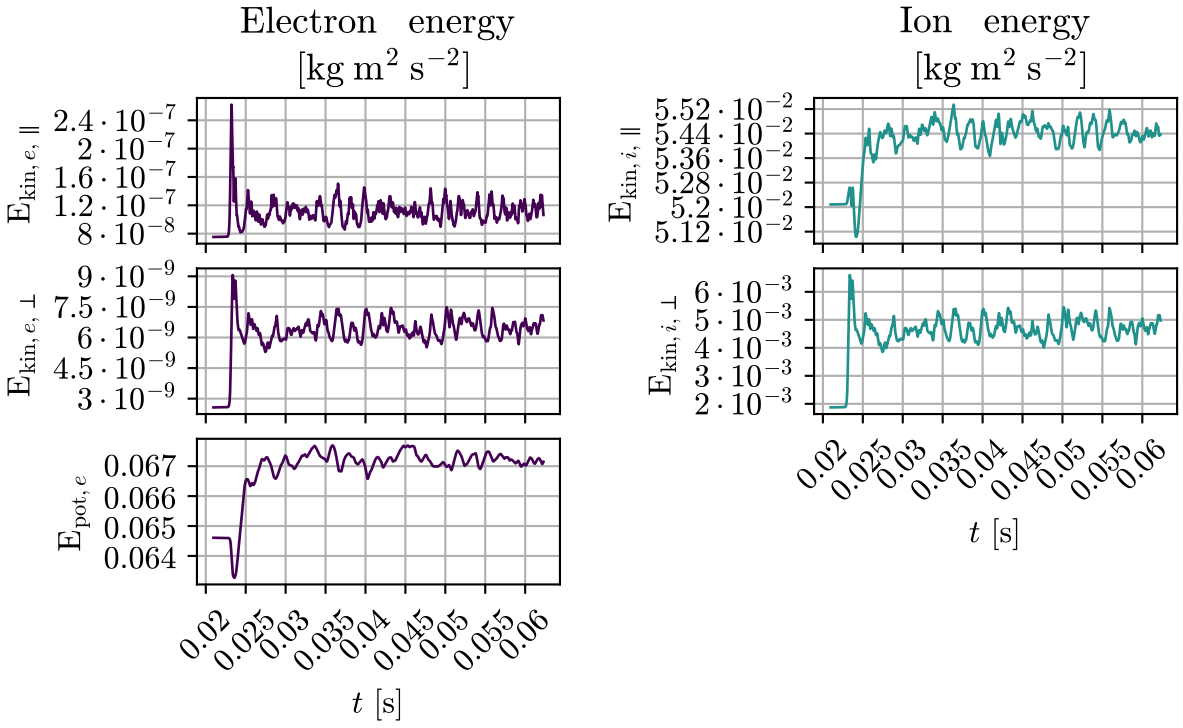

Figure 14.1: Time trace of the energy for $B = 0.08$ T.

eddies evolve at a faster pace at the transition as compared with the saturated turbulent state. In order to exclude the effects of the transients, we define the start of the saturated turbulence as sometime after the overshoot, around the time where the parallel ion energy is approaching the mean of the rest of the time series.

In the saturated turbulence state, the fluctuations are no longer in an ordered pattern as they were in the linear phase (as shown in fig. 14.2). The fluctuations in this state are

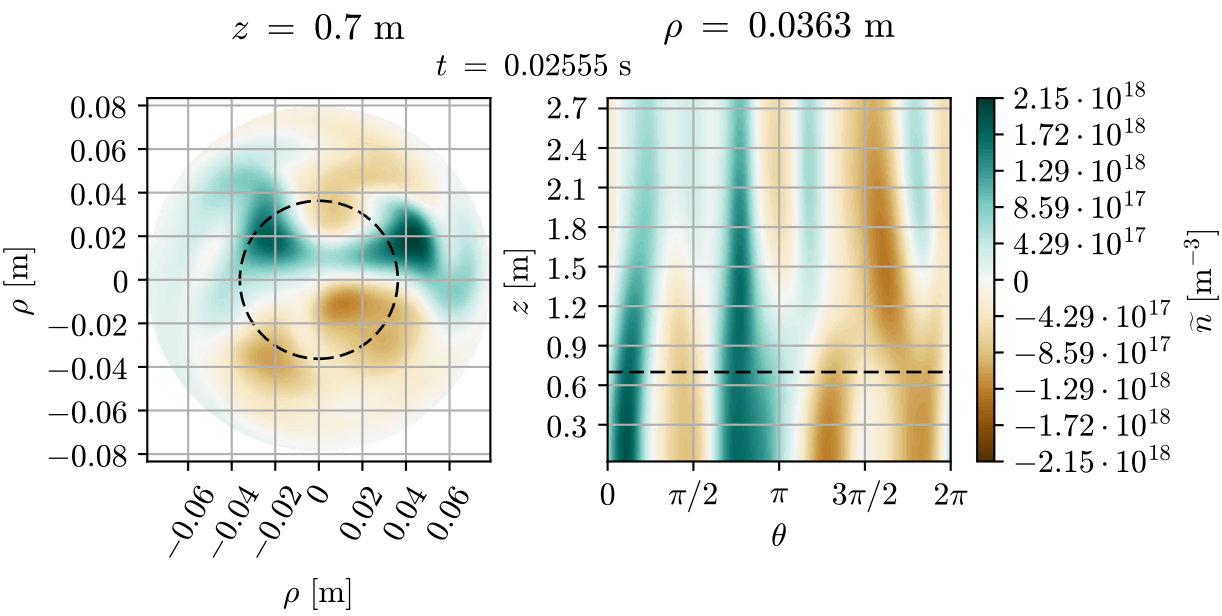

Figure 14.2: Fluctuations in the turbulent state for $B = 0.1$ T. The B-field points into the paper, and the black dashed lines indicates the slicing of the opposite plot.

big enough to push the bulk part of the plasma off-center as observed in the snap-shots of this state in fig. 14.3.

Finally, it is important to note that although there might be one dominating instability which causes the onset to turbulence, the characteristic of the turbulence is more or less independent of the onsetting instability. In other words, one cannot easily extract the cause of the turbulence by looking at the turbulence alone.

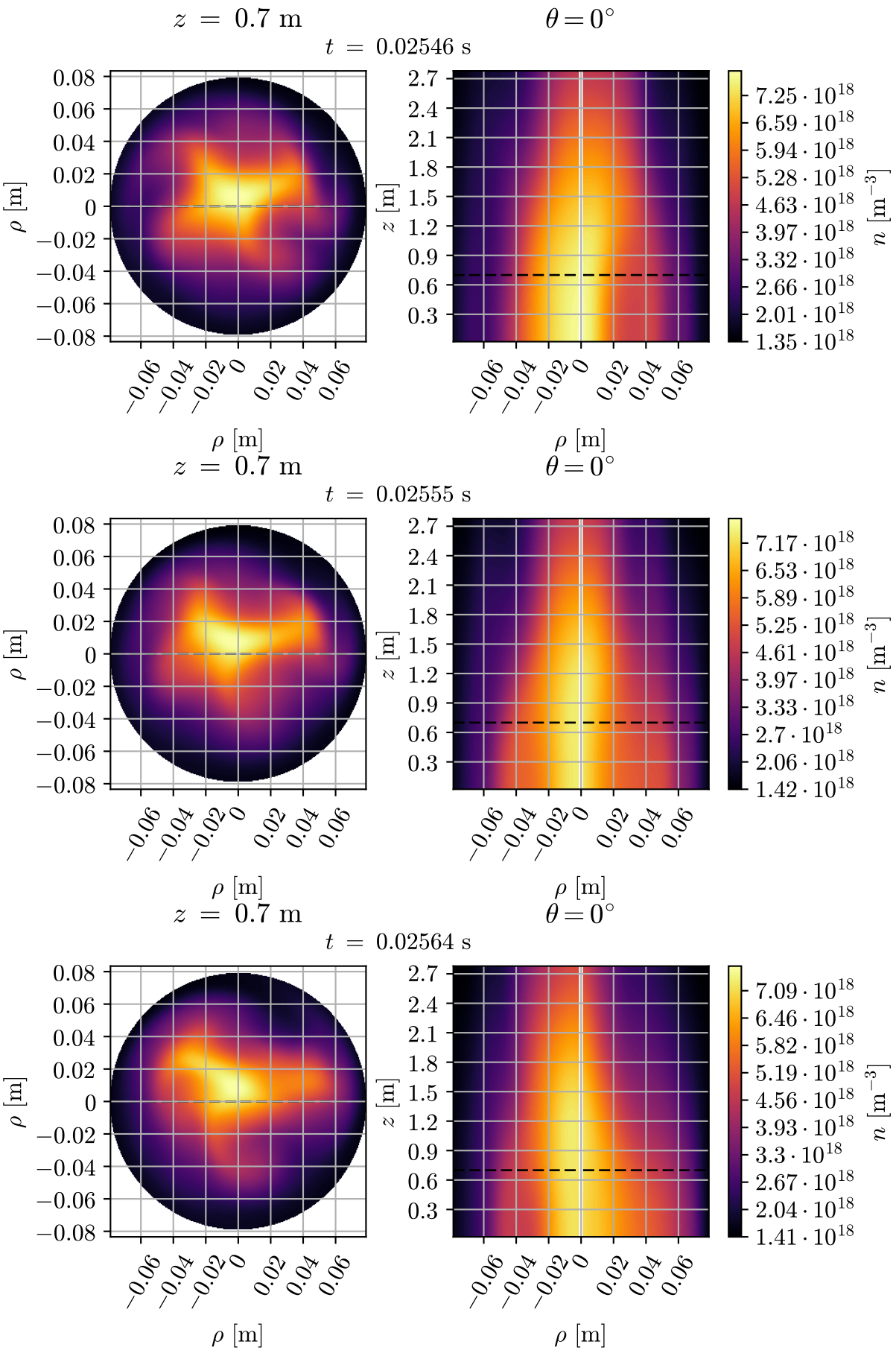

Figure 14.3: Evolution of the plasma in the saturated turbulence phase. Here shown for $B = 0.1$ T. The B-field points into the paper, and the black dashed lines indicates the slicing of the opposite plot

Chapter 15

Characteristics of the turbulent fluctuations

We will in this chapter characterize the fluctuations.

Fluctuation levels around 20% of n_0 are normal in the saturated turbulence state (see fig. 14.2). Strong fluctuation levels has also been observed experimentally (see for example reference [104]). The phase-shift between the fluctuations of density and potential gives rise to a radial turbulent flux. This radial flux will be discussed more in depth in section 15.1, but for now it suffices to say that if the radial flux approaches the levels of the parallel flux, the profiles will flattened as depicted in the two top-most plots in fig. 15.1. In the two bottom-most plots we can see that the largest fluctuations are found around

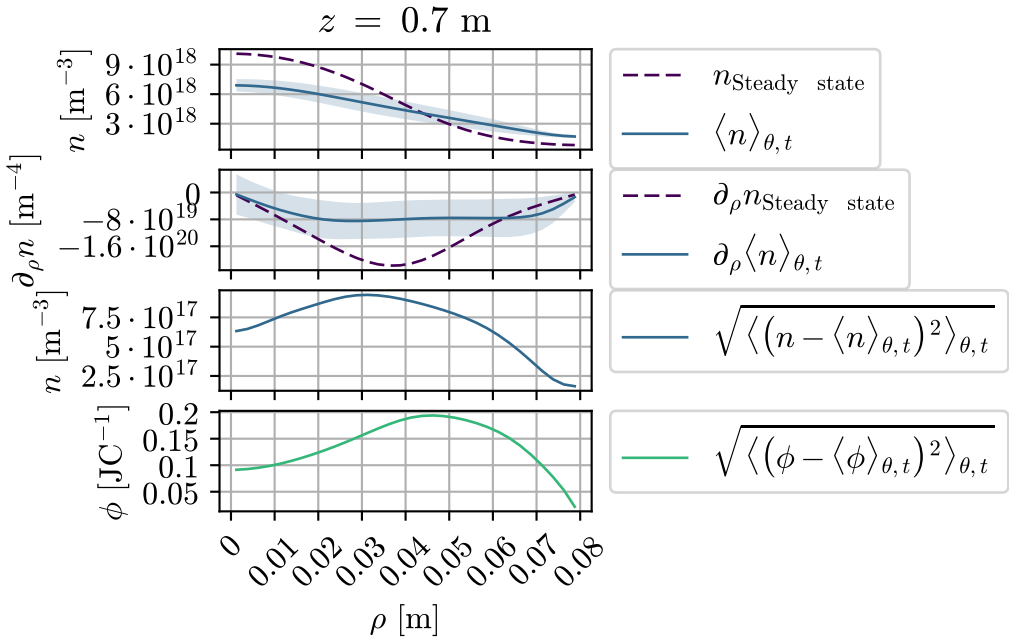

Figure 15.1: Flattening of the radial profiles together with the position of the fluctuations for $B = 0.1$ T. The subscripted $_{\text{Steady state}}$ denotes steady state variables, whereas variables without subscript denotes quantities in the saturated turbulence phase. A poloidal and temporal average (containing the whole time series) have been done in order to get a good averaged picture of the turbulent profile. The shaded area represents the standard deviation.

the maximum gradient. The flattening of the profiles is an important feature which need

to be considered when modeling the plasma.

In models like Hasegawa-Wakatani [105, 106], the fluctuations are separated from the mean (a so-called Reynolds decomposition). The model only evolves the fluctuation in time, whilst keeping the mean fixed as a static background. In such models, the free energy in the background gradients are driving the fluctuations, and the feedback of the fluctuation on the background profiles are neglected. This approximation is good if the fluctuations are small. On the other hand, if the fluctuations are large as in fig. 15.1, the background gradients are altered, and thus the drive for the fluctuations.

A global approach which doesn't uses the Reynolds decomposition is therefore needed. With the global approach, the change in the driving force for the turbulence is accounted for, and it enables one to investigate the back-reaction to the background from the fluctuations. Models like CYTO [74, 107, 108] and CELMA are using the global approach.

Further investigation of the turbulence can be done by investigating the fluctuations at a fixed point. This is done in fig. 15.2, where the time trace, the probability density function (PDF) and power spectra density (PSD) is shown at 3 different radial positions. We can observe that the fluctuations are large in amplitude, and increasingly intermittent

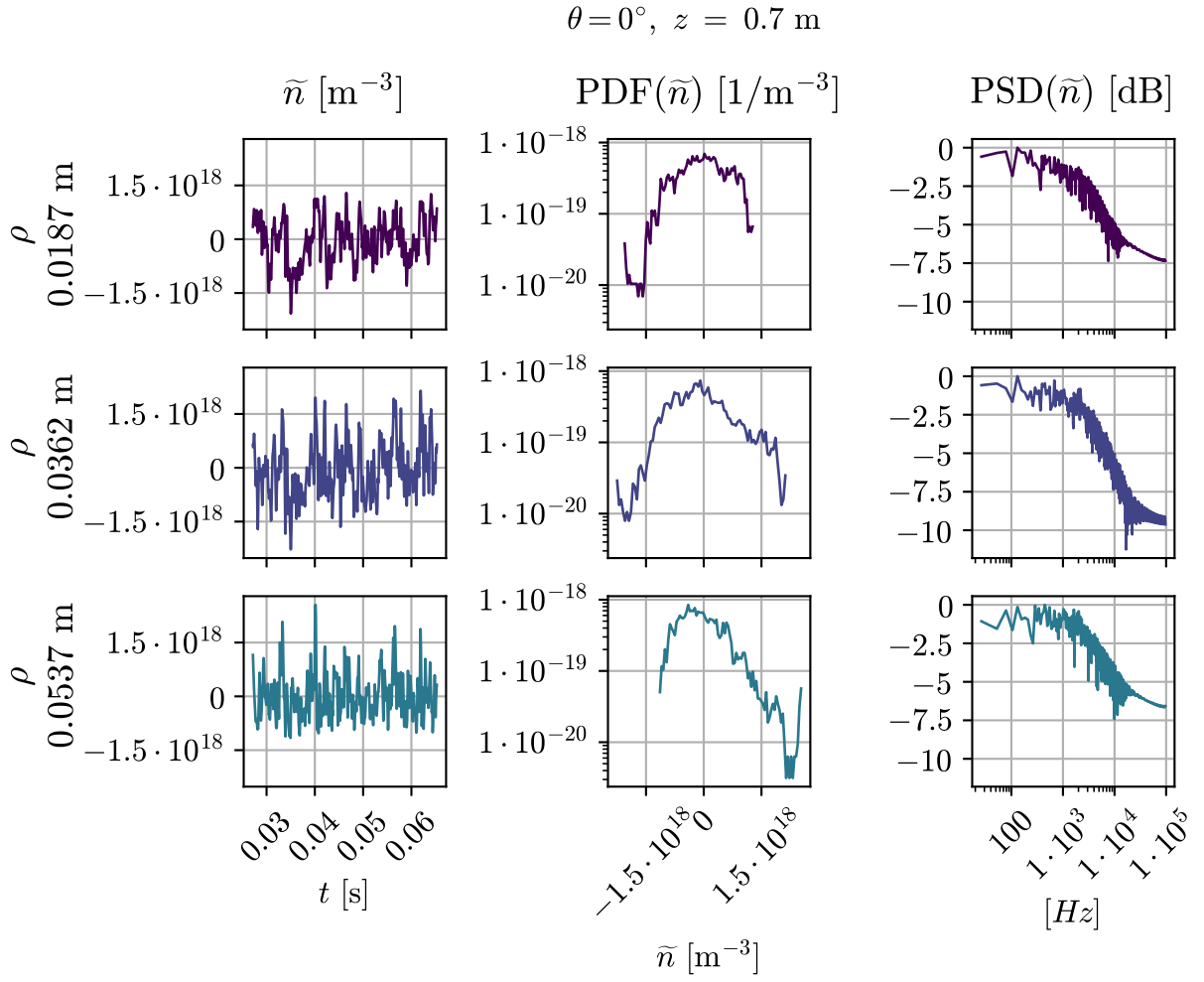

Figure 15.2: Characteristics of the time traces of the fluctuations at three radial positions for $B_0 = 0.08$ T. The top row shows data probed close to the axis of the cylinder, the middle row shows data probed at position of the highest density gradient, and the bottom shows data probed close to the edge of the plasma.

for higher radius. The power spectra density (PSD) shows that several frequencies are present simultaneously, and that the system is more turbulent at the edge (this is further emphasized in fig. 15.3). This behavior is captured by the probability density functions (PDF), which measures the chance to encounter a value within an infinitesimal range, if a value at a random time is withdrawn from the time trace. If the fluctuations are normal distributed, the PDF will have a Gaussian distribution. Deviations from the Gaussian distribution is usually measured by the statistical moments skewness[1] S and kurtosis[2] K, eventually the excess kurtosis K_E defined as

$$S = E\left[\left(\frac{X-\mu_X}{\sigma_X}\right)^3\right] \qquad K = E\left[\left(\frac{X-\mu_X}{\sigma_X}\right)^4\right] \qquad K_E = K - 3,$$

where E denotes the expectation value operator, μ_X the mean of the data X, and σ_X the standard deviation[3]. Figure 15.3 highlights how this varies with the radius.

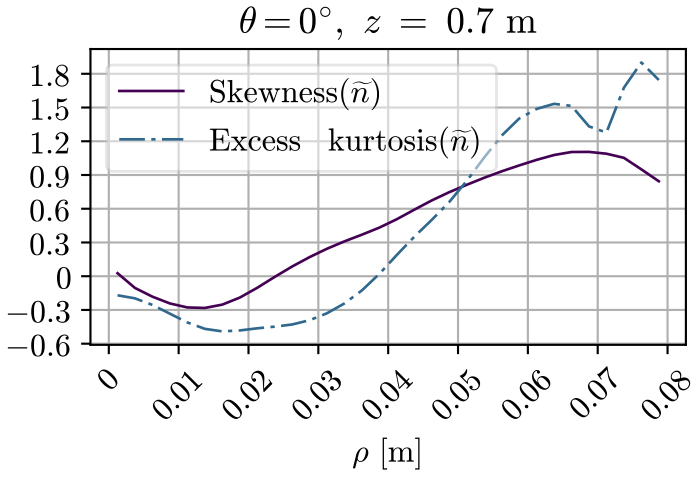

Figure 15.3: Radial variations of the skewness and excess kurtosis for $B_0 = 0.08$ T.

One can see that close to the center, it is more probable to encounter a negative fluctuation than a positive fluctuation. Then, for higher radii, large positive fluctuations become more and more frequent. From the excess kurtosis, we can see that extreme events are less likely than in a Gaussian random process, whereas extreme events are almost twice as likely in the edge as in a Gaussian random process. Similar foundings has been done at JET in [109].

We will proceed by investigating two of our observations further. First, from our phenomenological discussion in section 13.2, a large positive fluctuation in the density is not enough to give a positive flux (shown mathematically in [86]). A flux is only obtained when there is a phase shift between the density and the potential. Therefore, we would like to investigate the turbulent flux particle in the next section. After that, we will investigate the intermittency of the signal, and search for blobs and holes.

[1] The skewness is a measure of the mass of the distribution. If the skewness is negative, the left tail of the distribution is bigger than the right. For a pure Gaussian distribution the skewness is 0.

[2] The kurtosis is a measure of extreme events present in the distribution. For a pure Gaussian distribution the skewness is 3. If the kurtosis is less than 3 (platykurtic) the distribution produces fewer and less extreme outliers than a Gaussian distribution. If the kurtosis is greater than 3 (leptokurtic) there are more extreme outliners, and the tails approaches zero slower than a Gaussian distribution.

[3] We are assuming that the tail of the distribution are approaching fast enough to 0 in order for the moments to be defined.

15.1 Fluxes

The density flux (particles $\mathrm{m}^{-2}\,\mathrm{s}^{-1}$) in one point, such as the ones presented in fig. 15.2, tells us little about the total flux of particles out of the system. For example can a positive outflux in the point under consideration be outbalanced by a negative outflux in another point.

We will therefore integrate the density flux over a surface $\mathcal{S}$, which gives us the particle flux (particles per seconds). Naïvely, one could think that using the simulation domain as $\mathcal{S}$ would make sense. However, as we have enforced $\phi = 0$ at $\rho = L_\rho$, $u_{E,\rho} = 0$ as $\partial_\theta \phi = 0$ (see eq. (I.2)). As a side note, we note that very little plasma can escape the simulation domain radially as $\phi = 0$ and because the Neumann condition on the density at the outer radius gives a diffusion of $\partial_\rho^2 n \simeq 0$. Hence, almost all the plasma escapes in the parallel direction.

As we would like to investigate the radial turbulent particle flux, we therefore set the radius of $\mathcal{S}$ to be shorter than the radius where $\phi = 0$ enforcement starts, but still outside the main part of the particle source. The result is shown in fig. 15.4, and gives a comparison to the parallel density flux out of the simulation domain. In the

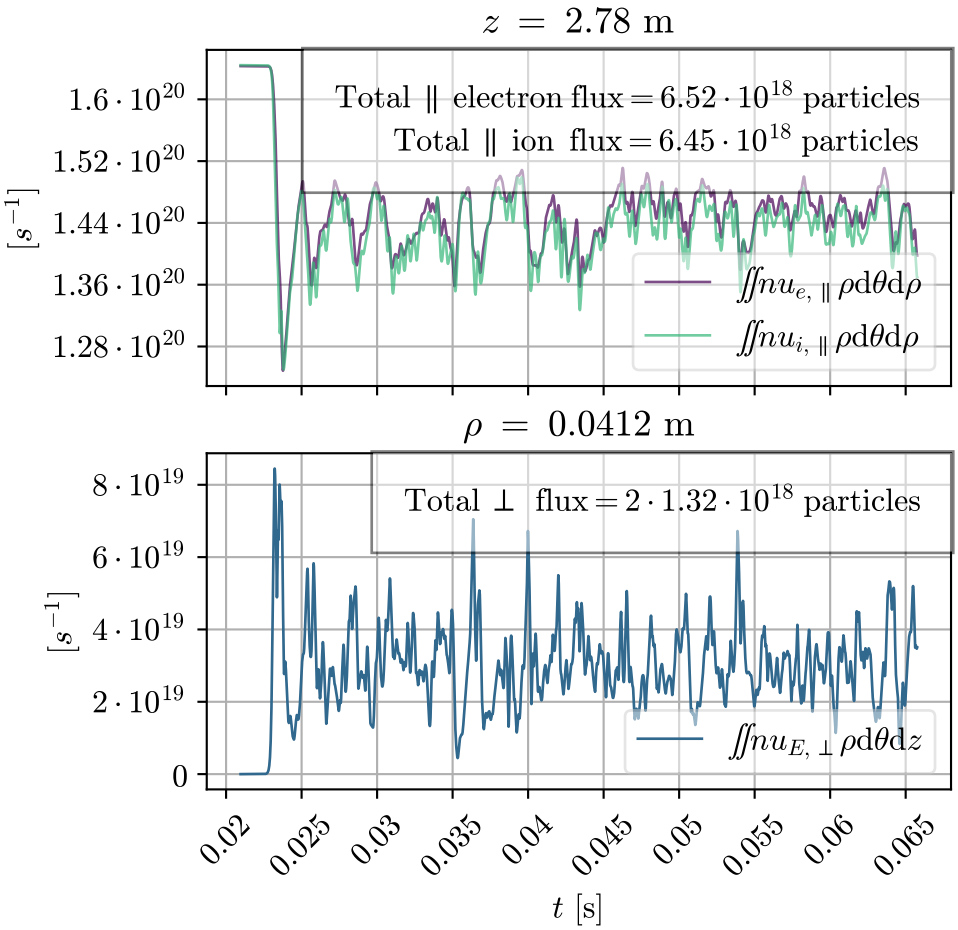

Figure 15.4: Integrated flux for $B = 0.08$ T

linear phase after 0.02 s, the radial flux is almost zero due to the small amplitudes of the fluctuations in the potential and density. An overshoot in the energy, just like the one seen in fig. 14.1 follows the linear phase. From that point in time the radial flux comes

burst-wise throughout the simulation.

Although the particles are not escaping the domain in the perpendicular direction, the total perpendicular particle flux through $\mathcal{S}$ is approximately 10% of the parallel flux out of the domain. We can also observe that almost as many ions as electrons are lost in the parallel direction (99%). Physically, this means that the plasma is charging up very little over time, and that the quasi-neutrality assumption is not broken.

15.2 Blobs and holes

The aim of this chapter is to characterize the intermittent structures observed in the time traces in fig. 15.2 by using a conditional averaging (CA) technique. It turns out that the intermittent structures shares characteristics with what has been described as blobs in the literature. We will here use the definition of a blob given in the review paper by D'Ippolito et al. [19]. In this definition, a blob is a structure which satisfies the following properties:

1. it has a monopole (single-peaked) density distribution with a peak value much higher than the surrounding rms fluctuations of the background plasma (typically $\geq 2-3$ times higher);
2. it is aligned parallel to the magnetic field B and its variation along B is much weaker than in the transverse direction, i.e., $\delta/L_{\|} \ll 1$;
3. it has a dominant convective $\boldsymbol{E} \times \boldsymbol{B}$ velocity component in the direction of a charge-polarizing force, and an associated potential and vorticity with a dipole structure in the direction transverse to its propagation.

Usually, the blobs observed in tokamaks are driven by magnetic field inhomogeneities through the so-called ∇B and curvature drifts. These drifts cause a charge separation, and the polarization is driving the blobs outwards through the $\boldsymbol{E} \times \boldsymbol{B}$ drift. The blobs in tokamaks are therefore self-propelled, and does not depend on local gradients of the plasma [110].

15.2.1 The conditionally averaging technique

The CA technique is often used to tell something about the average of coherent structures in turbulence. It has it roots in fluid dynamics [111], with the first application to plasma physics in [112]. Although improvements to the original technique has been done for e.g. noisy data recorded with a probe [113], we will use the simple, classic variant of the technique here:

1. Record a signal in a single point over time.
2. Set a threshold condition.
3. When the signal reaches the condition, record a sub-signal τ time units before and τ time units after. The recorded sub-signal will be one of the samples in the conditional averaging.
4. Take the average of all the samples, i.e. the recorded sub-samples.

Here, we will set the threshold condition on the radial flux. Alternatively, we could have set a condition on the perturbation in n itself. This would have the disadvantage of including samples of perturbation which arises from poloidal rotation of a slightly elongated plasma. In the end we are interested in structures which "has a dominant convective $\boldsymbol{E} \times \boldsymbol{B}$ velocity component" from point 3 in the definition of section 15.2.

15.2.2 The averaged structures

The time trace of the radial flux, together with three different conditions are shown in fig. 15.5. It is apparent that the trigger signal is highly intermittent, as seen from the

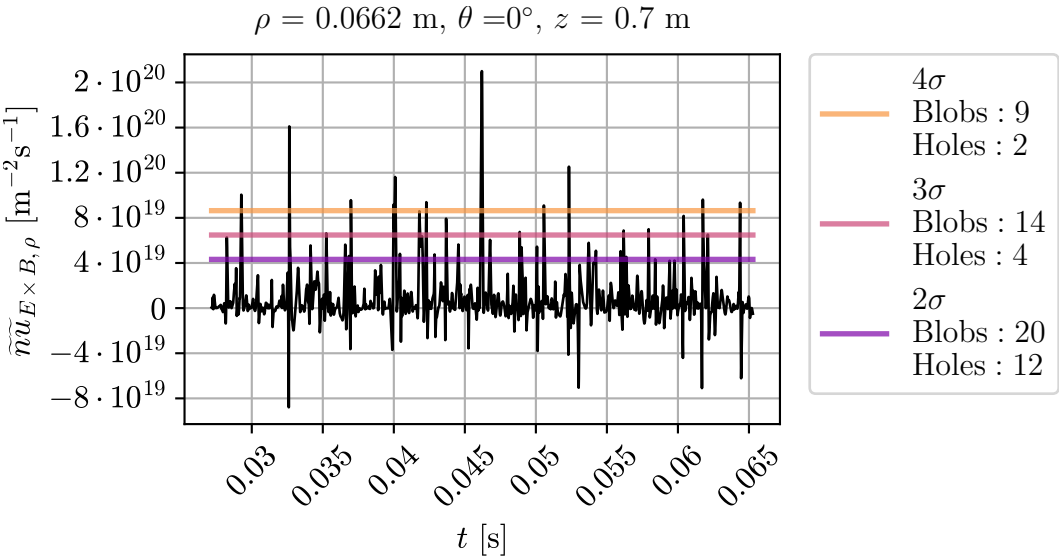

Figure 15.5: Time trace of the flux for $B = 0.08$ T. The trigger conditions for 2σ, 3σ and 4σ is indicated on the figure. The number of events found are indicated in the legend.

PDF in fig. 15.6a, which shows a skewness of approximately 3, and an excess kurtosis of around 16.7.

We now chose the time-window parameter τ to be 4 times the time of the maximum pulse duration (where the signal is above the threshold) of the flux[4]. From the flux signal we can now extract the times where the condition is met and its corresponding time-window. This can be used to sample any quantity in any spatial point. In other words, we can use these time-windows to conditionally sample the density n to search for blobs. Before doing so, we note that we are dealing with two types of events, both giving a positive radial flux. The events can either be:

[4]Note that it is usual to set τ to the autocorrelation time of the signal. However, as we would like to sample the densities given the trigger signal on the flux, we make the somewhat arbitrary choice of τ.

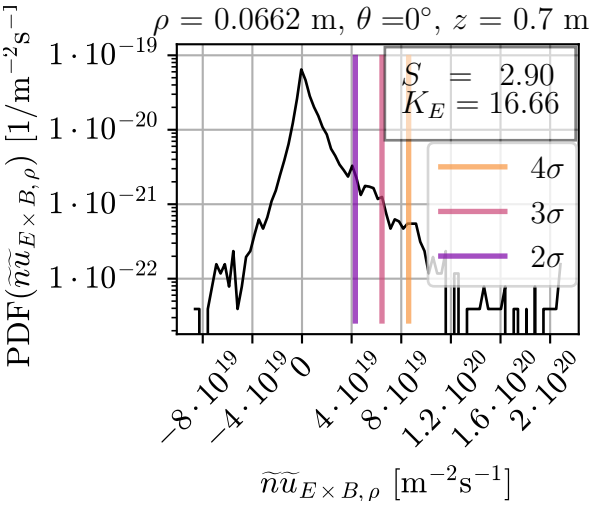

(a) The PDF of the radial flux.

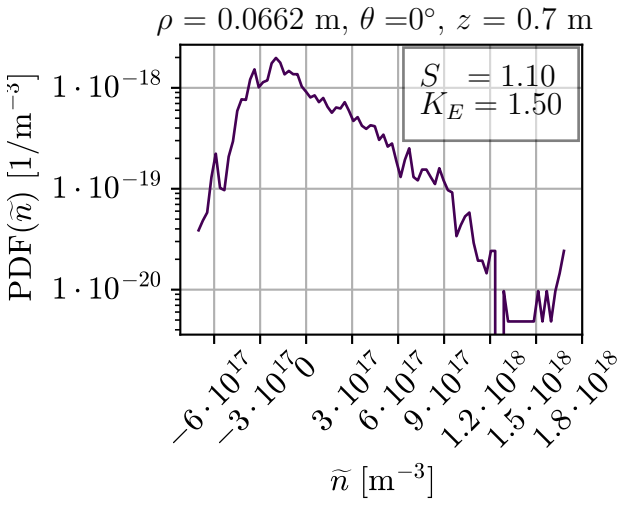

(b) The PDF of the density.

Figure 15.6: PDFs of the radial flux and the density measured in the same point as fig. 15.5 for $B = 0.08$ T. S indicates the skewness and K_E the excess kurtosis.

1. A blob: A positive perturbation propagating in positive ρ.
2. A hole: A negative perturbation propagating in negative ρ.

The time trace of the CA structures of both blobs and holes are shown together in fig. 15.7. Note that the amplitude of the blobs and the holes are relatively insensitive to the choice of

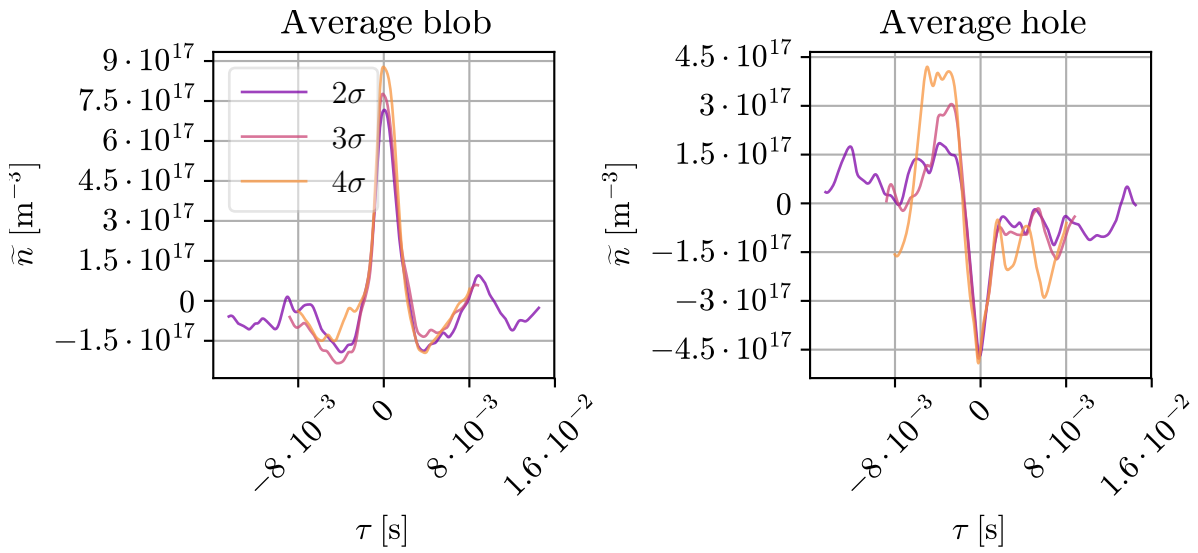

Figure 15.7: The averaged blob and hole density structures for $\rho = 0.0662\,m$, $\phi = 0°$ $z = 0.7\,m$ $B_0 = 0.08\,T$ found when using the trigger signal in fig. 15.5.

the condition. If we would set a condition on the same variable as we took the conditional average of, we would for a Gaussian white noise process have the relation [114]

$$\langle \widetilde{a} | a_* \rangle = a_* R(\widetilde{a}),$$

where we have used the notation

$$\text{Conditional average} = \langle \text{Signal to average} | \text{Trigger value} \rangle,$$

and where $R(\widetilde{a})$ denotes the normalized correlation function given by

$$R(\widetilde{a}) = \frac{(\widetilde{a} \star \widetilde{a})}{\langle \widetilde{a}^2 \rangle_t}.$$

However, it is unclear if the same holds when the CA is performed for $\langle n|\Gamma_* \rangle$ as the term contains a triple correlation[5].

One could be tempted to state that since the flux signal in fig. 15.6a is not Gaussian, the density signal must also be non-Gaussian, so we can conclude that the density signal is a result of coherent structures in the plasma, rather than an artifact of the conditional sampling technique. However, even if the both the PDF of the density fluctuations and the PDF of the $\boldsymbol{u}_{E\times B,\rho}$ fluctuations were Gaussian the product would not be Gaussian as shown in [116].

In order to tell if our structures are a consequence of Gaussian random noise, we must therefore look at the PDF of the density signal. The PDF of the density is shown in fig. 15.6b. With its skewness around 1 and an excess kurtosis of about 1.5 is not as intermittent as the radial flux, nor is it a Gaussian random process.

Instead of sampling the density at the same point as the condition is set, we can sample the whole perpendicular plane for the density fluctuations. Such a sample can also be made in experiments (under the assumptions that the experiments are reproducible) by fixing one probe for the triggering signal, and sweep another probe through the perpendicular plane, as done in for example [34]. The result is shown in fig. 15.8. Although we are setting the condition at the flux at $\theta = 0$, we can see that the blob start to form around $\theta = 3/2\pi$ at $\tau = -4.347\mu$s. The structure gets an associated potential dipole structure, which transports the structure radially outwards through the $\boldsymbol{E} \times \boldsymbol{B}$-drift. As the time evolves, the structure is also transported in the ion diamagnetic direction by the background flow set up by the background vorticity as shown in fig. 12.2. As the structure is transported radially outwards, it enters region with increasing background poloidal shear. This elongates the structure as seen at $\tau = 2.147\mu$s. After the shearing of the structure only background noise of the density and potential remains at $\tau \geq 4.347\mu$s.

One can now pose the question: "What mechanism is creating the associated potential dipole structure of the monopole density structure?". Obviously we have set the sampling condition on the radial flux, so the dipole structure may not be surprising. However, in blobs seen in tokamaks, the polarization of charge can be explained through the curvature and ∇B-drift. If we let $\boldsymbol{v}_\alpha$ denote the particle velocity for species α, these drifts are given by[6]

$$\boldsymbol{v}_{\mathcal{C},\alpha} + \boldsymbol{v}_{\nabla B,\alpha} = \frac{m v_{\alpha,\perp^2}}{2 q_\alpha B^2} \boldsymbol{b} \times \nabla B + \frac{m v_{\alpha,\|^2}}{q_\alpha B} \nabla \times \boldsymbol{b}, \tag{15.1}$$

where the charge separation comes about as q_α has opposite sign for electrons and ions. As the B field is homogeneous in our case, the drifts in eq. (15.1) cannot be the cause of the charge separation. Another possible candidate for the charge separation is the neutral wind, which gives rise to a charge separation through differences in the neutral temperatures [117]. However, as the plasma in the simulations presented in this chapter is fully ionized (i.e. no neutrals), we can rule out the neutral wind as a candidate for the charge separation.

[5] One could find out if the relation holds by generating a random synthetic signal of pulses of $\widetilde{n}$ and $\widetilde{\boldsymbol{u}}_{E\times B,\rho}$ and pack the pulses close enough together in order to make the signal Gaussian [115]

[6] For the equivalent drift in the fluid picture, see [30].

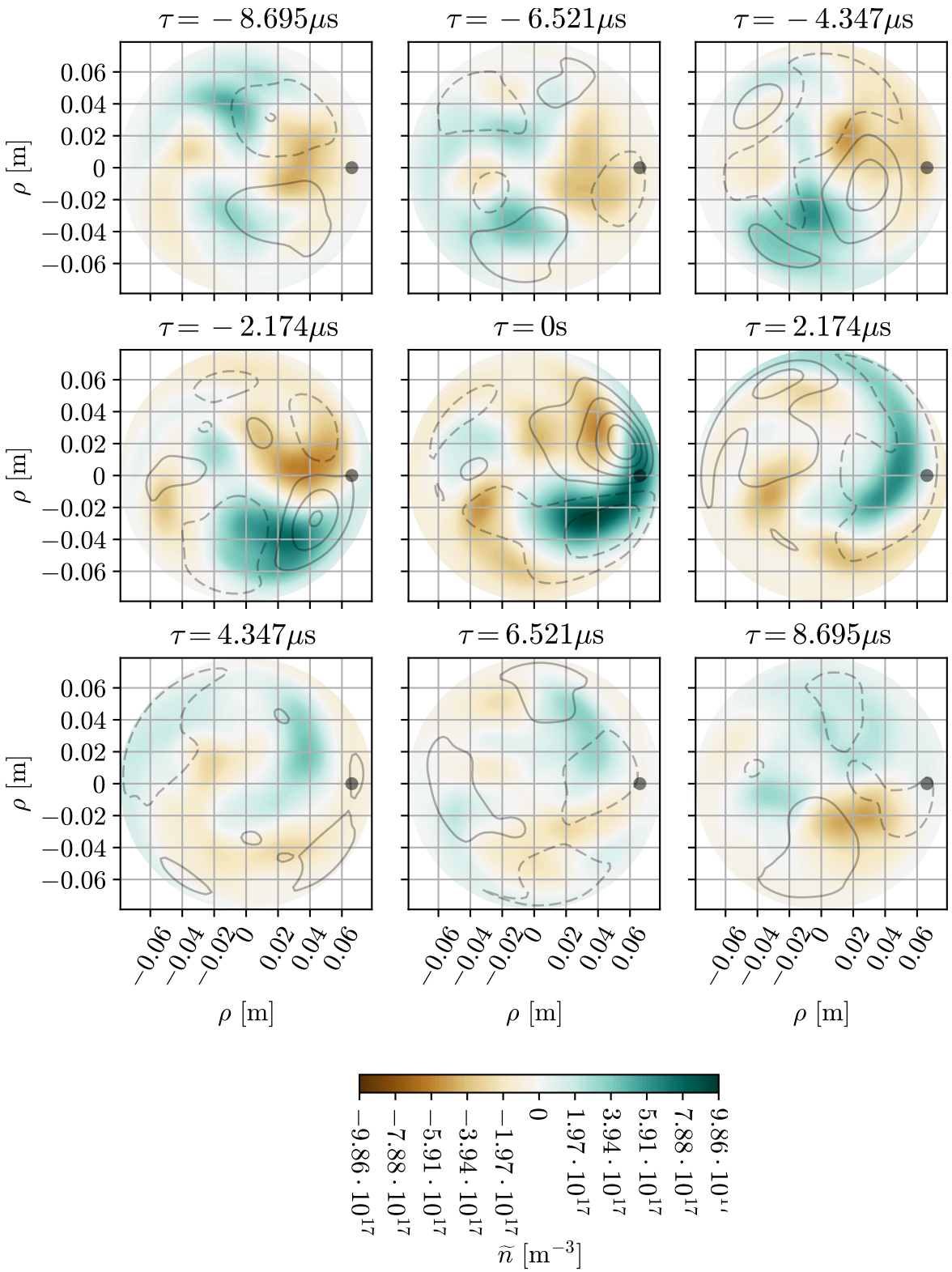

Figure 15.8: Perpendicular snapshot of a conditionally averaged blob at $z = 0.7$ m for $B = 0.08$ T. The color-map represents the density fluctuations, the contour lines the potential, whilst the black dot denotes the position where the trigger signal for radial flux is set to 3σ. The B-field points into the paper.

A possible candidate for the charge separation is the Kelvin-Helmholtz instability

[118, 119]. In a slab geometry, one can show that the linearized set of equations for this instability gives an eigenfunction for potential which consist of an alternating chain of positive and negative perturbations. This chain is slightly staggered in the radial direction, almost giving a dipole structure. It is therefore plausible that a positive and negative perturbation could approach each other by a turbulent perturbation, which would give rise to a potential dipole structure. Such radially propagating structures has been observed in for example [34].

15.2.3 Waiting times and pulse width distribution

Although we have few events[7], we would briefly indicate the trend of the waiting times and pulse width distribution. A similar exercise is done in for example [120], where it is found that the average temporal width of the pulse is a fraction of the period of a characteristic drift-wave, the peak of the waiting time PDF occurs approximately around one drift-wave period and the waiting time is much longer than a drift-wave period. The waiting time and pulse widths in our case is shown in fig. 15.9. As expected, the time widths shift to longer pulse widths as the pulses are larger as the triggering condition decreases. For the waiting time, it is hard to say whether the distribution is changed due to lesser counts for lower triggering conditions.

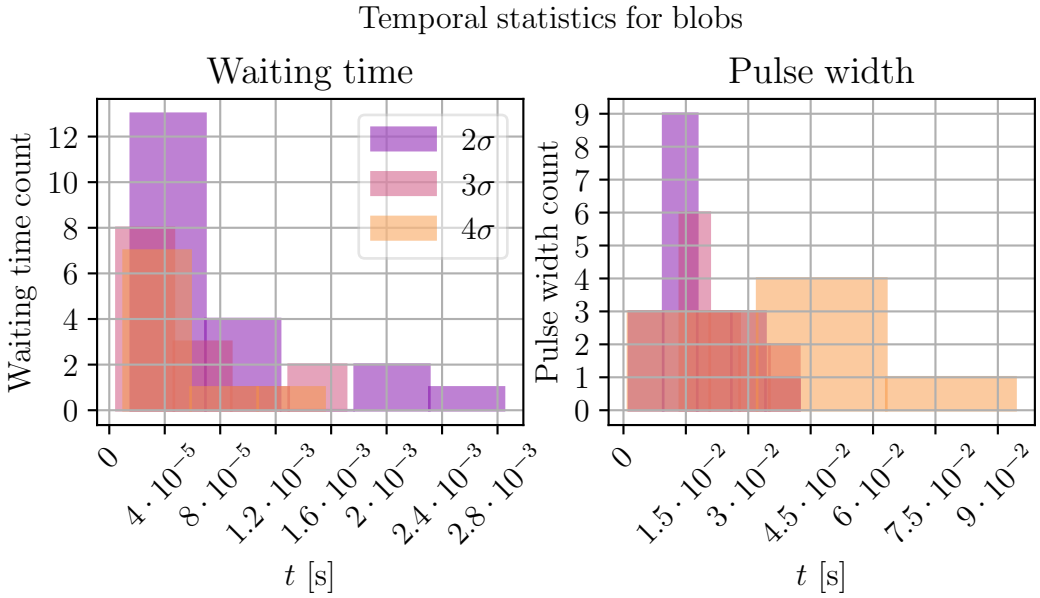

Figure 15.9: Waiting times and pulse widths of n for the conditional samples found for $B = 0.08\ T$.

[7] More events can be made by running the simulations for longer time. The only limit is relatively long simulation times together with large data files.

Chapter 16

Sheared poloidal flows

We will in this chapter discuss radially sheared poloidal flows with $m_\theta = 0$ in short. Such flows have gained a lot attention in the recent years due to its ability to suppress the turbulence transport through decorrelation of eddies, and is associated with transport barriers and the high confinement mode in tokamaks [121, 122, 123]. In plasma physics, one sometimes distinguish between a time fluctuating "zonal flow"[1], and a time stationary mean background poloidal flow.

The zonal flow can be initiated through a parametric decay of drift-waves to an $m_\theta = 0$ wave together with a modulation instability of the same waves [122]. Once initiated, it sets up a predator-prey relationship between the turbulence and the zonal flow. The turbulence drives a zonal flow which suppresses the turbulence. When the turbulence is suppressed the zonal flow is not fed, so it dies out. This means that the turbulence grows up, and the story repeats itself.

The mechanisms behind the time stationary flow can be found by investigating the force balance in the ion momentum equation[2]. From such a consideration, one find that a poloidal background flow can be created through a radial electric field generated by a strong radial ion pressure gradient, by a radial gradient in the Reynold stresses [3]and plasma rotation [121]. Notice that a poloidal mean flow may also develop if the radial boundary conditions causes gradients in ϕ. Reference [103] suggest that inverse cascading (through the Reynolds stresses) of the turbulent energy is a generation mechanism of their observed steady poloidal mean flow in a cylindrical device like the one we have simulated here. The shear is visible both through the radial profile of the velocity, and through a suppressed turbulence outside the shear visible from the radial power spectrum density.

It is therefore interesting to see whether such a poloidal mean flow is observed in our simulations. As we do not have accounted for the ion pressure in our model, a radial pressure gradient is ruled out as a candidate for any possibly observed poloidal flow. We can also rule out plasma rotation as we are looking at a linear device. Remaining candidates for poloidal flows are therefore Reynold stresses and the zonal flows and flows arising from the boundaries. The acceleration in poloidal flow can be found from the material time derivate of the vorticity, and yields [48]

$$\partial_t \langle \boldsymbol{u}_{E\times B,\theta} \rangle_\theta = \langle \partial_\rho \left(\widetilde{\boldsymbol{u}}_{E\times B,\rho} \widetilde{\boldsymbol{u}}_{E\times B,\theta} \right) \rangle_\theta .$$

[1]The term "zonal flow" is used in meteorology to describe atmospheric and oceanic circulation along latitudinal lines, such as those observed in Jupiter [124].

[2]The ions are investigated rather than the electrons as the momentum is mainly carried by the ions due to the mass difference.

[3]Stresses on the mean flow generated by turbulence. See [42] for details.

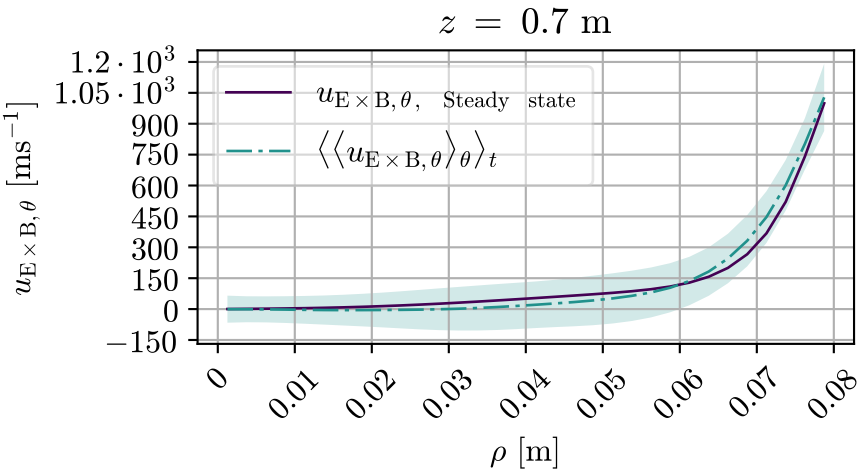

Figure 16.1: Poloidal velocity in the system for $B = 0.01$ T. The solid line represents the steady state, the dashed line the temporal and poloidal mean in the saturated turbulence phase. The shaded area represents the standard deviation found in the turbulent phase.

Figure 16.1 shows the radial poloidal velocity profile from our simulations. We can observe a strong poloidal shear at the edge of the plasma in the steady state. This is attributed to the strong potential gradient which is a result of our boundary conditions as mentioned in chapter 12. Although we found in chapter 15 the turbulence modifies the profiles, we can observe that the mean of the turbulence phase do not deviate much from the steady state solution (less than 10% at max). In other words the fluctuations in the poloidal velocity oscillates around the mean. Despite having poloidal velocity fluctuation levels in the orders of 10%, no large suppression of the density fluctuations observed in fig. 16.2. The spectral broadening is in qualitative accordance with what was found in [103], albeit a broader spectra was found in the reference. However, the shear and the resulting suppression of turbulence is not found in this work. This suggest that either a broader turbulence spectra is needed for the poloidal shear velocity to occur, that the ion dynamics which we have ignored is important, or it comes as a result of the differences between the numerical and experimental set-up.

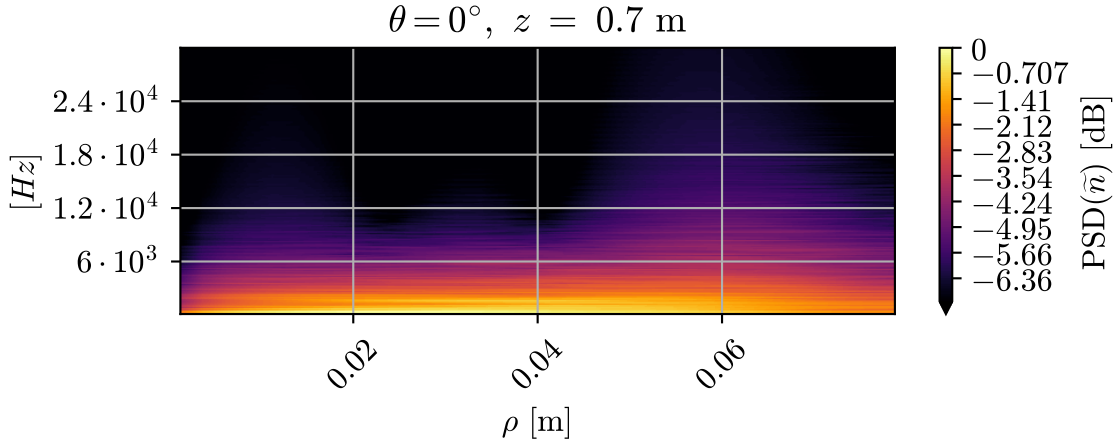

(a) $B = 0.06\ T$

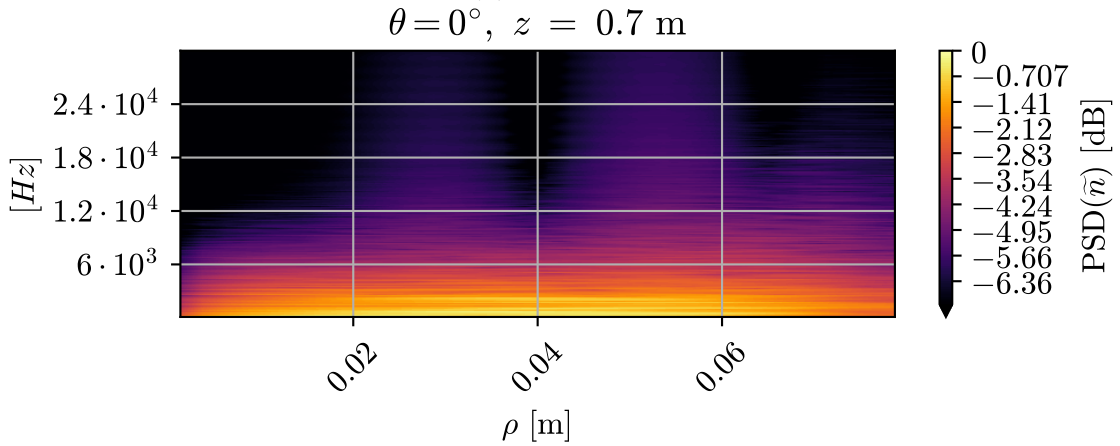

(b) $B = 0.08\ T$

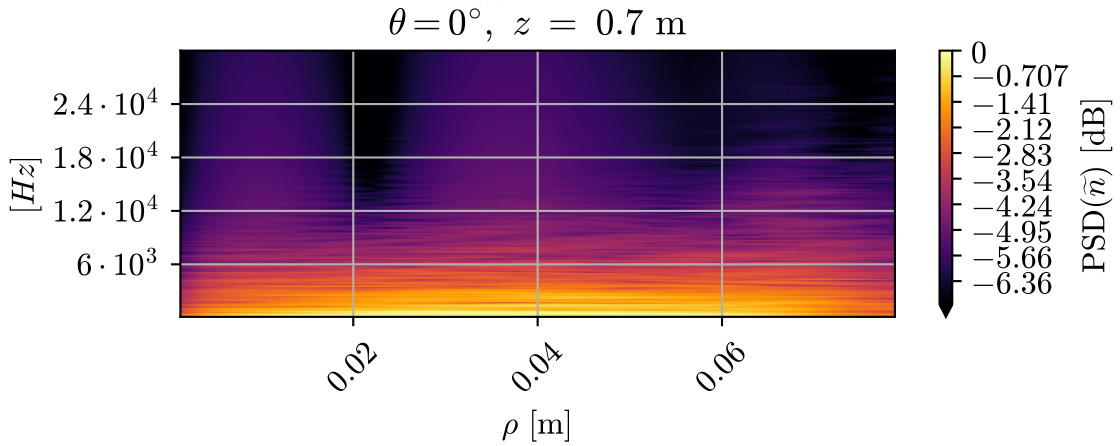

(c) $B = 0.01\ T$

Figure 16.2: Radial dependency on the power spectral density.

Chapter 17

B-field scan

We will here investigate how our results scales with B. In chapter 13 we saw how the linear growth rates depends on B. The comparison will be done by comparing the profiles in the steady state and the result from the saturated turbulent phase for different field strength B.

This is motivated by the experimental findings in linear machines, where one has observed a gradual onset of the turbulence with more and more modes interacting with an increasing B-field [125, 126, 104]. The saturation in form of singular modes has not been observed in the B-field scan. Instead, a threshold B_0 is found for the onset of turbulence (see fig. 13.6a). Therefore, only $B_0 = 0.06\,\mathrm{T} \rightarrow 0.1\,\mathrm{T}$ reaches the saturated turbulent state in the simulations. The simulations with $B_0 = 0.02\,\mathrm{T}$ is stable against the perturbation, and the simulations with $B_0 = 0.04\,\mathrm{T}$ has a very slow growth rate[1] . This is in qualitative agreement with what is observed in [104].

Finally, note that the normalizing B in eqs. (5.21) to (5.26) can always be chosen to be 1. However, B appears in the set of equations through ω_{ci}, which means that it effectively sets the time-step (in real variables) through $\breve{t} = t\omega_{ci}^{-1}$. This in turn affects the ρ_s (as $\rho_s = c_s/\omega_{ci}$), and thus the normalized domain size.

17.1 The steady state profiles

Figure 17.1 shows the parallel profile variations as a function of B_0. We note that n is increasing with increasing B-field. This can be explained by the increase in parallel velocities, which will be further explained in the discussion of the radial profiles. Although $j_\parallel \propto n$, we can observe that the absolute magnitude decreases with increasing B, signifying that the parallel electron and ion velocities are closer to each other. As a consequence, the parallel derivatives of $j_\parallel$ decreases, which in turn means that the absolute amplitude of the vorticity decreases. ϕ retains a Boltzmann-like distribution for all B-fields, which means that ϕ must decrease in the parallel direction as n decreases.

As indicated in the radial direction in fig. 17.2, ϕ is increasing with increasing B-field due to the Boltzmann-like distribution for each parallel position. Since the potential is fixed to 0 at $\rho = L_\rho$, we must have that the gradients gets sharper for increasing B-fields.

[1] It is expected that $B_0 = 0.04\,\mathrm{T}$ eventually will reach the saturated turbulent state as the growth rate is positive. However, as the maximum growth rate of $B_0 = 0.04\,\mathrm{T}$ is about one tenth of the maximum growth rate of $B_0 = 0.06\,\mathrm{T}$, the simulations would be need to be run approximately ten times longer in order to reach the saturated turbulent state.

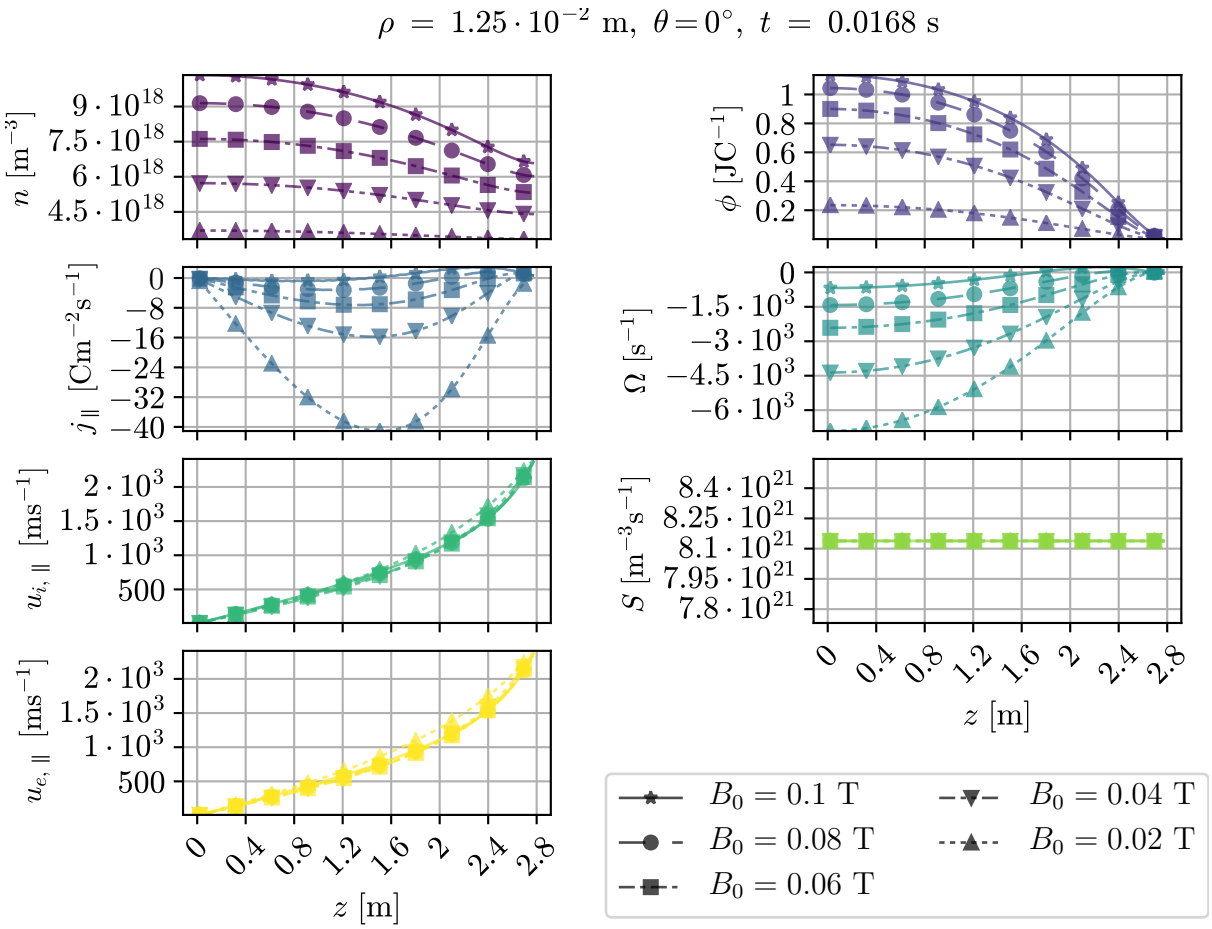

Figure 17.1: The parallel steady state profiles as a function of B_0.

This has the consequence that the vorticity gets higher for increasing B.

From this, we will here give an explanation for the observed increase in n for increasing B. As mentioned in section 15.1, almost no plasma can leave the domain in the perpendicular direction due to the boundary condition $\phi|_{L_\rho} = 0$ and shallow parallel second derivatives. Hence, we must find mechanisms in which the plasma can leave the domain in the parallel direction. We note that the in the parallel momentum equation, the right hand side to first order equals $-T_\alpha \nabla_\parallel n + n_\alpha q_\alpha \nabla_\parallel \phi$. As the parallel density gradients increases for increasing B field, the pressure term cannot account for the increased parallel outflux. On the other hand, the potential term can account for at least part of the increased parallel outflux. As the sign of this term depends on the species types, there will be less difference in this term for lower values of B, and since the system seeks a steady state the ions will slow the electrons less. However, as the decrease in $\nabla_\parallel \phi$ comes from the decrease in n with decreasing B, it cannot account for the initial depletion of density for decreasing B. Is it possible that this initial depletion can come from the fact that the systems searches for balance between the parallel currents and Ω in order to reach the steady state, and that the higher radial boundary value at Ω must be balanced by higher parallel velocities.

$n \propto B$ is also observed in helicon experiments, as stated by for example [103]. However, this trend in the experiments is more likely due to the coupling between the helicon wave and resonances in the plasma. Of course, higher confinement due to smaller Larmor radii is also contributing to this, but the contribution is believed to be small as the plasma

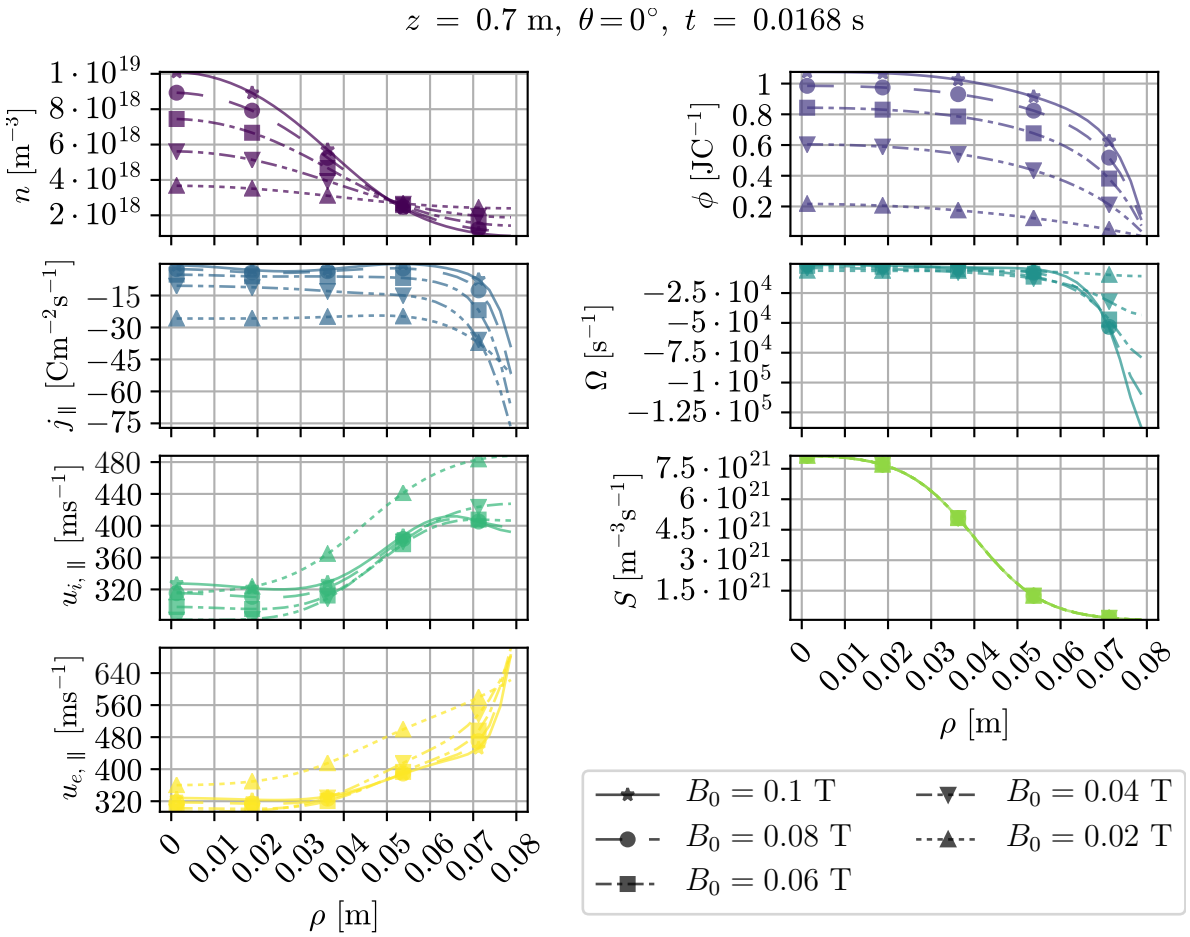

Figure 17.2: The radial steady state profiles as a function of B_0.

is lost at a higher rate in the parallel direction than in the radial direction due to high parallel velocities.

Finally, it is worth nothing that the artificial viscosity is kept constant in the normalized equations. This means that they will increase for decreasing B, as they are normalized with ω_{ci}. However, they are small compared with the other terms, and can therefore not account for the trend in n when the magnetic field strength changes.

17.2 Variations in turbulence

From what we discussed in section 17.1, it is intuitive to expect that the turbulence levels increases with increasing B as the gradients gets steeper, and can therefore act as a bigger source of energy to the turbulent fluctuations. That the turbulent amplitude is decreasing can be seen from the standard deviation of the time average of the poloidal average of n in fig. 17.3.

The position of the maximum fluctuation amplitude stays the same, whereas the maximum itself decreases for decreasing B. The same behavior is found in the potential fluctuations. Consequently, the density profiles are flattened for all B, but decreasing with decreasing B due to the lower amplitude of the fluctuations.

We can also investigate how the skewness and kurtosis is changing when varying B, by inspecting fig. 17.4. Note that these parameters does not say anything about

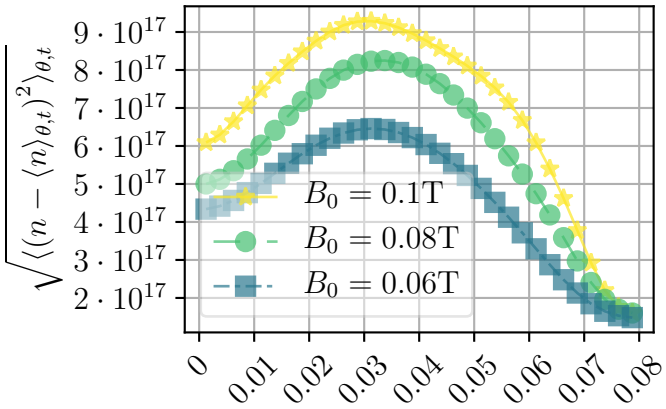

Figure 17.3: The standard deviation for the turbulent cases.

the amplitude of the perturbation, but rather how the probability of perturbations are distributed. We can observe that although the amplitude of the perturbations are changing, the distribution stays roughly the same, with exception of the edge of the cylinder, where the there is a higher chance for extreme events in the case of $B = 0.06\,\text{T}$. This does not necessarily mean that more "blobs" or "holes" are found, as the triggering signal is set for the radial flux.

The blob and hole count per time as a function of the magnetic field is given in fig. 17.5. One must be careful to say anything conclusive about this as very few events was found, as shown in table 17.1, but the decrease of the blob and holes count could be account for by the strong poloidal shear seen from the vorticity in fig. 17.1.

Field strength in [T]	Blobs count	Holes count
0.06	19	2
0.08	14	4
0.10	2	1

Table 17.1: The number of blobs and holes found from simulations with different field strengths.

Finally, in this section, we will address how the flux is scaling with the magnetic field strength. Figure 17.6 shows the trend. As discussed above, the increased electron and ion velocities will give rise to a higher parallel flux. Hence, we observe a decrease in the parallel flux for higher B. The converse is true for the perpendicular flux. This is consistent with what was observed in fig. 17.3, where the amplitude level increased with increasing B.

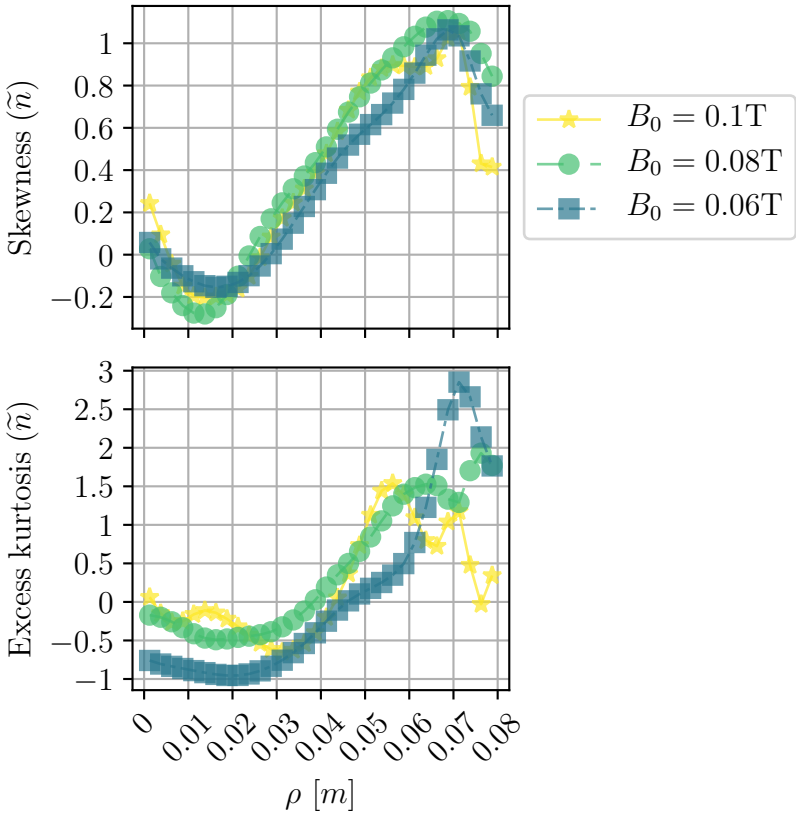

Figure 17.4: The skewness and kurtosis for the turbulent cases.

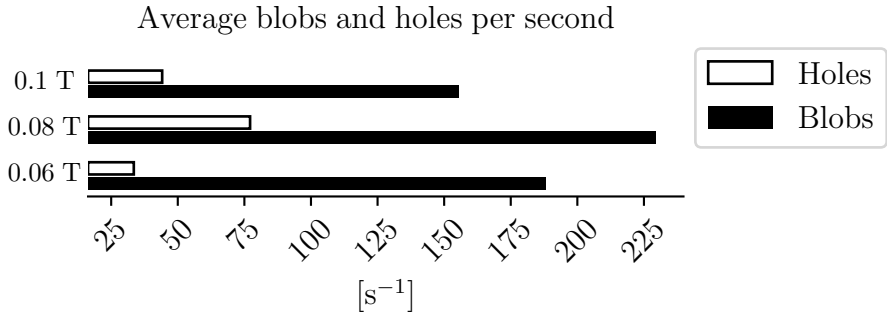

Figure 17.5: The blob count as a function of B_0 for a triggering signal of 3σ on the radial flux.

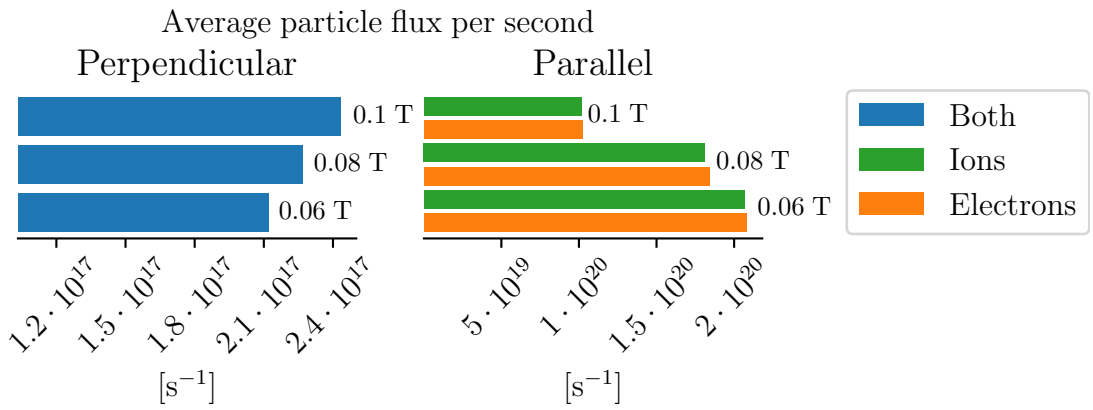

Figure 17.6: The total flux as a function of B_0. The point of measurement is the same as in fig. 15.4.

Chapter 18

Comparison with the Boussinesq approximation

In this chapter we will make a comparison between the simulation using the full set of CELMA equations (**C**ELMA-**F**ull, or simply CF), with the simulations using the Boussinesq approximation (**C**ELMA-**B**oussinesq, or simply CB). We will see that the missing n in the vorticity equation causes a difference in the parallel electron and ion flux, and that the energy will drift with time.

18.1 Steady state profiles

If we start by comparing the steady state profiles, we can first note that any difference between the CF and the CB model lays in the vorticity equation. The biggest difference between eq. (5.26) and eq. (6.2) is how the density factor in the compression of the density times the ion polarization term is treated. By using the Boussinesq approximation, we assumed that the mentioned n was the same as a flat background n_0. This n_0 then got normalized out, meaning that the n-dependency in this term disappeared. As a result, we ended up with a source term in the CB model not present in the CF model since this term got canceled with the source term from the density equation which we "smuggled" inside the d_t^E operator in the CF case. Finally, the $\boldsymbol{E}\times\boldsymbol{B}$ advection terms are different in the two cases. These differences affect both the background profiles and the fluctuations.

Hence, it should come as no surprise that the radial vorticity profile has changed. This is indicated in fig. 18.1, which shows the difference between the CF and CB simulation for $B = 0.1\,\mathrm{T}$. As the radial vorticity profiles changes, it will lead to changes in the radial potential profile[1]. The radial density profile stays roughly the same for the CF and CB case, which will be discussed in further detail below. For the radial profile of the parallel currents we can observe that the CB case gives slower velocities when $\rho \to L_\rho$ This, in turn, makes small changes in the radial parallel current profile, but gives a more shallow approach as $\rho \to L_\rho$.

On the other hand, the parallel $j_\parallel$ profile has changed, as seen in fig. 18.2. First of all, the see-sawing seen in the non-Boussinesq case seem to have disappeared. Although the oscillating patterns in the parallel current is still there, they are much less pronounced

[1] One could say that it is the potential which determines the vorticity through $\Omega = \nabla_\perp^2\phi$, but since we are evolving the vorticity in time we are instead inverting the equation for ϕ. In that respect Ω determines ϕ.

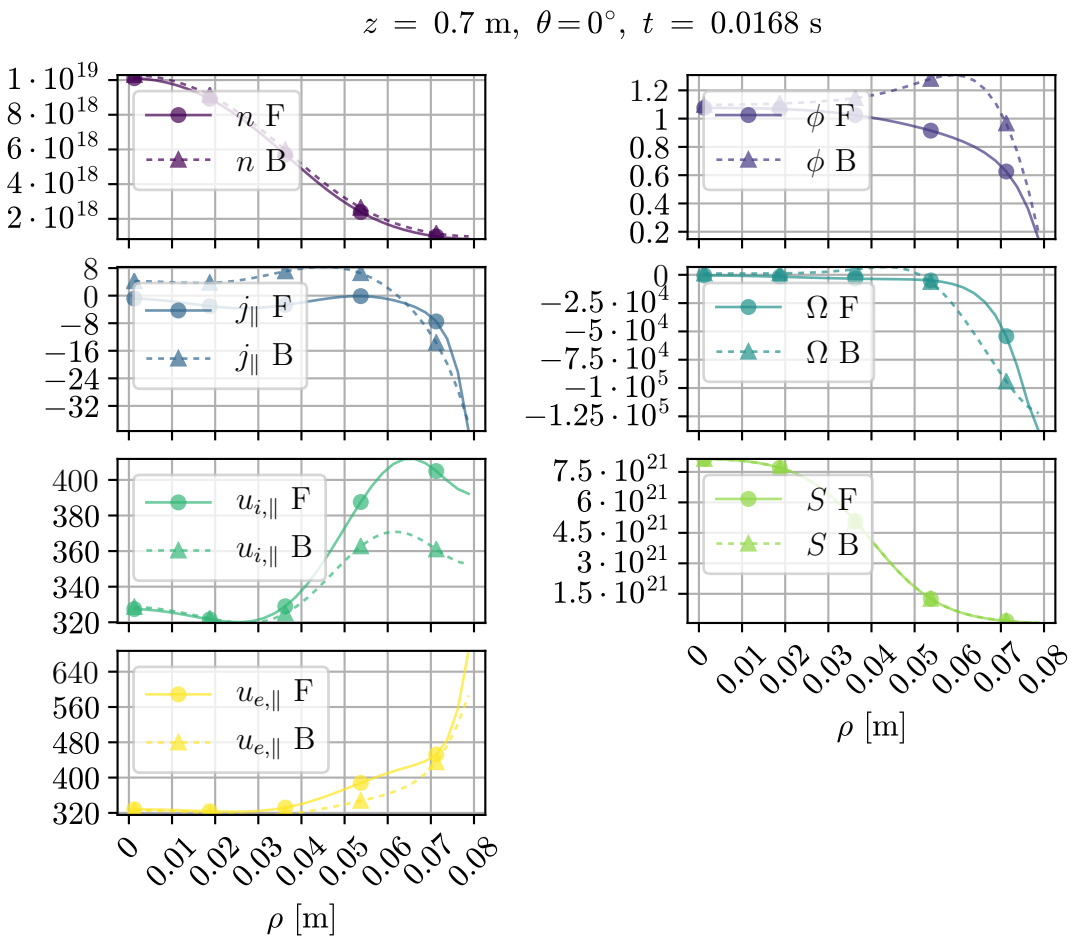

Figure 18.1: Radial steady state profiles with and without the Boussinesq approximation for $B_0 = 0.1$ T. Dots denotes the full simulation (but does not indicate the location of a grid point). Triangles denotes the simulation with the Boussinesq approximation (but does not indicate the location of a grid point). The units are the same as those used in fig. 12.2.

due to the higher values of $j_\parallel$. Secondly, the parallel current is around 5 time larger in magnitude close to the sheath entrance. This comes from the fact that the balancing terms in the vorticity equation has changed. In the non-Boussinesq case, the n in $\nabla \cdot (nu_{p,i})$ helped to reduce the terms in the modified vorticity, and thereby the parallel current as n was lower closer to the sheath. As mentioned above, this n disappears when using the Boussinesq approximation, so it can no longer help to reduce the parallel current. We can see that this change cannot have its origin in the $\boldsymbol{E} \times \boldsymbol{B}$ advection terms, as these are not active during the steady state since the ϕ-field is axisymmetric. Neither can it origin from the additional source term due to the lack of n dependence.

The higher values of $j_\parallel$ in the CB case causes Ω to be shifted to a higher value. For the CB case, Ω is approximately $1500\,\mathrm{s}^{-1}$ and does no longer cross 0. In other words, the local rotation of the plasma is in the same direction for all radii. Finally, it is worth noting that the system still follows a Boltzmann relation to a high degree, as is the case in the non-Boussinesq case. This can also explain why the density profile in the CB case is almost the same as in the CF case in the radial direction, as the Boltzmann relation approximately holds for each magnetic field line.

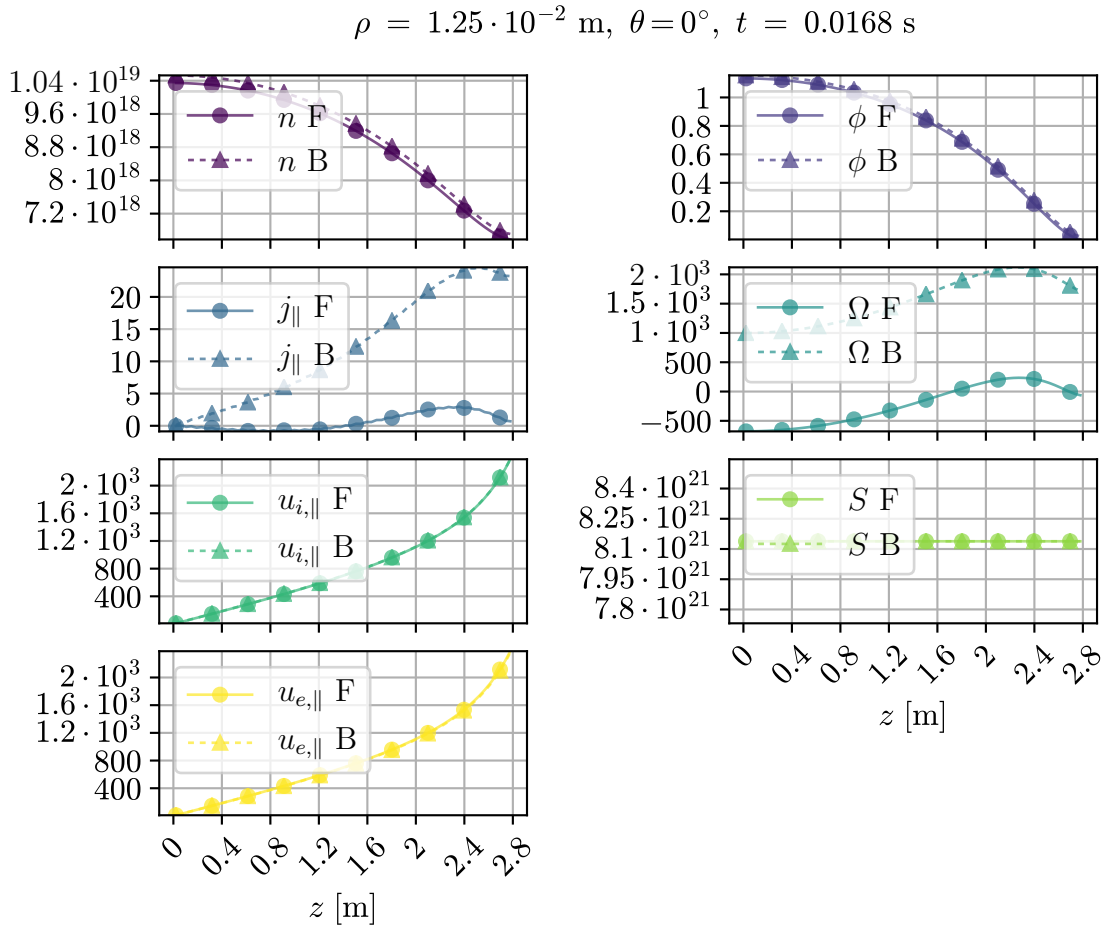

Figure 18.2: Parallel steady state profiles with and without the Boussinesq approximation for $B_0 = 0.1$ T. Dots denotes the full simulation (but does not indicate the location of a grid point). Triangles denotes the simulation with the Boussinesq approximation (but does not indicate the location of a grid point). The units are the same as those used in fig. 12.1.

18.2 The linear state

The change in the vorticity equation has a profound effect on the linear phase. In the CF case, identifying the linear phase based on the definition given in chapter 13 was fairly straight forward. In the CB case the time trace of the Fourier modes are a bit more complicated. An example of this is shown in fig. 18.3. In the CF case (fig. 18.3a), the perturbations shows a clear exponential growth. The intermediate phase between the linear phase and the saturated phase is relatively short. The CB case (fig. 18.3b) has a very short exponential growth after the initial perturbations have died out. This is followed by a rather long phase where the modes at some times are growing, whilst at others decaying. The final state for $B_0 = 0.06$ T seems to be indeterminate. Some modes are decaying, whereas the modes with the largest amplitudes are neither growing nor decaying.

Although challenging, we can still try to find the dispersion from the definition of the linear phase given in chapter 13. The result is given in figs. 18.4a and 18.4b. From fig. 18.4b, we can see that the growth rates of the modes are still increasing with increasing B-field. However, the maximum growth is observed in one mode-number less than compared with the CF case. There is also a steeper decrease in the growth rates

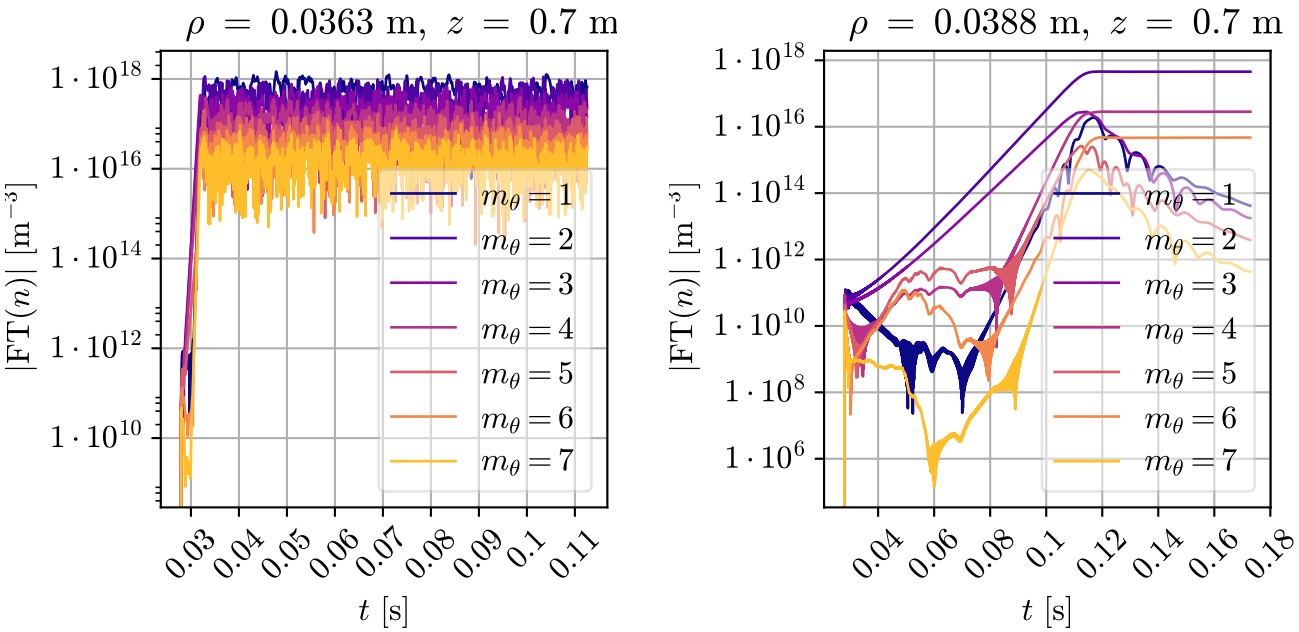

(a) Without the Boussinesq approximation.

(b) With the Boussinesq approximation.

Figure 18.3: The time trace of the absolute value of the Fourier modes for $B_0 = 0.06$ T for the non-Boussinesq and the Boussinesq case at the position of maximum linear gradient.

for higher mode numbers in the CR case. We observe that the maximum growth rates for the individual B-fields is less than half of what it is in the CF case. One should also emphasize that in the CB case, only $B_0 \geq 0.08\,\mathrm{T}$ reaches the saturated[2] turbulent state, compared with $B_0 \geq 0.06\,\mathrm{T}$ in the CF case.

The real part of the dispersion relation is also quite different from the CF case. As in the CF case, the decaying modes is rotating in the ion diamagnetic direction, but with a rate almost 10 times higher than compared with the CF case. This trend ceases for mode 6 and 7, where the CB modes suddenly rotates strongly in the electron diamagnetic direction. A bigger difference is that in the CB case, also $B_0 = 0.04\,\mathrm{T}$ rotates in the ion diamagnetic direction, and also exceeds the rotation velocity of the $B_0 = 0.02\,\mathrm{T}$ case. Only $B_0 \geq 0.06\,\mathrm{T}$ shows rotation in the electron diamagnetic direction. For these magnetic field strengths the rotation increases with increasing magnetic field strength (with exception of the highest modes in $B_0 = 0.06\,\mathrm{T}$, which rotates in the ion diamagnetic direction). This is also what was found in the CF case.

[2]As will be shown in section 18.3, the turbulence in the Boussinesq approximation does not really saturate in terms of energy. We will still refer to this state as "saturated" in the CB case to distinguish it from the intermediate turbulent phase preceding the linear state.

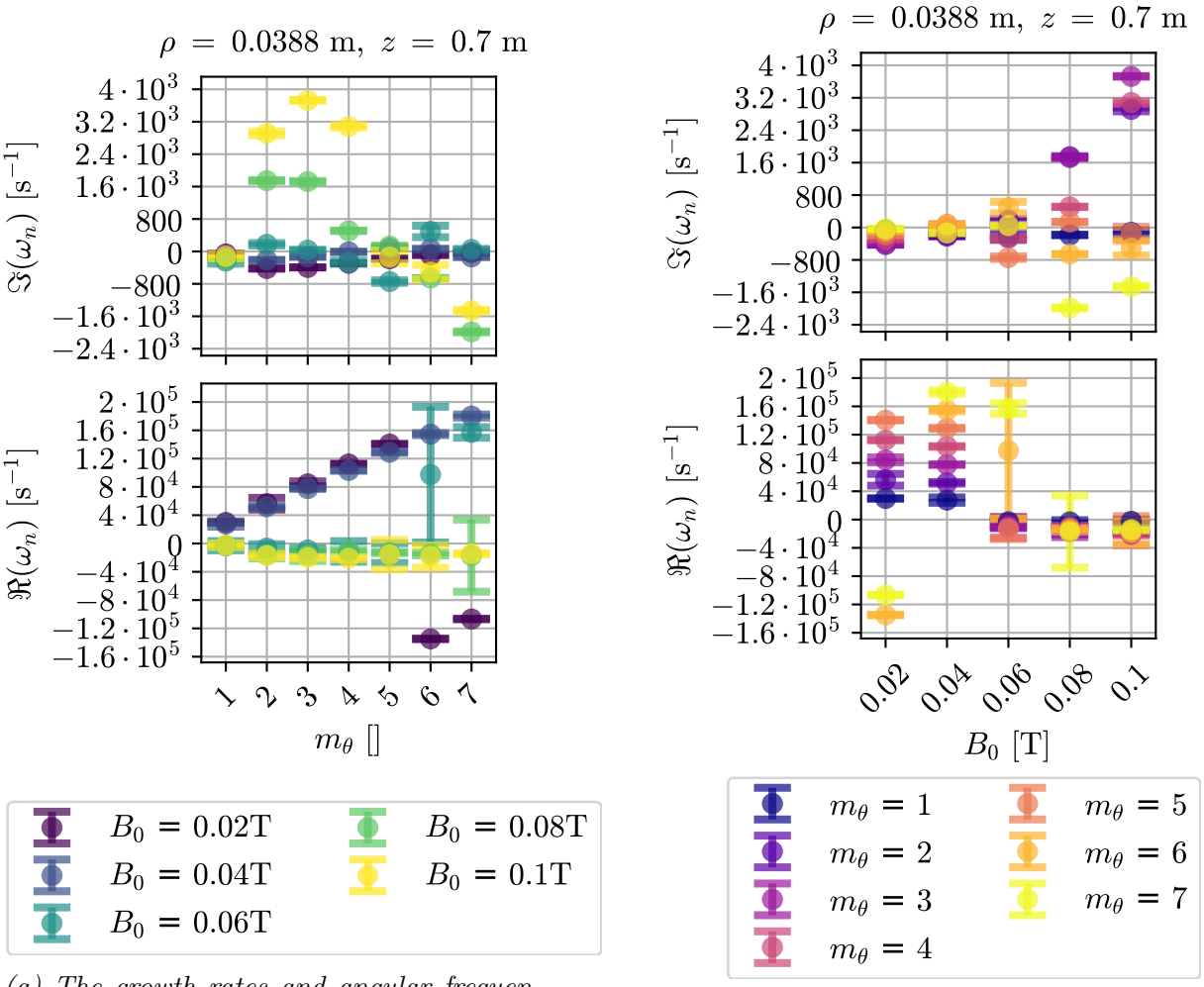

(a) The growth rates and angular frequencies as a function of B_0.

(b) The growth rates and angular frequencies as a function of the mode number.

Figure 18.4: The growth rates and angular frequencies in the CB case.

18.3 The turbulence phase

There is also a large difference between the Boussinesq and the non-Boussinesq case in the turbulent state. When investigating the energy in fig. 18.5 we notice three things. Firstly, in contrast to what is observed in simulations without the Boussinesq approximation, the energy is increasing in the linear phase (with exception of the parallel electron energy, which after close inspection actually shows a slight decrease in the linear phase). For the potential energy, this means that the total number of particles in the system is increasing as the electron temperature and volume is constant. If the density is increasing, this would also explain why the other energies are increasing as well. The parallel electron energy can then only be decreasing if the parallel electron velocity is decreasing.

Next, the energy overshoot is absent for magnetic fields below 0.1 T. This fact can also be seen by visual inspection the temporal evolution of the fields. The dynamics does not appear to be much faster during the onset of the turbulence then during the turbulent state.

Finally, the energy appears to be drifting to higher values with time. The absolute values of the energies are of approximately same order as for the CF case.

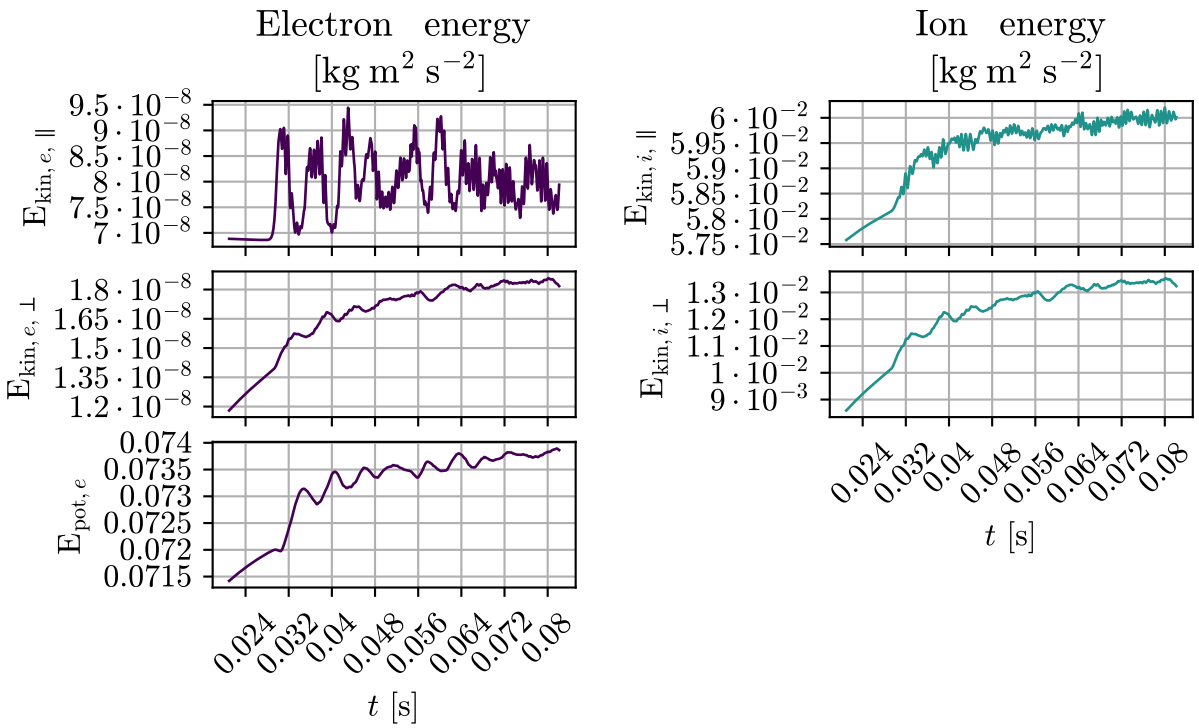

Figure 18.5: Time trace of the energy for $B = 0.08$ T using the Boussinesq approximation.

Visual inspection of the fields shows that the eddies evolves slower in the turbulence phase as when compared to the non-Boussinesq case. Whereas the plasma in the CF develops filamentary structures, these structures are less pronounced in the CB case, and the plasma as a whole appear to be more coherent. The dynamics in the CB also develops at a slower pace, as can be seen by comparing fig. 14.3 with fig. 18.6.

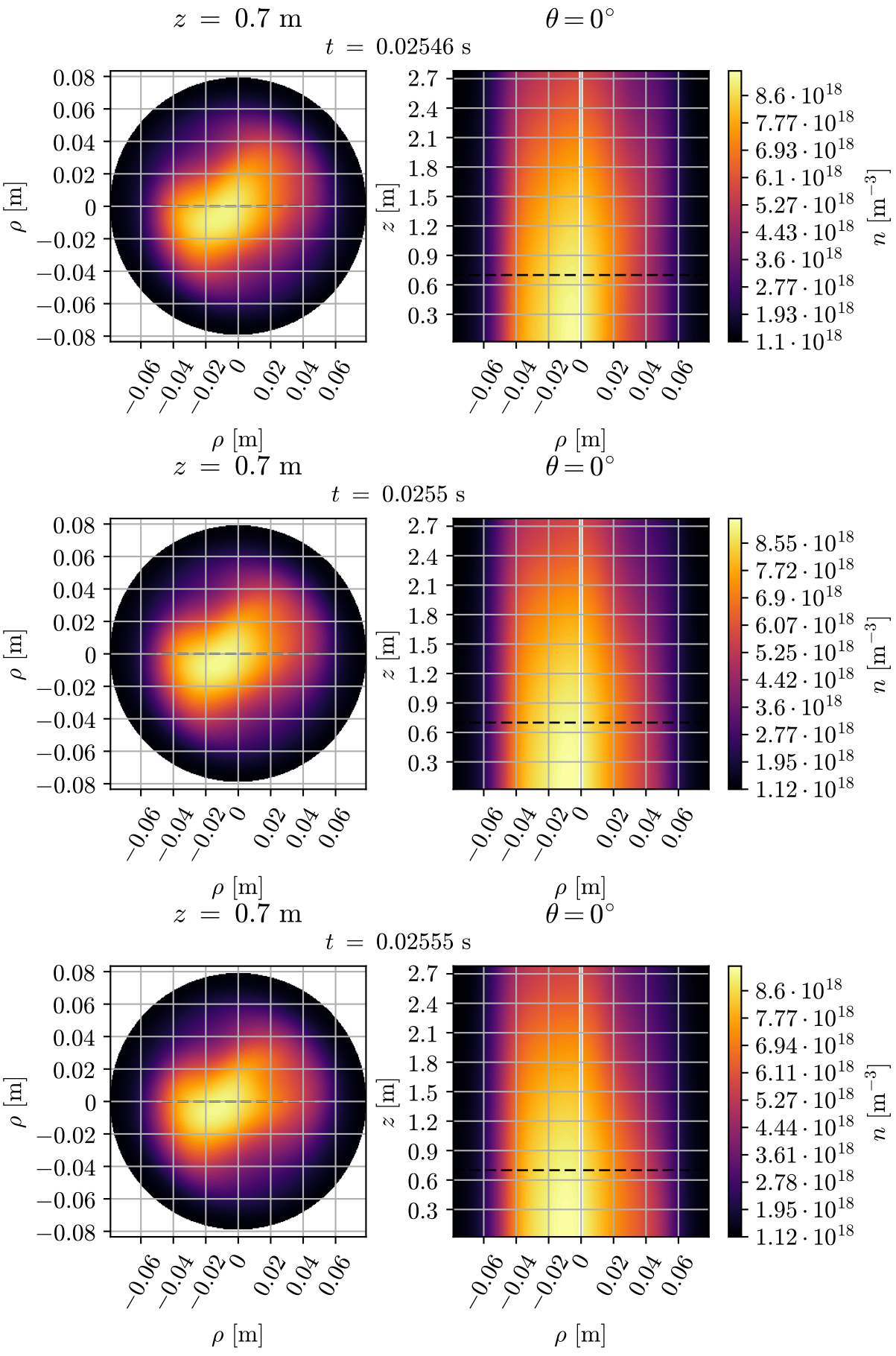

Figure 18.6: Evolution of the plasma in the saturated turbulence phase when using the Boussinesq approximation. Here shown for $B = 0.1$ T. The B-field points into the paper, and the black dashed lines indicates the slicing of the opposite plot.

18.3.1 Fluxes

Related to the drift in the energies as a function of time is the particle flux in the system. This is depicted in fig. 18.7. It is apparent that there are more ions than electrons being

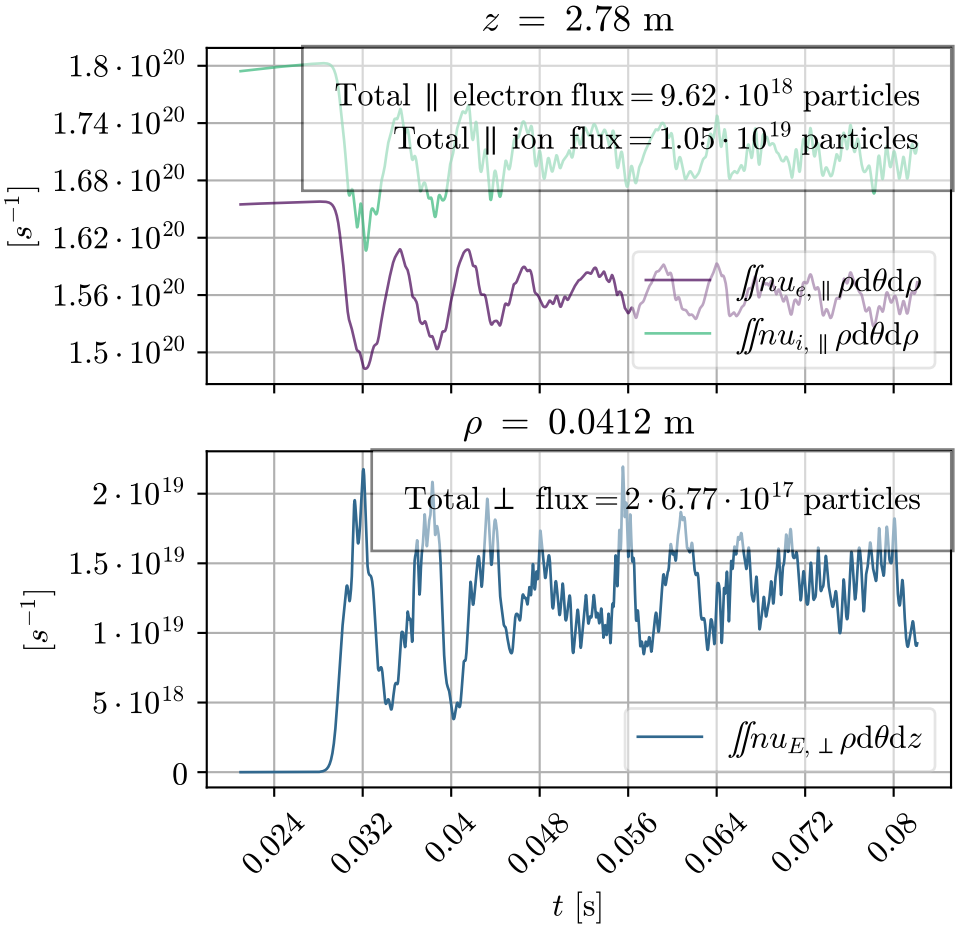

Figure 18.7: Integrated flux for $B = 0.08$ T using the Boussinesq approximation.

lost in the system. As a consequence, the plasma will be negatively charged with time. Moreover, the continuous charging of the plasma will at some point break the quasi-neutral assumption, which is one of the back-bone assumptions in the drift-fluid approximation, and therefore also in the CELMA model. In other words, the Boussinesq approximation in the current form is not consistent with its own assumptions.

Besides this very important fact, we can observe that the parallel fluxes in the CB case is of the same order of magnitude as the CF case, with the CB ion flux exceeding that of the CF case. Furthermore, the perpendicular flux is less than half of what it is in the CF case. This is consistent with the observation of less filamentation of the plasma as mentioned above.

18.4 Fluctuations

The coherent rotation of the plasma structure is also apparent from the time traces and PDF of n, shown in fig. 18.8. The time traces for the three positions are more periodic than what was observed in fig. 15.2, which hints to the fact that there may be some

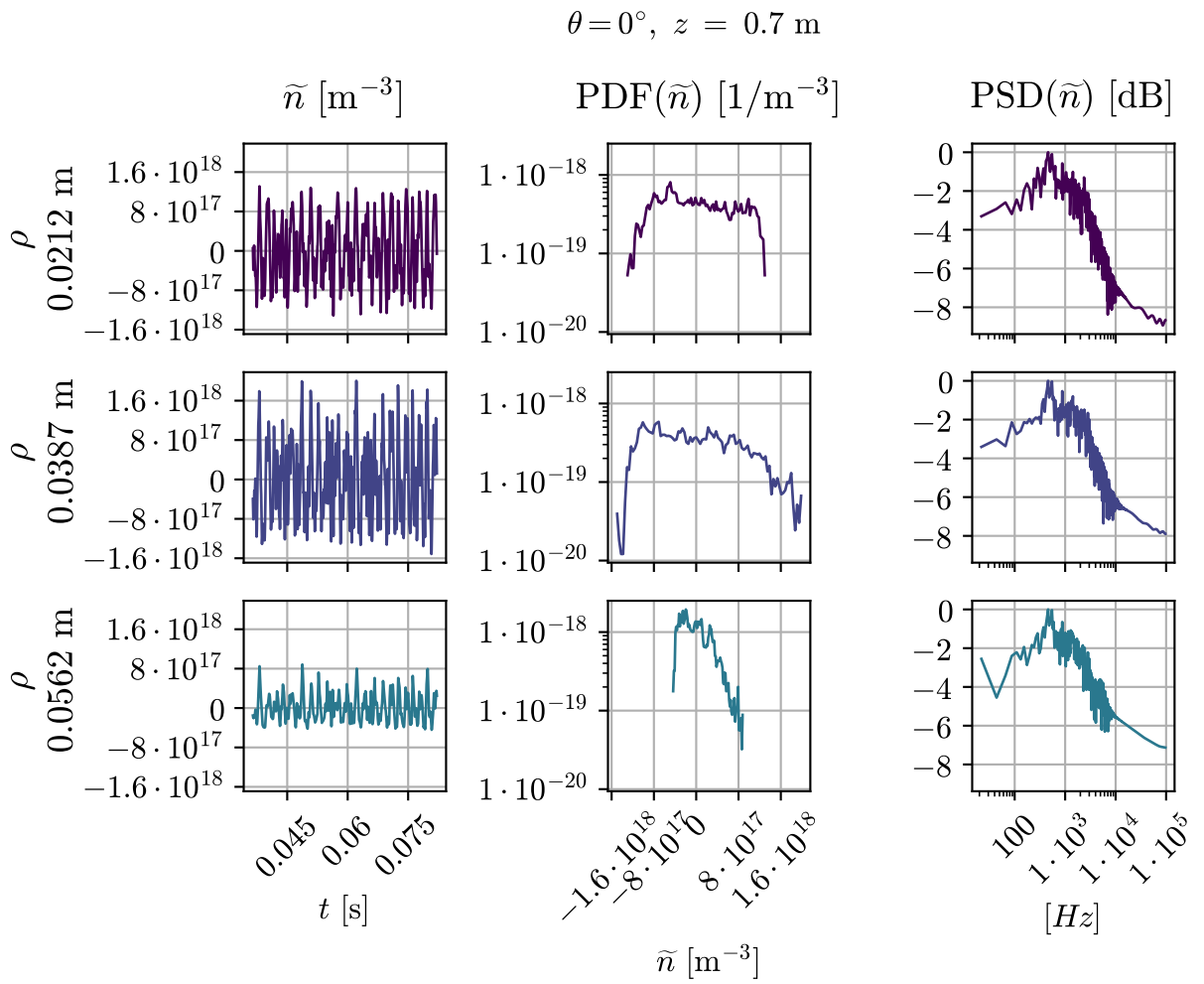

Figure 18.8: Time traces in three fixed positions around the maximum gradient for $B = 0.08$ T.

rotation going on in the plasma. One can observe that the PDFs in fig. 15.2 are more Gaussian-like, something which is supported by the observed skewness and kurtosis in fig. 18.9. The CB case has a lower skewness coefficient compared to the CF case, and the kurtosis coefficient is even lower than for a Gaussian distribution. This means that plasma bursts of plasma are less likely, and that the plasma stays more coherent.

Returning to fig. 18.8 and fig. 15.2, we note that in the CB case, the maximum of the power density spectrum is shifted to a higher frequency by a factor of approximately 3, and falls off at a slightly faster rate than for the CF case. The position of the maximum gradient is also shifted slightly outwards.

Furthermore, lower fluctuation amplitudes can be seen in fig. 18.10 where the profiles are less flattened than in the CF case. Outside the position of the absolute maximum gradient the density profile follows the steady state profile to a good degree. Finally, the potential is shifted closer to the absolute maximum of the gradient in the steady state.

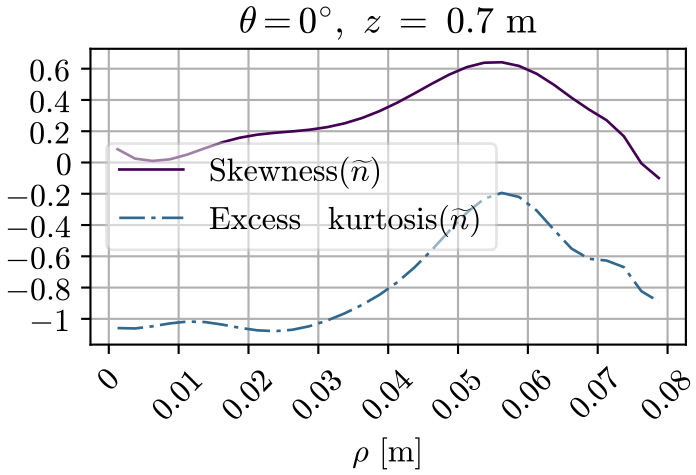

Figure 18.9: Skewness and kurtosis for $B = 0.1$ T using the Boussinesq approximation.

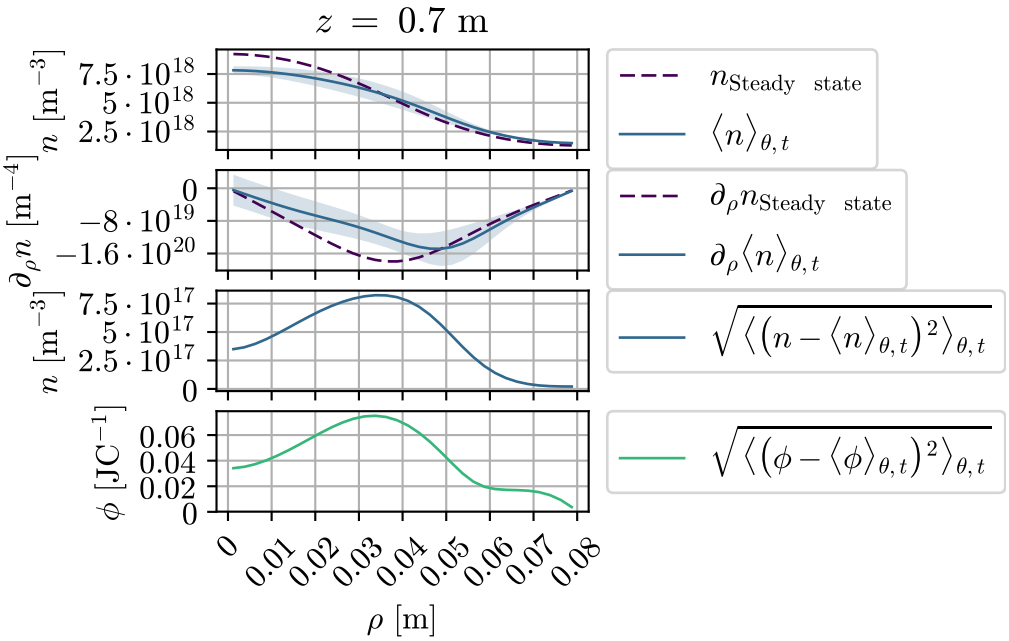

Figure 18.10: Steady state and averaged turbulent density profiles together with the radial distribution of the standard deviations of the fluctuations using the Boussinesq approximation with $B = 0.1$ T.

Chapter 19

Neutral scan

In this chapter, we would like to see how our results scales with the neutral density using our simple model for neutral collision of eq. (C.5). By fixing the magnetic B-field to $B_0 = 0.06\,\mathrm{T}$, we scan the degree of ionization d in 80%, 60%, 40%, 20%, 1%, where d is given by

$$d = \frac{n_i}{n_i + n_n},$$

where we take $n_i = n_0$ based on our quasi-neutral assumption. This corresponds to neutral density values of $2.5 \cdot 10^{18}\,\mathrm{m}^{-3}$, $6.7 \cdot 10^{18}\,\mathrm{m}^{-3}$, $1.5 \cdot 10^{19}\,\mathrm{m}^{-3}$, $4.0 \cdot 10^{19}\,\mathrm{m}^{-3}$ and $9.9 \cdot 10^{20}\,\mathrm{m}^{-3}$ respectively. In experiments, ionization degrees from 0.1% up to 100% has been observed [50].

With our parameters, the neutral collisions ranges from $\nu_{en} = 1.87 \cdot 10^5\,\mathrm{s}^{-1}$ at $d = 80\%$, and scales linearly with n_n up until $d = 1\%$, where $\nu_{en} = 7.38 \cdot 10^7\,\mathrm{s}^{-1}$. The electron-ion collision frequency is $\nu_{ei} = 7.25 \cdot 10^7\,\mathrm{s}^{-1}$ throughout the scan range, meaning that the neutral collisions will dominate firstly only at $d = 1\%$.

To keep the model consistent, ν_{in} will be kept to zero as $T_i = 0$. The physical justification for this is questionable as we assume that ions are streaming against stationary ions (see appendix C for details). However, if all the ions are misaligned with respect to the neutrals, no collision will take place. In any case, we usually have $\nu_{in} \ll \nu_{en}$ [50], which means that the ν_{in} term in eq. (5.26) is negligible.

19.1 The steady state

Starting with the parallel profiles shown in fig. 19.1, we can note that the profiles remains constant until $d = 1\%$. At $d = 1\%$ the peak density drops with almost 10%, and the parallel profiles flattens. More importantly, the system no longer follows the Boltzmann response. In fact, n and ϕ now behaves inversely. For high n, the potential is low and vice versa. As explained in chapter 12, there is a tight connection between ϕ, $j_\parallel$ and Ω. If one of them changes, the rest follows. We recall that ϕ is not evolved in time like n, but is entirely determined by the *radial* profile of Ω^D in each parallel point. Therefore, we will explain the change in the parallel profiles by explaining the radial profiles.

The radial profiles are shown in fig. 19.2. In terms of the density, there is a minimal change in the profile when the ionization degree is changed. The potential, on the other hand, has changed sign, and is negative for all the radii until the boundary condition,

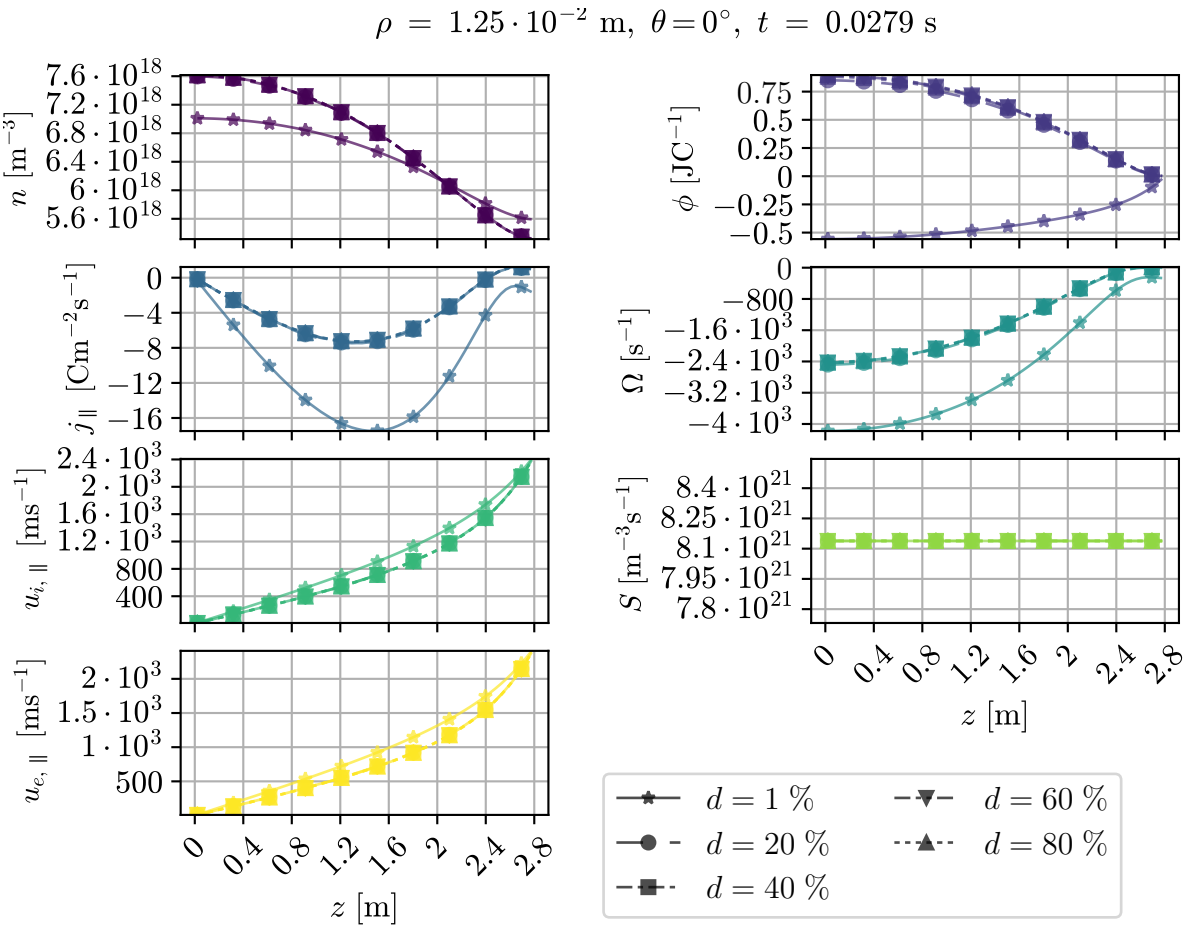

Figure 19.1: The parallel steady state profiles as a function of d.

which is set at 0. This can be explained from the Ω-profile which for $d = 1\%$ takes higher values for increasing ρ, which is opposite of the other ionization degrees. To explain this behavior, we must look at the balancing terms of the modified vorticity, which is shown in fig. 19.3. In the fully ionized plasma the time change of the modified vorticity is kept to zero as the parallel derivate of the current is balancing the parallel derivative of the ion velocity multiplied modified vorticity. This same terms accounts for the balance in the $d = 1\%$ case. However, in the $d = 1\%$ case, the profiles crosses zero and behaves opposite for high ρ than what is observed for the $d = 100\%$ case. As Ω^D does not contain any ν_{en} terms, we will explain this behavior by looking into the balancing terms for the parallel current displayed in fig. 19.4. In the $d = 100\%$ case the Boltzmann term is balanced by the electron-ion resistivity. On the other hand, for $d = 1\%$ the electron-neutral term is dominating the electron-ion resistivity term by one order magnitude. As a consequence, the resulting $j_\parallel$ profile must change. Since the $j_\parallel$ profile changes, the Ω^D balance changes, and the ϕ profile changes. As ϕ changes, the Boltzmann term changes, which again changes the $j_\parallel$. From this feed-back loop the vorticity profile changes in the radial direction.

We can now return to the initial question on why the parallel profiles changes. Recall that the parallel potential profile is determined by the perpendicular vorticity plane. The radial modified vorticity profiles are shown in fig. 19.5. We observe that although the profiles differs in value, the shapes of the balance remains the same. This explains why the shape of the vorticity profiles in fig. 19.1 remains the same, only differing in values.

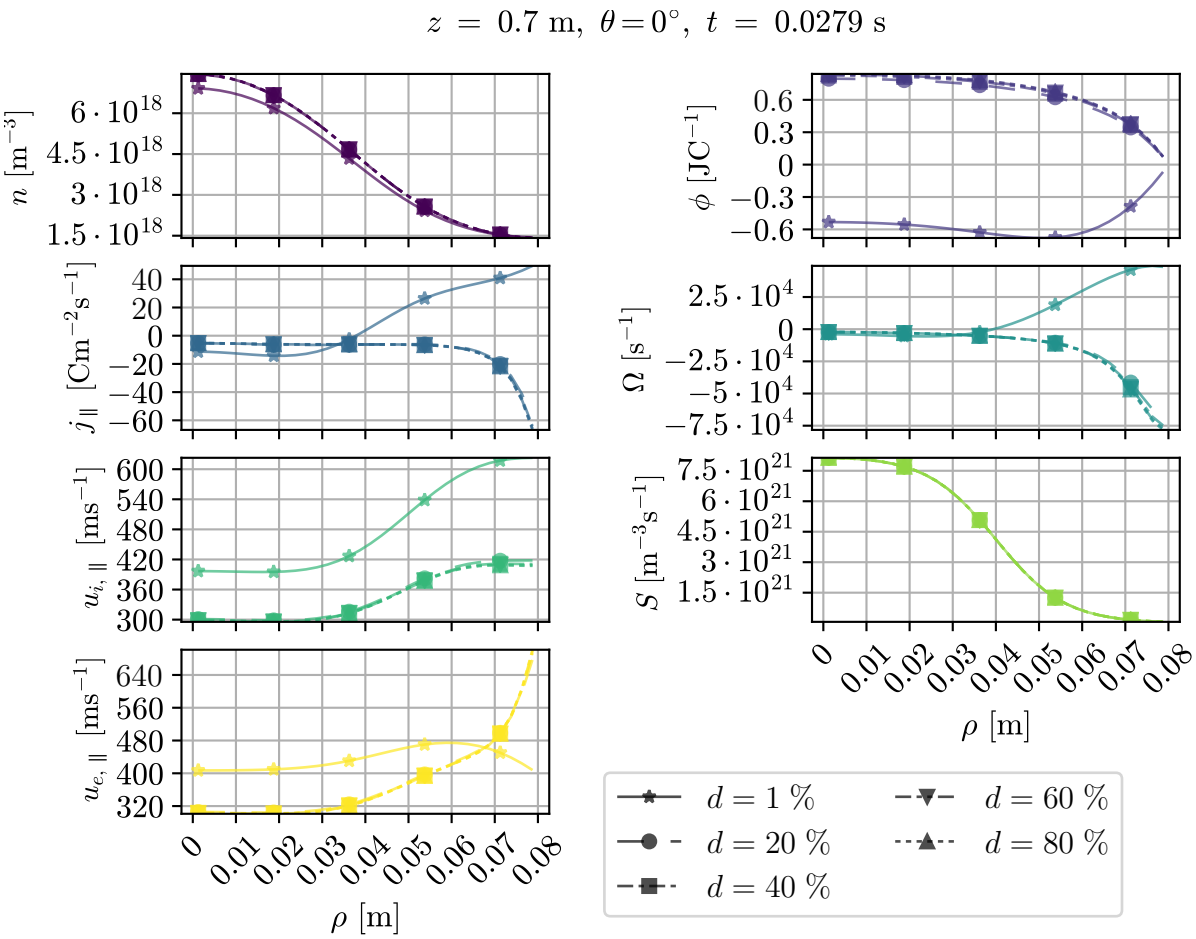

Figure 19.2: The radial steady state profiles as a function of d.

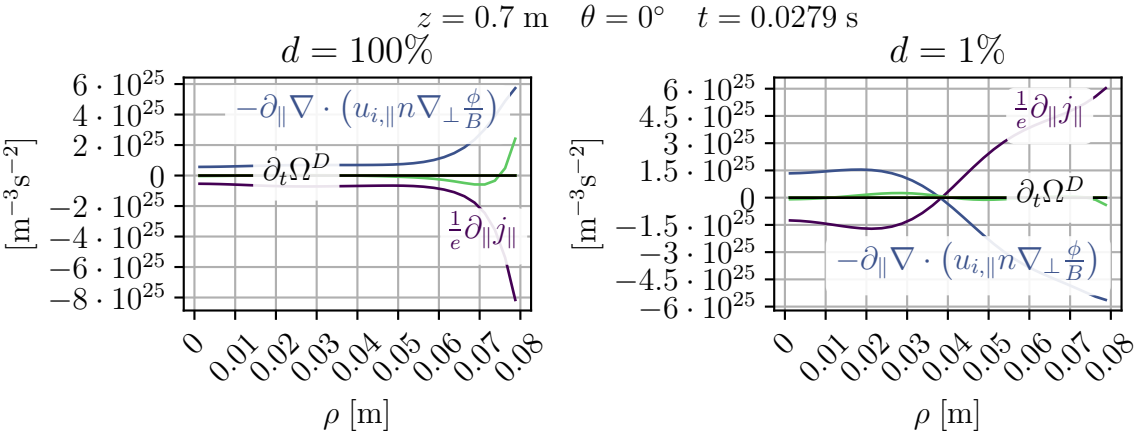

Figure 19.3: The radial steady state balance for the modified vorticity for $d = 100\%$ and $d = 1\%$. The green, unlabeled line denotes the artificial vorticity.

The parallel change of the radial profiles is just modified by the parallel current profiles, which is shown in fig. 19.6. This determines the strength of the parallel current which is balancing the perpendicular vorticity. As the perpendicular balance is changed, the parallel potential profile is changed.

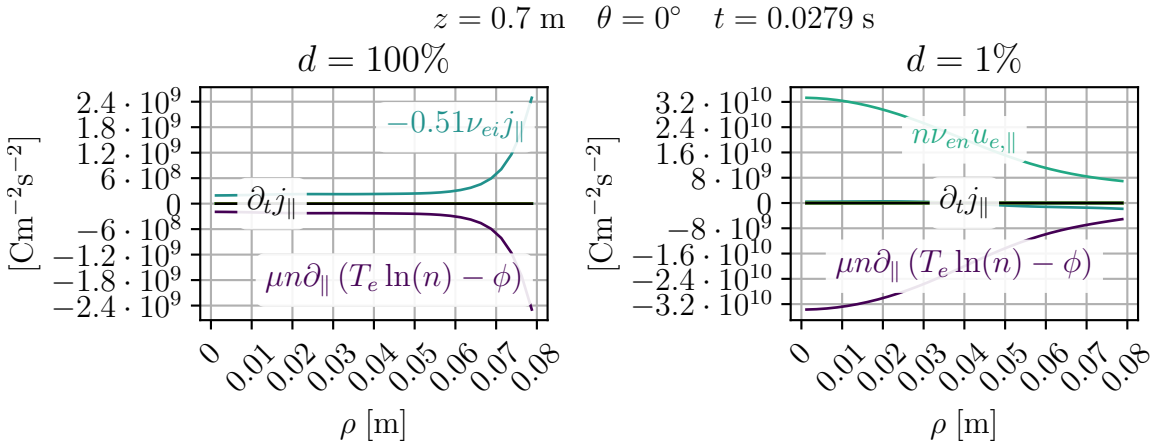

Figure 19.4: The radial steady state balance for the parallel current for $d = 100\%$ and $d = 1\%$.

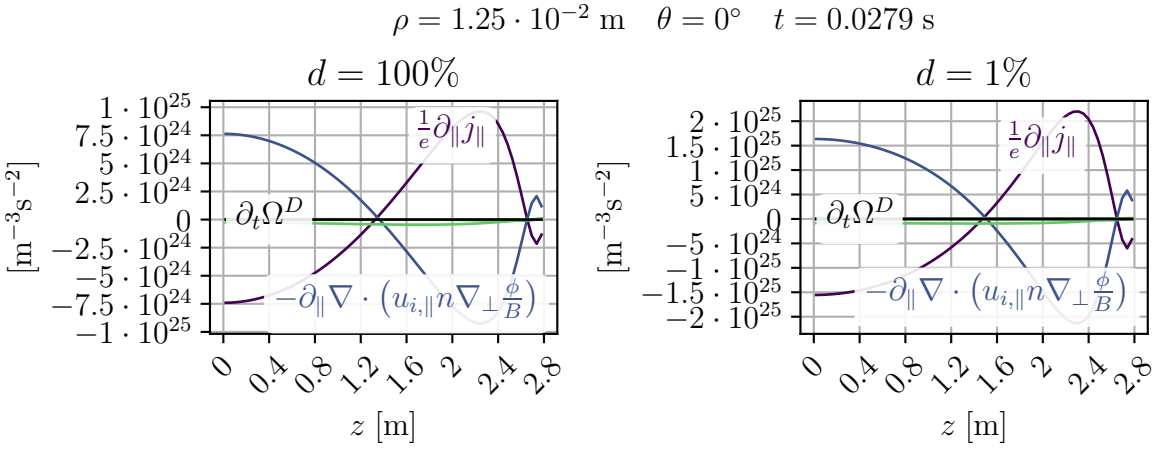

Figure 19.5: Parallel profiles of the modified vorticity balance.

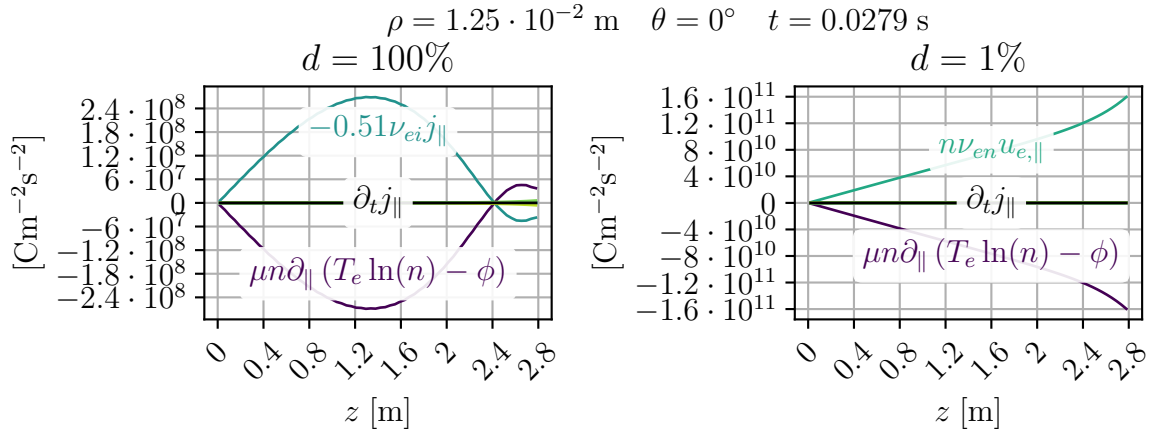

Figure 19.6: Parallel profile of the parallel current.

19.2 The linear phase

We find the growth rates in the same manner as described in section 13.4. The result is presented in figs. 19.7a and 19.7b. We observe that the general trend is that the growth

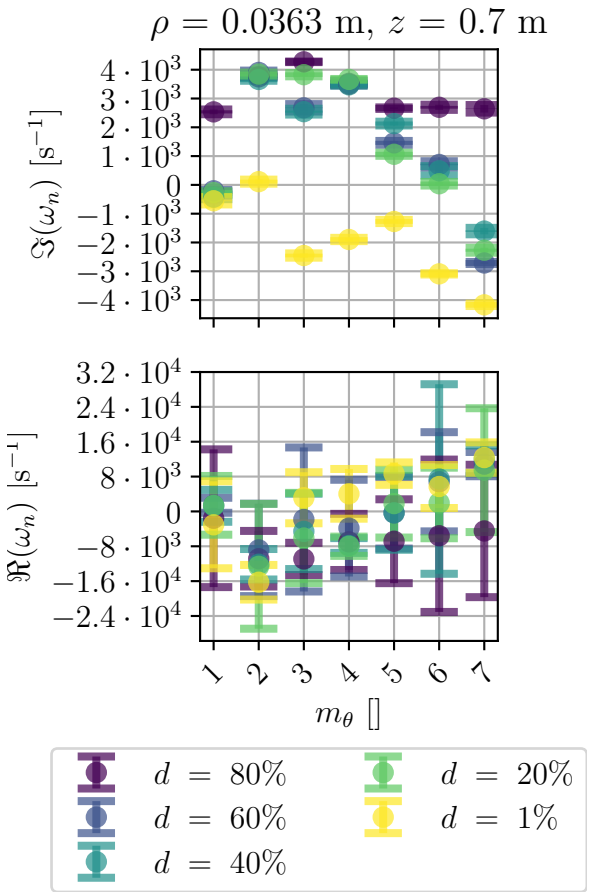

(a) Growth rates and angular frequencies as a function of mode numbers.

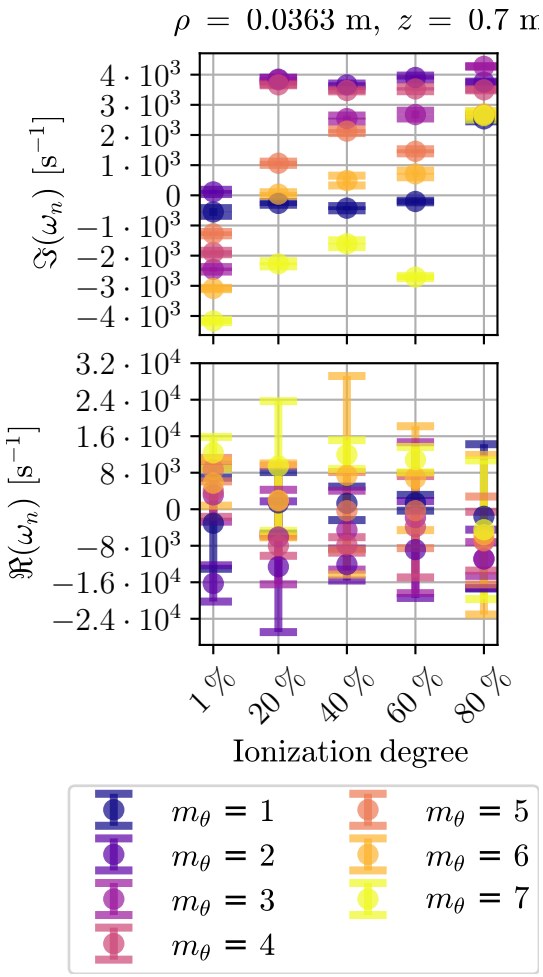

(b) Growth rates and angular frequencies as a function of d

rate decreases for decreasing ionization degree. For higher mode numbers the rotation increases with decreasing d, whereas the converse is true for the low mode numbers.

The max growth rate is found around $m_\theta = 2 - 3$. As in the case with a fully ionized plasma, the decaying modes are rotating in the ion diamagnetic direction. Of the growing modes, we can observe that there is less rotation for higher modes, with exception of the first mode, which is unstable for all the ionization levels with exception of $d = 80\%$. Finally, we note that $d = 1\%$ is only slightly unstable.

This low ionization level is also the only one which does not reach a saturated steady state, but rather saturates in a situation where the modes are rotating without growing. This is depicted in fig. 19.8.

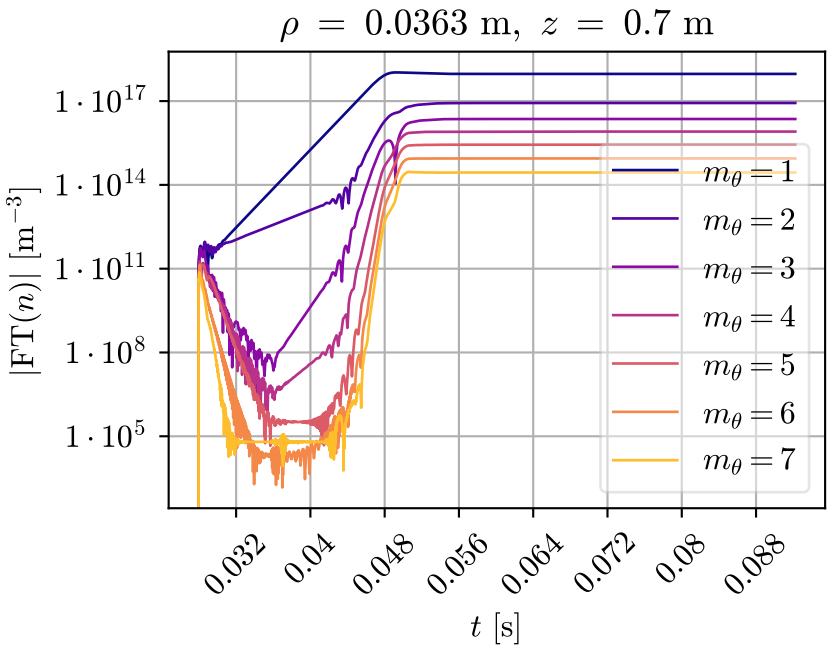

Figure 19.8: Time trace of the absolute amplitude of the Fourier transformed density for $d = 1\%$.

19.3 The saturated turbulence state

As $d = 1\%$ is not reaching a saturated steady state it will not be considered here. The time trace of the parallel energy becomes more intermittent for decreasing ionization. However, there are only minor changes in the radial direction. The position of the fluctuations stays the same for all d, as shown in fig. 19.9. The skewness and kurtosis shows no general

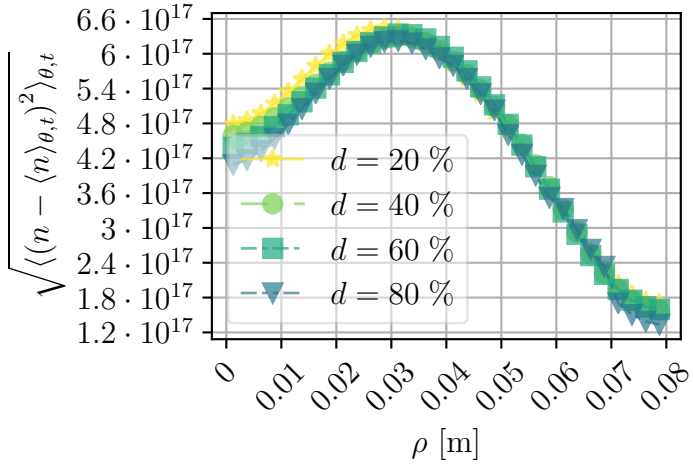

Figure 19.9: The standard deviation for the turbulent cases.

trend when changing d. For the regions of low poloidal shear the skewness and kurtosis of $d = 20\%$ and $d = 40\%$ have approximately the same values for the skewness and the kurtosis. Both the skewness and kurtosis increases in this region for $d = 60\%$, before it approximately falls to the levels of $d = 20\%$ for the $d = 80\%$ case. In the region of strong shear the intermittency increases for $d = 20\%$, whereas it decreases for $d = 80\%$.

By looking at the flux in fig. 15.4, we can observe an increase in both the parallel and perpendicular flux for lower ionization degrees. For the perpendicular case, this means

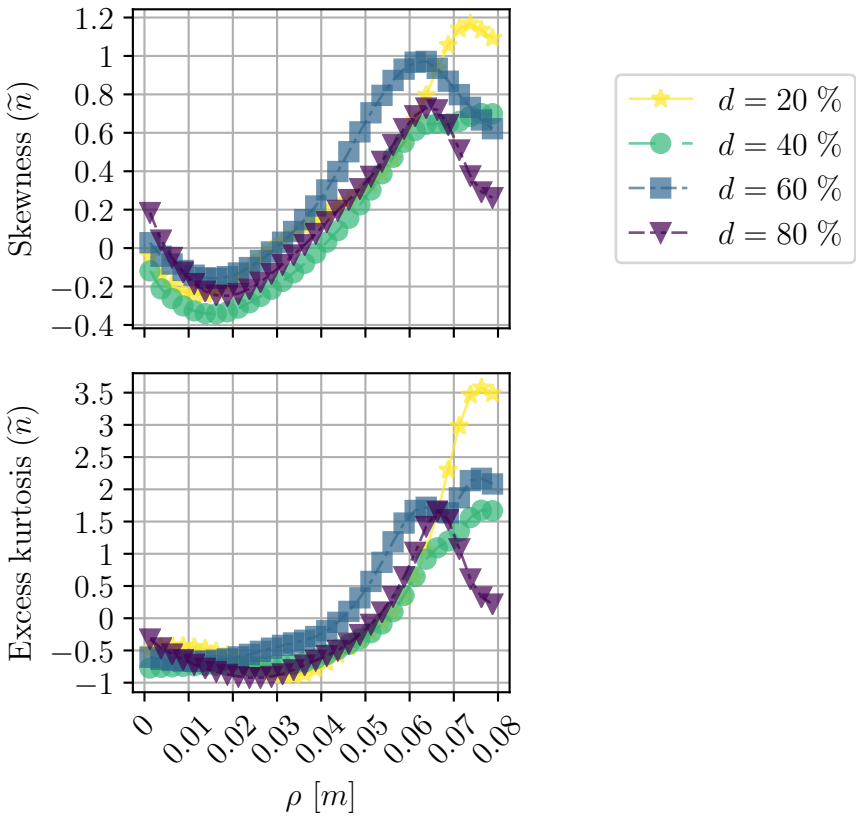

Figure 19.10: The skewness and kurtosis for the turbulent cases.

that the radial turbulent transport is increasing.

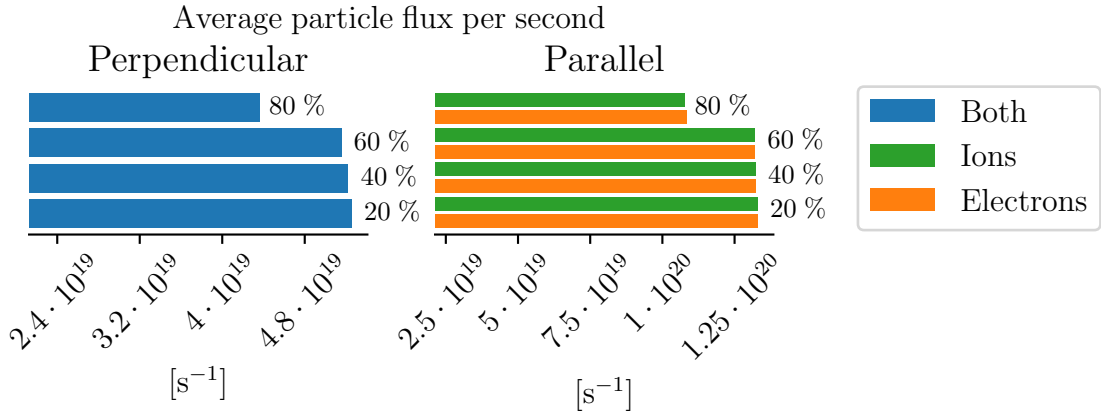

Figure 19.11: The variation of the total flux as a function of d. The point of measurement is the same as in fig. 15.4.

Finally, the average blob count presented in fig. 19.12 reveals that the number of coherent structures increases with decreasing ionization level until $d = 20\%$, where the blob and hole count is decreasing. The decrease can be attributed to the overall decrease in growth in fig. 19.7a together with more damping through the increased neutral resistivity.

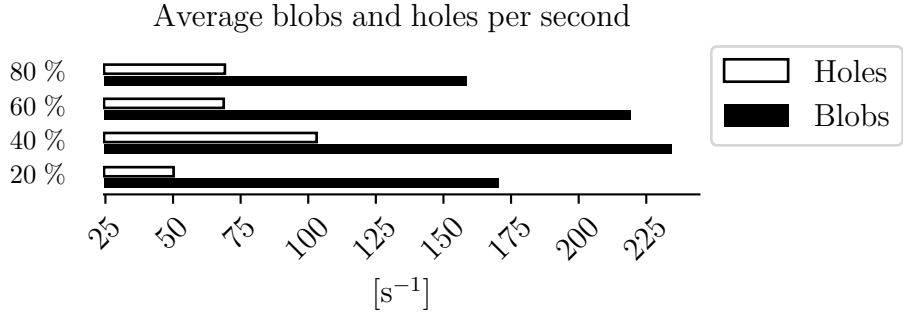

Figure 19.12: The blob count as a function of d for a triggering signal of 3σ on the radial flux.

Chapter 20

Performance

We will here briefly present the performance of the CELMA-code. As there are many ways to measure the performance, we will focus on the average internal iterations per output time-step. As long as the number of processors used is constant, and as long as the underlying solver framework does not change, this number is expected to be more or less constant. The observed wall-time for the simulations will on the other hand depend on parameters such as the machine the simulations are executed at, if the computational load on the machine on that day was high etc. Although the `4.0.0`-version of BOUT++ includes improvements on the memory handling and on the way certain arithmetic operations are operating on the field, the number of iterations presented here should stay roughly the same.

The performance of the B_0-scan (without the use of the Boussinesq approximation) is presented in fig. 20.2. We observe that number of iterations are somewhat high if

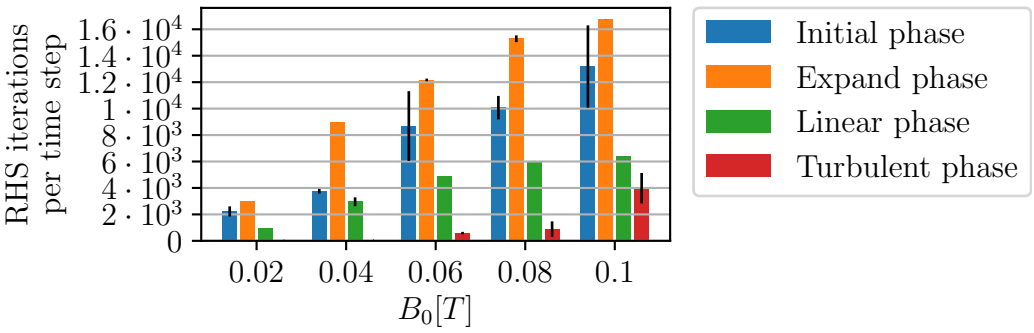

Figure 20.1: Performance of the B-field scan.

compared to other codes using the BOUT++ framework. This is of course dependent of the underlying physical model, which may be stiff under certain conditions [43]. The two phases responsible for obtaining the steady-state solution requires the most iteration per time-step, despite the fact that the fast dynamics is present only at the beginning of the initialization phase. Once the perturbation are added to the steady states, the iteration count drops in the linear phase, and drops even further in the turbulent phase. This is contrary to what is usually observed in turbulence simulations, where the simulation slows down at the onset of turbulence as the solver must resolve a larger specter of eigenmodes. There may be several reasons for the iteration count in the initialization exceeds that of the turbulent phase, but this has not been investigated in depth in this work. Instead, we will here present some plausible reasons for the high observed iteration count for the

steady state. It could be that the see-sawing pattern described in section 11.3 is limiting the time-step as spurious gradients are being set up between each perpendicular plane. Next, there may be some numerically fast-traveling waves in the system which might be mitigated by introducing electromagnetic effects [44]. The time solver may also be sub-optimized, and it tries to resolve the system at the noise level, or the adaptive time-step controller is frequently choosing time-steps close to a numerical unstable region so that the internal time-step observed comes from the time-step controller trying to find the correct time-step. In any case, we can see that the number of iterations needed for the next output time-step scales almost linearly with B_0 for all phases with exception of the turbulent phase, where the increase in required time-step exceeds a linear scaling. This scaling is expected as we need to resolve smaller scales at higher magnetic field strengths as ρ_s decreases with B.

We can compare our findings of the B-scan simulations using the Boussinesq approximation. This is depicted in fig. 20.2. The first thing to note is that the there

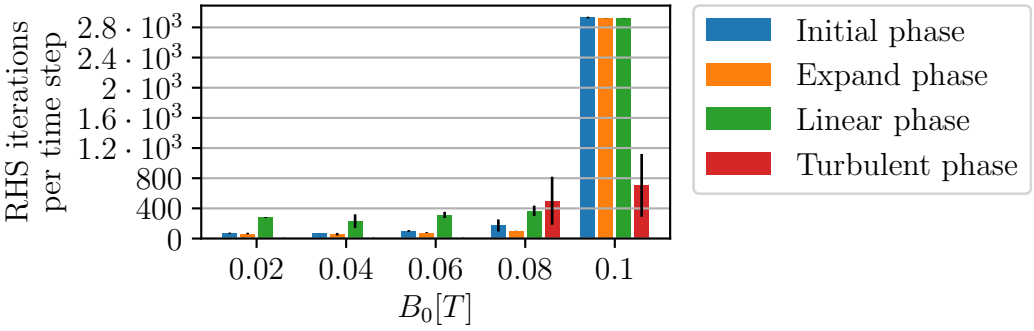

Figure 20.2: Performance of the B-field scan using the Boussinesq approximation.

is up to 90% reduction of the iteration count in these simulations, with 80% reduction of the iterations of the turbulent phase for $B_0 = 0.1\,\mathrm{T}$. This can indicate that the Boussinesq model is less stiff than the model which do not use the approximation. We also note that, with exception of $B_0 = 0.1\,\mathrm{T}$, the turbulent phase is the most computational demanding in terms of the iteration count.

The iteration count investigation has also been done for the neutral scan, and is shown in fig. 20.3, and we observe a reduction in the number of iterations for increasing neutral density. This can be understood in terms of the increased collisionality as the neutral

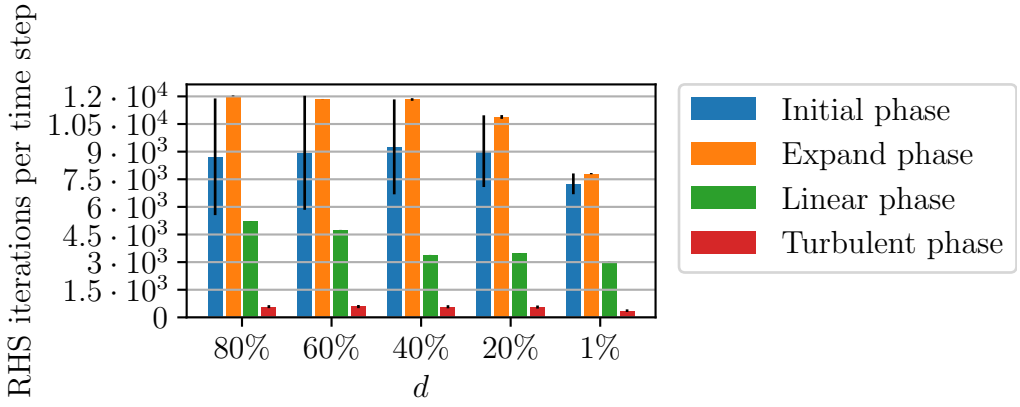

Figure 20.3: Performance of the neutral scan using $B_0 = 0.06\ T$.

collisions adds dissipations to the system.

It is also interesting to investigate what kind of numerical operation which contributes most to the computation time. This is presented for the $B_0 = 0.06\,\mathrm{T}$ with $n_n = 0$ in fig. 20.4, and for $B_0 = 0.06\,\mathrm{T}$ with $n_n = 1.5 \cdot 10^{19}\,\mathrm{m}^{-3}$ in fig. 20.5. The figures are almost

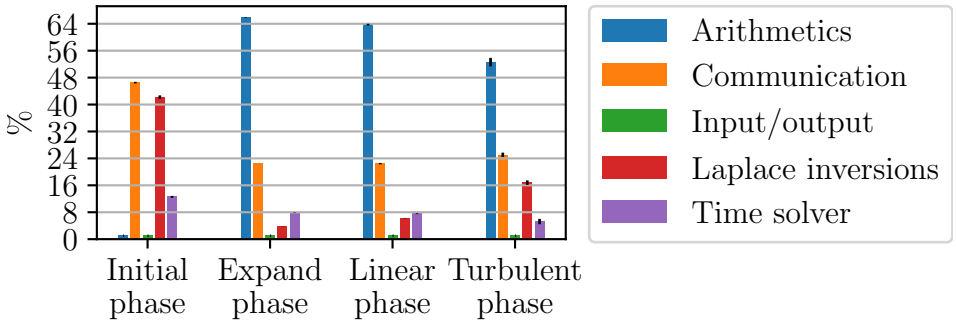

Figure 20.4: The time spent on of each computational task in per cent for $B_0 = 0.06$ T.

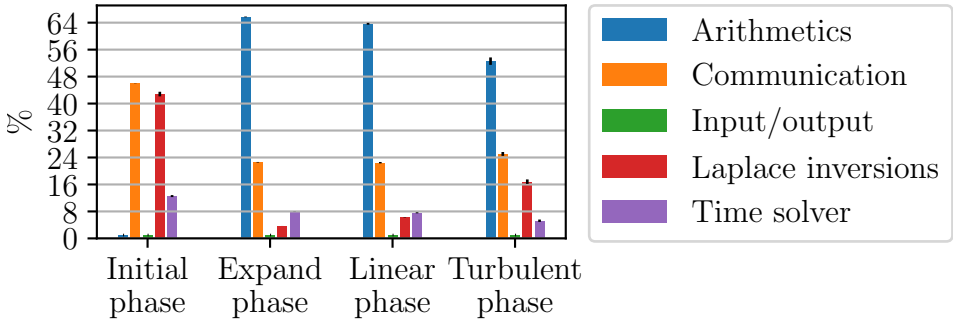

Figure 20.5: The time spent on of each computational task in per cent for $B_0 = 0.06$ T with an ionization degree of $d = 40\%$.

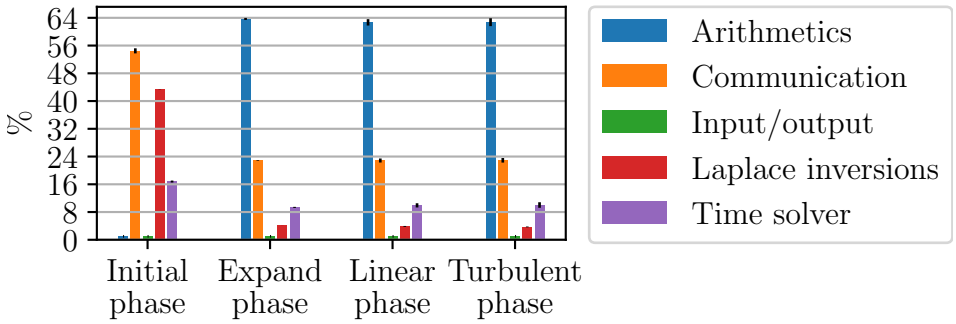

Figure 20.6: The time spent on of each computational task in per cent for $B_0 = 0.08$ T using the Boussinesq approximation.

identical in terms of the computational work distribution for all phases. Although the added collisionality may reduce the iteration count, there is no obvious reason for why the computational work distribution should change. In the neutral simulations only the value of ν_{en} is changed. Although $\nu_{en} = 0$, the neutral collision terms are still being calculated in the code, which means that the time spent on doing arithmetic operations on fields (like $+$, $-$ etc.) is not expected to change. From figs. 20.4 and 20.5 we can see that

most of the communication is spent at arithmetic operations, followed by communication of the domain boundary between the different processors[1]. The Laplace inversions done with the iterative Naulin solver seems to be important only in the turbulence phase. It is found that the solver uses between $3 - 10$ iteration per time-step in this phase.

We can compare this workload with the ones found for the Boussinesq approximation for $B_0 = 0.08\,\mathrm{T}$, shown in fig. 20.6. The work load is still dominated by the arithmetics and communications. However, there is a decrease in time spent in the Laplace solver, which can be explained by the fact that only one inversion is needed per iteration. This may also contribute to the decrease of the iteration count presented above.

[1]Parallelization in the simulations is done by a domain split in the ρ and z direction with domain boundary communication using `Message Parsing Interface` included in the BOUT++ framework.

Part IV

Conclusion and outlook

We are now in a position to answer the questions posed in the introduction, and we will in this part sum up the work in done in this thesis. In the end, an outlook for further work is given together with known shortcomings.

Conclusion

In this thesis, a drift-fluid model with a particle source has been derived from first principles without using the Boussinesq approximation. From the derivations and assumptions, it is found that this model is suitable for modeling the low frequency turbulence observed in a linear machine.

The approaches used for solving this model can be summarized as follows: The main implementation has been done using the BOUT++ framework. Additional implementation has been needed for treatment of the singularity, the Naulin Solver, the $\{\boldsymbol{u}_E^2, n\}$-advection and for the artificial boundary conditions. The singularity has been treated by using ghost-points across the cylinder axis, and the potential is found from inversion using the Naulin Solver. In order to run without unphysical generation of energy and enstrophy, which eventually leads to a simulation crash, the $\{\boldsymbol{u}_E^2, n\}$-advection has been implemented in an Arakawa-like manner. Finally, artificial boundary conditions in the parallel direction has been done using fourth order extrapolation schemes. The BOUT++ implementations has been verified using the method of manufactured solution, whereas additional implementation has been verified through the method of exact solution. From numerical experiment, it is found that the grid size oscillation is reduced by increasing grid size in the parallel direction.

In part III we discussed how the plasma evolves in the linear machine. In the steady-state the evolution of the radial and parallel profiles has been emphasized. A Boltzmann like behavior was found in the parallel direction. It is also found that the source sets the radial density gradients, and that the vorticity profiles can be explained through the balance of parallel and perpendicular currents. The growth rates together with the angular frequency was found in from the simulations in the linear phase, and they were found to be in qualitatively agreement with what was found from an analytic expression for drift-waves derived from a simplified slab geometry. Both the growth rate and the angular frequency increases with B in absolute numbers. These drift-waves are in the end evolving into turbulence. Increased intermittency is found at increased radii from the position of the maximum gradient in n. The perpendicular turbulent flux is causing a profile flattening, which increases with B. It is found that the parallel flux decreases with increasing magnetic field strength, whereas the perpendicular particle transport increases.

A poloidal sheared flow was found as a consequence of the radial boundary conditions. This shear flow did not change much in the turbulent phase.

A statistical picture of coherent structures has been found by using the conditional averaging technique, and these structures has been identified as blobs and holes.

The Boussinesq-approximation is often made in the literature, and it has in this thesis been demonstrated that this approximation can lead to different dynamics which again leading to different conclusions as compared with the full model. In the worst case scenario, simulations with the Boussinesq-approximation can break the quasi-neutral assumption of the model, rendering consecutive results doubtful.

Despite the fact that CELMA is a crude model, we found similarities with what has been reported in the literature.

In this thesis drift-waves has been realized in its simplest three-dimensional form in a linear machine. To elevate the discussion, let us briefly indicate why the drift-waves and the other topics discussed in this thesis are important. A proper understanding of the drift-waves are important for the understanding of the turbulence found at the edge of fusion plasmas. The drift-waves are as such important in themselves, but it their understanding also sheds light on instabilities such as the ion temperature gradient which is closely related to the pure drift-wave, and which is partially responsible for the core turbulence in fusion plasmas. A key point is that drift-wave like behavior is found whenever there is a difference in the parallel streaming of the electrons. Several mechanisms are responsible for a delay of the electron response to a pressure perturbations, and this inevitably leads to an unstable growth of the perturbation. This kind of instability is therefore quite universal in plasmas.

As these instabilities are prevalent in the edge of the plasma, they contribute to setting the condition of the scrape-off layer. Knowing the conditions of the scrape-off layer is of paramount importance. Firstly, it is important to know the power deposition to the divertor in order not to damage or melt any divertor tiles, and it is therefore important to know the relationship of parallel and radial fluxes. An understanding of self-propagating blobs is important to understand in order prevent damages to the first wall. The conditions in the scrape-off layer sets the coupling between the plasma and electromagnetic waves used for heating and diagnostics, and ultimately sets the boundary condition needed for simulations of the core plasma.

Outlook

To extend the work performed here, this section will suggest some interesting topics which can done with the model and the code.

The model and the code has been made transparent and readily available at celma-project.github.iofor anyone who wishes to peruse further work.

Firstly, the investigations done in this thesis can be extended by investigating how the results scales when the background plasma amplitude and source is changed, as these parameters effectively sets the gradient length scale which drives the instability.

Changes to the physical domain size is also of interest. Of particular interest is varying the parallel direction as this affects the dispersion relation and the ratio of parallel to perpendicular outflux. The ratio of radial source extension to radial domain is also of interest in order to see how the perpendicular propagation of the coherent structures changes. It should be noted that extensions of the domain will come at a higher computational price if the resolution is kept constant. This is because every additional grid-point d_a in direction a gives $d_b \times d_c$ as many equations to solve for each iteration, where b and c denotes directions perpendicular to a. Increasing the parallel direction with one grid point also means that the potential inversion has to be done at one more perpendicular plane.

The simulation can also be done using more fusion relevant gases such as H, D, T and He. This will reduce the difference in electron and ion mass, and therefore increase the ion mobility. As a consequence the drift-wave dynamics will change, which may have an effect on the coherent structures. Although reducing μ, the resolution of the code needs to be increased in order to keep the same resolution as the normalized domain size increases for decreasing ion mass. If neutral interaction is to be included, the neutral collision terms

should be changed as elastic collision processes is not dominating over processes such as the charge exchange in these gases.

Further, the simplest form of the Boussinesq approximation has been used here, resulting in a drift of the energy. Several variants of the Boussinesq approximation exists, and it is possible to derive an energy conserving model using Boussinesq approximation by looking at energy transfer terms, and compare simulations of such a model with the results presented here.

Next, the assumption of isothermal electrons and ions can be relaxed, and the set of equations can be closed using the Braginskii closure. This would enable studies of the heat transport, and the heat load at the sheath entrance. It would also enable the study of neutral interaction with plasma turbulence by for example adding equations for hot and cold neutrals. Further, the code can readily be made periodic in the parallel direction. A material annulus with the sheath boundary condition on both sides can be introduced. This would give a crude model of the scrape off layer without curvature effects, and more interesting wall load studies can be made.

Finally, more advanced studies can be made by relaxing the assumption of a straight magnetic field, but this would require large modification of both the model and the code. As long as the metric is orthogonal, the Naulin Solver (modified with the ∇B-effects) can still be used to invert for the potential. The parallel sheath boundary condition would need to be changed if the magnetic field enters the sheath entrance with an angle. Effects of magnetic shear and curvature can be studied. For the BOUT++ operators, changes of the metric can easily be done by either changing the metric tensor, or by using the Flux Coordinate Independent scheme for the parallel direction.

From a numerical point of view, the code has a potential to be speed-up with means not investigated in the work performed here. A different configuration of the adaptive step-size controller of the time solver may be speed up the simulations. Preconditioning of the system is also desirable as even a very approximate preconditioner is expected to speed-up the simulations.

20.1 Shortcomings

Finally, we would like to comment on the shortcomings in this thesis which we are aware of. We would like to be as open as possible about the shortcomings of this thesis, so that the reader will be aware that alteration of the shortcomings may affect the obtained results. We will differentiate between two types of shortcomings: Major and minor. The major shortcomings address issues which are believed to have severe impacts on the results, whereas the minor issues are believed to have a lesser impact.

20.1.1 Major

- The plasma is assumed to be isothermal. This assumption would be good if the heat flux were enough to equilibrate the temperature everywhere in the plasma for the time under consideration. However, the heat fluxes are not big enough, and temperature gradients have been found experimentally [50].
- Not all the boundary conditions are physically justified. As mentioned in section 5.5, the boundary conditions opposite to the sheath are justified assuming that this point serves as a stagnation point for the plasma. At the SE, the BC on $u_{i,\parallel}$ and $u_{e,\parallel}$ are

justified in the steady state, and are appropriate in the steady state as well if the potential change at the SE changes faster than the parallel fluid dynamics. However, the rest of the boundary conditions are not physically justified.

20.1.2 Minor

- We have changed the true viscosity in the system with artificial viscosity. This is done as it has been observed that the computation time becomes much longer when using the true viscosity.

Part V

Appendices

Appendix A

Averages

We will here define the averages used in this thesis.

A.1 Velocity average over the distribution function

The weighted velocity average of A is defined as

$$\langle A \rangle_{f_\alpha} \stackrel{\text{def}}{=} \frac{\int_{-\infty}^{\infty} A f_\alpha \, \mathrm{d}^3 v}{\int_{-\infty}^{\infty} f_\alpha \, \mathrm{d}^3 v} = \frac{\int_{-\infty}^{\infty} A f_\alpha \, \mathrm{d}^3 v}{n_\alpha} \tag{A.1}$$

A.2 The poloidal average

The poloidal average of A is defined as

$$\langle f \rangle_\theta \stackrel{\text{def}}{=} \frac{\int_0^{2\pi} f J \, \mathrm{d}\theta}{\int_0^{2\pi} J \, \mathrm{d}\theta} = \frac{J \int_0^{2\pi} A \, \mathrm{d}\theta}{J \int_0^{2\pi} \, \mathrm{d}\theta} = \frac{\int_0^{2\pi} A \, \mathrm{d}\theta}{2\pi}$$

where we have used that the definition of the differential arc length (equation (2.5.46) in [127]).

A.3 The temporal average

The temporal average of A is defined as

$$\langle A \rangle_t \stackrel{\text{def}}{=} \frac{\int_{t_1}^{t_2} A \, \mathrm{d}t}{\int_{t_1}^{t_2} \, \mathrm{d}t} = \frac{\int_{t_1}^{t_2} A \, \mathrm{d}t}{t_2 - t_1}$$

Appendix B

Drift ordering

We will in this section look at big and small terms in the perpendicular momentum equation in eq. (3.6). The motivation for this is to make a drift ordering similar to what is done in [28] and from this get algebraic equations for each order of the perpendicular velocities. We will do so by looking at characteristic scales of the system. Before starting, we will have a brief look at the definition of the gradient length scales and of the quasi-neutrality of the system.

B.1 Gradient length scale

We will here do order of magnitude estimates[1], and will therefore introduce the *gradient length scale*. The gradient scale length serves as an estimate for the size of ∇. That is, it tells us over how large distances there are sharp gradients for a bounded, smooth function. For a field f, the gradient length scale L_f is defined as[2]

$$\frac{1}{L_f} \stackrel{\text{def}}{=} \frac{\|\max\{\text{abs}(\nabla f)\}\|}{\text{abs}\left(f\Big|_{\|\max\{\text{abs}(\nabla f)\}\|}\right)}, \tag{B.1}$$

i.e. short and sharp gradients in f have a short L_f. We can similarly define the temporal scale as

$$\omega_f = \frac{1}{\tau_f} \stackrel{\text{def}}{=} \frac{\max\{\text{abs}(\partial_t f)\}}{\text{abs}\left(f\Big|_{\max\{\text{abs}(\partial_t f)\}}\right)}. \tag{B.2}$$

The definitions in eqs. (B.1) and (B.2) are quite strict, and we will in this thesis use a more approximate estimate for the gradient length scale. Thus, when referring to gradient length scales in this thesis, we will mean "typical" values for the gradient scale lengths,

[1] Easy, approximate ways to estimate some numbers within the same orders of magnitudes as we would have reached by doing a more correct and rigorous study.

[2] Note that the inverse gradient length scale is often denoted k in the literature. This make sense for plane wave perturbations, which happens to have $\frac{1}{L_f} = k$, where k is the inverse wave number. However, in order to avoid ambiguity, we will in this thesis use L_f for the gradient scale length.

so that

$$\nabla \sim \frac{1}{L},$$

where $\sim$ denotes "of same order".

B.2 Quasi-neutrality

To get the condition of whether the system is quasi-neutral or not, we can do an order of magnitude estimate comparison of Zn_i and $Zn_i - n_e$. We find that

$$\frac{Zn_i - n_e}{Zn_i} = \frac{e(Zn_i - n_e)}{eZn_i} = \frac{\varepsilon_0 \nabla \cdot \boldsymbol{E}}{eZn_i} \sim \frac{\varepsilon_0 |E|}{|L_E| eZn_i}. \tag{B.3}$$

We can find an approximate expression for E through Faraday's induction law:

$$\begin{aligned} \nabla \times \boldsymbol{E} &= -\partial_t B \\ \frac{|E|}{|L_E|} &\sim \frac{|B|}{\tau_B} \\ |E| &\sim \frac{|L_E||B|}{\tau_B}. \end{aligned}$$

Inserting this in eq. (B.3) yields

$$\frac{Zn_i - n_e}{Zn_i} \sim \frac{\varepsilon_0 |L_E||B|}{|L_E| eZn_i \tau_B} \frac{m_i Ze}{m_i Ze} = \frac{\omega_{ci}\varepsilon_0}{Zen_i\tau_B} \frac{m_i}{Ze} = \frac{\omega_{ci}}{\tau_B \omega_{pi}^2},$$

where ω_{pi} denotes the ion plasma frequency[3] . We will now assume that the fastest time scales which can occur in our system is much slower than the ion cyclotron frequency. If we therefore set $1/\tau_B \to \omega_{ci}$, we get

$$\frac{Zn_i - n_e}{Zn_i} \simeq \frac{\omega_{ci}^2}{\omega_{pi}^2} = \frac{\omega_{ci}^2}{\omega_{pi}^2}, \tag{B.4}$$

which for our interest is a quantity much smaller than 1.

Equivalently, if we introduce the *normalizing* ion sound speed[4]

$$c_s = \sqrt{\frac{T_e}{m_i}},$$

and the ion hybrid radius (the ion gyro radius at the electron temperature)

$$\rho_s = \frac{c_s}{\omega_{ci}}.$$

[3]This can be interpreted as something like the typical frequency the ions would oscillate with if the ions where perturbed in a completely quiescent plasma.

[4]Although the real ion sound speed is given by $c_s = \sqrt{\frac{T_e + \gamma' T_i}{m_i}}$ $\gamma' = \frac{N+2}{N}$ for N degrees of freedom, we will in this thesis use the symbol c_s for $\sqrt{\frac{T_e}{m_i}}$, as this term frequently pops up in the derivations.

Equation (B.4) can be stated as

$$\frac{Zn_i - n_e}{Zn_i} \simeq \frac{\omega_{ci}^2}{\omega_{pi}^2} = \frac{c_s^2\omega_{ci}^2}{c_s^2\omega_{pi}^2} = \frac{c_s^2}{\rho_s^2\omega_{pi}^2} = \frac{\frac{T_e}{m_i}}{\rho_s^2\frac{n_i Z^2 e^2}{m_i \varepsilon_0}} = \frac{\frac{T_e\varepsilon_0}{n_i Z^2 e^2}}{\rho_s^2} = \frac{\lambda_D^2}{\rho_s^2},$$

where λ_D is the Debye length. The Debye length tells us at what distance an isolated charge is effectively electrically shielded by surrounding charged particles.

In other words, the quasi-neutrality is just a statement of what scales we are looking at. Note that this does not imply that there cannot be large electrical field throughout the plasma, rather that the left hand side of

$$\frac{\nabla \cdot \boldsymbol{E}}{Zn_i} = \frac{e}{\varepsilon_0}\frac{Zn_i - n_e}{Zn_i}$$

is small (as e and ε_0 is of the same order of magnitude). We therefore have

$$n \simeq Zn_i \simeq n_e.$$

B.3 The inertia term

The left hand side of eq. (3.6) reads

$$\begin{aligned}
&\frac{1}{\omega_{c\alpha}}\left(\partial_t \boldsymbol{u}_{\alpha,\perp} + \left[\boldsymbol{u}_{\alpha,\perp} + \boldsymbol{u}_{\alpha,\parallel}\right]\cdot\nabla\boldsymbol{u}_{\alpha,\perp}\right)\\
=&\frac{1}{\omega_{c\alpha}}\left(\partial_t \boldsymbol{u}_{\alpha,\perp} + \left[\boldsymbol{u}_{\alpha,\perp} + \boldsymbol{u}_{\alpha,\parallel}\right]\cdot\nabla\boldsymbol{u}_{\alpha,\perp}\right)\\
=&\frac{1}{\omega_{c\alpha}}\left(\partial_t \boldsymbol{u}_{\alpha,\perp} + \boldsymbol{u}_{\alpha,\perp}\cdot\nabla_\perp\boldsymbol{u}_{\alpha,\perp} + \boldsymbol{u}_{\alpha,\parallel}\cdot\nabla_\parallel\boldsymbol{u}_{\alpha,\perp}\right).
\end{aligned} \tag{B.5}$$

From this, we can extract a characteristic timescale of change of the perpendicular velocity, a characteristic gradient length scale and a characteristic perpendicular velocity. We will use the notation for a field f

$$f = f^c\breve{f},$$

where the superscript f^c denotes the characteristic size of f so that $\breve{f}$ is of $\mathcal{O}(1)$. If we now apply this on eq. (B.5), we get

$$\begin{aligned}
&\frac{1}{\omega_{c\alpha}}\left(\omega_{\alpha,\perp}^c u_{\alpha,\perp}^c \partial_{\breve{t}}\breve{\boldsymbol{u}}_{\alpha,\perp} + \frac{u_{\alpha,\perp}^c u_{\alpha,\perp}^c}{L_{\perp,u_{\alpha,\perp}}}\breve{\boldsymbol{u}}_{\alpha,\perp}\cdot\breve{\nabla}_\perp\breve{\boldsymbol{u}}_{\alpha,\perp} + \frac{u_{\alpha,\perp}^c u_{\alpha,\parallel}^c}{L_{\parallel,u_{\alpha,\perp}}}\breve{\boldsymbol{u}}_{\alpha,\parallel}\cdot\breve{\nabla}_\parallel\breve{\boldsymbol{u}}_{\alpha,\perp}\right)\\
=&\frac{u_{\alpha,\perp}^c}{\omega_{c\alpha}}\left(\omega_{\alpha,\perp}^c \partial_{\breve{t}}\breve{\boldsymbol{u}}_{\alpha,\perp} + \frac{u_{\alpha,\perp}^c}{L_{\perp,u_{\alpha,\perp}}}\breve{\boldsymbol{u}}_{\alpha,\perp}\cdot\breve{\nabla}_\perp\breve{\boldsymbol{u}}_{\alpha,\perp} + \frac{u_{\alpha,\parallel}^c}{L_{\parallel,u_{\alpha,\perp}}}\breve{\boldsymbol{u}}_{\alpha,\parallel}\cdot\breve{\nabla}_\parallel\breve{\boldsymbol{u}}_{\alpha,\perp}\right).
\end{aligned}$$

We now relate the velocities to c_s, so that

$$\lambda \overset{\text{def}}{=} \frac{u^c}{c_s^c}.$$

Further, by using the ion hybrid radius, we get

$$\lambda_{u_{\alpha,\perp}}\frac{c_s^c}{\omega_{c\alpha}}\left(\omega_{\alpha,\perp}^c \partial_{\breve{t}}\breve{\boldsymbol{u}}_{\alpha,\perp} + \lambda_{u_{\alpha,\perp}}\frac{c_s^c}{L_{\perp,u_{\alpha,\perp}}}\breve{\boldsymbol{u}}_{\alpha,\perp}\cdot\breve{\nabla}_\perp\breve{\boldsymbol{u}}_{\alpha,\perp} + \lambda_{u_{\alpha,\parallel}}\frac{L_{\perp,u_{\alpha,\perp}}}{L_{\perp,u_{\alpha,\perp}}}\frac{c_s^c}{L_{\parallel,u_{\alpha,\perp}}}\breve{\boldsymbol{u}}_{\alpha,\parallel}\cdot\breve{\nabla}_\parallel\breve{\boldsymbol{u}}_{\alpha,\perp}\right)$$

$$=\lambda_{u_{\alpha,\perp}}\frac{c_s^c}{\omega_{c\alpha}}\left(\omega^c_{\alpha,\perp}\partial_{\breve{t}}\breve{\boldsymbol{u}}_{\alpha,\perp}+\lambda_{u_{\alpha,\perp}}\frac{\rho_s^c}{L_{\perp,u_{\alpha,\perp}}}\omega^c_{ci}\breve{\boldsymbol{u}}_{\alpha,\perp}\cdot\breve{\nabla}_\perp\breve{\boldsymbol{u}}_{\alpha,\perp}+\lambda_{u_{\alpha,\parallel}}\frac{L_{\perp,u_{\alpha,\perp}}}{L_{\parallel,u_{\alpha,\perp}}}\frac{\rho_s^c}{L_{\perp,u_{\alpha,\perp}}}\omega^c_{ci}\breve{\boldsymbol{u}}_{\alpha,\parallel}\cdot\breve{\nabla}_\parallel\breve{\boldsymbol{u}}_{\alpha,\perp}\right).$$

We will now assume that the scales for the ions and electrons are the same. This is, we are constraining the system in the following way

$$\begin{aligned}\lambda&\sim\lambda_{u_{e,\perp}}\sim\lambda_{u_{i,\perp}}\\ \omega^c&\sim\omega^c_{e,\perp}\sim\omega^c_{i,\perp}\\ L_{\perp,u_\perp}&\sim L_{\perp,u_{e,\perp}}\sim L_{\perp,u_{i,\perp}}\\ L_{\parallel,u_\perp}&\sim L_{\parallel,u_{e,\perp}}\sim L_{\parallel,u_{i,\perp}}.\end{aligned}$$

If we at the same time introduce

$$\frac{\rho_s^c}{L_{\perp,u_\perp}}\stackrel{\text{def}}{=}\gamma,$$

we get

$$\lambda\frac{c_s^c}{\omega_{c\alpha}}\left(\omega^c\partial_{\breve{t}}\breve{\boldsymbol{u}}_{\alpha,\perp}+\lambda\gamma\omega^c_{ci}\breve{\boldsymbol{u}}_{\alpha,\perp}\cdot\breve{\nabla}_\perp\breve{\boldsymbol{u}}_{\alpha,\perp}+\lambda_{u_{\alpha,\parallel}}\frac{L_{\perp,u_{\alpha,\perp}}}{L_{\parallel,u_{\alpha,\perp}}}\gamma\omega^c_{ci}\breve{\boldsymbol{u}}_{\alpha,\parallel}\cdot\breve{\nabla}_\parallel\breve{\boldsymbol{u}}_{\alpha,\perp}\right).\tag{B.6}$$

In order for these terms to be of the same order, we must have that

$$\begin{aligned}\omega^c&\sim\lambda\gamma\omega^c_{ci}\sim\lambda_{u_{\alpha,\parallel}}\frac{L_\perp}{L_{\parallel,u_\perp}}\gamma\omega^c_{ci}\\ \frac{\omega^c}{\omega^c_{ci}}&\sim\lambda\gamma\sim\lambda_{u_{\alpha,\parallel}}\frac{L_\perp}{L_{\parallel,u_\perp}}\gamma.\end{aligned}\tag{B.7}$$

If we assume low frequency turbulence, we must have that

$$\frac{\omega^c}{\omega^c_{ci}}\stackrel{\text{def}}{=}\varepsilon\ll 1.$$

Comparing the two first terms in eq. (B.7) gives

$$\begin{aligned}\frac{\omega^c}{\omega^c_{ci}}&\sim\lambda\gamma\\ \varepsilon&\sim\lambda\gamma\end{aligned}$$

in order to have a balanced restriction between gradient scale lengths and velocities. We can set

$$\begin{aligned}\lambda&\sim\sqrt{\varepsilon}\\ \gamma&\sim\sqrt{\varepsilon}.\end{aligned}$$

Note that if we had started our constraint by saying $\sqrt{\varepsilon}\ll 1$ instead, the non-linear terms would be negligible.

Finally, we put the restriction on the parallel velocity and scale lengths. We now define

$$\frac{L_\perp}{L_{\parallel,u_{\alpha,\perp}}}\stackrel{\text{def}}{=}\zeta.$$

By assuming $u^c_{\alpha,\parallel} \sim c^c_s$, and that

$$\zeta \sim \sqrt{\varepsilon},$$

we find that

$$\lambda_{u_{\alpha,\parallel}} \frac{L_\perp}{L_{\parallel,u_{\alpha,\perp}}} \gamma = \lambda_{u_{\alpha,\parallel}} \zeta \gamma \sim 1 \sqrt{\varepsilon}^2 = \varepsilon.$$

This means that the left hand side of eq. (3.6) can in an order of magnitude estimate be written as (assuming that $\omega_{c\alpha} \sim \omega^c_{c\alpha}$)

$$\begin{aligned}
&\lambda \frac{m_i}{m_i} \frac{c^c_s}{\omega^c_{c\alpha}} \left(\omega^c \partial_{\breve{t}} \breve{\boldsymbol{u}}_{\alpha,\perp} + \lambda \gamma \omega^c_{ci} \breve{\boldsymbol{u}}_{\alpha,\perp} \cdot \breve{\nabla}_\perp \breve{\boldsymbol{u}}_{\alpha,\perp} + \lambda_{u_{\alpha,\parallel}} \frac{L_{\perp,u_{\alpha,\perp}}}{L_{\parallel,u_{\alpha,\perp}}} \gamma \omega^c_{ci} \breve{\boldsymbol{u}}_{\alpha,\parallel} \cdot \breve{\nabla}_\parallel \breve{\boldsymbol{u}}_{\alpha,\perp} \right) \\
&= \lambda \frac{m_\alpha}{m_i} \frac{c^c_s}{\omega^c_{ci}} \left(\omega^c \partial_{\breve{t}} \breve{\boldsymbol{u}}_{\alpha,\perp} + \varepsilon \omega^c_{ci} \breve{\boldsymbol{u}}_{\alpha,\perp} \cdot \breve{\nabla}_\perp \breve{\boldsymbol{u}}_{\alpha,\perp} + \varepsilon \omega^c_{ci} \breve{\boldsymbol{u}}_{\alpha,\parallel} \cdot \breve{\nabla}_\parallel \breve{\boldsymbol{u}}_{\alpha,\perp} \right) \\
&= \lambda \frac{m_\alpha}{m_i} c^c_s \left(\frac{\omega^c}{\omega_{ci}} \partial_{\breve{t}} \breve{\boldsymbol{u}}_{\alpha,\perp} + \varepsilon \breve{\boldsymbol{u}}_{\alpha,\perp} \cdot \breve{\nabla}_\perp \breve{\boldsymbol{u}}_{\alpha,\perp} + \varepsilon \breve{\boldsymbol{u}}_{\alpha,\parallel} \cdot \breve{\nabla}_\parallel \breve{\boldsymbol{u}}_{\alpha,\perp} \right) \\
&= \lambda c^c_s \frac{m_\alpha}{m_i} \varepsilon \left(\partial_{\breve{t}} \breve{\boldsymbol{u}}_{\alpha,\perp} + \breve{\boldsymbol{u}}_{\alpha,\perp} \cdot \breve{\nabla}_\perp \breve{\boldsymbol{u}}_{\alpha,\perp} + \breve{\boldsymbol{u}}_{\alpha,\parallel} \cdot \breve{\nabla}_\parallel \breve{\boldsymbol{u}}_{\alpha,\perp} \right) \\
&= \lambda c^c_s \frac{m_\alpha}{m_i} \varepsilon \breve{\mathrm{d}}_{t,\alpha} \breve{\boldsymbol{u}}_{\alpha,\perp}.
\end{aligned} \tag{B.8}$$

B.4 Pressure, electric field and perpendicular velocities

We will now group the three next terms in eq. (3.6), and we will in the end see that these have the same order under the right assumptions. We have that

$$\begin{aligned}
-\frac{\nabla_\perp p_\alpha}{n_\alpha q_\alpha B} + \frac{\boldsymbol{E}_\perp}{B} + \boldsymbol{u}_{\alpha,\perp} \times \boldsymbol{b} &= - \frac{n^c T^c_\alpha}{L_{\perp,p_\alpha} n^c q_\alpha B^c} \frac{\breve{\nabla}_\perp \breve{p}_\alpha}{\breve{n}_\alpha \breve{B}} + \frac{E^c_\perp}{B^c} \frac{\breve{\boldsymbol{E}}_\perp}{\breve{B}} + \boldsymbol{u}^c_{\alpha,\perp} \breve{\boldsymbol{u}}_{\alpha,\perp} \times \boldsymbol{b} \\
&= - \frac{T^c_\alpha}{L_{\perp,p_\alpha} q_\alpha B^c} \frac{\breve{\nabla}_\perp \breve{p}_\alpha}{\breve{n}_\alpha \breve{B}} + \frac{E^c_\perp}{B^c} \frac{\breve{\boldsymbol{E}}_\perp}{\breve{B}} + \lambda c^c_s \breve{\boldsymbol{u}}_{\alpha,\perp} \times \boldsymbol{b}.
\end{aligned} \tag{B.9}$$

We will now constrain the system further by saying that

$$\begin{aligned}
L_\perp &\sim L_{\perp,p_\alpha} \sim L_{\perp,u_\perp} \\
T^c &\sim T^c_e \sim T^c_i.
\end{aligned}$$

This means that $c^c_s = \sqrt{\frac{T^c}{m_i}}$. Using this in eq. (B.9) gives

$$\begin{aligned}
-\frac{m_i}{m_i} \frac{T^c}{q_\alpha B^c} \frac{1}{L_\perp} \frac{\breve{\nabla}_\perp \breve{p}_\alpha}{\breve{n}_\alpha \breve{B}} + \frac{E^c_\perp}{B^c} \frac{\breve{\boldsymbol{E}}_\perp}{\breve{B}} + \lambda c^c_s \breve{\boldsymbol{u}}_{\alpha,\perp} \times \boldsymbol{b} &= - (c^c_s)^2 \frac{q_i}{q_\alpha} \frac{1}{\omega^c_{ci}} \frac{1}{L_\perp} \frac{\breve{\nabla}_\perp \breve{p}_\alpha}{\breve{n}_\alpha \breve{B}} + \frac{E^c_\perp}{B^c} \frac{\breve{\boldsymbol{E}}_\perp}{\breve{B}} + \lambda c^c_s \breve{\boldsymbol{u}}_{\alpha,\perp} \times \boldsymbol{b} \\
&= - c^c_s \frac{q_i}{q_\alpha} \frac{c^c_s}{\omega^c_{ci}} \frac{1}{L_\perp} \frac{\breve{\nabla}_\perp \breve{p}_\alpha}{\breve{n}_\alpha \breve{B}} + \frac{E^c_\perp}{B^c} \frac{\breve{\boldsymbol{E}}_\perp}{\breve{B}} + \lambda c^c_s \breve{\boldsymbol{u}}_{\alpha,\perp} \times \boldsymbol{b} \\
&= - c^c_s \frac{q_i}{q_\alpha} \frac{\rho^c_s}{L_\perp} \frac{\breve{\nabla}_\perp \breve{p}_\alpha}{\breve{n}_\alpha \breve{B}} + \frac{E^c_\perp}{B^c} \frac{\breve{\boldsymbol{E}}_\perp}{\breve{B}} + \lambda c^c_s \breve{\boldsymbol{u}}_{\alpha,\perp} \times \boldsymbol{b}
\end{aligned}$$

$$= - c_s^c \frac{q_i}{q_\alpha} \gamma \frac{\breve{\nabla}_\perp \breve{p}_\alpha}{\breve{n}_\alpha \breve{B}} + \frac{E_\perp^c}{B^c} \frac{\breve{\boldsymbol{E}}_\perp}{\breve{B}} + \lambda c_s^c \breve{\boldsymbol{u}}_{\alpha,\perp} \times \boldsymbol{b}. \tag{B.10}$$

For these to be of the same order, we must have

$$\gamma c_s^c \sim \frac{E_\perp^c}{B^c} \sim \lambda c_s^c$$
$$\gamma \sim \frac{E_\perp^c}{c_s^c B^c} \sim \lambda.$$

This gives

$$\Xi \overset{\text{def}}{=} \frac{E_\perp^c}{c_s^c B^c} \sim \sqrt{\varepsilon}.$$

Inserting this in eq. (B.10) yields

$$-c_s^c \frac{q_i}{q_\alpha} \gamma \frac{\breve{\nabla}_\perp \breve{p}_\alpha}{\breve{n}_\alpha \breve{B}} + \frac{c_s^c}{c_s^c} \frac{E_\perp^c}{B^c} \frac{\breve{\boldsymbol{E}}_\perp}{\breve{B}} + \lambda c_s^c \breve{\boldsymbol{u}}_{\alpha,\perp} \times \boldsymbol{b} = - c_s^c \left(\gamma \frac{q_i}{q_\alpha} \frac{\breve{\nabla}_\perp \breve{p}_\alpha}{\breve{n}_\alpha \breve{B}} + \frac{1}{c_s^c} \frac{E_\perp^c}{B^c} \frac{\breve{\boldsymbol{E}}_\perp}{\breve{B}} + \lambda \breve{\boldsymbol{u}}_{\alpha,\perp} \times \boldsymbol{b} \right)$$
$$= - c_s^c \sqrt{\varepsilon} \left(\frac{q_i}{q_\alpha} \frac{\breve{\nabla}_\perp \breve{p}_\alpha}{\breve{n}_\alpha \breve{B}} + \frac{\breve{\boldsymbol{E}}_\perp}{\breve{B}} + \breve{\boldsymbol{u}}_{\alpha,\perp} \times \boldsymbol{b} \right).$$

B.5 Collisionalities and sources

Next, we look at the collisionalities and sources of eq. (3.6). We would like these to be (at most) of the same order of magnitude as the inertia terms of appendix B.3. We will assume quasi-neutrality (discussed in appendix B.2), i.e. that

$$n \sim n_e \sim Z n_i.$$

B.5.1 Coulomb collisions

For the electron-ion collisionalities, we find

$$\begin{aligned}
\frac{\boldsymbol{R}_{\beta\to\alpha,\perp}}{n_\alpha q_\alpha B} =& \frac{m_e n_e \nu_{ei} \left(\boldsymbol{u}_{e,\perp} - \boldsymbol{u}_{i,\perp} \right)}{n_\alpha q_\alpha B} \\
=& \frac{m_e \nu_{ei}^c \lambda c_s^c n^c}{q_\alpha n^c B^c} \frac{\breve{n}_\alpha \breve{\nu}_{ei} \left(\breve{\boldsymbol{u}}_{e,\perp} - \breve{\boldsymbol{u}}_{i,\perp} \right)}{\breve{n}_\alpha \breve{B}} \\
=& \lambda c_s^c \frac{m_i q_i}{m_i q_i} \frac{m_e}{q_\alpha B^c} \nu_{ei}^c \frac{\breve{\boldsymbol{R}}_{\beta\to\alpha,\perp}}{\breve{n}_\alpha \breve{B}} \\
=& \lambda c_s^c \frac{q_i}{q_\alpha} \frac{m_e}{m_i} \frac{\nu_{ei}^c}{\omega_{ci}^c} \frac{\breve{\boldsymbol{R}}_{\beta\to\alpha,\perp}}{\breve{n}_\alpha \breve{B}} \qquad \mu \overset{\text{def}}{=} \frac{m_i}{m_e} \\
=& \lambda c_s^c \frac{q_i}{q_\alpha} \frac{1}{\mu} \frac{\nu_{ei}^c}{\omega_{ci}^c} \frac{\breve{\boldsymbol{R}}_{\beta\to\alpha,\perp}}{\breve{n}_\alpha \breve{B}}.
\end{aligned} \tag{B.11}$$

We will now set the ordering condition according to the ions. If the ion equation of eq. (B.11) is to be at the same order as the ion equation of eq. (B.8) we get the condition

$$\begin{aligned}\frac{1}{\mu}\frac{\nu_{ei}^c}{\omega_{ci}^c}\lambda c_s^c \sim& \lambda c_s^c \varepsilon \\ \xi \overset{\text{def}}{=} \frac{1}{\mu}\frac{\nu_{ei}^c}{\omega_{ci}^c} \sim& \varepsilon,\end{aligned}$$

where we have used that the masses in eq. (B.8) cancels, and as all the terms with breve are of order $\mathcal{O}(1)$ Equation (B.11) can therefore be written as

$$\frac{\boldsymbol{R}_{\beta\to\alpha,\perp}}{n_\alpha q_\alpha B} \sim \lambda c_s^c \frac{q_i}{q_\alpha}\xi \frac{\breve{\boldsymbol{R}}_{\beta\to\alpha,\perp}}{\breve{n}_\alpha \breve{B}}.$$

B.5.2 Neutral collisions

For the neutral collisions, we find that

Quasi-neutrality

$$\begin{aligned}\frac{\boldsymbol{R}_{n\to\alpha,\perp}}{n_\alpha q_\alpha B} =& \frac{m_\alpha n_\alpha \nu_{\alpha n}\boldsymbol{u}_{\alpha,\perp}}{n_\alpha q_\alpha B} \\ =& \frac{m_\alpha n^c}{n^c q_\alpha B^c}\nu_{\alpha n}^c \lambda c_s^c \frac{\breve{n}_\alpha \breve{\nu}_{\alpha n}\breve{\boldsymbol{u}}_{\alpha,\perp}}{\breve{n}_\alpha \breve{B}} \\ =& \frac{m_i q_i}{m_i q_i}\frac{m_\alpha}{q_\alpha B^c}\nu_{\alpha n}^c \lambda c_s^c \frac{\breve{\boldsymbol{R}}_{n\to\alpha,\perp}}{\breve{n}_\alpha \breve{B}} \\ =& \frac{q_i}{q_\alpha}\frac{m_\alpha}{m_i}\frac{\nu_{\alpha n}^c}{\omega_{ci}^c}\lambda c_s^c \frac{\breve{\boldsymbol{R}}_{n\to\alpha,\perp}}{\breve{n}_\alpha \breve{B}}.\end{aligned}$$

We will now try to relate ν_{en}^c to ν_{in}^c. For Hydrogen, we can approximate (see appendix C)

$$\nu_{en} \propto \frac{n_n a_0^2 \sqrt{T_e}}{\sqrt{m_e}} \qquad\qquad \nu_{in} \propto \frac{n_n a_0^2 \sqrt{T_i}}{\sqrt{m_i}}.$$

As we have that $T_e \sim T_i$, we get

$$\begin{aligned}\nu_{en} \propto& \frac{\sqrt{m_i}}{\sqrt{m_i}}\frac{n_n a_0^2\sqrt{T_e}}{\sqrt{m_e}} \\ \propto& \frac{\sqrt{m_i}}{\sqrt{m_e}}\frac{n_n a_0^2\sqrt{T_e}}{\sqrt{m_i}} \\ \sim& \frac{\sqrt{m_i}}{\sqrt{m_e}}\nu_{in}.\end{aligned}$$

We will do a crude assumption and assume that the same relation holds for other gases as well, at least within orders of magnitudes. This gives

$$\begin{aligned}\frac{q_i}{q_\alpha}\frac{m_\alpha}{m_i}\frac{\sqrt{m_i}}{\sqrt{m_i}}\frac{\nu_{\alpha n}^c}{\omega_{ci}^c}\lambda c_s^c \frac{\breve{\boldsymbol{R}}_{n\to\alpha,\perp}}{\breve{n}_\alpha \breve{B}} \sim& \frac{q_i}{q_\alpha}\frac{m_\alpha}{m_i}\frac{\sqrt{m_i}}{\sqrt{m_\alpha}}\frac{\nu_{in}^c}{\omega_{ci}^c}\lambda c_s^c \frac{\breve{\boldsymbol{R}}_{n\to\alpha,\perp}}{\breve{n}_\alpha \breve{B}} \\ =& \frac{q_i}{q_\alpha}\frac{\sqrt{m_\alpha}}{\sqrt{m_i}}\frac{\nu_{in}^c}{\omega_{ci}^c}\lambda c_s^c \frac{\breve{\boldsymbol{R}}_{n\to\alpha,\perp}}{\breve{n}_\alpha \breve{B}}. \qquad \text{(B.12)}\end{aligned}$$

Again, we can do an ordering condition according to the ions. The ion equation of eq. (B.12) is of the same order as the ion equation of eq. (B.8) when

$$\begin{aligned}\lambda c_s^c \varepsilon \sim& \frac{\nu_{in}^c}{\omega_{ci}^c}\lambda c_s^c \\ \varepsilon \sim& \frac{\nu_{in}^c}{\omega_{ci}^c} \stackrel{\text{def}}{=} \Theta,\end{aligned}$$

as the charges and masses of equation eq. (B.12) cancels for ions. Thus, the order of magnitude estimate of the neutral collisions can be written

$$\frac{\boldsymbol{R}_{n\to\alpha,\perp}}{n_\alpha q_\alpha B} \sim \lambda c_s^c \frac{q_i}{q_\alpha}\frac{\sqrt{m_\alpha}}{\sqrt{m_i}}\Theta \frac{\breve{\boldsymbol{R}}_{n\to\alpha,\perp}}{\breve{n}_\alpha \breve{B}}.$$

B.5.3 Source terms

By using eq. (2.2), the source term can be written

$$\begin{aligned}\frac{S_{\alpha,n}\boldsymbol{u}_{\alpha,\perp}}{n_\alpha \omega_{c\alpha}} =& \frac{|q_\alpha|}{e}\frac{m_i}{m_i}\frac{S_{i,n}\boldsymbol{u}_{\alpha,\perp}}{n_\alpha\omega_{c\alpha}} \\ =& \frac{|q_\alpha|}{e}\frac{m_\alpha}{m_i}\frac{S_{i,n}\boldsymbol{u}_{\alpha,\perp}}{n_\alpha\omega_{ci}^c} \\ =& \frac{|q_\alpha|}{e}\frac{m_\alpha}{m_i}\frac{S_{i,n}^c c_s^c}{n^c\omega_{ci}^c}\frac{\breve{S}_{i,n}\breve{\boldsymbol{u}}_{\alpha,\perp}}{\breve{n}_\alpha} \\ =& \frac{|q_\alpha|}{e}\frac{m_\alpha}{m_i}\frac{\nu_{S_{i,n}}^c c_s^c}{\omega_{ci}^c}\frac{\breve{S}_{i,n}\breve{\boldsymbol{u}}_{\alpha,\perp}}{\breve{n}_\alpha}.\end{aligned} \tag{B.13}$$

Quasi-neutrality

The order of the ion equation of eq. (B.13) would be of same the same order as eq. (B.8) if

$$\begin{aligned}\lambda c_s^c \varepsilon \sim& \frac{\nu_{S_{i,n}}^c c_s^c}{\omega_{ci}^c} \\ \varepsilon \sim& \frac{1}{\lambda}\frac{\nu_{S_{i,n}}^c}{\omega_{ci}^c} \stackrel{\text{def}}{=} \sigma.\end{aligned}$$

Hence, we have that the source terms give

$$\frac{S_{\alpha,n}\boldsymbol{u}_{\alpha,\perp}}{n_\alpha\omega_{c\alpha}} \sim \lambda c_s^c \frac{|q_\alpha|}{e}\frac{m_\alpha}{m_i}\sigma\frac{\breve{S}_{i,n}\breve{\boldsymbol{u}}_{\alpha,\perp}}{\breve{n}_\alpha}.$$

Notice the change from m_i to m_e due to the definition of σ.

B.6 Viscosities

Finally, we deal with the viscosities in our drift ordering. If we assume constant viscosity coefficients $\eta_{\alpha,N}$, where $N \in \{1,2,3,4\}$, and that $\eta_{\alpha,0}$ is dominating (see appendix D), we get[5]

$$\left(\nabla\cdot\overline{\overline{\boldsymbol{\pi}}}_\alpha\right)_\perp \simeq \frac{2}{3}\eta_{\alpha,0}\left(\boldsymbol{e}_x\partial_x\partial_\parallel u_{\alpha,\parallel} + \boldsymbol{e}_y\partial_y\partial_\parallel u_{\alpha,\parallel}\right). \tag{B.14}$$

[5] Note that although we use drift ordering in appendix D, the results should still be approximately valid as we already have constrained our system in a way so that the terms in appendix B.4 are of leading order.

We will now assume that

$$\partial_x u_{\alpha,\parallel} \sim \partial_y u_{\alpha,\parallel} \sim \frac{1}{L_{\perp,u_{\alpha,\parallel}}} u^c_{\alpha,\parallel},$$

and also that

$$L_{\perp,u_{\alpha,\parallel}} \sim L_\perp L_{\parallel,u_{\alpha,\parallel}} \sim L_{\parallel,u_{\alpha,\perp}} \sim L_\parallel.$$

This means that

$$\begin{aligned}
\boldsymbol{e}_x\partial_x\partial_\parallel u_{\alpha,\parallel} + \boldsymbol{e}_y\partial_y\partial_\parallel u_{\alpha,\parallel} \sim& \frac{c_s^c}{L_\perp L_\parallel}\left(\boldsymbol{e}_x\partial_{\breve{x}}\partial_{\breve{\parallel}}\breve{u}_{\alpha,\parallel} + \boldsymbol{e}_y\partial_{\breve{y}}\partial_{\breve{\parallel}}\breve{u}_{\alpha,\parallel}\right)\\
=& c_s^c\frac{L_\perp}{L_\perp}\frac{1}{L_\perp L_\parallel}\left(\boldsymbol{e}_x\partial_{\breve{x}}\partial_{\breve{\parallel}}\breve{u}_{\alpha,\parallel} + \boldsymbol{e}_y\partial_{\breve{y}}\partial_{\breve{\parallel}}\breve{u}_{\alpha,\parallel}\right)\\
=& \rho_s^c\omega_{ci}^c\frac{1}{L_\perp^2}\zeta\left(\boldsymbol{e}_x\partial_{\breve{x}}\partial_{\breve{\parallel}}\breve{u}_{\alpha,\parallel} + \boldsymbol{e}_y\partial_{\breve{y}}\partial_{\breve{\parallel}}\breve{u}_{\alpha,\parallel}\right)\\
=& \omega_{ci}^c\frac{1}{L_\perp}\gamma\zeta\left(\boldsymbol{e}_x\partial_{\breve{x}}\partial_{\breve{\parallel}}\breve{u}_{\alpha,\parallel} + \boldsymbol{e}_y\partial_{\breve{y}}\partial_{\breve{\parallel}}\breve{u}_{\alpha,\parallel}\right). \qquad \text{(B.15)}
\end{aligned}$$

If we insert eq. (B.15) into eq. (B.14), we obtain

$$\begin{aligned}
\left(\nabla\cdot\overline{\overline{\boldsymbol{\pi}}}_\alpha\right)_\perp \simeq& \frac{2}{3}\eta_{\alpha,0}\left(\boldsymbol{e}_x\partial_x\partial_\parallel u_{\alpha,\parallel} + \boldsymbol{e}_y\partial_y\partial_\parallel u_{\alpha,\parallel}\right)\\
\sim& \frac{2}{3}\omega_{ci}^c\frac{1}{L_\perp}\gamma\zeta\eta_{\alpha,0}^c\breve{\eta}_{\alpha,0}\left(\boldsymbol{e}_x\partial_{\breve{x}}\partial_{\breve{\parallel}}\breve{u}_{\alpha,\parallel} + \boldsymbol{e}_y\partial_{\breve{y}}\partial_{\breve{\parallel}}\breve{u}_{\alpha,\parallel}\right)\\
=& \frac{2}{3}\omega_{ci}^c\frac{1}{L_\perp}\gamma\zeta\eta_{\alpha,0}^c\left(\breve{\nabla}\cdot\breve{\overline{\overline{\boldsymbol{\pi}}}}_\alpha\right)_\perp.
\end{aligned}$$

From appendix D we have that $\eta_{\alpha,0} = \dfrac{C_{\eta_{\alpha,0}} n_\alpha T_\alpha}{\nu_{\alpha i}}$, where $C_{\eta_{e,0}} = 0.73$ and $C_{\eta_{i,0}} = 0.96\sqrt{2}$. As we have assumed $T_e \sim T_i$, and since $\nu_{ei} \propto \dfrac{1}{\sqrt{m_e}}$ and $\nu_{\alpha i} \propto \dfrac{1}{\sqrt{m_i}}$ we have that $\nu_{\alpha i} \sim \dfrac{\sqrt{m_e}}{\sqrt{m_\alpha}}\nu_{ei}$. This gives

$$\begin{aligned}
\frac{2}{3}\omega_{ci}^c\frac{1}{L_\perp}\gamma\zeta\eta_{\alpha,0}^c\left(\breve{\nabla}\cdot\breve{\overline{\overline{\boldsymbol{\pi}}}}_\alpha\right)_\perp =& \frac{2}{3}\omega_{ci}^c\frac{1}{L_\perp}\gamma\zeta\frac{C_{\eta_{\alpha,0}} n^c T_\alpha^c}{\frac{\sqrt{m_e}}{\sqrt{m_\alpha}}\nu_{ei}^c}\left(\breve{\nabla}\cdot\breve{\overline{\overline{\boldsymbol{\pi}}}}_\alpha\right)_\perp\\
=& \frac{2}{3}C_{\eta_{\alpha,0}}\omega_{ci}^c\frac{1}{L_\perp}\gamma\zeta\frac{\sqrt{m_\alpha}}{\sqrt{m_e}}\frac{n^c T_\alpha^c}{\nu_{ei}^c}\left(\breve{\nabla}\cdot\breve{\overline{\overline{\boldsymbol{\pi}}}}_\alpha\right)_\perp.
\end{aligned}$$

Thus

$$\begin{aligned}
\frac{\left(\nabla\cdot\overline{\overline{\boldsymbol{\pi}}}_\alpha\right)_\perp}{n_\alpha q_\alpha B} \sim& \frac{2}{3}C_{\eta_{\alpha,0}}\omega_{ci}^c\frac{1}{L_\perp}\gamma\zeta\frac{1}{n^c q_\alpha B^c}\frac{\sqrt{m_\alpha}}{\sqrt{m_e}}\frac{n^c T_\alpha^c}{\nu_{ei}^c}\frac{\left(\breve{\nabla}\cdot\breve{\overline{\overline{\boldsymbol{\pi}}}}_\alpha\right)_\perp}{\breve{n}_\alpha\breve{B}}\\
=& \frac{2}{3}C_{\eta_{\alpha,0}}\omega_{ci}^c\frac{1}{L_\perp}\gamma\zeta\frac{m_i}{m_i}\frac{q_i}{q_i}\frac{1}{q_\alpha B^c}\frac{\sqrt{m_\alpha}}{\sqrt{m_e}}\frac{m_e}{m_e}\frac{T_\alpha^c}{\nu_{ei}^c}\frac{\left(\breve{\nabla}\cdot\breve{\overline{\overline{\boldsymbol{\pi}}}}_\alpha\right)_\perp}{\breve{n}_\alpha\breve{B}}\\
=& \frac{2}{3}C_{\eta_{\alpha,0}}\omega_{ci}^c\frac{1}{L_\perp}\gamma\zeta\frac{m_e}{m_i}\frac{q_i}{q_\alpha}\frac{1}{\omega_{ci}^c}\frac{\sqrt{m_\alpha}}{\sqrt{m_e}}\left(c_s^c\right)^2\frac{1}{\nu_{ei}^c}\frac{\left(\breve{\nabla}\cdot\breve{\overline{\overline{\boldsymbol{\pi}}}}_\alpha\right)_\perp}{\breve{n}_\alpha\breve{B}}
\end{aligned}$$

$$
\begin{aligned}
&= \frac{2}{3} C_{\eta_{\alpha,0}} \left(c_s^c\right)^2 \frac{1}{L_\perp} \gamma\zeta \frac{1}{\mu} \frac{q_i}{q_\alpha} \frac{\sqrt{m_\alpha}}{\sqrt{m_e}} \frac{1}{\nu_{ei}^c} \frac{\left(\breve{\nabla} \cdot \breve{\overline{\overline{\boldsymbol{\pi}}}}_\alpha\right)_\perp}{\breve{n}_\alpha \breve{B}} \\
&= \frac{2}{3} C_{\eta_{\alpha,0}} c_s^c \rho_s^c \omega_{ci}^c \frac{q_i}{q_\alpha} \frac{\sqrt{m_\alpha}}{\sqrt{m_e}} \frac{1}{L_\perp} \gamma\zeta \frac{1}{\mu} \frac{1}{\nu_{ei}^c} \frac{\left(\breve{\nabla} \cdot \breve{\overline{\overline{\boldsymbol{\pi}}}}_\alpha\right)_\perp}{\breve{n}_\alpha \breve{B}} \\
&= \frac{2}{3} C_{\eta_{\alpha,0}} c_s^c \frac{q_i}{q_\alpha} \frac{\sqrt{m_\alpha}}{\sqrt{m_e}} \frac{\rho_s^c}{L_\perp} \gamma\zeta \frac{1}{\mu} \frac{\omega_{ci}^c}{\nu_{ei}^c} \frac{\left(\breve{\nabla} \cdot \breve{\overline{\overline{\boldsymbol{\pi}}}}_\alpha\right)_\perp}{\breve{n}_\alpha \breve{B}} \\
&= \frac{2}{3} C_{\eta_{\alpha,0}} c_s^c \frac{q_i}{q_\alpha} \frac{\sqrt{m_\alpha}}{\sqrt{m_e}} \gamma^2 \zeta\xi \frac{\left(\breve{\nabla} \cdot \breve{\overline{\overline{\boldsymbol{\pi}}}}_\alpha\right)_\perp}{\breve{n}_\alpha \breve{B}}.
\end{aligned}
$$

B.7 The ordering of the terms

Before we order the terms in eq. (3.6), let us briefly recapitulate the size of the non-dimensional terms

$$
\begin{array}{llll}
\varepsilon \overset{\text{def}}{=} \dfrac{\omega^c}{\omega_{ci}^c} \ll 1 & \xi \overset{\text{def}}{=} \dfrac{1}{\mu} \dfrac{\nu_{ei}^c}{\omega_{ci}^c} \sim \varepsilon & \Theta \overset{\text{def}}{=} \dfrac{\nu_{in}^c}{\omega_{ci}^c} \sim \varepsilon & \sigma \overset{\text{def}}{=} \dfrac{1}{\lambda} \dfrac{\nu_{S_{i,n}}^c}{\omega_{ci}^c} \sim \varepsilon \\
\lambda \overset{\text{def}}{=} \dfrac{u^c}{c_s^c} \sim \sqrt{\varepsilon} & \gamma \overset{\text{def}}{=} \dfrac{\rho_s^c}{L_\perp} \sim \sqrt{\varepsilon} & \zeta \overset{\text{def}}{=} \dfrac{L_\perp}{L_\parallel} \sim \sqrt{\varepsilon} & \Xi \overset{\text{def}}{=} \dfrac{E_\perp^c}{c_s^c B^c} \sim \sqrt{\varepsilon},
\end{array}
$$

where we have assumed

$$
\begin{array}{llll}
T_e^c \sim T_i^c & \omega_{u_{e,\perp}}^c \sim \omega_{u_{i,\perp}}^c & n_e \sim Z n_i & u_{e,\perp} \sim u_{i,\perp} \\
L_{\perp,u_{e,\perp}} \sim L_{\perp,u_{i,\perp}} & L_{\perp,p_\alpha} \sim L_{\perp,u_{\alpha,\perp}} & u_{e,\parallel} \sim u_{i,\parallel}, &
\end{array}
$$

The order of magnitude estimate of eq. (3.6) now yields

$$
\begin{aligned}
\lambda c_s^c \frac{m_\alpha}{m_i} \varepsilon \breve{\mathrm{d}}_{t,\alpha} \breve{\boldsymbol{u}}_{\alpha,\perp} = &- c_s^c \sqrt{\varepsilon} \left(\frac{q_i}{q_\alpha} \frac{\breve{\nabla}_\perp \breve{p}_\alpha}{\breve{n}_\alpha \breve{B}} + \frac{\breve{\boldsymbol{E}}_\perp}{\breve{B}} + \breve{\boldsymbol{u}}_{\alpha,\perp} \times \boldsymbol{b} \right) \\
&- \frac{2}{3} C_{\eta_{\alpha,0}} c_s^c \frac{q_i}{q_\alpha} \frac{\sqrt{m_\alpha}}{\sqrt{m_e}} \gamma^2 \zeta\xi \frac{\left(\breve{\nabla} \cdot \breve{\overline{\overline{\boldsymbol{\pi}}}}_\alpha\right)_\perp}{\breve{n}_\alpha \breve{B}} \\
&+ \lambda c_s^c \frac{q_i}{q_\alpha} \xi \frac{\breve{\boldsymbol{R}}_{\beta\to\alpha,\perp}}{\breve{n}_\alpha \breve{B}} + \lambda c_s^c \frac{q_i}{q_\alpha} \frac{\sqrt{m_\alpha}}{\sqrt{m_i}} \Theta \frac{\breve{\boldsymbol{R}}_{n\to\alpha,\perp}}{\breve{n}_\alpha \breve{B}} - \lambda c_s^c \frac{|q_\alpha|}{e} \frac{m_\alpha}{m_i} \sigma \frac{\breve{S}_{i,n} \breve{\boldsymbol{u}}_{\alpha,\perp}}{\breve{n}_\alpha} \\
\frac{m_\alpha}{m_i} \varepsilon \breve{\mathrm{d}}_{t,\alpha} \breve{\boldsymbol{u}}_{\alpha,\perp} = &- \frac{\sqrt{\varepsilon}}{\lambda} \left(\frac{q_i}{q_\alpha} \frac{\breve{\nabla}_\perp \breve{p}_\alpha}{\breve{n}_\alpha \breve{B}} + \frac{\breve{\boldsymbol{E}}_\perp}{\breve{B}} + \breve{\boldsymbol{u}}_{\alpha,\perp} \times \boldsymbol{b} \right) \\
&- \frac{2}{3} \frac{1}{\lambda} C_{\eta_{\alpha,0}} \frac{q_i}{q_\alpha} \frac{\sqrt{m_\alpha}}{\sqrt{m_e}} \gamma^2 \zeta\xi \frac{\left(\breve{\nabla} \cdot \breve{\overline{\overline{\boldsymbol{\pi}}}}_\alpha\right)_\perp}{\breve{n}_\alpha \breve{B}} \\
&+ \frac{q_i}{q_\alpha} \xi \frac{\breve{\boldsymbol{R}}_{\beta\to\alpha,\perp}}{\breve{n}_\alpha \breve{B}} + \frac{q_i}{q_\alpha} \frac{\sqrt{m_\alpha}}{\sqrt{m_i}} \Theta \frac{\breve{\boldsymbol{R}}_{n\to\alpha,\perp}}{\breve{n}_\alpha \breve{B}} - \frac{|q_\alpha|}{e} \frac{m_\alpha}{m_i} \sigma \frac{\breve{S}_{i,n} \breve{\boldsymbol{u}}_{\alpha,\perp}}{\breve{n}_\alpha}
\end{aligned}
$$

$$
\begin{aligned}
\frac{m_\alpha}{m_i}\varepsilon \breve{\mathrm{d}}_{t,\alpha}\breve{\boldsymbol{u}}_{\alpha,\perp} =& -\frac{\sqrt{\varepsilon}}{\sqrt{\varepsilon}}\left(\frac{q_i}{q_\alpha}\frac{\breve{\nabla}_\perp \breve{p}_\alpha}{\breve{n}_\alpha \breve{B}} + \frac{\breve{\boldsymbol{E}}_\perp}{\breve{B}} + \breve{\boldsymbol{u}}_{\alpha,\perp}\times \boldsymbol{b}\right) \\
&- \frac{2}{3}\frac{\varepsilon^2\sqrt{\varepsilon}}{\sqrt{\varepsilon}} C_{\eta_{\alpha,0}}\frac{q_i}{q_\alpha}\frac{\sqrt{m_\alpha}}{\sqrt{m_e}}\frac{\left(\breve{\nabla}\cdot\breve{\overline{\overline{\boldsymbol{\pi}}}}_\alpha\right)_\perp}{\breve{n}_\alpha\breve{B}} \\
&+ \varepsilon\frac{q_i}{q_\alpha}\frac{\breve{\boldsymbol{R}}_{\beta\to\alpha,\perp}}{\breve{n}_\alpha\breve{B}} + \varepsilon\frac{q_i}{q_\alpha}\frac{\sqrt{m_\alpha}}{\sqrt{m_i}}\frac{\breve{\boldsymbol{R}}_{n\to\alpha,\perp}}{\breve{n}_\alpha\breve{B}} - \varepsilon\frac{|q_\alpha|}{e}\frac{m_\alpha}{m_i}\frac{\breve{S}_{i,n}\breve{\boldsymbol{u}}_{\alpha,\perp}}{\breve{n}_\alpha} \\
=& -\left(\frac{q_i}{q_\alpha}\frac{\breve{\nabla}_\perp \breve{p}_\alpha}{\breve{n}_\alpha \breve{B}} + \frac{\breve{\boldsymbol{E}}_\perp}{\breve{B}} + \breve{\boldsymbol{u}}_{\alpha,\perp}\times \boldsymbol{b}\right) \\
&- \varepsilon^2\frac{2}{3} C_{\eta_{\alpha,0}}\frac{q_i}{q_\alpha}\frac{\sqrt{m_\alpha}}{\sqrt{m_e}}\frac{\left(\breve{\nabla}\cdot\breve{\overline{\overline{\boldsymbol{\pi}}}}_\alpha\right)_\perp}{\breve{n}_\alpha\breve{B}} \\
&+ \varepsilon\left(\frac{q_i}{q_\alpha}\frac{\breve{\boldsymbol{R}}_{\beta\to\alpha,\perp}}{\breve{n}_\alpha\breve{B}} + \frac{q_i}{q_\alpha}\frac{\sqrt{m_\alpha}}{\sqrt{m_i}}\frac{\breve{\boldsymbol{R}}_{n\to\alpha,\perp}}{\breve{n}_\alpha\breve{B}} - \frac{|q_\alpha|}{e}\frac{m_\alpha}{m_i}\frac{\breve{S}_{i,n}\breve{\boldsymbol{u}}_{\alpha,\perp}}{\breve{n}_\alpha}\right).
\end{aligned}
\tag{B.16}
$$

Notice that the quantities in the breves are of order $\mathcal{O}(1)$, so that the only large or small terms appear in front of the terms in breve. From this we can for example see that the electron inertia term is small compared to most other terms and can probably be neglected. We also note that although the ion viscosity is small, it is questionable if it should be neglected.

Appendix C

Collisions

We will here derive an estimate for the elastic electron-neutral and ion-neutral collision frequencies, in the same way as the electron-ion and the ion-ion collision frequency is derived in [128]. In order to do so, we start by calculating the frictional force experienced by species α as it is drifting with respect to the stationary species β. We have

$$\boldsymbol{F}_\alpha = -n_\alpha m_\alpha \langle n_\beta \sigma_{\alpha\beta} v \boldsymbol{v} \rangle_\alpha$$

where $\langle \cdot \rangle_\alpha$ denotes the average over the drifting distribution function of species α, and $\sigma_{\alpha\beta}$ is the cross section of the process. If we let the particles stream towards the stationary target along z, so that the fluid velocity $\boldsymbol{u}_\alpha = u_z \boldsymbol{e}_z$, we get

$$\begin{aligned}
f_\alpha =& \frac{n_\alpha}{(2\pi)^{3/2} v_{th,\alpha}^3} \exp\left(-\frac{[\boldsymbol{v}-\boldsymbol{u}]^2}{2v_{th,\alpha}^2} \right) && \text{Assume } \boldsymbol{u} \ll v_{th,\alpha}^2 \\
\simeq& \frac{n_\alpha}{(2\pi)^{3/2} v_{th,\alpha}^3} \left(\exp\left[-\frac{(\boldsymbol{v}-\boldsymbol{u})^2}{2v_{th,\alpha}^2} \right]\Bigg|_{\boldsymbol{u}=0} + \boldsymbol{u} \cdot \left[-2\frac{(\boldsymbol{v}-\boldsymbol{u})}{2v_{th,\alpha}^2}(-1) \exp\left(-\frac{(\boldsymbol{v}-\boldsymbol{u})^2}{2v_{th,\alpha}^2} \right) \right]_{\boldsymbol{u}=0} \right) \\
=& \frac{n_\alpha}{(2\pi)^{3/2} v_{th,\alpha}^3} \left(\exp\left[-\frac{\boldsymbol{v}^2}{2v_{th,\alpha}^2} \right] + 2\frac{\boldsymbol{u}\cdot\boldsymbol{v}}{2v_{th,\alpha}^2} \exp\left[-\frac{\boldsymbol{v}^2}{2v_{th,\alpha}^2} \right] \right) \\
=& \frac{n_\alpha}{(2\pi)^{3/2} v_{th,\alpha}^3} \left(1 + \frac{2u_z v_z}{2v_{th,\alpha}^2} \right) \exp\left(-\frac{\boldsymbol{v}^2}{2v_{th,\alpha}^2} \right) \\
=& \left(1 + \frac{u_z v_z}{v_{th,\alpha}^2} \right) f_{\alpha,0}
\end{aligned}$$

where $\boldsymbol{v}$ denotes the particle velocity, $f_{\alpha,0}$ denotes the unshifted Maxwellian and

$$v_{th,\alpha} \stackrel{\text{def}}{=} \sqrt{\frac{T_\alpha}{m_\alpha}}.$$

Thus, the friction force in the direction of the drifting is

$$\begin{aligned}
F_{\alpha,z} =& -n_\alpha m_\alpha \langle n_\beta \sigma_{\alpha\beta} v v_z \rangle_\alpha \\
\simeq& -n_\alpha m_\alpha \frac{n_\beta}{n_\alpha} \iiint \left(1 + \frac{u_z v_z}{v_{th,\alpha}^2} \right) f_{\alpha,0} \sigma_{\alpha\beta} v v_z \mathrm{d}^3 v
\end{aligned}$$

$$
\begin{aligned}
&= - n_\alpha m_\alpha \frac{n_\beta}{n_\alpha}\left(u_z \iiint \frac{v_z}{v_{th,\alpha}^2} f_{\alpha,0}\sigma_{\alpha\beta} v v_z \mathrm{d}^3 v + \iiint f_{\alpha,0}\sigma_{\alpha\beta} v v_z \mathrm{d}^3 v\right) && \text{Second integral even in } v_z \\
&= - n_\alpha m_\alpha \frac{n_\beta}{n_\alpha}\left(u_z \iiint \frac{v_z^2}{v_{th,\alpha}^2} f_{\alpha,0}\sigma_{\alpha\beta} v \mathrm{d}^3 v\right) && \text{Integral over } v_z^2 \text{ is 1/3 of integral over } v^2 \text{ due to spherical symmetry} \\
&= - n_\alpha m_\alpha \frac{n_\beta}{n_\alpha}\frac{1}{3}\left(u_z \iiint \frac{1}{v_{th,\alpha}^2} f_{\alpha,0}\sigma_{\alpha\beta} v^3 \mathrm{d}^3 v\right) \\
&= - n_\alpha m_\alpha u_z \frac{n_\beta}{n_\alpha}\frac{1}{3}\frac{1}{v_{th,\alpha}^2} \iiint f_{\alpha,0}\sigma_{\alpha\beta} v^3 \mathrm{d}^3 v && \text{Spherical coordinates} \\
&= - n_\alpha m_\alpha u_z \frac{n_\beta}{n_\alpha}\frac{1}{3}\frac{1}{v_{th,\alpha}^2} \int_0^\infty \int_0^{2\pi} \int_0^\pi f_{\alpha,0}\sigma_{\alpha\beta} v^5 \sin\theta \mathrm{d}\theta \mathrm{d}\phi \mathrm{d}v \\
&= - n_\alpha m_\alpha u_z \frac{n_\beta}{n_\alpha}\frac{1}{3}\frac{1}{v_{th,\alpha}^2} 4\pi \int_0^\infty f_{\alpha,0}\sigma_{\alpha\beta} v^5 \mathrm{d}v \\
&= - n_\alpha m_\alpha u_z \nu_{\alpha\beta,\text{stationary target}}
\end{aligned}
$$

where we here have defined the averaged collision frequency

$$
\begin{aligned}
\nu_{\alpha\beta,\text{stationary target}} &\overset{\text{def}}{=} \frac{n_\beta}{n_\alpha}\frac{1}{3}\frac{1}{v_{th,\alpha}^2} 4\pi \int_0^\infty f_{\alpha,0}\sigma_{\alpha\beta} v^5 \mathrm{d}v \\
&= \frac{n_\beta}{n_\alpha}\frac{4\pi}{3v_{th,\alpha}^2} \int_0^\infty \frac{n_\alpha}{(2\pi)^{3/2} v_{th,\alpha}^3} \exp\left(-\frac{\boldsymbol{v}^2}{2v_{th,\alpha}^2}\right) \sigma_{\alpha\beta} v^5 \mathrm{d}v \\
&= \frac{n_\beta 4\pi}{3(2\pi)^{3/2} v_{th,\alpha}^5} \int_0^\infty \exp\left(-\frac{\boldsymbol{v}^2}{2v_{th,\alpha}^2}\right) \sigma_{\alpha\beta} v^5 \mathrm{d}v
\end{aligned}
$$

The subscript $_{\text{stationary target}}$ will be dropped from here on.

For a $\sigma_{\alpha\beta}$ constant in v, the integral reads

$$
\begin{aligned}
\nu_{\alpha\beta,\text{ Constant }\sigma} &= \frac{n_\beta 4\pi}{3(2\pi)^{3/2} v_{th,\alpha}^5} \sigma_{\alpha\beta,\text{ Constant}} \int_0^\infty \exp\left(-\frac{\boldsymbol{v}^2}{2v_{th,\alpha}^2}\right) v^5 \mathrm{d}v \\
&= \frac{n_\beta 4\pi}{3(2\pi)^{3/2} v_{th,\alpha}^5} \sigma_{\alpha\beta,\text{ Constant}} 8 v_{th,\alpha}^6 \\
&= \frac{8\sqrt{2}}{3}\frac{n_\beta}{\sqrt{\pi}} v_{th,\alpha} \sigma_{\alpha\beta,\text{ Constant}} \\
&= \frac{8\sqrt{2}}{3}\frac{n_\beta}{\sqrt{\pi}} \sqrt{\frac{T_\alpha}{m_\alpha}} \sigma_{\alpha\beta,\text{ Constant}}
\end{aligned} \tag{C.1}
$$

C.1 Electron collisions

C.1.1 Electron ion collision

Using the cross section for electron ion collisions

$$
\sigma_{ei} = \frac{Z^2 e^4 \ln\Lambda}{4\pi\varepsilon_0^2 m_e^2 v^4} \qquad \ln\Lambda = \ln\left(\frac{12\pi n \lambda_D^3}{Z}\right) \qquad \lambda_D = \sqrt{\frac{\varepsilon_0 T_e}{n_e e^2}}
$$

yields

$$\begin{aligned}
\nu_{ei} =& \frac{n_i 4\pi}{3(2\pi)^{3/2} v_{th,e}^5} \int_0^\infty \exp\left(-\frac{\boldsymbol{v}^2}{2v_{th,e}^2}\right) \frac{Z^2 e^4 \ln\Lambda}{4\pi\varepsilon_0^2 m_e^2 v^4} v^5 \mathrm{d}v \\
=& \frac{n_i}{2^{1/2} 6\pi^{3/2} v_{th,e}^5} \frac{Z^2 e^4 \ln\Lambda}{\varepsilon_0^2 m_e^2} \int_0^\infty \exp\left(-\frac{\boldsymbol{v}^2}{2v_{th,e}^2}\right) v \mathrm{d}v \\
=& \frac{2}{2} \frac{n_i}{2^{1/2} 6\pi^{3/2} v_{th,e}^5} \frac{Z^2 e^4 \ln\Lambda}{\varepsilon_0^2 m_e^2} v_{th,e}^2 \\
=& \frac{2^{1/2} n_i Z^2 e^4 \ln\Lambda}{12\pi^{3/2} e_0^2 m_e^2 \left(\sqrt{\frac{T_e}{m_e}}\right)^3} \\
=& \frac{2^{1/2} n_i Z^2 e^4 \ln\Lambda}{12\pi^{3/2} e_0^2 m_e^{1/2} T_e^{3/2}}
\end{aligned}$$

C.1.2 Electron hydrogen collision

A rough estimate for the hydrogen collision cross section can be obtained from the Bohr radius, and reads

$$\sigma_{en_\mathrm{H}} = \pi a_0^2$$

inserting this in eq. (C.1) yields

$$\nu_{en_\mathrm{H}} = \frac{8\sqrt{2}}{3} \frac{n_{n_\mathrm{H}}}{\sqrt{\pi}} \sqrt{\frac{T_e}{m_e}} \pi a_0^2 = \frac{8\sqrt{2}}{3} \sqrt{\pi} n_{n_\mathrm{H}} a_0^2 \sqrt{\frac{T_e}{m_e}}$$

C.1.3 Electron argon collisions

A formula for the electron argon cross section is given in [129]. The cross section can be integrated numerically, as done in [50]. A sixth order polynomial which fits the integrated data in the range $0.1 - 10\,\mathrm{eV}$ reads[1]

$$\nu_{en_\mathrm{Ar}}[\mathrm{s}^{-1}] = \frac{n_\mathrm{Ar}[\mathrm{m}^{-3}]}{2.5 \cdot 10^{19}[\mathrm{m}^{-3}]} \tag{C.2}$$

$$\begin{aligned}
&(\quad 33640.349990 \cdot T_e[\mathrm{eV}]^0 - 33174.059200 \cdot T_e[\mathrm{eV}]^1 && \text{(C.3)} \\
&+ 642273.100111 \cdot T_e[\mathrm{eV}]^2 - 188328.743082 \cdot T_e[\mathrm{eV}]^3 && \text{(C.4)} \\
&+ 25742.288823 \cdot T_e[\mathrm{eV}]^4 - 1784.118597 \cdot T_e[\mathrm{eV}]^5 + 50.336945 \cdot T_e[\mathrm{eV}]^6) && \text{(C.5)}
\end{aligned}$$

C.2 Ion collisions

C.2.1 Ion-ion collisions

The analysis done above was valid when the target was stationary with respect to the moving particles. This is a fairly good approximation when the stationary particles are

[1] Data from [50] has been read using [130] to obtain these values.

much heavier than the moving particles. Hence, the derivation of the average ion-ion collision frequency or the average ion-neutral collision frequency is strictly not valid. However, according to [128], the analysis yields the correct result within factors of orders of unity.

One could do the analysis by going to the center of mass frame (which in the end gives an additional factor $2^{-1/2}$) and use relative velocities. This gives

$$\nu_{ii} = \frac{n_i Z^2 e^4 \ln \Lambda}{12\pi^{3/2} e_0^2 m_i^{1/2} T_i^{3/2}}$$

C.2.2 Ion-hydrogen collisions

As the mass of the neutral atom is approximately the same as the ion mass (as we are considering neutrals of the same species as the plasma), we get for the ion-neutral collision

$$\nu_{in_{\mathrm{H}}} = \frac{8}{3}\sqrt{\pi} n_{n_{\mathrm{H}}} a_0^2 \frac{\sqrt{T_i}}{\sqrt{m_H}}$$

C.2.3 Ion-argon collisions

Although several atomic processes are involved when an Argon ion collides with an Argon atom in the ground state, most can be neglected under temperatures under 100 eV. The charge exchange reaction and the elastic collisions dominated, and are approximately equally big [131]. The following formula for the cross section is given in [132] for the charge exchange reaction $\mathrm{Ar} + \mathrm{Ar}^+ \rightarrow \mathrm{Ar}^+ + \mathrm{Ar}$ at low energies

$$\sigma_{ce}[\mathrm{m}^2] = 4.8 \cdot 10^{-19}[\mathrm{m}^2] \left(1 + 0.14 \ln\left[\frac{1[\mathrm{eV}]}{T_i[\mathrm{eV}]}\right]\right)^2$$

so that

$$\sigma_{in_{\mathrm{Ar}}}[\mathrm{m}^2] \simeq 9.6 \cdot 10^{-19}[\mathrm{m}^2] \left(1 + 0.14 \ln\left[\frac{1[\mathrm{eV}]}{T_i[\mathrm{eV}]}\right]\right)^2$$

Inserting this into eq. (C.1) gives us

$$\nu_{in_{\mathrm{Ar}}} \simeq \frac{8\sqrt{2}}{3} \frac{n_{\mathrm{Ar}}}{\sqrt{\pi}} \sqrt{\frac{T_i[\mathrm{J}]}{m_{\mathrm{Ar}}}} 9.6 \cdot 10^{-19}[\mathrm{m}^2] \left(1 + 0.14 \ln\left[\frac{1[\mathrm{eV}]}{T_i[\mathrm{eV}]}\right]\right)^2$$

Appendix D

The viscosity tensor

We will here make an estimate of the viscosities in the system. We should note that this estimate is rather crude. Following [24], (which again is based on [25]), we see that in a Cartesian coordinate system the rate of strain tensor is given by

$$W_\alpha^{ij} \stackrel{\text{def}}{=} \partial_j u_\alpha^i + \partial_i u_\alpha^j - \frac{2}{3}\delta_i^j \nabla \cdot \boldsymbol{u}_\alpha,$$

which gives

$$\begin{aligned}
W^{xx} + W^{yy} =& \partial_x u_\alpha^x + \partial_x u_\alpha^x - \frac{2}{3}\nabla \cdot \boldsymbol{u}_\alpha + \partial_y u_\alpha^y + \partial_y u_\alpha^y - \frac{2}{3}\nabla \cdot \boldsymbol{u}_\alpha \\
=& 2\partial_x u_\alpha^x + 2\partial_y u_\alpha^y - \frac{4}{3}\nabla \cdot \boldsymbol{u}_\alpha \\
=& 2\left(\partial_x u_\alpha^x + \partial_y u_\alpha^y - \frac{2}{3}\left[\partial_x u_\alpha^x + \partial_y u_\alpha^y + \partial_z u_\alpha^z\right]\right) \\
=& \frac{2}{3}\left(\partial_x u_\alpha^x + \partial_y u_\alpha^y - 2\partial_z u_\alpha^z\right) \\
W^{xx} - W^{yy} =& \partial_x u_\alpha^x + \partial_x u_\alpha^x - \frac{2}{3}\nabla \cdot \boldsymbol{u}_\alpha - \partial_y u_\alpha^y - \partial_y u_\alpha^y + \frac{2}{3}\nabla \cdot \boldsymbol{u}_\alpha \\
=& 2\partial_x u_\alpha^x - 2\partial_y u_\alpha^y \\
=& 2\left(\partial_x u_\alpha^x - \partial_y u_\alpha^y\right) \\
W^{zz} =& \partial_z u_\alpha^z + \partial_z u_\alpha^z - \frac{2}{3}\nabla \cdot \boldsymbol{u}_\alpha \\
=& 2\partial_z u_\alpha^z - \frac{2}{3}\left(\partial_x u_\alpha^x + \partial_y u_\alpha^y + \partial_z u_\alpha^z\right) \\
=& \frac{4}{3}\partial_z u_\alpha^z - \frac{2}{3}\left(\partial_x u_\alpha^x + \partial_y u_\alpha^y\right) \\
W^{xy} =& \partial_x u_\alpha^y + \partial_y u_\alpha^x \\
W^{xz} =& \partial_x u_\alpha^z + \partial_z u_\alpha^x \\
W^{yz} =& \partial_y u_\alpha^z + \partial_z u_\alpha^y.
\end{aligned}$$

We use this to calculate the components of the stress tensor. We get

$$\begin{aligned}
\pi_\alpha^{xx} =& -\frac{\eta_{\alpha,0}}{2}\left(W^{xx} + W^{yy}\right) - \frac{\eta_{\alpha,1}}{2}\left(W^{xx} - W^{yy}\right) - \eta_{\alpha,3} W^{xy} \\
=& -\frac{\eta_{\alpha,0}}{2}\frac{2}{3}\left(\partial_x u_\alpha^x + \partial_y u_\alpha^y - 2\partial_z u_\alpha^z\right) - \frac{\eta_{\alpha,1}}{2} 2\left(\partial_x u_\alpha^x - \partial_y u_\alpha^y\right) - \eta_{\alpha,3}\left(\partial_x u_\alpha^y + \partial_y u_\alpha^x\right)
\end{aligned}$$

$$
\begin{aligned}
&= -\frac{\eta_{\alpha,0}}{3}\left(\partial_x u_\alpha^x + \partial_y u_\alpha^y - 2\partial_z u_\alpha^z\right) - \eta_{\alpha,1}\left(\partial_x u_\alpha^x - \partial_y u_\alpha^y\right) - \eta_{\alpha,3}\left(\partial_x u_\alpha^y + \partial_y u_\alpha^x\right)\\
\pi_\alpha^{yy} &= -\frac{\eta_{\alpha,0}}{2}\left(W^{xx} + W^{yy}\right) - \frac{\eta_{\alpha,1}}{2}\left(W^{yy} - W^{xx}\right) + \eta_{\alpha,3}W^{xy}\\
&= -\frac{\eta_{\alpha,0}}{2}\frac{2}{3}\left(\partial_x u_\alpha^x + \partial_y u_\alpha^y - 2\partial_z u_\alpha^z\right) + \frac{\eta_{\alpha,1}}{2}2\left(\partial_x u_\alpha^x - \partial_y u_\alpha^y\right) + \eta_{\alpha,3}\left(\partial_x u_\alpha^y + \partial_y u_\alpha^x\right)\\
&= -\frac{\eta_{\alpha,0}}{3}\left(\partial_x u_\alpha^x + \partial_y u_\alpha^y - 2\partial_z u_\alpha^z\right) + \eta_{\alpha,1}\left(\partial_x u_\alpha^x - \partial_y u_\alpha^y\right) + \eta_{\alpha,3}\left(\partial_x u_\alpha^y + \partial_y u_\alpha^x\right)\\
\pi_\alpha^{zz} &= -\eta_{\alpha,0}W^{zz}\\
&= -\eta_{\alpha,0}\left(\frac{4}{3}\partial_z u_\alpha^z - \frac{2}{3}\left[\partial_x u_\alpha^x + \partial_y u_\alpha^y\right]\right)\\
&= -\frac{2\eta_{\alpha,0}}{3}\left(2\partial_z u_\alpha^z - \left[\partial_x u_\alpha^x + \partial_y u_\alpha^y\right]\right)\\
\pi_\alpha^{xy} = \pi_\alpha^{yx} &= -\eta_{\alpha,1}W^{xy} + \frac{\eta_{\alpha,3}}{2}\left(W^{xx} - W^{yy}\right)\\
&= -\eta_{\alpha,1}\left(\partial_x u_\alpha^y + \partial_y u_\alpha^x\right) + \frac{\eta_{\alpha,3}}{2}2\left(\partial_x u_\alpha^x - \partial_y u_\alpha^y\right)\\
&= -\eta_{\alpha,1}\left(\partial_x u_\alpha^y + \partial_y u_\alpha^x\right) + \eta_{\alpha,3}\left(\partial_x u_\alpha^x - \partial_y u_\alpha^y\right)\\
\pi_\alpha^{xz} = \pi_\alpha^{zx} &= -\eta_{\alpha,2}W^{xz} - \eta_{\alpha,4}W^{yz}\\
&= -\eta_{\alpha,2}\left(\partial_x u_\alpha^z + \partial_z u_\alpha^x\right) - \eta_{\alpha,4}\left(\partial_y u_\alpha^z + \partial_z u_\alpha^y\right)\\
\pi_\alpha^{yz} = \pi_\alpha^{zy} &= -\eta_{\alpha,2}W^{yz} + \eta_{\alpha,4}W^{xz}\\
&= -\eta_{\alpha,2}\left(\partial_y u_\alpha^z + \partial_z u_\alpha^y\right) + \eta_{\alpha,4}\left(\partial_x u_\alpha^z + \partial_z u_\alpha^x\right).
\end{aligned}
$$

By taking the divergence of this, we find that

Cartesian system

$$
\begin{aligned}
\nabla\cdot\overline{\overline{\boldsymbol{\pi}}}_\alpha =& \boldsymbol{e}^i\cdot\partial_i\pi_\alpha^{jk}\boldsymbol{e}_j\boldsymbol{e}_k\\
=& \boldsymbol{e}^i\cdot\boldsymbol{e}_j\boldsymbol{e}_k\partial_i\pi_\alpha^{jk}\\
=& \boldsymbol{e}_k\partial_i\pi_\alpha^{ik}\\
=& \quad \boldsymbol{e}_x\left(\partial_x\pi_\alpha^{xx} + \partial_y\pi_\alpha^{yx} + \partial_z\pi_\alpha^{zx}\right)\\
&+ \boldsymbol{e}_y\left(\partial_x\pi_\alpha^{xy} + \partial_y\pi_\alpha^{yy} + \partial_z\pi_\alpha^{zy}\right)\\
&+ \boldsymbol{e}_z\left(\partial_x\pi_\alpha^{xz} + \partial_y\pi_\alpha^{yz} + \partial_z\pi_\alpha^{zz}\right)\\
=& \quad \boldsymbol{e}_x\Big(\partial_x\left[-\frac{\eta_{\alpha,0}}{3}\left(\partial_x u_\alpha^x + \partial_y u_\alpha^y - 2\partial_z u_\alpha^z\right) - \eta_{\alpha,1}\left(\partial_x u_\alpha^x - \partial_y u_\alpha^y\right) - \eta_{\alpha,3}\left(\partial_x u_\alpha^y + \partial_y u_\alpha^x\right)\right]\\
&\qquad +\partial_y\left[-\eta_{\alpha,1}\left(\partial_x u_\alpha^y + \partial_y u_\alpha^x\right) + \eta_{\alpha,3}\left(\partial_x u_\alpha^x - \partial_y u_\alpha^y\right)\right]\\
&\qquad +\partial_z\left[-\eta_{\alpha,2}\left(\partial_x u_\alpha^z + \partial_z u_\alpha^x\right) - \eta_{\alpha,4}\left(\partial_y u_\alpha^z + \partial_z u_\alpha^y\right)\right]\Big)\\
&+ \boldsymbol{e}_y\Big(\partial_x\left[-\eta_{\alpha,1}\left(\partial_x u_\alpha^y + \partial_y u_\alpha^x\right) + \eta_{\alpha,3}\left(\partial_x u_\alpha^x - \partial_y u_\alpha^y\right)\right]\\
&\qquad +\partial_y\left[-\frac{\eta_{\alpha,0}}{3}\left(\partial_x u_\alpha^x + \partial_y u_\alpha^y - 2\partial_z u_\alpha^z\right) + \eta_{\alpha,1}\left(\partial_x u_\alpha^x - \partial_y u_\alpha^y\right) + \eta_{\alpha,3}\left(\partial_x u_\alpha^y + \partial_y u_\alpha^x\right)\right]\\
&\qquad +\partial_z\left[-\eta_{\alpha,2}\left(\partial_y u_\alpha^z + \partial_z u_\alpha^y\right) + \eta_{\alpha,4}\left(\partial_x u_\alpha^z + \partial_z u_\alpha^x\right)\right]\Big)\\
&+ \boldsymbol{e}_z\Big(\partial_x\left[-\eta_{\alpha,2}\left(\partial_x u_\alpha^z + \partial_z u_\alpha^x\right) - \eta_{\alpha,4}\left(\partial_y u_\alpha^z + \partial_z u_\alpha^y\right)\right]\\
&\qquad +\partial_y\left[-\eta_{\alpha,2}\left(\partial_y u_\alpha^z + \partial_z u_\alpha^y\right) + \eta_{\alpha,4}\left(\partial_x u_\alpha^z + \partial_z u_\alpha^x\right)\right]\\
&\qquad +\partial_z\left[-\frac{2\eta_{\alpha,0}}{3}\left(2\partial_z u_\alpha^z - \left[\partial_x u_\alpha^x + \partial_y u_\alpha^y\right]\right)\right]\Big).
\end{aligned}
$$

Up until this point, we have not made any assumptions of the $\overline{\overline{\boldsymbol{\pi}}}$ tensor, that has not already been made in [25]. Here, however, we simplify the expression (on the cost of

accuracy), and say that we assume that the viscosities are constants (note that we already did such an approximation when calculating the resistivity in section 4.1.2). We then get

$$
\begin{aligned}
\nabla\cdot\overline{\overline{\boldsymbol{\pi}}}_\alpha \simeq\quad & \boldsymbol{e}_x\Big(-\frac{\eta_{\alpha,0}}{3}\left[\partial_x^2u_\alpha^x+\partial_x\partial_yu_\alpha^y-2\partial_x\partial_zu_\alpha^z\right]-\eta_{\alpha,1}\left[\partial_x^2u_\alpha^x-\partial_x\partial_yu_\alpha^y\right]-\eta_{\alpha,3}\left[\partial_x^2u_\alpha^y+\partial_x\partial_yu_\alpha^x\right]\\
&-\eta_{\alpha,1}\left[\partial_y\partial_xu_\alpha^y+\partial_y^2u_\alpha^x\right]+\eta_{\alpha,3}\left[\partial_y\partial_xu_\alpha^x-\partial_y^2u_\alpha^y\right]\\
&-\eta_{\alpha,2}\left[\partial_z\partial_xu_\alpha^z+\partial_z^2u_\alpha^x\right]-\eta_{\alpha,4}\left[\partial_z\partial_yu_\alpha^z+\partial_z^2u_\alpha^y\right]\Big)\\
&+\boldsymbol{e}_y\Big(-\eta_{\alpha,1}\left[\partial_x^2u_\alpha^y+\partial_x\partial_yu_\alpha^x\right]+\eta_{\alpha,3}\left[\partial_x^2u_\alpha^x-\partial_x\partial_yu_\alpha^y\right]\\
&-\frac{\eta_{\alpha,0}}{3}\left[\partial_y\partial_xu_\alpha^x+\partial_y^2u_\alpha^y-2\partial_y\partial_zu_\alpha^z\right]+\eta_{\alpha,1}\left[\partial_y\partial_xu_\alpha^x-\partial_y^2u_\alpha^y\right]+\eta_{\alpha,3}\left[\partial_y\partial_xu_\alpha^y+\partial_y^2u_\alpha^x\right]\\
&-\eta_{\alpha,2}\left[\partial_z\partial_yu_\alpha^z+\partial_z^2u_\alpha^y\right]+\eta_{\alpha,4}\left[\partial_z\partial_xu_\alpha^z+\partial_z^2u_\alpha^x\right]\Big)\\
&+\boldsymbol{e}_z\Big(-\eta_{\alpha,2}\left[\partial_x^2u_\alpha^z+\partial_x\partial_zu_\alpha^x\right]-\eta_{\alpha,4}\left[\partial_x\partial_yu_\alpha^z+\partial_x\partial_zu_\alpha^y\right]\\
&-\eta_{\alpha,2}\left[\partial_y^2u_\alpha^z+\partial_y\partial_zu_\alpha^y\right]+\eta_{\alpha,4}\left[\partial_y\partial_xu_\alpha^z+\partial_y\partial_zu_\alpha^x\right]\\
&-\frac{2\eta_{\alpha,0}}{3}\left[2\partial_z^2u_\alpha^z-(\partial_z\partial_xu_\alpha^x+\partial_z\partial_yu_\alpha^y)\right]\Big)\\
=\quad & \boldsymbol{e}_x\Big(-\frac{\eta_{\alpha,0}}{3}\left[\partial_x^2u_\alpha^x+\partial_x\partial_yu_\alpha^y-2\partial_x\partial_zu_\alpha^z\right]-\eta_{\alpha,1}\left[\left(\partial_x^2+\partial_y^2\right)u_\alpha^x\right]\\
&-\eta_{\alpha,3}\left[\left(\partial_x^2+\partial_y^2\right)u_\alpha^y\right]\\
&-\eta_{\alpha,2}\left[\partial_z\partial_xu_\alpha^z+\partial_z^2u_\alpha^x\right]-\eta_{\alpha,4}\left[\partial_z\partial_yu_\alpha^z+\partial_z^2u_\alpha^y\right]\Big)\\
&+\boldsymbol{e}_y\Big(-\frac{\eta_{\alpha,0}}{3}\left[\partial_y\partial_xu_\alpha^x+\partial_y^2u_\alpha^y-2\partial_y\partial_zu_\alpha^z\right]-\eta_{\alpha,1}\left[\left(\partial_x^2+\partial_y^2\right)u_\alpha^y\right]\\
&+\eta_{\alpha,3}\left[\left(\partial_x^2+\partial_y^2\right)u_\alpha^x\right]\\
&-\eta_{\alpha,2}\left[\partial_z\partial_yu_\alpha^z+\partial_z^2u_\alpha^y\right]+\eta_{\alpha,4}\left[\partial_z\partial_xu_\alpha^z+\partial_z^2u_\alpha^x\right]\Big)\\
&+\boldsymbol{e}_z\Big(-\frac{2\eta_{\alpha,0}}{3}\left[2\partial_z^2u_\alpha^z-(\partial_z\partial_xu_\alpha^x+\partial_z\partial_yu_\alpha^y)\right]\\
&-\eta_{\alpha,2}\left[\left(\partial_x^2+\partial_y^2\right)u_\alpha^z+\partial_x\partial_zu_\alpha^x+\partial_y\partial_zu_\alpha^y\right]\\
&+\eta_{\alpha,4}\left[\partial_y\partial_zu_\alpha^x-\partial_x\partial_zu_\alpha^y\right]\Big).
\end{aligned}
$$

We have that

$$
\begin{aligned}
&\eta_{0,i}=\frac{0.96n_iT_i\sqrt{2}}{\nu_{ii}} \quad \eta_{1,i}=\frac{3n_iT_i\nu_{ii}}{10\omega_{ci}^2\sqrt{2}} \quad \eta_{2,i}=\frac{12n_iT_i\nu_{ii}}{10\omega_{ci}^2\sqrt{2}} \quad \eta_{3,i}=\frac{n_iT_i}{2\omega_{ci}} \quad \eta_{4,i}=\frac{n_iT_i}{\omega_{ci}}\\
&\eta_{0,e}=\frac{0.73n_eT_e}{\nu_{ei}} \quad \eta_{1,e}=0.51\frac{n_eT_e\nu_{ei}}{\omega_{ce}^2} \quad \eta_{2,e}=2.04\frac{n_eT_e\nu_{ei}}{\omega_{ce}^2} \quad \eta_{3,e}=\frac{n_eT_e}{2\omega_{ce}} \quad \eta_{4,e}=\frac{n_eT_e}{\omega_{ce}},
\end{aligned}
$$

and from fig. D.1 we see that $\eta_{\alpha,0}\gg\eta_{\alpha,j}\quad j\in\{1,2,3,4\}$ for the parameter range that we are interested in. Although one should look at the different terms as a whole, one could again make an approximation and say that only the terms $\propto\eta_{\alpha,0}$ are contributing to the viscosity tensor. Note that this may not be a bad approximation due to the difference in magnitude for the different ηs. This would yield

$$
\begin{aligned}
\nabla\cdot\overline{\overline{\boldsymbol{\pi}}}_\alpha \simeq\quad & \boldsymbol{e}_x\left(-\frac{\eta_{\alpha,0}}{3}\left[\partial_x^2u_\alpha^x+\partial_x\partial_yu_\alpha^y-2\partial_x\partial_zu_\alpha^z\right]\right)\\
&+\boldsymbol{e}_y\left(-\frac{\eta_{\alpha,0}}{3}\left[\partial_y\partial_xu_\alpha^x+\partial_y^2u_\alpha^y-2\partial_y\partial_zu_\alpha^z\right]\right)\\
&+\boldsymbol{e}_z\left(-\frac{2\eta_{\alpha,0}}{3}\left[2\partial_z^2u_\alpha^z-(\partial_z\partial_xu_\alpha^x+\partial_z\partial_yu_\alpha^y)\right]\right).
\end{aligned}
$$

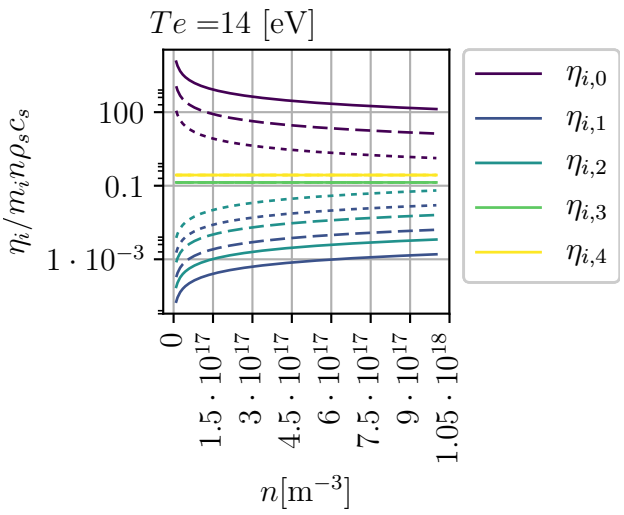

(a) The normalized ion viscosities as a function of n

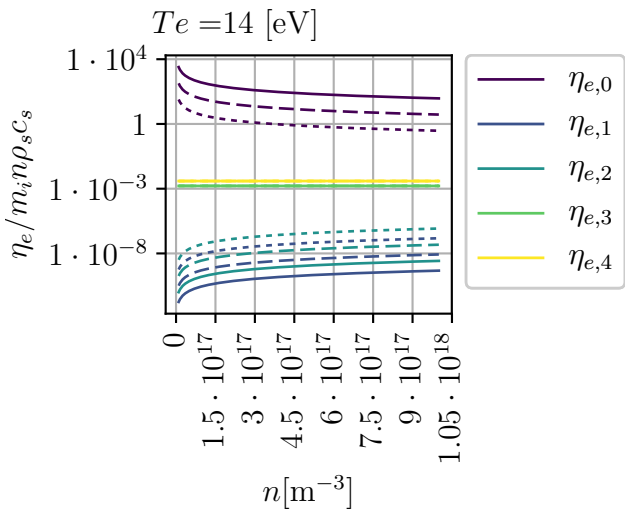

(b) The normalized electron viscosities as a function of n

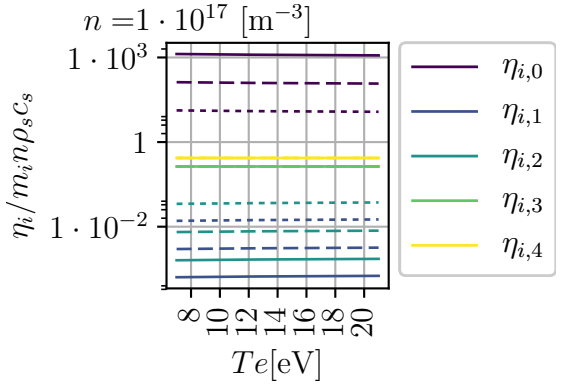

(c) The normalized ion viscosities as a function of T_e

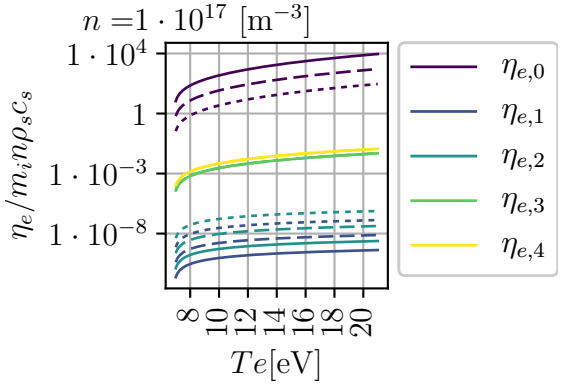

(d) The normalized electron viscosities as a function of T_e

Figure D.1: η scans. The solid lines are taken at $B = 1$ T, the dashed at $B = 0.1$ T, and the dotted at $B = 0.01$ T

We will use that, to first order, only the $\boldsymbol{E} \times \boldsymbol{B}$ drift advects particles perpendicularly. In Clebsch coordinates, we have that $\boldsymbol{u}_E$ is given by eq. (I.1), which means that we get

$$\begin{aligned}
\boldsymbol{u}_E =& \frac{1}{JB}\left(-g_{zz}\boldsymbol{e}_y\partial_x + g_{zz}\boldsymbol{e}_x\partial_y\right)\phi = \frac{1}{B}\left(-\boldsymbol{e}_y\partial_x + \boldsymbol{e}_x\partial_y\right)\phi \\
u_E^x =& \frac{1}{B}\partial_y\phi \qquad u_E^y = -\frac{1}{B}\partial_x\phi \qquad u_E^z = 0.
\end{aligned}$$

We note that we are operating with a left-handed coordinate system. Using this, we find that

$$\begin{aligned}
\nabla\cdot\overline{\overline{\boldsymbol{\pi}}}_\alpha \simeq\ & \boldsymbol{e}_x\left(-\frac{\eta_{\alpha,0}}{3}\left[\frac{1}{B}\partial_x^2\partial_y\phi - \frac{1}{B}\partial_x^2\partial_y\phi - 2\partial_x\partial_z u_\alpha^z\right]\right) \\
&+ \boldsymbol{e}_y\left(-\frac{\eta_{\alpha,0}}{3}\left[\frac{1}{B}\partial_y^2\partial_x\phi - \frac{1}{B}\partial_y^2\partial_x\phi - 2\partial_y\partial_z u_\alpha^z\right]\right) \\
&+ \boldsymbol{e}_z\left(-\frac{2\eta_{\alpha,0}}{3}\left[2\partial_z^2 u_\alpha^z - \frac{1}{B}\left(\partial_z\partial_x\partial_y\phi - \partial_z\partial_y\partial_x\phi\right)\right]\right)
\end{aligned}$$

$$= \quad \boldsymbol{e}_x \frac{2\eta_{\alpha,0}}{3}\partial_x\partial_z u_\alpha^z + \boldsymbol{e}_y \frac{2\eta_{\alpha,0}}{3}\partial_y\partial_z u_\alpha^z - \boldsymbol{e}_z \frac{4\eta_{\alpha,0}}{3}\partial_z^2 u_\alpha^z. \tag{D.1}$$

We found in appendix B that the viscosity played a minor role in the perpendicular velocities (assuming that $\mu\varepsilon^2$ is small in the ion equation). We will, however, retain the parallel part of $\nabla \cdot \overline{\overline{\boldsymbol{\pi}}}_\alpha$ (that is $\frac{4\eta_{\alpha,0}}{3}\partial_z^2 u_\alpha^z$) in the parallel momentum equations in the derivations to see how this term propagates through the set of equations. It the end we will drop the terms and use artificial viscosity instead.

Appendix E

The electrostatic approximation

We will here address the electrostatic approximation. Note that in all cases, we assume that the magnetic field perturbation from the plasma is negligible as compared with the background magnetic field. The approximation states that $\partial_t \boldsymbol{B} \sim 0$, which through the Maxwell-Faraday equation states that $\nabla \times \boldsymbol{E} \sim 0$. In general, we have that the $\boldsymbol{E}$ field can be expressed through the potentials

$$\boldsymbol{E} = -\nabla\phi - \partial_t \boldsymbol{A}, \tag{E.1}$$

(see for example [133, 134]). The magnetic potential carries with it a degree of freedom, and we are free to use the Coulomb gauge without loss of generality. That is

$$\nabla \cdot \boldsymbol{A} = 0.$$

We note that eq. (E.1) fulfills Gauss' law and Maxwell-Faraday's law of induction, and that $\partial_t \boldsymbol{A} = 0$ implies an electrostatic condition. With the Coulomb gauge, we have that Ampère's circuit law reads

$$\begin{aligned} \nabla \times \nabla \times \boldsymbol{A} =& \nabla \times \boldsymbol{B} \\ \nabla^2 \boldsymbol{A} - \nabla(\nabla \cdot \boldsymbol{A}) =& \mu_0 \boldsymbol{j} \\ \frac{\nabla^2 \boldsymbol{A}}{\mu_0} =& \boldsymbol{j} \end{aligned} \tag{E.2}$$

Low frequency

Coloumb gauge

in the low frequency case. Notice that $\nabla^2 \boldsymbol{A} = \boldsymbol{j}\mu_0$ is nothing but three Poisson equations, so that the solution can be written in terms of Green's functions (assuming that the currents vanishes at infinity) as

$$\boldsymbol{A}(\boldsymbol{r}, t) = \frac{\mu_0}{4\pi} \int_V \frac{\boldsymbol{j}(\boldsymbol{r}', t')}{|\boldsymbol{r} - \boldsymbol{r}'|} \, \mathrm{d}^3 \boldsymbol{r}', \tag{E.3}$$

$$\partial_t \boldsymbol{A}(\boldsymbol{r}, t) = \frac{\mu_0}{4\pi} \int_V \partial_t \left(\frac{\boldsymbol{j}(\boldsymbol{r}', t')}{|\boldsymbol{r} - \boldsymbol{r}'|} \right) \mathrm{d}^3 \boldsymbol{r}', \tag{E.4}$$

where $\boldsymbol{r}$ is the general position vector, $\boldsymbol{r'}$ is the position of the current distribution and $t' = t - \dfrac{|\boldsymbol{r} - \boldsymbol{r}'|}{c}$ is the retarded time. We now see that $\partial_t \boldsymbol{A}$ is large whenever the time derivative of the current is large.

E.1 Small time derivatives of the perpendicular magnetic potential

In the drift ordering, we have assumed that the evolution of the perpendicular ion and electron velocity are of the same order of magnitude and small compared to ω_{ci}. Assuming that the evolution of the density is also restricted by this time evolution[1], the perpendicular current would also be restricted. This would lead to a small $\partial_t \boldsymbol{A}_\perp$, which then could be neglected in the perpendicular set of equations as the ordering would imply that $-\nabla_\perp \phi$ would be of a higher order of magnitude.

E.2 Small time derivatives of the parallel magnetic potential

Next, we will check if $\partial_t \boldsymbol{A}_\parallel$ is small by comparing it with the other terms of eq. (5.14)[2]. Writing out the $E_\parallel$-term in eq. (5.14) gives

$$\begin{aligned}
\partial_t j_\parallel =& - e\boldsymbol{u}_E \cdot \nabla j_\parallel \\
& - en\left(u_{i,\parallel}\partial_\parallel u_{i,\parallel} - u_{e,\parallel}\partial_\parallel u_{e,\parallel}\right) - \frac{j_\parallel}{n}\partial_\parallel\left(nu_{e,\parallel}\right) \\
& + \frac{e}{m_e}T_e\partial_\parallel n + \frac{e^2}{m_e}n\left(-\partial_\parallel\phi - \partial_t\boldsymbol{A}\right) - 0.51\nu_{ei}j_\parallel \\
& + en\left(\nu_{en}u_{e,\parallel} - \nu_{in}u_{i,\parallel}\right) - \frac{e}{m_e}\frac{4\eta_{e,0}}{3}\partial_z^2 u_{e,\parallel}.
\end{aligned} \tag{E.5}$$

From eq. (E.2), we get that

$$\begin{aligned}
\frac{\nabla^2\boldsymbol{A}}{\mu_0} =& \boldsymbol{j} \\
\boldsymbol{b}\cdot\frac{\nabla^2\boldsymbol{A}}{\mu_0} =& \boldsymbol{b}\cdot\boldsymbol{j} \qquad \text{Assuming } \partial_i\boldsymbol{b} = 0 \\
\frac{\nabla^2 A_\parallel}{\mu_0} =& j_\parallel,
\end{aligned} \tag{E.6}$$

which means that the left hand side of eq. (E.5) can be written

$$\partial_t j_\parallel = \partial_t \frac{\nabla^2 A_\parallel}{\mu_0}.$$

As these three terms can be expressed in terms of $A_\parallel$, we can now readily can compare $\partial_t A_\parallel$ with $\partial_t j_\parallel$ or $\nu_{ei} j_\parallel$ to check if the term is small. Thus, the $\partial_t A_\parallel$ term can be neglected if

$$\partial_t \frac{\nabla_\perp^2 A_\parallel}{\mu_0} \gg \frac{ne^2}{m_e}\partial_t A_\parallel,$$

[1] Note that if this was not the case, the fast evolution of n would still couple to the evolution of $\boldsymbol{u}$ through the set of equations.

[2] A similar approach is done in [50].

which using order of magnitude estimates gives

$$\begin{aligned}
\frac{1}{\tau_{A_\parallel}}\frac{A_\parallel}{L_{A_\parallel}\mu_0} &\gg \frac{ne^2}{m_e}\frac{1}{\tau_{A_\parallel}}A_\parallel \\
\frac{1}{L_{A_\parallel}^2\mu_0} &\gg \frac{ne^2}{m_e} \\
\frac{1}{L_{A_\parallel}^2} &\gg \frac{2}{2}\frac{m_i^2}{m_i^2}\frac{B^2}{B^2}\frac{T_e}{T_e}\frac{e^2}{m_e}n\mu_0 \\
\frac{1}{L_{A_\parallel}^2} &\gg \frac{1}{2}\frac{m_i}{m_e}\frac{m_i}{T_e}\frac{e^2B^2}{m_i^2}\frac{2n\mu_0 T_e}{B^2} \\
\frac{1}{L_{A_\parallel}^2} &\gg \frac{1}{2}\mu\frac{\omega_{ci}^2}{c_s^2}\beta \\
\frac{\rho_s^2}{L_{A_\parallel}^2} &\gg \frac{1}{2}\mu\beta, \qquad \text{(E.7)}
\end{aligned}$$

where the plasma beta $\beta = \dfrac{nT_e}{\frac{B^2}{2\mu_0}}$ can be interpreted as the electron kinetic pressure over the magnetic pressure. Also, the $\partial_t A_\parallel$ term can be neglected if

$$0.51\nu_{ei}j_\parallel \gg \frac{ne^2}{m_e}\partial_t A_\parallel.$$

By using orders of magnitude estimates and eq. (E.6), we get

$$\begin{aligned}
0.51\nu_{ei}\frac{\nabla^2 A_\parallel}{\mu_0} &\gg \frac{ne^2}{m_e}\partial_t A_\parallel \\
0.51\nu_{ei}\frac{A_\parallel}{L_{A_\parallel}\mu_0} &\gg \frac{ne^2}{m_e}\frac{1}{\tau_{A_\parallel}}A_\parallel \\
\frac{1}{L_{A_\parallel}^2} &\gg \frac{ne^2}{m_e}\frac{\mu_0}{0.51\nu_{ei}}\omega_{A_\parallel} \qquad \text{As eq. (E.7)} \\
\frac{\rho_s^2}{L_{A_\parallel}^2} &\gg \frac{1}{2}\frac{\omega_{A_\parallel}}{0.51\nu_{ei}}\mu\beta.
\end{aligned}$$

Note that even though $\partial_t A_\parallel$ is small, it may improve numerical stability to include it.

Appendix F

Parallel current equation with electromagnetic effects

We will here continue the derivation of eq. (5.18) when keeping the $\partial_t A_\parallel$ term. If we assume that $\nabla_\perp^2 A_\parallel \gg \nabla_\parallel^2 A_\parallel$, we have from eq. (E.2) that

$$\begin{aligned} \boldsymbol{b}\cdot\boldsymbol{J} \simeq & \boldsymbol{b}\cdot\frac{\nabla_\perp^2\boldsymbol{A}}{\mu_0} \qquad \partial_i\boldsymbol{b}\simeq 0 \\ j_\parallel \simeq & \frac{\nabla_\perp^2 A_\parallel}{\mu_0}. \end{aligned}$$

We can normalize Ampère's law, using $\boldsymbol{A} = \breve{\boldsymbol{A}}\frac{T_e}{ec_s}$, which gives

$$\begin{aligned} en_0c_sj_\parallel =& \frac{1}{\mu_0}\frac{1}{\rho_s^2}\frac{T_e}{ec_s}\nabla_\perp^2 A_\parallel \\ =& \frac{1}{\mu_0}\frac{\omega_{ci}^2}{c_s^2}\frac{T_e}{ec_s}\nabla_\perp^2 A_\parallel \\ j_\parallel =& \frac{1}{\mu_0}\frac{\omega_{ci}^2}{c_s^4}\frac{T_e}{e^2n_0}\nabla_\perp^2 A_\parallel \\ =& \frac{1}{\mu_0}\frac{e^2B^2}{m_i^2}\frac{m_i^2}{T_e^2}\frac{T_e}{e^2n_0}\nabla_\perp^2 A_\parallel \\ =& \frac{B^2}{\mu_0}\frac{1}{T_e}\frac{1}{n_0}\nabla_\perp^2 A_\parallel \\ =& \frac{2}{2}\frac{B^2}{\mu_0 T_e n_0}\nabla_\perp^2 A_\parallel \\ =& \frac{2}{\beta}\nabla_\perp^2 A_\parallel. \end{aligned}$$

This equation can now be inverted in order to obtain $A_\parallel$. In other words, eq. (5.18) can be rewritten to

$$\begin{aligned} \partial_t j_\parallel =& -\boldsymbol{u}_E\cdot\nabla j_\parallel \\ & - n\left(u_{i,\parallel}\partial_\parallel u_{i,\parallel} - u_{e,\parallel}\partial_\parallel u_{e,\parallel}\right) - \frac{j_\parallel}{n}\partial_\parallel\left(nu_{e,\parallel}\right) \\ & + \mu T_e\partial_\parallel n + \mu n\left(-\partial_\parallel\phi - \partial_t\boldsymbol{A}\right) - 0.51\nu_{ei}j_\parallel \end{aligned}$$

$$
\begin{aligned}
&+ n\left(\nu_{en}u_{e,\parallel} - \nu_{in}u_{i,\parallel}\right) - \mu\frac{4\eta_{e,0}}{3}\partial_z^2 u_{e,\parallel} \\
=& - \boldsymbol{u}_E \cdot \nabla j_\parallel \\
&- n\left(u_{i,\parallel}\partial_\parallel u_{i,\parallel} - u_{e,\parallel}\partial_\parallel u_{e,\parallel}\right) - \frac{j_\parallel}{n}\partial_\parallel\left(nu_{e,\parallel}\right) \\
&+ \mu T_e\partial_\parallel n - \mu n\partial_\parallel\phi - \partial_t\left(\mu n\boldsymbol{A}\right) + \mu\boldsymbol{A}\partial_t n - 0.51\nu_{ei}j_\parallel \\
&+ n\left(\nu_{en}u_{e,\parallel} - \nu_{in}u_{i,\parallel}\right) - \mu\frac{4\eta_{e,0}}{3}\partial_z^2 u_{e,\parallel} \\
\partial_t\left(j_\parallel + \mu n A_\parallel\right) =& - \boldsymbol{u}_E \cdot \nabla j_\parallel \\
&- n\left(u_{i,\parallel}\partial_\parallel u_{i,\parallel} - u_{e,\parallel}\partial_\parallel u_{e,\parallel}\right) - \frac{j_\parallel}{n}\partial_\parallel\left(nu_{e,\parallel}\right) \\
&+ \mu\left(T_e\partial_\parallel n - n\partial_\parallel\phi + \boldsymbol{A}\frac{n}{n}\partial_t n\right) - 0.51\nu_{ei}j_\parallel \\
&+ n\left(\nu_{en}u_{e,\parallel} - \nu_{in}u_{i,\parallel}\right) - \mu\frac{4\eta_{e,0}}{3}\partial_z^2 u_{e,\parallel} \\
\partial_t j_\parallel^M =& - \boldsymbol{u}_E \cdot \nabla j_\parallel \\
&- n\left(u_{i,\parallel}\partial_\parallel u_{i,\parallel} - u_{e,\parallel}\partial_\parallel u_{e,\parallel}\right) - \frac{j_\parallel}{n}\partial_\parallel\left(nu_{e,\parallel}\right) \\
&+ \mu\left(T_e\partial_\parallel n - n\partial_\parallel\phi + \boldsymbol{A}n\partial_t\ln[n]\right) - 0.51\nu_{ei}j_\parallel \\
&+ n\left(\nu_{en}u_{e,\parallel} - \nu_{in}u_{i,\parallel}\right) - \mu\frac{4\eta_{e,0}}{3}\partial_z^2 u_{e,\parallel},
\end{aligned}
$$

where $j_\parallel^M = j_\parallel + \mu n A_\parallel$. For numerical purposes, in order for $A_\parallel$ not to be much larger than the rest of the quantities, it is common practice to re-normalize $A_{\parallel,\text{old}} = \frac{1}{2}\beta A_{\parallel,\text{new}}$. Dropping the $_{\text{new}}$ subscript yields

$$
\begin{aligned}
j_\parallel =& \nabla_\perp^2 A_\parallel \\
j_\parallel^M =& j_\parallel + \frac{1}{2}\beta\mu n A_\parallel.
\end{aligned}
$$

Appendix G

Energies

We will in this appendix briefly comment on the energy of the system. We will here only focus on the kinetic and potential energy, and will ignore the energies entering and leaving the system through the source and the boundaries. The potential energy will here be taken as the energy from the pressure, as it is "bound" to the system, but could do work if for example the volume changed. One should note that the kinetic and potential energy of the system can be found stringently of one derive the set of equations using the variational principle of the Lagrangian of the system.

G.1 The kinetic energy

The kinetic energy density is defined as

$$\mathcal{E}_{\text{kin},\alpha} = \frac{1}{2} m_a n \boldsymbol{u}_\alpha^2.$$

Due to gyroviscous cancellation, we have (to first order) that only the $E \times B$-drift carries particles, so

$$\mathcal{E}_{\text{kin},\alpha} = \frac{1}{2} m_a n \left(\mathbf{u}_E^2 + \mathbf{u}_{\alpha,\parallel} \right)$$

Integrating this over the volume gives the global kinetic energy, which can be written

$$\begin{aligned}
E_{\text{kin},\alpha} =& \frac{1}{2} m_\alpha \int n \mathbf{u}_E^2 + n \mathbf{u}_{\alpha,\parallel}^2 \mathrm{d}V \\
=& \frac{1}{2} m_\alpha \int n \left(\frac{-\nabla_\perp \phi \times \mathbf{b}}{B} \right)^2 + n \mathbf{u}_{\alpha,\parallel}^2 \mathrm{d}V \\
=& \frac{1}{2} m_\alpha \int n \left(\left[\frac{-\nabla_\perp \phi}{B} \right]^2 + [\mathbf{u}_{\alpha,\parallel}]^2 \right) \mathrm{d}V \\
=& \frac{1}{2} m_\alpha \iiint n \left(\left[\frac{-\nabla_\perp \phi}{B} \right]^2 + [\mathbf{u}_{\alpha,\parallel}]^2 \right) J \mathrm{d}\rho \mathrm{d}\theta \mathrm{d}z \\
=& \frac{1}{2} m_i \frac{m_\alpha}{m_i} n_0 c_s^2 \rho_s^3 \iiint \breve{n} \breve{u}_\alpha^2 \breve{J} \mathrm{d}\breve{\rho} \mathrm{d}\theta \mathrm{d}\breve{z} \\
=& m_i n_0 c_s^2 \rho_s^3 \breve{E}_{\text{kin},\alpha}
\end{aligned}$$

$$= n_0 T_{e,0} \rho_s^3 \breve{E}_{\mathrm{kin},\alpha},$$

where we have used (V.4) in [127], that α denotes the particle species, and where $\breve{E}_{\mathrm{kin},\alpha} = \frac{m_\alpha}{m_i} \iiint \breve{n}\breve{u}_\alpha^2 \breve{J} \mathrm{d}\breve{\rho}\mathrm{d}\theta\mathrm{d}\breve{z}$.

G.2 The potential energy

The potential energy will here be given by the kinetic pressure nT [1]. As $T_i = 0$, only the electrons will give rise to the potential energy, meaning that the energy density is

$$\mathcal{E}_{\mathrm{pot}} = nT_e.$$

The global potential energy is therefore found by integration over the volume, and yields

$$\begin{aligned} E_{\mathrm{pot}} &= \int nT_e \mathrm{d}V \\ &= \iiint nT_e J \mathrm{d}\rho\mathrm{d}\theta\mathrm{d}z \\ &= n_0 T_{e,0} \rho_s^3 \iiint \breve{n}\breve{T}_e \breve{J} \mathrm{d}\breve{\rho}\mathrm{d}\theta\mathrm{d}\breve{z} \\ &= n_0 T_{e,0} \rho_s^3 \breve{E}_{\mathrm{pot}}, \end{aligned}$$

where $\breve{E}_{\mathrm{pot}} = \iiint \breve{n}\breve{T}_e \breve{J} \mathrm{d}\breve{\rho}\mathrm{d}\theta\mathrm{d}\breve{z}$.

[1] In [135] it is stated that the potential energy can be obtained from the Helmholtz free equation, and reads $E_{\mathrm{pot}} = nT_e \log(N)$. However, the classical partition yields $E_{\mathrm{pot}} = nT_e$ as shown in [136].

Appendix H

The coordinate system

The coordinates in a cylindrical geometry are written

$$\begin{aligned} x =& \rho\cos\theta \\ y =& \rho\sin\theta \\ z =& z \end{aligned} \qquad\qquad \begin{aligned} \rho =& \sqrt{x^2+y^2} \\ \theta =& \text{atan}\left(\frac{y}{x}\right) \\ z =& z. \end{aligned}$$

H.1 The metrics

We have that

$$\boldsymbol{e}_i = \partial_i \qquad\qquad \boldsymbol{e}^i = \mathrm{d}u_i,$$

where u_i is the set of the coordinate curves

To coordinate transform a covariant basis vector, we can consider an arbitrary line f passing through the point under consideration written in the new set of coordinates. We then use the chain rule to determine how the basis vector is written in the new set of coordinates. We have

$$\frac{\partial f(\rho,\theta,z)}{\partial x_i} = \frac{\partial f}{\partial \rho}\frac{\partial \rho}{\partial x_i} + \frac{\partial f}{\partial \theta}\frac{\partial \theta}{\partial x_i} + \frac{\partial f}{\partial z}\frac{\partial z}{\partial x_i}.$$

As the line f is arbitrary, we have

$$\boldsymbol{e}_i = \frac{\partial}{\partial x_i} = \frac{\partial \rho}{\partial x_i}\frac{\partial}{\partial \rho} + \frac{\partial \theta}{\partial x_i}\frac{\partial}{\partial \theta} + \frac{\partial z}{\partial x_i}\frac{\partial}{\partial z} = \frac{\partial \rho}{\partial x_i}\boldsymbol{e}_\rho + \frac{\partial \theta}{\partial x_i}\boldsymbol{e}_\theta + \frac{\partial z}{\partial x_i}\boldsymbol{e}_z,$$

where in our case $x_i \in \{x, y, z\}$.

To coordinate transform a contravariant basis vector, we can apply the chain rule directly to determine how the basis vector is written in the new set of coordinates. We have

$$\boldsymbol{e}^i = \mathrm{d}u^i(x,y,z) = \frac{\partial u_i}{\partial x}\mathrm{d}x + \frac{\partial u_i}{\partial y}\mathrm{d}y + \frac{\partial u_i}{\partial z}\mathrm{d}z = \frac{\partial u_i}{\partial x}\boldsymbol{e}^x + \frac{\partial u_i}{\partial y}\boldsymbol{e}^y + \frac{\partial u_i}{\partial z}\boldsymbol{e}^z.$$

At this point we note that there is no difference between co and contravariant basis vectors in a Cartesian coordinate system.

In the following, we are going to make use of the following relations

$$\begin{aligned}
\partial_x\rho =&\partial_x\sqrt{x^2+y^2} = \frac{x}{\rho} = \cos\theta \\
\partial_y\rho =&\partial_y\sqrt{x^2+y^2} = \frac{y}{\rho} = \sin\theta \\
\partial_z\rho =&\partial_z\sqrt{x^2+y^2} = 0 \\
\partial_x\theta =&\partial_x \text{atan}\left(\frac{y}{x}\right) = -\frac{y}{\rho^2} = -\frac{1}{\rho}\sin\theta \\
\partial_y\theta =&\partial_y \text{atan}\left(\frac{y}{x}\right) = \frac{x}{\rho^2} = \frac{1}{\rho}\cos\theta \\
\partial_z\theta =&\partial_z \text{atan}\left(\frac{y}{x}\right) = 0
\end{aligned}$$

$$\begin{aligned}
\partial_\rho x =&\partial_\rho \rho\cos\theta = \cos\theta \\
\partial_\rho y =&\partial_\rho \rho\sin\theta = \sin\theta \\
\partial_\rho z =&0 \\
\partial_\theta x =&\partial_\theta \rho\cos\theta = -\rho\sin\theta \\
\partial_\theta y =&\partial_\theta \rho\sin\theta = \rho\cos\theta \\
\partial_\theta z =&0.
\end{aligned}$$

This means that a basis vector written in a Cartesian basis can be written with a covariant basis vector using cylindrical coordinates as

$$\begin{aligned}
\boldsymbol{e}_x &= \frac{\partial\rho}{\partial x}\boldsymbol{e}_\rho + \frac{\partial\theta}{\partial x}\boldsymbol{e}_\theta + \frac{\partial z}{\partial x}\boldsymbol{e}_z = \cos\theta\boldsymbol{e}_\rho - \frac{1}{\rho}\sin\theta\boldsymbol{e}_\theta \\
\boldsymbol{e}_y &= \frac{\partial\rho}{\partial y}\boldsymbol{e}_\rho + \frac{\partial\theta}{\partial y}\boldsymbol{e}_\theta + \frac{\partial z}{\partial y}\boldsymbol{e}_z = \sin\theta\boldsymbol{e}_\rho + \frac{1}{\rho}\cos\theta\boldsymbol{e}_\theta \\
\boldsymbol{e}_z &= \frac{\partial\rho}{\partial z}\boldsymbol{e}_\rho + \frac{\partial\theta}{\partial z}\boldsymbol{e}_\theta + \frac{\partial z}{\partial z}\boldsymbol{e}_z = \boldsymbol{e}_z.
\end{aligned}$$

For the back transformation we have

$$\begin{aligned}
\boldsymbol{e}_\rho &= \frac{\partial x}{\partial\rho}\boldsymbol{e}_x + \frac{\partial y}{\partial\rho}\boldsymbol{e}_y + \frac{\partial z}{\partial\rho}\boldsymbol{e}_z = \cos\theta\boldsymbol{e}_x + \sin\theta\boldsymbol{e}_y \\
\boldsymbol{e}_\theta &= \frac{\partial x}{\partial\theta}\boldsymbol{e}_x + \frac{\partial y}{\partial\theta}\boldsymbol{e}_y + \frac{\partial z}{\partial\theta}\boldsymbol{e}_z = -\rho\sin\theta\boldsymbol{e}_x + \rho\cos\theta\boldsymbol{e}_y \\
\boldsymbol{e}_z &= \frac{\partial x}{\partial z}\boldsymbol{e}_x + \frac{\partial y}{\partial z}\boldsymbol{e}_y + \frac{\partial z}{\partial z}\boldsymbol{e}_z = \boldsymbol{e}_z.
\end{aligned}$$

Further, a basis vector written in a Cartesian basis can be written with a contravariant basis vector using cylindrical coordinates as

$$\begin{aligned}
\boldsymbol{e}^\rho &= \frac{\partial\rho}{\partial x}\boldsymbol{e}^x + \frac{\partial\rho}{\partial y}\boldsymbol{e}^y + \frac{\partial\rho}{\partial z}\boldsymbol{e}^z = \cos\theta\boldsymbol{e}^x + \sin\theta\boldsymbol{e}^y \\
\boldsymbol{e}^\theta &= \frac{\partial\theta}{\partial x}\boldsymbol{e}^x + \frac{\partial\theta}{\partial y}\boldsymbol{e}^y + \frac{\partial\theta}{\partial z}\boldsymbol{e}^z = -\frac{1}{\rho}\sin\theta\boldsymbol{e}^x + \frac{1}{\rho}\cos\theta\boldsymbol{e}^y \\
\boldsymbol{e}^z &= \frac{\partial z}{\partial x}\boldsymbol{e}^x + \frac{\partial z}{\partial y}\boldsymbol{e}^y + \frac{\partial z}{\partial z}\boldsymbol{e}^z = \boldsymbol{e}^z.
\end{aligned}$$

The covariant metric tensor $g^{ij} = \boldsymbol{e}^i \cdot \boldsymbol{e}^j$ and the contravariant metric tensor $g_{ij} = \boldsymbol{e}_i \cdot \boldsymbol{e}_j$ can now be computed. For the contravariant components, we get

$$\begin{aligned}
g^{\rho\rho} &= (\cos\theta\boldsymbol{e}^x + \sin\theta\boldsymbol{e}^y)\cdot(\cos\theta\boldsymbol{e}^x + \sin\theta\boldsymbol{e}^y) = \cos^2\theta + \sin^2\theta = 1 \\
g^{\rho\theta} &= g^{\theta\rho} = (\cos\theta\boldsymbol{e}^x + \sin\theta\boldsymbol{e}^y)\cdot\left(-\frac{1}{\rho}\cos\theta\boldsymbol{e}^x + \frac{1}{\rho}\sin\theta\boldsymbol{e}^y\right) = -\frac{1}{\rho}\cos\theta\sin\theta + \frac{1}{\rho}\sin\theta\cos\theta = 0 \\
g^{\rho z} &= g^{z\rho} = (\cos\theta\boldsymbol{e}^x + \sin\theta\boldsymbol{e}^y)\cdot\boldsymbol{e}^z = 0
\end{aligned}$$

$$
\begin{aligned}
g^{\theta\theta} &= \left(-\frac{1}{\rho}\cos\theta \boldsymbol{e}^x + \frac{1}{\rho}\sin\theta \boldsymbol{e}^y\right)\cdot\left(-\frac{1}{\rho}\cos\theta \boldsymbol{e}^x + \frac{1}{\rho}\sin\theta \boldsymbol{e}^y\right) = \frac{1}{\rho^2}\cos^2\theta + \frac{1}{\rho^2}\sin^2\theta = \frac{1}{\rho^2}\\
g^{z\theta} &= g^{\theta z} = \left(-\frac{1}{\rho}\cos\theta \boldsymbol{e}^x + \frac{1}{\rho}\sin\theta \boldsymbol{e}^y\right)\cdot \boldsymbol{e}^z = 0\\
g^{zz} &= \boldsymbol{e}^z\cdot\boldsymbol{e}^z = 1.
\end{aligned}
$$

For the covariant components, we get

$$
\begin{aligned}
g_{\rho\rho} &= (\cos\theta \boldsymbol{e}_x + \sin\theta \boldsymbol{e}_y)\cdot(\cos\theta \boldsymbol{e}_x + \sin\theta \boldsymbol{e}_y) = \cos^2\theta + \sin^2\theta = 1\\
g_{\rho\theta} &= g_{\theta\rho} = (\cos\theta \boldsymbol{e}_x + \sin\theta \boldsymbol{e}_y)\cdot(-\rho\sin\theta \boldsymbol{e}_x + \rho\cos\theta \boldsymbol{e}_y) = -\rho\cos\theta\sin\theta + \rho\sin\theta\cos\theta = 0\\
g_{\rho z} &= g_{z\rho} = (\cos\theta \boldsymbol{e}_x + \sin\theta \boldsymbol{e}_y)\cdot \boldsymbol{e}_z = 0\\
g_{\theta\theta} &= (-\rho\sin\theta \boldsymbol{e}_x + \rho\cos\theta \boldsymbol{e}_y)\cdot(-\rho\sin\theta \boldsymbol{e}_x + \rho\cos\theta \boldsymbol{e}_y) = \rho^2\cos^2\theta + \rho^2\sin^2\theta = \rho^2\\
g_{z\theta} &= g_{\theta z} = (-\rho\sin\theta \boldsymbol{e}_x + \rho\cos\theta \boldsymbol{e}_y)\cdot \boldsymbol{e}_z = 0\\
g_{zz} &= \boldsymbol{e}_z\cdot\boldsymbol{e}_z = 1.
\end{aligned}
$$

Further, we have that the Jacobian J is given by

$$J = \sqrt{\det(g_{ij})} = \rho.$$

Finally, we calculate the derivatives of the contravariant basis vectors. From what is calculated above, we see that $\partial_z e^i = 0$ and $\partial_i e^z = 0$. The other basis vectors gives

$$
\begin{aligned}
\partial_\rho \boldsymbol{e}^\theta &= \partial_\rho\left(-\frac{1}{\rho}\sin\theta \boldsymbol{e}^x + \frac{1}{\rho}\cos\theta \boldsymbol{e}^y\right) = \frac{\sin\theta}{\rho^2}\boldsymbol{e}^x - \frac{\cos\theta}{\rho^2}\boldsymbol{e}^y = -\frac{1}{\rho}\left(-\frac{1}{\rho}\sin\theta \boldsymbol{e}^x + \frac{1}{\rho}\cos\theta \boldsymbol{e}^y\right) = -\frac{1}{\rho}\boldsymbol{e}^\theta\\
\partial_\rho \boldsymbol{e}^\rho &= \partial_\rho\left(\cos\theta \boldsymbol{e}^x + \sin\theta \boldsymbol{e}^y\right) = 0\\
\partial_\theta \boldsymbol{e}^\theta &= \partial_\theta\left(-\frac{1}{\rho}\sin\theta \boldsymbol{e}^x + \frac{1}{\rho}\cos\theta \boldsymbol{e}^y\right) = \left(-\frac{1}{\rho}\cos\theta \boldsymbol{e}^x - \frac{1}{\rho}\sin\theta \boldsymbol{e}^y\right) = -\frac{1}{\rho}\left(\cos\theta \boldsymbol{e}^x + \sin\theta \boldsymbol{e}^y\right) = -\frac{1}{\rho}\boldsymbol{e}^\rho\\
\partial_\theta \boldsymbol{e}^\rho &= \partial_\theta\left(\cos\theta \boldsymbol{e}^x + \sin\theta \boldsymbol{e}^y\right) = -\sin\theta \boldsymbol{e}^x + \cos\theta \boldsymbol{e}^y = \rho\left(-\frac{1}{\rho}\sin\theta \boldsymbol{e}^x + \frac{1}{\rho}\cos\theta \boldsymbol{e}^y\right) = \rho\boldsymbol{e}^\theta.
\end{aligned}
$$

H.1.1 Summary

Basis vector transformations

$$
\begin{aligned}
\boldsymbol{e}_x &= \cos\theta \boldsymbol{e}_\rho - \frac{1}{\rho}\sin\theta \boldsymbol{e}_\theta & \boldsymbol{e}_\rho &= \cos\theta \boldsymbol{e}_x + \sin\theta \boldsymbol{e}_y & \boldsymbol{e}^\rho &= \cos\theta \boldsymbol{e}^x + \sin\theta \boldsymbol{e}^y\\
\boldsymbol{e}_y &= \sin\theta \boldsymbol{e}_\rho + \frac{1}{\rho}\cos\theta \boldsymbol{e}_\theta & \boldsymbol{e}_\theta &= -\rho\sin\theta \boldsymbol{e}_x + \rho\cos\theta \boldsymbol{e}_y & \boldsymbol{e}^\theta &= -\frac{1}{\rho}\sin\theta \boldsymbol{e}^x + \frac{1}{\rho}\cos\theta \boldsymbol{e}^y\\
\boldsymbol{e}_z &= \boldsymbol{e}_z & \boldsymbol{e}_z &= \boldsymbol{e}_z & \boldsymbol{e}^z &= \boldsymbol{e}^z
\end{aligned}
$$

Metric tensors

$$
\begin{aligned}
g^{\rho\theta} &= g^{\theta\rho} = g^{\rho z} = g^{z\rho} = g^{z\theta} = g^{\theta z} = 0 & g_{\rho\theta} &= g_{\theta\rho} = g_{\rho z} = g_{z\rho} = g_{z\theta} = g_{\theta z} = 0\\
g^{\rho\rho} &= g^{zz} = 1 & g_{\rho\rho} &= g_{zz} = 1\\
g^{\theta\theta} &= \frac{1}{\rho^2} & g_{\theta\theta} &= \rho^2
\end{aligned}
$$

The Jacobian

$$J = \rho$$

The derivatives of the contravariant basis vectors.

$$\begin{aligned}
\partial_\rho \boldsymbol{e}^\rho =& \partial_\rho \boldsymbol{e}^z = \partial_\theta \boldsymbol{e}^z = \partial_z \boldsymbol{e}^\rho = \partial_z \boldsymbol{e}^\theta = \partial_z \boldsymbol{e}^z = 0 \\
\partial_\rho \boldsymbol{e}^\theta =& -\frac{1}{\rho}\boldsymbol{e}^\theta \\
\partial_\theta \boldsymbol{e}^\theta =& -\frac{1}{\rho}\boldsymbol{e}^\rho \\
\partial_\theta \boldsymbol{e}^\rho =& \rho \boldsymbol{e}^\theta
\end{aligned}$$

H.2 Alignment with the Clebsch formalism

As most of the numerical differentiation operators in BOUT++ are only valid for a coordinate system written on the Clebsch form (at least at the time of writing), it makes sense to align our coordinates with the Clebsch coordinates. Note as whereas the Clebsch coordinate system gives

$$\begin{aligned}
\boldsymbol{B}_{\text{Clebsch}} =& \boldsymbol{e}^3 \times \boldsymbol{e}^1 \\
J^{-1}\boldsymbol{e}_2 =& \boldsymbol{e}^3 \times \boldsymbol{e}^1
\end{aligned} \tag{H.1}$$

so that

$$B_{\text{Clebsch}} \overset{\text{def}}{=} \sqrt{\boldsymbol{B}_{\text{Clebsch}} \cdot \boldsymbol{B}_{\text{Clebsch}}} = \sqrt{J^{-1}\boldsymbol{e}_2 \cdot J^{-1}\boldsymbol{e}_2} = \sqrt{J^{-2}g_{22}} = J^{-1}\sqrt{g_{22}},$$

and

$$\begin{aligned}
\boldsymbol{B}_{\text{Clebsch}} =& B_{\text{Clebsch}}\boldsymbol{b}_{\text{Clebsch}} \\
\boldsymbol{b}_{\text{Clebsch}} =& \frac{\boldsymbol{B}_{\text{Clebsch}}}{B_{\text{Clebsch}}} = \frac{J^{-1}\boldsymbol{e}_2}{J^{-1}\sqrt{g_{22}}} = \frac{\boldsymbol{e}_2}{\sqrt{g_{22}}}.
\end{aligned}$$

The B-field in our case is constant. This can be obtained if we let[1][2]

$$\begin{aligned}
1 &\to \rho \\
2 &\to z \\
3 &\to \theta.
\end{aligned}$$

We now have that $\boldsymbol{B}_{\text{Cylinder}} = B_0 J \boldsymbol{B}_{\text{Clebsch}}$, where B_0 is a constant value, which means that

$$B_{\text{Cylinder}} \overset{\text{def}}{=} \sqrt{B_0 J \boldsymbol{B}_{\text{Clebsch}} \cdot B_0 J \boldsymbol{B}_{\text{Clebsch}}} = \sqrt{B_0 \boldsymbol{e}_z \cdot B_0 \boldsymbol{e}_z} = B_0\sqrt{g_{zz}} = B_0$$

[1] BOUT++ uses the indices $\{x, y, z\}$ for $\{1, 2, 3\}$. Be aware that this can be a source of confusion as y in BOUT++ coordinates maps to z in cylindrical coordinates as shown below

Generic		BOUT++ indices		Cylindrical coordinates
1	$\to$	x	$\to$	ρ
2	$\to$	y	$\to$	z
3	$\to$	z	$\to$	θ

[2] Note that this system is left-handed.

and

$$\boldsymbol{B}_{\text{Cylinder}} = B_{\text{Cylinder}} \boldsymbol{b}_{\text{Clebsch}}.$$

In other words, we see that the cylindrical coordinate system overlaps with the Clebsch coordinate system in the sense that the basis vectors and the Jacobian are the same. However, eq. (H.1) is not fulfilled for the pure cylindrical coordinate system. Care must therefore be taken when using BOUT++ operators which explicitly uses B_{Clebsch}. In the scope of this thesis, it means that care must be taken whenever using the Poisson bracket, as explained in appendix I.

To clarify the notation: $\boldsymbol{B}$ and B are unspecified prior to chapter 5 and referring to $\boldsymbol{B}_{\text{Cylinder}}$ and B_{Cylinder} after and including chapter 5.

Appendix I

The Poisson bracket operator

We will here derive the bracket operators used for perpendicular advection. Under electrostatic conditions, we have that $\boldsymbol{u}_{E,\text{with Clebsch B}} = -\dfrac{\nabla\phi \times \boldsymbol{b}_{\text{Clebsch}}}{B_{\text{Clebsch}}}$, which is similar to $\boldsymbol{u} = \boldsymbol{k} \times \nabla\psi$ found in incompressible fluid flow

$$
\begin{aligned}
\boldsymbol{u}_{E,\text{with Clebsch B}} =& -\frac{\nabla\phi \times \boldsymbol{b}_{\text{Clebsch}}}{B_{\text{Clebsch}}} \\
=& -\frac{\nabla\phi \times \boldsymbol{e}_2}{\sqrt{g_{22}}J^{-1}\sqrt{g_{22}}} \\
=& -\frac{J}{g_{22}}\nabla\phi \times \boldsymbol{e}_2 \\
=& \frac{J}{g_{22}}\boldsymbol{e}_2 \times \nabla\phi \\
=& \frac{J}{g_{22}}\boldsymbol{e}_2 \times \left(\boldsymbol{e}^1\partial_1 + \boldsymbol{e}^3\partial_3\right)\phi \\
=& \frac{J}{g_{22}}\left(g_{21}\boldsymbol{e}^1 + g_{22}\boldsymbol{e}^2 + g_{23}\boldsymbol{e}^3\right) \times \left(\boldsymbol{e}^1\partial_1 + \boldsymbol{e}^2\partial_2 + \boldsymbol{e}^3\partial_3\right)\phi \\
=& \frac{J}{g_{22}}\big(g_{21}\boldsymbol{e}^1 \times \boldsymbol{e}^1\partial_1 + g_{22}\boldsymbol{e}^2 \times \boldsymbol{e}^1\partial_1 + g_{23}\boldsymbol{e}^3 \times \boldsymbol{e}^1\partial_1 \\
& + g_{21}\boldsymbol{e}^1 \times \boldsymbol{e}^2\partial_2 + g_{22}\boldsymbol{e}^2 \times \boldsymbol{e}^2\partial_2 + g_{23}\boldsymbol{e}^3 \times \boldsymbol{e}^2\partial_2 \\
& + g_{21}\boldsymbol{e}^1 \times \boldsymbol{e}^3\partial_3 + g_{22}\boldsymbol{e}^2 \times \boldsymbol{e}^3\partial_3 + g_{23}\boldsymbol{e}^3 \times \boldsymbol{e}^3\partial_3\big)\phi \\
=& \frac{J}{g_{22}}\big(-g_{22}\boldsymbol{e}^2 \times \boldsymbol{e}^1\partial_1 + g_{23}\boldsymbol{e}^3 \times \boldsymbol{e}^1\partial_1 \\
& + g_{21}\boldsymbol{e}^1 \times \boldsymbol{e}^2\partial_2 - g_{23}\boldsymbol{e}^3 \times \boldsymbol{e}^2\partial_2 \\
& - g_{21}\boldsymbol{e}^1 \times \boldsymbol{e}^3\partial_3 + g_{22}\boldsymbol{e}^2 \times \boldsymbol{e}^3\partial_3\big)\phi \\
=& \frac{1}{g_{22}}\left(-g_{22}\boldsymbol{e}_3\partial_1 + g_{23}\boldsymbol{e}_2\partial_1 + g_{21}\boldsymbol{e}_3\partial_2 - g_{23}\boldsymbol{e}_1\partial_2 - g_{21}\boldsymbol{e}_2\partial_3 + g_{22}\boldsymbol{e}_1\partial_3\right)\phi.
\end{aligned}
\tag{I.1}
$$

We note that eq. (I.1) is derived for a system where we are using B_{Clebsch}. Translating this into a cylindrical coordinate system using $B_{\text{Cylindrical}}$ gives

$$
\boldsymbol{u}_{E,\text{with constant B}} = -\frac{\nabla\phi \times \boldsymbol{b}_{\text{Clebsch}}}{B_{\text{Cylinder}}}
$$

$$
\begin{aligned}
&= -\frac{B_{\text{Clebsch}}}{B_{\text{Clebsch}}}\frac{\nabla\phi\times\boldsymbol{b}_{\text{Clebsch}}}{B_{\text{Cylinder}}}\\
&= -\frac{B_{\text{Clebsch}}}{B_{\text{Cylinder}}}\frac{\nabla\phi\times\boldsymbol{b}_{\text{Clebsch}}}{B_{\text{Clebsch}}}\\
&=\frac{\sqrt{g_{zz}}}{JB_{\text{Cylinder}}}\boldsymbol{u}_{E,\text{with Clebsch B}}\\
&=\frac{1}{JB_{\text{Cylinder}}}\frac{1}{g_{zz}}\left(-g_{zz}\boldsymbol{e}_\theta\partial_\rho+g_{z\theta}\boldsymbol{e}_z\partial_\rho+g_{z\rho}\boldsymbol{e}_\theta\partial_z-g_{z\theta}\boldsymbol{e}_\rho\partial_z-g_{z\rho}\boldsymbol{e}_z\partial_\theta+g_{zz}\boldsymbol{e}_\rho\partial_\theta\right)\phi\\
&=\frac{1}{JB_{\text{Cylinder}}}\left(-\boldsymbol{e}_\theta\partial_\rho+\boldsymbol{e}_\rho\partial_\theta\right)\phi. \qquad \text{(I.2)}
\end{aligned}
$$

Continuing from eq. (I.1), we see that in general coordinates the electrostatic $\boldsymbol{E}\times\boldsymbol{B}$ advection operator becomes

$$
\begin{aligned}
\boldsymbol{u}_{E,\text{with Clebsch B}}\cdot\nabla =& -\frac{\nabla\phi\times\boldsymbol{b}_{\text{Clebsch}}}{B_{\text{Clebsch}}}\cdot\nabla\\
=&\frac{1}{g_{22}}\left(-g_{22}\boldsymbol{e}_3\partial_1+g_{23}\boldsymbol{e}_2\partial_1+g_{21}\boldsymbol{e}_3\partial_2-g_{23}\boldsymbol{e}_1\partial_2-g_{21}\boldsymbol{e}_2\partial_3+g_{22}\boldsymbol{e}_1\partial_3\right)\phi\\
&\cdot\left(\boldsymbol{e}^1\partial_1+\boldsymbol{e}^2\partial_2+\boldsymbol{e}^3\partial_3\right)\\
=&\frac{1}{g_{22}}\left(-g_{22}\partial_1\phi\partial_3+g_{23}\partial_1\phi\partial_2+g_{21}\partial_2\phi\partial_3-g_{23}\partial_2\phi\partial_1-g_{21}\partial_3\phi\partial_2+g_{22}\partial_3\phi\partial_1\right)\\
=&\frac{1}{g_{22}}\left(\left[g_{22}\partial_3\phi-g_{23}\partial_2\phi\right]\partial_1+\left[g_{23}\partial_1\phi-g_{21}\partial_3\phi\right]\partial_2+\left[g_{21}\partial_2\phi-g_{22}\partial_1\phi\right]\partial_3\right)\\
=&\frac{1}{g_{22}}\left(g_{21}\{\phi,\cdot\}_{2,3}+g_{22}\{\phi,\cdot\}_{3,1}+g_{23}\{\phi,\cdot\}_{1,2}\right),
\end{aligned}
$$

where we have used the definition of the Poisson bracket

$$
\{f,g\}_{i,j}=\left(\partial_i f\right)\partial_j g-\left(\partial_j f\right)\partial_i g.
$$

In an orthogonal system, all the off diagonal elements are zero, so

$$
\boldsymbol{u}_{E,\text{with Clebsch B}}\cdot\nabla=\frac{1}{g_{22}}\left(g_{22}\{\phi,\cdot\}_{3,1}\right)=\{\phi,\cdot\}_{3,1}=\partial_3\phi\partial_1-\partial_1\phi\partial_3=\partial_\theta\phi\partial_\rho-\partial_\rho\phi\partial_\theta. \qquad \text{(I.3)}
$$

As eq. (I.3) is derived with B_{Clebsch}, we get that

$$
\begin{aligned}
\boldsymbol{u}_{E,\text{with const B}}\cdot\nabla =&\frac{B_{\text{Clebsch}}}{B_{\text{Cylindrical}}}\boldsymbol{u}_{E,\text{with Clebsch B}}\cdot\nabla\\
=&\frac{\sqrt{g_{zz}}}{JB_{\text{Cylindrical}}}(\partial_\theta\phi\partial_\rho-\partial_\rho\phi\partial_\theta)\\
=&\frac{1}{JB}(\partial_\theta\phi\partial_\rho-\partial_\rho\phi\partial_\theta). \qquad \text{(I.4)}
\end{aligned}
$$

Appendix J

Advection of Ω^D

We will here derive the advection of the modified vorticity

$$\frac{1}{\omega_{ci}}\nabla\cdot\left(\boldsymbol{u}_E\cdot\nabla\left[n\frac{\nabla_\perp\phi}{B}\right]\right) \tag{J.1}$$

in cylindrical coordinates. Similar derivations have been done in [54, 59]

The first thing we notice is that eq. (J.1) can only have perpendicular components. As it is shown in eq. (I.4)

$$\boldsymbol{u}_E\cdot\nabla=\frac{1}{JB}(\partial_\theta\phi\partial_\rho-\partial_\rho\phi\partial_\theta).$$

When this term is acting on $\nabla_\perp\phi$, no $\boldsymbol{e}_z$ or $\boldsymbol{e}^z$ terms will be created as seen from appendix H.1.1. The same holds when one takes the divergence of the resulting quantity. Thus,

$$\begin{aligned}\frac{1}{\omega_{ci}}\nabla\cdot\left(\boldsymbol{u}_E\cdot\nabla\left[n\frac{\nabla_\perp\phi}{B}\right]\right)=&\frac{1}{\omega_{ci}}\nabla_\perp\cdot\left(\frac{1}{JB}\left\{\phi,n\frac{\nabla_\perp\phi}{B}\right\}\right)\\ =&\frac{1}{\omega_{ci}}\left\{\phi,n\frac{\nabla_\perp\phi}{B}\right\}\cdot\nabla_\perp\frac{1}{JB}+\frac{1}{\omega_{ci}}\frac{1}{JB}\nabla_\perp\cdot\left\{\phi,n\frac{\nabla_\perp\phi}{B}\right\}.\end{aligned} \tag{J.2}$$

Expansion of the first term of eq. (J.2) gives

$$\begin{aligned}\frac{1}{\omega_{ci}}\left\{\phi,n\frac{\nabla_\perp\phi}{B}\right\}\cdot\nabla_\perp\frac{1}{JB}=&\frac{1}{\omega_{ci}}\left\{\phi,n\frac{\nabla_\perp\phi}{B}\right\}\cdot\left(\boldsymbol{e}^\rho\partial_\rho+\boldsymbol{e}^\theta\partial_\theta\right)\frac{1}{B\rho}\\ =&-\frac{1}{\omega_{ci}}\left\{\phi,n\frac{\nabla_\perp\phi}{B}\right\}\cdot\boldsymbol{e}^\rho\frac{1}{B\rho^2}.\end{aligned} \tag{J.3}$$

Constant B

When calculating the second term of eq. (J.2), we will use that for a general scalar field c and a general vector $\boldsymbol{d}$, we have that

$$\begin{aligned}\nabla_\perp\cdot\{c,\boldsymbol{d}\}=&\nabla_\perp\cdot(\partial_\theta c\partial_\rho\boldsymbol{d}-\partial_\rho c\partial_\theta\boldsymbol{d})\\ =&\quad(\partial_\theta c)\,\nabla_\perp\cdot\partial_\rho\boldsymbol{d}+\nabla_\perp(\partial_\theta c)\cdot\partial_\rho\boldsymbol{d}\\ &-([\partial_\rho c]\,\nabla_\perp\cdot\partial_\theta\boldsymbol{d}+\nabla_\perp[\partial_\rho c]\cdot\partial_\theta\boldsymbol{d})\\ =&\quad(\partial_\theta c)\,\partial_\rho(\nabla_\perp\cdot\boldsymbol{d})-(\partial_\theta c)\,\partial_i\boldsymbol{d}\cdot\partial_\rho\boldsymbol{e}^i\end{aligned}$$

$\boldsymbol{e}^i\partial_j f=\partial_j\left(\boldsymbol{e}^i\partial_i f\right)-\partial_i f\partial_j\boldsymbol{e}^i$

$$
\begin{aligned}
&+ (\partial_\theta \nabla_\perp c) \cdot \partial_\rho \boldsymbol{d} - \left(\partial_i c \partial_\theta \boldsymbol{e}^i\right) \cdot \partial_\rho \boldsymbol{d} \\
&- \Big(\quad [\partial_\rho c]\, \partial_\theta \left[\nabla_\perp \cdot \boldsymbol{d}\right] - [\partial_\rho c]\, \partial_i \boldsymbol{d} \cdot \partial_\theta \boldsymbol{e}^i \\
&\quad + [\partial_\rho \nabla_\perp c] \cdot \partial_\theta \boldsymbol{d} - \left[\partial_i c \partial_\rho \boldsymbol{e}^i\right] \cdot \partial_\theta \boldsymbol{d} \Big) \\
=&\{c, \nabla_\perp \cdot \boldsymbol{d}\} + \{\nabla_\perp c; \boldsymbol{d}\} \\
&- (\partial_\theta c)\, \partial_i \boldsymbol{d} \cdot \partial_\rho \boldsymbol{e}^i - \left(\partial_i c \partial_\theta \boldsymbol{e}^i\right) \cdot \partial_\rho \boldsymbol{d} + (\partial_\rho c)\, \partial_i \boldsymbol{d} \cdot \partial_\theta \boldsymbol{e}^i + \left(\partial_i c \partial_\rho \boldsymbol{e}^i\right) \cdot \partial_\theta \boldsymbol{d} \qquad \text{; denotes the dot-product} \\
=&\{c, \nabla_\perp \cdot \boldsymbol{d}\} + \{\nabla_\perp c; \boldsymbol{d}\} + \mathcal{G},
\end{aligned}
$$

where $\mathcal{G}$ is the correction coming from the geometry. We have

$$
\begin{aligned}
\mathcal{G} =& - (\partial_\theta c)\, \partial_i \boldsymbol{d} \cdot \partial_\rho \boldsymbol{e}^i \\
&- \left(\partial_i c \partial_\theta \boldsymbol{e}^i\right) \cdot \partial_\rho \boldsymbol{d} \\
&+ (\partial_\rho c)\, \partial_i \boldsymbol{d} \cdot \partial_\theta \boldsymbol{e}^i \\
&+ \left(\partial_i c \partial_\rho \boldsymbol{e}^i\right) \cdot \partial_\theta \boldsymbol{d} \\
=& - (\partial_\theta c)\, \partial_\rho \boldsymbol{d} \cdot \partial_\rho \boldsymbol{e}^\rho - (\partial_\theta c)\, \partial_\theta \boldsymbol{d} \cdot \partial_\rho \boldsymbol{e}^\theta \\
&- (\partial_\rho c \partial_\theta \boldsymbol{e}^\rho) \cdot \partial_\rho \boldsymbol{d} - \left(\partial_\theta c \partial_\theta \boldsymbol{e}^\theta\right) \cdot \partial_\rho \boldsymbol{d} \\
&+ (\partial_\rho c)\, \partial_\rho \boldsymbol{d} \cdot \partial_\theta \boldsymbol{e}^\rho + (\partial_\rho c)\, \partial_\theta \boldsymbol{d} \cdot \partial_\theta \boldsymbol{e}^\theta \\
&+ (\partial_\rho c \partial_\rho \boldsymbol{e}^\rho) \cdot \partial_\theta \boldsymbol{d} + \left(\partial_\theta c \partial_\rho \boldsymbol{e}^\theta\right) \cdot \partial_\theta \boldsymbol{d} \\
=& - 0 - (\partial_\theta c)\, \partial_\theta \boldsymbol{d} \cdot \left(-\frac{1}{\rho} \boldsymbol{e}^\theta\right) \\
&- \rho \boldsymbol{e}^\theta\, (\partial_\rho c) \cdot \partial_\rho \boldsymbol{d} - \left(-\frac{1}{\rho} \boldsymbol{e}^\rho\right) (\partial_\theta c) \cdot \partial_\rho \boldsymbol{d} \\
&+ (\partial_\rho c)\, \partial_\rho \boldsymbol{d} \cdot \left(\rho \boldsymbol{e}^\theta\right) + (\partial_\rho c)\, \partial_\theta \boldsymbol{d} \cdot \left(-\frac{1}{\rho} \boldsymbol{e}^\rho\right) \\
&+ 0 + \left(-\frac{1}{\rho} \boldsymbol{e}^\theta\right) (\partial_\theta c) \cdot \partial_\theta \boldsymbol{d} \\
=& \frac{1}{\rho} \boldsymbol{e}^\theta \cdot (\partial_\theta c)\, \partial_\theta \boldsymbol{d} - \frac{1}{\rho} \boldsymbol{e}^\theta \cdot (\partial_\theta c)\, \partial_\theta \boldsymbol{d} \\
&- \rho \boldsymbol{e}^\theta \cdot (\partial_\rho c)\, \partial_\rho \boldsymbol{d} + \rho \boldsymbol{e}^\theta \cdot (\partial_\rho c)\, \partial_\rho \boldsymbol{d} \\
&- \frac{1}{\rho} \boldsymbol{e}^\rho \cdot (\partial_\rho c)\, \partial_\theta \boldsymbol{d} + \frac{1}{\rho} \boldsymbol{e}^\rho \cdot (\partial_\theta c)\, \partial_\rho \boldsymbol{d} \\
=& \frac{1}{\rho} \boldsymbol{e}^\rho \cdot \{c, \boldsymbol{d}\}\,.
\end{aligned}
$$

Thus, expansion of the second term in eq. (J.2) gives

$$
\begin{aligned}
\frac{1}{\omega_{ci}} \frac{1}{JB} \nabla_\perp \cdot \left\{\phi, n \frac{\nabla_\perp \phi}{B}\right\} &= \frac{1}{\omega_{ci}} \frac{1}{B\rho} \left(\left\{\phi, \nabla_\perp \cdot n \frac{\nabla_\perp \phi}{B}\right\} + \left\{\nabla_\perp \phi; n \frac{\nabla_\perp \phi}{B}\right\} + \frac{1}{\rho} \boldsymbol{e}^\rho \cdot \left\{\phi, n \frac{\nabla_\perp \phi}{B}\right\} \right) \\
&= \frac{1}{\omega_{ci}} \frac{1}{B\rho} \{\phi, \Omega^D\} + \frac{1}{\omega_{ci}} \frac{1}{B\rho} \left\{\nabla_\perp \phi; n \frac{\nabla_\perp \phi}{B}\right\} + \frac{1}{\omega_{ci}} \frac{1}{B\rho^2} \boldsymbol{e}^\rho \cdot \left\{\phi, n \frac{\nabla_\perp \phi}{B}\right\}.
\end{aligned} \tag{J.4}
$$

Combining eq. (J.3) and eq. (J.4), we get that

$$
\frac{1}{\omega_{ci}} \nabla \cdot \left(\boldsymbol{u}_E \cdot \nabla \left[n \frac{\nabla_\perp \phi}{B} \phi \right] \right) = - \frac{1}{\omega_{ci}} \left\{\phi, n \frac{\nabla_\perp \phi}{B} \phi\right\} \cdot \boldsymbol{e}^\rho \frac{1}{B\rho^2}
$$

$$
\begin{aligned}
&+\frac{1}{\omega_{ci}}\frac{1}{B\rho}\{\phi,\Omega^D\}+\frac{1}{\omega_{ci}}\frac{1}{B\rho}\left\{\nabla_\perp\phi;n\frac{\nabla_\perp\phi}{B}\right\}\\
&+\frac{1}{\omega_{ci}}\frac{1}{B\rho^2}\boldsymbol{e}^\rho\cdot\left\{\phi,n\frac{\nabla_\perp\phi}{B}\right\}\\
=&\frac{1}{\omega_{ci}}\frac{1}{B\rho}\{\phi,\Omega^D\}+\frac{1}{\omega_{ci}}\frac{1}{B\rho}\left\{\nabla_\perp\phi;n\frac{\nabla_\perp\phi}{B}\phi\right\} && \text{Product rule}\\
=&\frac{1}{\omega_{ci}}\frac{1}{B\rho}\{\phi,\Omega^D\}+\frac{1}{\omega_{ci}}n\frac{1}{B\rho}\left\{\nabla_\perp\phi;\frac{\nabla_\perp\phi}{B}\right\} && \left\{a,\frac{a}{B}\right\}=\\
&+\frac{1}{\omega_{ci}}\frac{1}{B\rho}\frac{\nabla_\perp\phi}{B}\cdot\{\nabla_\perp\phi,n\} && \frac{1}{B}\{a,a\}=0\\
=&\frac{1}{\omega_{ci}}\frac{1}{B\rho}\{\phi,\Omega^D\}+\frac{1}{\omega_{ci}}\frac{1}{B\rho}\frac{\nabla_\perp\phi}{B}\cdot\{\nabla_\perp\phi,n\} && \partial_i(ff)=2f\partial f\\
=&\frac{1}{\omega_{ci}}\frac{1}{B\rho}\{\phi,\Omega^D\}+\frac{1}{\omega_{ci}}\frac{1}{2B^2\rho}\{(\nabla_\perp\phi)^2,n\} && \text{Constant } B\\
=&\frac{1}{\omega_{ci}}\frac{1}{B\rho}\{\phi,\Omega^D\}+\frac{1}{\omega_{ci}}\frac{1}{2\rho}\left\{\left(\frac{\nabla_\perp\phi}{B}\right)^2,n\right\}\\
=&\frac{1}{\omega_{ci}}\frac{1}{B\rho}\{\phi,\Omega^D\}+\frac{1}{\omega_{ci}}\frac{1}{2\rho}\{\boldsymbol{u}_E^2,n\}.
\end{aligned}
$$

Appendix K

Laplace inversion using FFT

We will here explain how $\Omega = \dfrac{\nabla_\perp^2 \phi}{B}$ can be solved numerically using the Fourier transform.

This is a special case of the equation

$$d\nabla_\perp^2 f + \frac{1}{c_1}\left(\nabla_\perp c_2\right) \cdot \nabla_\perp f + af = b, \tag{K.1}$$

which the BOUT++ framework has an own class of inverting for.

In order to explain the numerical implementation, we must first look at how the Laplacian operator looks like Clebsch coordinates. Part of this appendix is also included in the `user_manual` and `coordinates` manual of the BOUT++ version mentioned in chapter 8.

We will in this chapter use the BOUT++ coordinates mentioned in footnote 1 of appendix H.

K.1 The Laplacian

The Laplacian operator is defined

$$\nabla^2 f \stackrel{\text{def}}{=} \nabla \cdot \nabla f.$$

In general we have (from equation (2.6.39) in D'Haeseleer [127])

$$\nabla \cdot \boldsymbol{A} = \frac{1}{J}\partial_i \left(JA^i\right), \tag{K.2}$$

and that

$$A^i = \boldsymbol{A} \cdot \boldsymbol{e}^i.$$

In our case $\boldsymbol{A} \to \nabla$, so that

$$\nabla^i = (\nabla) \cdot \boldsymbol{e}^i = \boldsymbol{e}^i \cdot (\nabla) = \boldsymbol{e}^i \cdot \left(\boldsymbol{e}^j \partial_j\right) = g^{ij}\partial_j.$$

Thus

$$\nabla^2 = \frac{1}{J}\partial_i \left(Jg^{ij}\partial_j\right)$$

$$
\begin{aligned}
&= \frac{1}{J} g^{ij} J \partial_i \partial_j + \frac{1}{J} \partial_i \left(J g^{ij} \right) \partial_j \\
&= g^{ij} \partial_i \partial_j + G^j \partial_j,
\end{aligned} \tag{K.3}
$$

where we have defined[1]

$$
\begin{aligned}
G^j &= \frac{1}{J} \partial_i \left(J g^{ij} \right) \\
&= \frac{1}{J} \left(\partial_1 \left[J g^{1j} \right] + \partial_2 \left[J g^{2j} \right] + \partial_3 \left[J g^{3j} \right] \right).
\end{aligned}
$$

By expanding the terms in eq. (K.3) yields

$$
\begin{aligned}
\nabla^2 &= g^{ij} \partial_i \partial_j + G^j \partial_j \\
&= \left(g^{1j} \partial_1 \partial_j + g^{2j} \partial_2 \partial_j + g^{3j} \partial_3 \partial_j \right) + \left(G^j \partial_j \right) \\
&= \quad \left(g^{11} \partial_1^2 + g^{21} \partial_2 \partial_1 + g^{31} \partial_3 \partial_1 \right) + \left(G^1 \partial_1 \right) \\
&\quad + \left(g^{12} \partial_1 \partial_2 + g^{22} \partial_2^2 + g^{32} \partial_3 \partial_2 \right) + \left(G^2 \partial_2 \right) \\
&\quad + \left(g^{13} \partial_1 \partial_3 + g^{23} \partial_2 \partial_3 + g^{33} \partial_3^2 \right) + \left(G^3 \partial_3 \right).
\end{aligned}
$$

We now use that the metric tensor is symmetric (by definition), so that $g^{ij} = g^{ji}$, and $g_{ij} = g_{ji}$. At the same time, we will use that the partial derivatives commutes for smooth functions $\partial_i \partial_j = \partial_j \partial_i$. This gives

$$
\begin{aligned}
\nabla^2 = \quad & \left(g^{11} \partial_1^2 \right) + \left(G^1 \partial_1 \right) \\
& + \left(g^{22} \partial_2^2 \right) + \left(G^2 \partial_2 \right) \\
& + \left(g^{33} \partial_3^2 \right) + \left(G^3 \partial_3 \right) \\
& + 2 \left(g^{12} \partial_1 \partial_2 + g^{13} \partial_1 \partial_3 + g^{23} \partial_2 \partial_3 \right) \\
= \quad & \left(g^{11} \partial_1^2 \right) + \left(\frac{1}{J} \left[\partial_1 \left\{ J g^{11} \right\} + \partial_2 \left\{ J g^{21} \right\} + \partial_3 \left\{ J g^{31} \right\} \right] \partial_1 \right) \\
& + \left(g^{22} \partial_2^2 \right) + \left(\frac{1}{J} \left[\partial_1 \left\{ J g^{12} \right\} + \partial_2 \left\{ J g^{22} \right\} + \partial_3 \left\{ J g^{32} \right\} \right] \partial_2 \right) \\
& + \left(g^{33} \partial_3^2 \right) + \left(\frac{1}{J} \left[\partial_1 \left\{ J g^{13} \right\} + \partial_2 \left\{ J g^{23} \right\} + \partial_3 \left\{ J g^{33} \right\} \right] \partial_3 \right) \\
& + 2 \left(g^{12} \partial_1 \partial_2 + g^{13} \partial_1 \partial_3 + g^{23} \partial_2 \partial_3 \right).
\end{aligned}
$$

K.1.1 The parallel Laplacian

From chapter 3, we have that

$$
\nabla_{\parallel} \stackrel{\text{def}}{=} (\boldsymbol{b} \cdot \nabla) \boldsymbol{b} \; = \boldsymbol{b}\boldsymbol{b} \cdot \nabla = \frac{\boldsymbol{e}_2 \boldsymbol{e}_2}{g_{22}} \cdot \nabla = \frac{\boldsymbol{e}_2 \boldsymbol{e}_2}{g_{22}} \cdot \boldsymbol{e}^i \partial_i = \frac{\boldsymbol{e}_2}{g_{22}} \partial_2 \tag{K.4}
$$

such that

$$
\nabla_{\parallel}^i = \left(\frac{\boldsymbol{e}_2}{g_{22}} \partial_2 \right) \cdot \boldsymbol{e}^i = \boldsymbol{e}^i \cdot \left(\frac{\boldsymbol{e}_2}{g_{22}} \partial_2 \right).
$$

[1] Do **not** confuse G^i with the *Christoffel symbols of second kind* (also known as the *connection coefficients*, which reads $\Gamma^i_{jk} = \boldsymbol{e}^i \cdot \partial_k \boldsymbol{e}_j$).

By using eq. (K.2) on eq. (K.4), we get

$$\begin{aligned}\nabla_{\parallel}^2 =&\nabla\cdot(\boldsymbol{bb}\cdot\nabla)\\ =&\nabla\cdot\left(\frac{\boldsymbol{e}_2}{g_{22}}\cdot\partial_2\right)\\ =&\frac{1}{J}\partial_i\left(J\boldsymbol{e}^i\cdot\left[\frac{\boldsymbol{e}_2}{g_{22}}\partial_2\right]\right)\\ =&\frac{1}{J}\partial_2\left(\frac{J}{g_{22}}\partial_2\right).\end{aligned}$$

K.1.2 The perpendicular Laplacian

We are now ready to expand the perpendicular Laplacian. From chapter 3 we have that

$$\begin{aligned}\nabla_{\perp}^2 =&\nabla^2-\nabla_{\parallel}^2\\ =&g^{ij}\partial_i\partial_j+G^j\partial_j-\frac{1}{J}\partial_2\left(\frac{J}{g_{22}}\partial_2\right)\\ =&\quad\left(g^{11}\partial_1^2\right)+\left(\frac{1}{J}\left[\partial_1\left\{Jg^{11}\right\}+\partial_2\left\{Jg^{21}\right\}+\partial_3\left\{Jg^{31}\right\}\right]\partial_1\right)\\ &+\left(g^{22}\partial_2^2\right)+\left(\frac{1}{J}\left[\partial_1\left\{Jg^{12}\right\}+\partial_2\left\{Jg^{22}\right\}+\partial_3\left\{Jg^{32}\right\}\right]\partial_2\right)\\ &+\left(g^{33}\partial_3^2\right)+\left(\frac{1}{J}\left[\partial_1\left\{Jg^{13}\right\}+\partial_2\left\{Jg^{23}\right\}+\partial_3\left\{Jg^{33}\right\}\right]\partial_3\right)\\ &+2\left(g^{12}\partial_1\partial_2+g^{13}\partial_1\partial_3+g^{23}\partial_2\partial_3\right)\\ &-\frac{1}{J}\partial_2\left(\frac{J}{g_{22}}\partial_2\right).\end{aligned}\tag{K.5}$$

The BOUT++ implementation of the inversion algorithm assumes small parallel gradients in the dependent variable, so that

$$\begin{aligned}\nabla_{\perp}^2\simeq&\quad\left(g^{11}\partial_1^2\right)+\left(\frac{1}{J}\left[\partial_1\left\{Jg^{11}\right\}+\partial_2\left\{Jg^{21}\right\}+\partial_3\left\{Jg^{31}\right\}\right]\partial_1\right)\\ &+\left(g^{33}\partial_3^2\right)+\left(\frac{1}{J}\left[\partial_1\left\{Jg^{13}\right\}+\partial_2\left\{Jg^{23}\right\}+\partial_3\left\{Jg^{33}\right\}\right]\partial_3\right)\\ &+2\left(g^{13}\partial_1\partial_3\right)\\ =&\left(g^{11}\partial_1^2\right)+G^1\partial_1+\left(g^{33}\partial_3^2\right)+G^3\partial_3+2\left(g^{13}\partial_1\partial_3\right).\end{aligned}\tag{K.6}$$

However, this approximation is not needed when using a cylindrical coordinates, as only the diagonal terms in the metric tensor is non-zero, and because the $-\frac{1}{J}\partial_2\left(\frac{J}{g_{22}}\partial_2\right)$ term cancels with $g^{22}\partial_2^2$ in eq. (K.5).

K.1.3 The perpendicular gradient

Finally, the perpendicular gradient can be found from

$$\nabla_{\perp}=\nabla-\nabla_{\parallel},$$

where

$$\nabla = \boldsymbol{e}^i \partial_i = \boldsymbol{e}^1 \partial_1 + \boldsymbol{e}^2 \partial_2 + \boldsymbol{e}^z \partial_3.$$

By using eq. (K.4), this gives

$$\begin{aligned}
\nabla_\perp =& \nabla - \nabla_\parallel \\
=& \boldsymbol{e}^1 \partial_1 + \boldsymbol{e}^2 \partial_2 + \boldsymbol{e}^3 \partial_3 - \frac{\boldsymbol{e}_2}{g_{22}} \partial_2 \\
=& \boldsymbol{e}^1 \partial_1 + \boldsymbol{e}^2 \partial_2 + \boldsymbol{e}^3 \partial_3 - \frac{g_{2i} \boldsymbol{e}^i}{g_{22}} \partial_2 \\
=& \boldsymbol{e}^1 \partial_1 + \boldsymbol{e}^2 \partial_2 + \boldsymbol{e}^3 \partial_3 - \frac{g_{21} \boldsymbol{e}^1 + g_{22} \boldsymbol{e}^2 + g_{23} \boldsymbol{e}^3}{g_{22}} \partial_2 \\
=& \boldsymbol{e}^1 \left(\partial_1 - \frac{g_{21}}{g_{22}} \partial_2 \right) + \boldsymbol{e}^3 \left(\partial_3 - \frac{g_{23}}{g_{22}} \partial_2 \right).
\end{aligned}$$

The BOUT++ implementation of the inversion algorithm assumes small parallel gradients in the dependent variable, so that

$$\nabla_\perp \simeq \boldsymbol{e}^1 \partial_1 + \boldsymbol{e}^3 \partial_3. \tag{K.7}$$

As mentioned, this approximation is not of concern when using cylindrical coordinates, as only the diagonal terms in the metric tensor is non-zero.

K.2 Numerical implementation

By inserting eqs. (K.6) and (K.6) into eq. (K.1), we get

$$\begin{aligned}
& d \left(g^{11} \partial_1^2 + G^1 \partial_1 + g^{33} \partial_3^2 + G^3 \partial_3 + 2 g^{13} \partial_1 \partial_3 \right) f \\
+ & \frac{1}{c_1} \left(\boldsymbol{e}^1 \partial_1 + \boldsymbol{e}^3 \partial_3 \right) c_2 \cdot \left(\boldsymbol{e}^1 \partial_1 + \boldsymbol{e}^3 \partial_3 \right) f \\
+ & a f = b,
\end{aligned} \tag{K.8}$$

which we would like to solve for f. As there are no parallel y-derivatives in equation (K.8), the equation can be inverted for each y plane. In addition, if the modes decouples[2] when Fourier transforming equation (K.8), we can use a tridiagonal solver to solve the equation for each Fourier mode. In other words, if n_x, n_y and n_z are the number of points in each of the three directions, we need to invert a $n_x \times n_x$ matrix n_z times for each of the n_y y-planes, rather than inverting a $n_x \cdot n_y \cdot n_z \times n_x \cdot n_y \cdot n_z$ matrix once.

Taking the Fourier transform of eq. (K.8) is equivalent with multiplying the left hand side and the right hand side with $\exp(-2\pi i z \xi)$ and integrating the periodic z-coordinate from $-\infty$ to ∞. The modes will only decouple if there are no products of functions depending on z [3] . Hence, we must require that a, c and d cannot be functions of z.

[2] Meaning that eq. (K.8) can be solved for one mode at the time rather than for all modes at the same time.

[3] If we define the Fourier transform as $F(x,y,\xi) = \int_{-\infty}^{\infty} f(x,y,z) \exp(-2\pi i z \xi) \, \mathrm{d}z$. One can show that (see [76] for details) $\int_{-\infty}^{\infty} a(x,y,z) f(x,y,z) \exp(-2\pi i z \xi) \, \mathrm{d}z = A(x,y,\xi) * F(x,y,\xi)$, where $*$ denotes the convolution product. I.e. $A(x,y,\xi) * F(x,y,\xi)$ mixes the modes of a and f together.

Because of this, the $\boldsymbol{e}^3\partial_3 c$ term in equation (K.8) is zero. In principle the modes would still decouple if the $\boldsymbol{e}^3\partial_3 f$ part of equation (K.8) was kept, but currently this part is also neglected in the implementation. Thus, the BOUT++ implementation solves equations on the form

$$\begin{aligned}
&d(x,y)\left(g^{11}(x,y)\partial_1^2 + G^1(x,y)\partial_1 + g^{33}(x,y)\partial_3^2 + G^3(x,y)\partial_3 + 2g^{13}(x,y)\partial_1\partial_3\right) f(x,y,z)\\
&+\frac{1}{c(x,y)}\left(\boldsymbol{e}^1\partial_1\right) c(x,y)\cdot\left(\boldsymbol{e}^1\partial_1\right) f(x,y,z)\\
&+a(x,y)f(x,y,z) = b(x,y,z).
\end{aligned} \tag{K.9}$$

K.2.1 The matrix to solve

By using what was discussed in appendix L, we see that the discrete Fourier transform of eq. (K.9) is

$$\begin{aligned}
&d\left(g^{11}\partial_1^2 F_Z + G^1\partial_1 F_Z + g^{33}[ik]^2 F_Z + G^3[ik]F_Z + 2g^{13}\partial_1[ik]F_Z\right)\\
&+\frac{1}{c}\left(\boldsymbol{e}^1\partial_1\right) c\cdot\left(\boldsymbol{e}^1\partial_1 F_Z\right)\\
&+aF_Z = B_Z,
\end{aligned}$$

which gives

$$\begin{aligned}
&d\left(g^{11}\partial_1^2 + G^1\partial_1 - k^2 g^{33} + ikG^3 + ik2g^{13}\partial_1\right) F_Z\\
&+\frac{g^{11}}{c}\left(\partial_1 c\right)\partial_1 F_Z\\
&+aF_Z = B_Z.
\end{aligned} \tag{K.10}$$

The second order centered approximation of the first and second derivatives in x read

$$\partial_x f \simeq \frac{-f_{n-1} + f_{n+1}}{2\mathrm{d}x} \qquad\qquad \partial_x^2 f \simeq \frac{f_{n-1} - f_n + f_{n+1}}{\mathrm{d}x^2},$$

which inserted in eq. (K.10) yields

$$\begin{aligned}
&d\left(g^{11}\frac{F_{Z,n-1} - 2F_{Z,n} + F_{Z,n+1}}{\mathrm{d}x^2} + G^1\frac{-F_{Z,n-1} + F_{Z,n+1}}{2\mathrm{d}x} - k^2 g^{33}F_{Z,n}\right.\\
&\qquad\left.+ikG^3F_{Z,n} + ik2g^{13}\frac{-F_{Z,n-1} + F_{Z,n+1}}{2\mathrm{d}x}\right)\\
&+\frac{g^{11}}{c}\left(\frac{-c_{n-1} + c_{n+1}}{2\mathrm{d}x}\right)\frac{-F_{Z,n-1} + F_{Z,n+1}}{2\mathrm{d}x}\\
&+aF_{Z,n} = B_{Z,n}.
\end{aligned} \tag{K.11}$$

If we now collect eq. (K.11) point by point, we get

$$\begin{aligned}
&\left(\frac{dg^{11}}{\mathrm{d}x^2} - \frac{dG^1}{2\mathrm{d}x} - \frac{g^{11}}{c_n}\frac{-c_{n-1} + c_{n+1}}{4\mathrm{d}x^2} - i\frac{dk2g^{13}}{2\mathrm{d}x}\right) F_{Z,n-1}\\
&+\left(-\frac{dg^{11}}{\mathrm{d}x^2} - dk^2 g^{33} + a + idkG^3\right) F_{Z,n}
\end{aligned}$$

$$
\begin{aligned}
&+\left(\frac{dg^{11}}{\mathrm{d}x^2}+\frac{dG^1}{2\mathrm{d}x}+\frac{g^{11}}{c_n}\frac{-c_{n-1}+c_{n+1}}{4\mathrm{d}x^2}+i\frac{dk2g^{13}}{2\mathrm{d}x}\right)F_{Z,n+1}\\
&=B_{Z,n}.
\end{aligned}
\tag{K.12}
$$

We now introduce

$$
\begin{aligned}
h_1&=\frac{dg^{11}}{\mathrm{d}x^2} & h_2&=dg^{33} & h_3&=\frac{2dg^{13}}{2\mathrm{d}x}\\
h_4&=\frac{dG^1+g^{11}\frac{-h_{n-1}+h_{n+1}}{2h_n\mathrm{d}x}}{2\mathrm{d}x} & h_5&=dG^3.
\end{aligned}
$$

Inserting this in equation (K.12) gives

$$
\begin{aligned}
&(h_1-h_4-ikh_3)\,F_{Z,n-1}\\
&+\left(-2h_1-k^2h_2+ikh_5+a\right)F_{Z,n}\\
&+(h_1+h_4+ikh_3)\,F_{Z,n+1}\\
&=B_{Z,n}.
\end{aligned}
$$

This can be formulated as the matrix equation

$$AF_Z=B_Z,$$

where the matrix A is tridiagonal. The boundary conditions are set by setting the first and last rows in A and B_Z.

Appendix L

Derivatives of the Fourier transform

By using the definition of the Fourier transformed, we have

$$F(x,y,\xi) = \int_{-\infty}^{\infty} f(x,y,z) \exp\left(-2\pi i z \xi\right) \mathrm{d}z.$$

This gives

$$\begin{aligned}
&\int_{-\infty}^{\infty} \left(\partial_z f[x,y,z]\right) \exp\left(-2\pi i z \xi\right) \mathrm{d}z \\
=&\int_{-\infty}^{\infty} \partial_z \left(f[x,y,z] \exp\left[-2\pi i z \xi\right]\right) \mathrm{d}z - \int_{-\infty}^{\infty} f(x,y,z) \partial_z \exp\left(-2\pi i z \xi\right) \mathrm{d}z \\
=&\left(f[x,y,z] \exp\left[-2\pi i z \xi\right]\right)\Big|_{-\infty}^{\infty} - \left(-2\pi i \xi\right) \int_{-\infty}^{\infty} f(x,y,z) \exp\left(-2\pi i z \xi\right) \mathrm{d}z \\
=&2\pi i \xi F(x,y,\xi), \qquad \text{(L.1)}
\end{aligned}$$

where we have used that $f(x,y,\pm\infty) = 0$ in order to have a well-defined Fourier transform. This means that

$$\partial_z^n F(x,y,\xi) = (2\pi i \xi)^n F(x,y,\xi).$$

In our case, we are dealing with periodic boundary conditions. Strictly speaking, the Fourier transform does not exist in such cases, but it is possible to define a Fourier transform in the limit which in the end leads to the Fourier series (see [76] for details).

By discretizing the spatial domain, it is no longer possible to represent the infinite amount of Fourier modes, but only $N+1$ number of modes, where N is the number of points (this includes the modes with negative frequencies, and the zeroth offset mode). For the discrete Fourier transform, we have

$$F(x,y)_k = \frac{1}{N} \sum_{Z=0}^{N-1} f(x,y)_Z \exp\left(\frac{-2\pi i k Z}{N}\right), \qquad \text{(L.2)}$$

where k is the mode number, N is the number of points in z. If we call the sampling points of z for z_Z, where $Z = 0, 1 \ldots N-1$, we have that $z_Z = Z\mathrm{d}z$. As our domain goes from $[0, 2\pi[$, we have that (since we have one less line segments than points) $\mathrm{d}z(N-1) = L_z = 2\pi - \mathrm{d}z$, which gives $\mathrm{d}z = \dfrac{2\pi}{N}$. Inserting this is equation (L.2)

yields

$$F(x,y)_k = \frac{1}{N}\sum_{Z=0}^{N-1} f(x,y)_Z \exp\left(-ikZ\mathrm{d}z\right) = \frac{1}{N}\sum_{Z=0}^{N-1} f(x,y)_Z \exp\left(-ikz_Z\right).$$

The discrete version of equation (L.1) thus gives

$$\partial_z^n F(x,y)_k = (ik)^n F(x,y)_k.$$

Part VI

Bibliography

Bibliography

[1] U. E. I. Administration, *International Energy Outlook 2016*. Washington: U.S. Energy Information Administration, 2011.

[2] J. Freidberg, *Plasma Physics and Fusion Energy*. Cambridge University Press, 2008.

[3] The ITER Organization, 2016. https://www.iter.org/, Visited: 2017.02.13.

[4] D. MacKay, *Sustainable Energy–without the Hot Air*. Without the Hot Air Series, UIT, 2009.

[5] J. Melorose, R. Perroy, and S. Careas, "World population prospects," *United Nations*, vol. 1, no. 6042, pp. 587–92, 2015.

[6] E. E. Bloom, "The challenge of developing structural materials for fusion power systems," *Journal of Nuclear Materials*, vol. 258-263, no. 1998, pp. 7–17, 1998.

[7] G. Kessler, *Sustainable and Safe Nuclear Fission Energy: Technology and Safety of Fast and Thermal Nuclear Reactors*. Power Systems, Springer Berlin Heidelberg, 2012.

[8] J. Ongena and G. Van Oost, "Energy for Future Centuries: Prospects for Fusion Power as a Future Energy Source," *Fusion Science and Technology*, vol. 61, no. 2T, pp. 3–16, 2012.

[9] D. Eckhartt, "Nuclear fuels for low-beta fusion reactors: Lithium resources revisited," *Journal of Fusion Energy*, vol. 14, no. 4, pp. 329–341, 1995.

[10] S. Balibar, 2009. http://news.bbc.co.uk/2/hi/science/nature/8103557.stm, Visited: 2017.02.13.

[11] W. J. Nuttall, "Fusion as an energy source: Challenges and Opportunities," *IOP Report*, no. 9, 2008.

[12] P. Stangeby, *The Plasma Boundary of Magnetic Fusion Devices*. Series in Plasma Physics and Fluid Dynamics, Taylor & Francis, 2000.

[13] W. Stacey, *Fusion Plasma Physics*. Physics textbook, Wiley, 2012.

[14] H. Zohm, "Edge localized modes (ELMs)," *Plasma Physics and Controlled Fusion*, vol. 38, pp. 105–128, 1996.

[15] B. D. Scott, "Drift wave versus interchange turbulence in tokamak geometry : Linear versus nonlinear mode structure," *Physics of Plasmas*, vol. 062314, no. 12, 2005.

[16] G. R. Tynan, A. Fujisawa, and G. McKee, "A review of experimental drift turbulence studies," *Plasma Physics and Controlled Fusion*, vol. 51, no. 11, p. 113001, 2009.

[17] K. H. Burrell, "Effects of E cross B velocity shear and magnetic shear on turbulence and transport in magnetic confinement devices," *Physics of Plasmas*, vol. 4, no. 1499, 1997.

[18] A. J. Wootton, B. A. Carreras, H. Matsumoto, K. McGuire, W. A. Peebles, C. P. Ritz, P. W. Terry, and S. J. Zweben, "Fluctuations and anomalous transport in tokamaks," *Physics of Fluids B-Plasma Physics*, vol. 2, no. 12, 1990.

[19] D. A. D'Ippolito, J. R. Myra, and S. J. Zweben, "Convective transport by intermittent blob-filaments: Comparison of theory and experiment," *Physics of Plasmas*, vol. 18, no. 6, p. 060501, 2011.

[20] J. Rapp, W. R. Koppers, H. J. N. Van Eck, G. J. Van Rooij, W. J. Goedheer, B. De Groot, R. Al, M. F. Graswinckel, M. A. Van Den Berg, O. Kruyt, P. Smeets, H. J. Van Der Meiden, W. Vijvers, J. Scholten, M. Van De Pol, S. Brons, W. Melissen, T. Van Der Grift, R. Koch, B. Schweer, U. Samm, V. Philipps, R. A. H. Engeln, D. C. Schram, N. J. Lopes Cardozo, and A. W. Kleyn, "Construction of the plasma-wall experiment Magnum-PSI," *Fusion Engineering and Design*, vol. 85, no. 7-9, pp. 1455–1459, 2010.

[21] H. Bohlin, A. Von Stechow, K. Rahbarnia, O. Grulke, and T. Klinger, "VINETA II: A linear magnetic reconnection experiment," *Review of Scientific Instruments*, vol. 85, no. 2, 2014.

[22] N. Ohno, "Plasma detachment in linear devices," *Plasma Physics and Controlled Fusion*, vol. 59, no. 034007, 2017.

[23] I. Klimontovich, *The kinetic theory of electromagnetic processes.* Springer series in synergetics, Springer-Verlag, 1983.

[24] P. Helander and D. Sigmar, *Collisional Transport in Magnetized Plasmas.* Cambridge Monographs on Plasma Physics, Cambridge University Press, 2002.

[25] S. I. Braginskii, "Transport processes in a plasma," *Reviews of Plasma Physics*, vol. 1, p. 205, 1965.

[26] S. Chapman and T. Cowling, *The Mathematical Theory of Non-uniform Gases: An Account of the Kinetic Theory of Viscosity, Thermal Conduction and Diffusion in Gases.* Cambridge Mathematical Library, Cambridge University Press, 1970.

[27] S. Brush, *Kinetic Theory: The Chapman-Enskog solution of the transport equation for moderately dense gases.* International series of monographs in natural philosophy, Pergamon Press, 1972.

[28] R. Fitzpatrick, *Plasma Physics: An Introduction.* Taylor & Francis, 2014.

[29] W. Baumjohann and R. Treumann, *Basic Space Plasma Physics.* Imperial College Press, 1997.

[30] O. E. Garcia, "Collective motions in non-uniformly magnetized plasmas," *European Journal of Physics*, vol. 24, no. 4, pp. 331–339, 2003.

[31] O. E. Garcia, V. Naulin, A. H. Nielsen, and J. J. Rasmussen, "Turbulence and intermittent transport at the boundary of magnetized plasmas," *Physics of Plasmas*, vol. 12, no. 6, p. 062309, 2005.

[32] Z. Chang and J. D. Callen, "Generalized gyroviscous force and its effect on the momentum balance equation," *Physics of Fluids B-Plasma Physics*, vol. 4, no. 1766, 1992.

[33] A. I. Smolyakov, "Gyroviscous forces in a collisionless plasma with temperature gradients," *Canadian Journal of Physics*, vol. 76, no. 4, pp. 321–331, 1998.

[34] A. H. Nielsen, H. L. Pécseli, and J. J. Rasmussen, "Turbulent transport in low-beta plasmas," *Physics of Plasmas*, vol. 3, no. 5, p. 1530, 1996.

[35] R. W. Boswell, "Very efficient plasma generation," *Plasma Physics*, vol. 26, 1984.

[36] K. P. Shamrai, "Stable modes and abrupt density jumps in a helicon plasma source," *Plasma Sources Sci. Technol.*, vol. 7, pp. 499–511, 1996.

[37] C. Schröder, O. Grulke, T. Klinger, and V. Naulin, "Drift waves in a high-density cylindrical helicon discharge," *Physics of Plasmas*, vol. 12, no. 4, pp. 1–6, 2005.

[38] S. Oldenbürger, S. Inagaki, T. Kobayashi, H. Arakawa, N. Ohyama, K. Kawashima, Y. Tobimatsu, a. Fujisawa, K. Itoh, and S.-I. Itoh, "Dynamics of particle flux in a cylindrical magnetized plasma," *Plasma Physics and Controlled Fusion*, vol. 54, no. 5, p. 055002, 2012.

[39] G. R. Tynan, M. J. Burin, C. Holland, G. Antar, N. Crocker, and P. H. Diamond, "Radially sheared azimuthal flows and turbulent transport in a cylindrical plasma," *Physics of Plasmas*, vol. 11, no. 11, pp. 5195–5203, 2004.

[40] W. Gekelman, H. Pfister, Z. Lucky, J. Bamber, D. Leneman, and J. Maggs, "Design, construction, and properties of the large plasma research device - The LAPD at UCLA," *Review of Scientific Instruments*, vol. 62, no. 12, pp. 2875–2883, 1991.

[41] W. Gekelman, P. Pribyl, Z. Lucky, M. Drandell, D. Leneman, J. Maggs, S. Vincena, B. Van Compernolle, S. K. P. Tripathi, G. Morales, T. A. Carter, Y. Wang, and T. DeHaas, "The upgraded Large Plasma Device, a machine for studying frontier basic plasma physics," *Review of Scientific Instruments*, vol. 87, no. 2, p. 25105, 2016.

[42] P. Kundu and I. Cohen, *Fluid Mechanics*. Elsevier Science, 2010.

[43] R. LeVeque, *Finite Difference Methods for Ordinary and Partial Differential Equations: Steady-State and Time-Dependent Problems*. Society for Industrial and Applied Mathematics, 2007.

[44] B. Dudson. Private communication, 2015.

[45] J. Loizu, P. Ricci, F. D. Halpern, and S. Jolliet, "Boundary conditions for plasma fluid models at the magnetic presheath entrance," *Physics of Plasmas*, vol. 19, no. 12, p. 122307, 2012.

[46] T. Yamada, S. Inagaki, T. Kobayashi, Y. Nagashima, T. Mitsuzono, Y. Miwa, K. Nakanishi, H. Fujino, M. Sasaki, N. Kasuya, M. Lesur, Y. Kosuga, A. Fujisawa, S.-I. Itoh, and K. Itoh, "End plate biasing experiments in linear magnetized plasmas," *Nuclear Fusion Nucl. Fusion*, vol. 54, pp. 114010–5, 2014.

[47] S. Chakraborty Thakur, M. Xu, P. Manz, N. Fedorczak, C. Holland, and G. R. Tynan, "Suppression of drift wave turbulence and zonal flow formation by changing axial boundary conditions in a cylindrical magnetized plasma device," *Physics of Plasmas*, vol. 20, no. 1, 2013.

[48] P. H. Diamond and Y. B. Kim, "Theory of Mean Poloidal Flow Generation by Turbulence," *Physics of Fluids B-Plasma Physics*, vol. 3, no. 7, pp. 1626–1633, 1991.

[49] C. Schröder, T. Klinger, D. Block, A. Piel, G. Bonhomme, and V. Naulin, "Mode selective control of drift wave turbulence," *Physical Review Letters*, vol. 86, no. 25, pp. 5711–5714, 2001.

[50] C. Schröder, *Experimental investigations on drift waves in linear magnetized plasmas*. PhD thesis, Ernst-Moritz-Arndt-Universität Greifswald, Greifswald, 2002.

[51] N. Kasuya, M. Yagi, and K. Itoh, "Simulation of resistive drift wave turbulence," *Journal of Plasma Physics*, vol. 72, pp. 957–960, 2006.

[52] M. Sasaki, N. Kasuya, K. Itoh, M. Yagi, and S.-I. Itoh, "Nonlinear competition of turbulent structures and improved confinement in magnetized cylindrical plasmas," *Nuclear Fusion*, vol. 54, no. 11, p. 114009, 2014.

[53] G. N. Kervalishvili, R. Kleiber, R. Schneider, B. D. Scott, O. Grulke, and T. Windisch, "Intermittent turbulence in the linear VINETA device," *Contributions to Plasma Physics*, vol. 48, no. 1-3, pp. 32–36, 2008.

[54] P. Popovich, M. V. Umansky, T. A. Carter, and B. Friedman, "Analysis of plasma instabilities and verification of the BOUT code for the Large Plasma Device," *Physics of Plasmas*, vol. 17, no. 10, 2010.

[55] P. Popovich, M. V. Umansky, T. A. Carter, and B. Friedman, "Modeling of plasma turbulence and transport in the Large Plasma Device," *Physics of Plasmas*, vol. 17, no. 12, 2010.

[56] B. N. Rogers and P. Ricci, "Low-frequency turbulence in a linear magnetized plasma," *Physical Review Letters*, vol. 104, no. 22, pp. 4–7, 2010.

[57] B. Friedman, T. A. Carter, M. V. Umansky, D. Schaffner, and B. Dudson, "Energy dynamics in a simulation of LAPD turbulence," *Physics of Plasmas*, vol. 19, no. 10, 2012.

[58] D. M. Fisher, B. N. Rogers, G. D. Rossi, and D. S. Guice, "Three-dimensional two-fluid Braginskii simulations of the large plasma device," *Physics of Plasmas*, vol. 22, no. 9, p. 092121, 2015.

[59] D. Reiser, "Revisited global drift fluid model for linear devices," *Physics of Plasmas*, vol. 19, no. 7, 2012.

[60] D. Reiser, N. Ohno, H. Tanaka, and L. Vela, "A plasma source driven predator-prey like mechanism as a potential cause of spiraling intermittencies in linear plasma devices," *Physics of Plasmas*, vol. 21, no. 3, 2014.

[61] B. D. Dudson, M. V. Umansky, X. Q. Xu, P. B. Snyder, and H. R. Wilson, "BOUT++: A framework for parallel plasma fluid simulations," *Computer Physics Communications*, vol. 180, pp. 1467–1480, sep 2009.

[62] B. D. Dudson, a. Allen, G. Breyiannis, E. Brugger, J. Buchanan, L. Easy, S. Farley, I. Joseph, M. Kim, a. D. McGann, J. T. Omotani, M. V. Umansky, N. R. Walkden, T. Xia, and X. Q. Xu, "BOUT++: Recent and current developments," *Journal of Plasma Physics*, vol. 81, no. 01, 2014.

[63] B. Dudson, J. Madsen, J. Omotani, P. Hill, L. Easy, and M. Løiten, "Verification of BOUT++ by the Method of Manufactured Solutions," *Physics of Plasmas*, vol. 062303, no. 23, 2016.

[64] X. Q. Xu and R. H. Cohen, "Scrape-Off Layer Turbulence Theory and Simulations," *Contributions to Plasma Physics*, vol. 38, no. 2-3, pp. 158–170, 1998.

[65] T. Rognlien, B. Braams, and D. A. Knoll, "Progress i n Integrated 2-D Models for Analysis," *Contributions to Plasma Physics*, vol. 36, pp. 105–116, 1996.

[66] M. Frigo and S. Johnson, "The Design and Implementation of {FFTW3}," *Proceedings of the IEEE*, vol. 93, no. 2, pp. 216–231, 2005.

[67] A. C. Hindmarsh and R. Serban, *User Documentation for cvode v2.7.0*. Center for Applied Scientific Computing Lawrence Livermore National Laboratory: Lawrence Livermore National Laboratory, 2012.

[68] Y. Saad, *Iterative Methods for Sparse Linear Systems: Second Edition*. Society for Industrial and Applied Mathematics, 2003.

[69] D. A. Knoll and D. E. Keyes, "Jacobian-free Newton-Krylov methods: A survey of approaches and applications," *Journal of Computational Physics*, vol. 193, no. 2, pp. 357–397, 2004.

[70] B. Dudson, S. Farley, and L. Curfman, "Improved Nonlinear Solvers in BOUT ++," *arXiv*, pp. 1–15, 2012.

[71] A. Arakawa, "Computational Design for Long Term Numerical Integration of the Equations of Fluid Motion: Two-Dimensional Incompressible Flow. Part I," *J. Comput. Phys.*, vol. 1, no. 122, pp. 119–143, 1966.

[72] N. A. Phillips, "An example of non-linear computational instability," 1959.

[73] M. Wiesenberger, *Gyrofluid computations of filament dynamics in tokamak scrape-off layers*. PhD thesis, Leopold-Franzens-Universität Innsbruck, Innsbruck, 2014.

[74] V. Naulin, T. Windisch, and O. Grulke, "Three-dimensional global fluid simulations of cylindrical magnetized plasmas," *Physics of Plasmas*, vol. 15, no. 1, pp. –, 2008.

[75] S. A. Orszag, "On the Elimination of Aliasing in Finite-Difference Schemes by Filtering High-Wavenumber Components," 1971.

[76] R. Bracewell, *The Fourier Transform and Its Applications*. Electrical engineering series, McGraw Hill, 2000.

[77] W. Oberkampf and C. Roy, *Verification and Validation in Scientific Computing*. Cambridge University Press, 2010.

[78] K. Salari and P. Knupp, *Code Verification by the Method of Manufactured Solutions SAND2000-1444*. Albuquerque: Sandia National Laboratories, 2000.

[79] B. Dudson. Private communication, 2017.

[80] A. E. Honein and P. Moin, "Higher entropy conservation and numerical stability of compressible turbulence simulations," *Journal of Computational Physics*, vol. 201, no. 2, pp. 531–545, 2004.

[81] S. Pirozzoli, "Stabilized non-dissipative approximations of Euler equations in generalized curvilinear coordinates," *Journal of Computational Physics*, vol. 230, no. 8, pp. 2997–3014, 2011.

[82] CINECA, 2016. https://wiki.u-gov.it/confluence/display/SCAIUS/UG3.1%3A+MARCONI+UserGuide, Visited: 2017.02.10.

[83] D. L. Jassby, "Transverse Velocity Shear Instabilities within a Magnetically Confined Plasma," *Physics of Fluids*, vol. 15, no. 9, p. 1590, 1972.

[84] U. Stroth, *Plasmaphysik, Phänomene, Grundlagen, Anwendungen*. Wiesbaden: Vieweg+Teubner, 2011.

[85] T. G. Shepherd, "Rossby waves and two-dimensional turbulence in a large-scale zonal jet," *J. Fluid Mech.*, vol. 183, pp. 467–509, 1987.

[86] O. E. Garcia, "Two-field transport models for magnetized plasmas," *Physics, J Plasma*, vol. 65, pp. 81–96, jul 2001.

[87] H. Pécseli, *Low Frequency Waves and Turbulence in Magnetized Laboratory Plasmas and in the Ionosphere*. 2053-2563, IOP Publishing, 2016.

[88] W. Horton, "Drift waves and transport," *Reviews of Modern Physics*, vol. 71, no. 3, pp. 735–778, 1999.

[89] R. F. Ellis, E. Marden-Marshall, and R. Majeski, "Collisional drift instability of a weakly ionized argon plasma," *Plasma Physics*, vol. 22, no. 2, pp. 113–131, 1980.

[90] J. J. Rasmussen, O. E. Garcia, V. Naulin, A. H. Nielsen, B. Stenum, L. J. A. van Bokhoven, and S. Delaux, "Generation of zonal flows in rotating fluids and magnetized plasmas," *Physica Scripta*, vol. T122, pp. 44–51, 2006.

[91] F. F. Chen, "Effect of Sheaths on Drift Instabilities in Thermionic Plasmas," *Physics of Fluids*, vol. 8, no. 4, p. 752, 1965.

[92] T. Huld, S. Iizuka, H. L. Pécseli, and J. J. Rasmussen, "Experimental investigation of flute-type electrostatic turbulence," *Plasma Physics and Controlled Fusion*, vol. 30, pp. 1297–1318, sep 1988.

[93] S. Miller and D. Childers, *Probability and Random Processes: With Applications to Signal Processing and Communications*. Elsevier Science, 2004.

[94] H. W. Hendel, "Collisional Drift Waves - Identification, Stabilization, and Enhanced Plasma Transport," *Physics of Fluids*, vol. 11, no. 11, p. 2426, 1968.

[95] C. P. Ritz, E. J. Powers, and R. D. Bengtson, "Experimental measurement of three-wave coupling and energy cascading," *Physics of Fluids B: Plasma Physics*, vol. 1, no. May 2015, pp. 153–163, 1989.

[96] G. Knorr, J. P. Lynov, and H. L. Pécseli, "Self-Organization in Three-Dimensional Hydrodynamic Turbulence," *Zeitschrift für Naturforschung A*, vol. 1073, pp. 1059–1073, 1990.

[97] a. N. Kolmogorov, "A refinement of previous hypotheses concerning the local structure of turbulence," *J. Fluid. Mech*, vol. 13, no. September, pp. 83–85, 1962.

[98] R. H. Kraichan and D. Montgomery, "Two-Dimensional Turbulence," *Reports on Progress in Physics*, vol. 43, 1980.

[99] R. Fjørtoft, "On the Changes in the Spectral Distribution of Kinetic Energy for Twodimensional, Nondivergent Flow," *Tellus*, vol. 5, no. 3, 1953.

[100] K. S. Smith, G. Boccaletti, C. C. Henning, I. Marinov, C. Y. Tam, I. M. Held, and G. K. Vallis, "Turbulent diffusion in the geostrophic inverse cascade," *Journal of Fluid Mechanics*, vol. 469, no. 2002, pp. 13–48, 2002.

[101] G. Boffetta, F. De Lillo, and S. Musacchio, "Inverse cascade in Charney-Hasegawa-Mima turbulence," *Europhysics Letters (EPL)*, vol. 59, no. 5, pp. 687–693, 2002.

[102] P. Manz, M. Ramisch, and U. Stroth, "Experimental estimation of the dual cascade in two-dimensional drift-wave turbulence," *Plasma Physics and Controlled Fusion*, vol. 51, no. 3, p. 035008, 2009.

[103] G. R. Tynan, C. Holland, J. H. Yu, A. James, D. Nishijima, M. Shimada, and N. Taheri, "Observation of turbulent-driven shear flow in a cylindrical laboratory plasma device," *Plasma Physics and Controlled Fusion*, vol. 48, no. 4, pp. S51–S73, 2006.

[104] M. J. Burin, G. R. Tynan, G. Y. Antar, N. A. Crocker, and C. Holland, "On the transition to drift turbulence in a magnetized plasma column," *Physics of Plasmas*, vol. 12, no. 5, pp. 1–14, 2005.

[105] A. Hasegawa and M. Wakatani, "Self-Organization of Electrostatic Turbulence in a Cylindrical Plasma," *Physical Review Letters*, vol. 59, no. 14, pp. 1581–1584, 1987.

[106] C. Holland, G. R. Tynan, A. James, J. H. Yu, D. Nishijima, M. Shimada, and N. Taheri, "Numerical simulations of collisional drift-wave turbulence in a magnetized plasma column," *Plasma Physics and Controlled Fusion*, vol. 49, no. 5A, pp. A109–A119, 2007.

[107] T. Windisch, O. Grulke, V. Naulin, and T. Klinger, "Intermittent transport events in a cylindrical plasma device: experiment and simulation," *Plasma Physics and Controlled Fusion*, vol. 53, no. 8, p. 085001, 2011.

[108] T. Windisch, O. Grulke, V. Naulin, and T. Klinger, "Formation of turbulent structures and the link to fluctuation driven sheared flows," *Plasma Physics and Controlled Fusion*, vol. 53, p. 124036, 2011.

[109] G. Xu, V. Naulin, W. Fundamenski, C. Hidalgo, J. Alonso, C. Silva, B. Gonçalves, A. Nielsen, J. J. Rasmussen, S. Krasheninnikov, B. Wan, M. Stamp, and J. E. Contributors, "Blob / hole formation and zonal-flow generation in the edge plasma of the JET tokamak," *Nuclear Fusion*, vol. 49, no. 092002, 2009.

[110] S. I. Krasheninnikov, D. A. D'Ippolito, and J. R. Myra, *Recent theoretical progress in understanding coherent structures in edge and SOL turbulence*, vol. 74. jan 2008.

[111] L. S. G. Kovasznay, V. Kibens, and R. F. Blackwelder, "Large-scale motion in the intermittent region of a turbulent boundary layer," *Journal of Fluid Mechanics*, vol. 41, no. 2, pp. 283–325, 1970.

[112] T. Huld, A. H. Nielsen, H. L. Pecseli, and J. J. Rasmussen, "Plasma vortices and their relation to cross-field diffusion: A laboratory study," *Phys. Rev. Lett.*, vol. 64, no. 25, pp. 3023–3026, 1990.

[113] I. Teliban, D. Block, A. Piel, and F. Greiner, "Improved conditional averaging technique for plasma fluctuation diagnostics," *Plasma Physics and Controlled Fusion*, vol. 49, pp. 485–497, apr 2007.

[114] R. V. Edwards and A. S. Jensen, "Particle-sampling statistics in laser anemometers: sample-and-hold systems and saturable systems," *J. Fluid Mech*, vol. 133, pp. 397–411, 1983.

[115] H. L. Pécseli. Private communication, 2017.

[116] A. S. Bergsaker, Å. Fredriksen, H. L. Pécseli, and J. K. Trulsen, "Models for the probability densities of the turbulent plasma flux in magnetized plasmas," *Physica Scripta*, vol. 90, no. 10, p. 108005, 2015.

[117] S. I. Krasheninnikov and A. I. Smolyakov, "On neutral wind and blob motion in linear devices," *Physics of Plasmas*, vol. 10, no. 7, pp. 3020–3021, 2003.

[118] W. Horton, T. Tajima, and T. Kamimura, "Kelvin-Helmholtz Instability and Vortices in Magnetized Plasma," *Physics of Fluids*, vol. 30, pp. 3485–3495, 1987.

[119] H. Pécseli, *Waves and Oscillations in Plasmas*. Series in Plasma Physics and Fluid Dynamics, Taylor & Francis, 2012.

[120] G. Hornung, B. Nold, J. E. Maggs, G. J. Morales, M. Ramisch, and U. Stroth, "Observation of exponential spectra and Lorentzian pulses in the TJ-K stellarator," *Physics of Plasmas*, vol. 18, no. 8, 2011.

[121] P. W. Terry, "Suppression of turbulence and transport by sheared flow," *Reviews of Modern Physics*, vol. 72, no. 1, pp. 109–165, 2000.

[122] P. H. Diamond, S.-I. Itoh, K. Itoh, and T. S. Hahm, "Zonal flows in plasma - a review," *Plasma Physics and Controlled Fusion*, vol. 47, no. 5, pp. R35–R161, 2005.

[123] E. Viezzer, *Radial electric field studies in the plasma edge of ASDEX Upgrade*. PhD thesis, Ludwig-Maximilians-Universität München, Munich, 2012.

[124] S. S. Limaye, "Jupiter: New estimates of the mean zonal flow at the cloud level," *Icarus*, vol. 65, no. 2-3, pp. 335–352, 1986.

[125] T. Klinger, A. Latten, A. Piel, G. Bonhomme, and T. Pierre, "Chaos and turbulence studies in low- plasmas," *Plasma Physics and Controlled Fusion*, vol. 39, no. 12B, pp. B145–B156, 1997.

[126] T. Klinger, a. Latten, a. Piel, G. Bonhomme, T. Pierre, and T. Dudok de Wit, "Route to Drift Wave Chaos and Turbulence in a Bounded Low- β Plasma Experiment," *Physical Review Letters*, vol. 79, no. 20, pp. 3913–3916, 1997.

[127] W. D'haeseleer, *Flux coordinates and magnetic field structure: a guide to a fundamental tool of plasma structure*. Springer series in computational physics, Springer-Verlag, 1991.

[128] R. Goldston and P. Rutherford, *Introduction to Plasma Physics*. CRC Press, 1995.

[129] M. Hayashi, *Recommended Values of Transport Cross Sections for Elastic Collision and Total Collision Cross Section for Electrons in Atomic and Molecular Gases*. IPPJ-AM reports, Institute of Plasma Physics, Nagoya University, 1981.

[130] A. Rohatgi, 2016. http://arohatgi.info/WebPlotDigitizer/, Visited: 2016.01.10.

[131] M. Lieberman and A. Lichtenberg, *Principles of Plasma Discharges and Materials Processing*. Wiley, 2005.

[132] A. Anders, *A Formulary for Plasma Physics*. John Wiley & Sons (Sd), 1990.

[133] D. Griffiths, *Introduction to Electrodynamics*. Always learning, Pearson, 2013.

[134] R. Fitzpatrick, *Maxwell's Equations and the Principles of Electromagnetism*. Infinity Science Series, Infinity Science Press, 2008.

[135] M. Wiesenberger, J. Madsen, and A. Kendl, "Radial convection of finite ion temperature, high amplitude plasma blobs," *Physics of Plasmas*, vol. 21, p. 92301, sep 2014.

[136] C. Kittel and H. Kroemer, *Thermal Physics*. W. H. Freeman, 1980.